Universiteit Gent
Faculteit van de Toegepaste Wetenschappen
Vakgroep Mechanica van Stroming,
Warmte en Verbranding

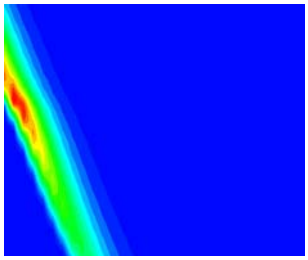

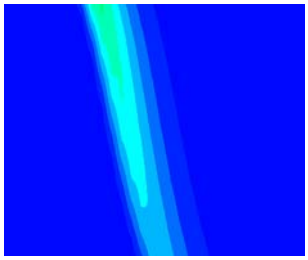

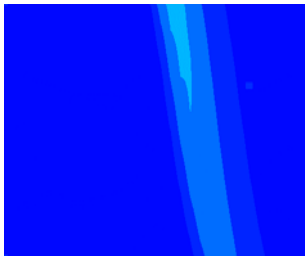

Numerieke modellering van vlamvoortplanting

Numerical modelling of flame spread

door **ir. E. Theuns**
Promotor **Prof. dr. ir. P. Vandevelde**

Proefschrift voorgelegd tot het bekomen van de graad van doctor in de toegepaste wetenschappen

Mei 2003

Acknowledgement

In the first place, I would like to thank my promotor Prof. dr. ir. P. Vandevelde for giving me the opportunity to do this research. I very much appreciated his confidence in me, as well the freedom he gave me to explore the fire research domain.

Also, I would like to thank Prof. ir. E. Dick for the several instructive discussions and for encouraging me to finish this research.

Further I am very grateful to Prof. dr. ir. J. Vierendeels for helping me with my numerical, programming and LaTeX problems. Without his help, I probably would not have finished this work.

I also would like to thank everybody of the department and laboratory for all the pleasant days that I have spend here.

And last but not least, I would like to thank my parents, my sister, and my wife for their support and encouragements, and for being a listening ear especially after less succesful days at work.

Toelating tot bruikleen

Contents

Nomenclature

A	Arrhenius factor (1/s)
a	gas absorption coefficient (1/m)
c	heat capacity (J/kg.K)
D	diameter (m)
D	molecular diffusion coefficient (m^2/s)
E	energy density (W/m^3)
E	total energy (J/kg)
E_a	activation energy (J/.mol)
f	mixture fraction
g	gravitational acceleration (m/s^2)
h	enthalpy (J/kg)
H	total enthalpy (J/kg)
H_c	heat of combustion (J/kg)
i	radiation intensity ($W/m^2.sr$)
k	reaction rate (1/s)
k	turbulent kinetic energy (m^2/s^2)
k_i	effective thermal conductivity (W/m.K)
l	length (m)
L	thickness (m)
L_v	heat of gasification (J/kg)
m	mass (kg)
N	number of meshes
p	pressure (Pa)
q	heat (J)
Q_{pyr}	pyrolysis heat (J/kg)
R_i	thermal resistance (m^2.K/W)
R_u	universal gasconstant (8.314 J/mol.K)
S	surface (m^2)
T	temperature (K)
t	time (s)
u	velocity (m/s)
u	internal energy (J/kg)
$\mathbf{v}$,v	velocity (m/s)
V	volume (m^3)
V_f	flame spread velocity (m/s)
$\mathbf{w}$,w	control volume velocity (m/s)
W	front velocity (m/s)
x	space coordinate (m)
Y	mass fraction

y	space coordinate (m)
z	space coordinate (m)

δ	layer thickness (m)
ϵ	emissivity coefficient
ε	turbulent kinetic dissipation (m^2/s^3)
θ	integrated temperature
θ	parameter controlling differencing scheme
λ	thermal conductivity (W/m.K)
μ	dynamic viscosity (kg/m.s)
ξ	char fraction
ρ	density (kg/m^3)
σ_t	turbulent Prandtl/Schmidt number
Φ	viscous dissipation (W/m^3)

Subscripts

b	burnout front
c	char
cond	conduction
conv	convection
ext	external
f	flame
F	fuel
ig	ignition
inc	incident
o	initial
O	oxygen
p,pyr	pyrolysis
r	radiation
rerad	reradiation
s	solid
t	turbulent
v	virgin
∞	ambient

Superscripts

$'$	per m
$''$	per m^2
$'''$	per m^3
$\cdot$	per s
$\bar{}$	mean or Reynolds averaging
$\tilde{}$	mass-weighted mean

Abbreviations

CFD	computational fluid dynamics
EBU	eddy break up
HRR	heat release rate (Cone Calorimeter)
LES	Large eddy simulation
LHS	left hand side
RHS	right hand side

Samenvatting - Summary in Dutch

Hoofdstuk 1: Inleiding

Deze thesis situeert zich in het domein brandveiligheid. Het doel van dit werk is het simuleren van branduitbreiding over verkolende vaste stoffen met behulp van numerieke stromingsmechanica. Als eerste zijn verschillende bestaande en nieuwe pyrolysemodellen voor vaste stof uitgewerkt en met elkaar vergeleken. Hieruit werd het meest geschikte pyrolysemodel gekozen om te koppelen aan een bestaand numeriek stromings- en stralingspakket. Het brandmodel laat toe vlamvoortplanting en branduitbreiding te bestuderen. Simulaties met het brandmodel worden vergeleken met experimenten beschreven in de literatuur.

Classificatie van brandmodellen

Deterministische brandmodellen voor branden in gesloten ruimten, kunnen worden verdeeld in:

1. CFD-modellen;
2. zonemodellen;
3. handberekeningen.

De CFD of veld berekeningen zijn met meest gesofisticeerd. Ze verdelen de ruimte op in een groot aantal kleine volumes. De behoudswetten van massa, impuls en energie worden toegepast op elk klein volume. De berekeningen zijn complex, en vergen veel computerkracht en tijd.

De zonemodellen verdelen de ruimte in een beperkt aantal zones, meestal twee of drie, namelijk de hete rookgaslaag, een koude luchtlaag en de rookpluim. Enkel het behoud van massa en energie wordt toegepast op deze

zones. Het voordeel van zonemodellen is dat ze eenvoudig en snel zijn. Hun toepassingsdomein is echter beperkt door verschillende vereenvoudigingen. Zonemodellen zijn ongeschikt voor het behandelen van complexe branden.

De laatste categorie (de handberekeningen), bestaat uit een reeks van eenvoudige formules die toepasbaar zijn voor slechts één enkel aspect van een brand. Bijvoorbeeld, voor de berekening van de vlamhoogte, of de vlamtemperatuur, of het massadebiet van een rookpluim, enz..

De drie verschillende brandmodellen zijn elk bruikbaar, maar wanneer nieuwe brandfenomen moeten worden onderzocht, zijn enkel de CFD-modellen geschikt. Zij zijn fundamenteler en hun toepassingsdomein is veel groter in vergelijking met de zonemodellen en de handberekeningen. Samen met steeds dalende reken- en computerkost zorgt dit voor een toenemend gebruik van CFD in brandveiligheid.

Toepassing van brandmodellen

Brand kan men zien als een ongewild verbrandingsproces. Bij branden sterven spijtig genoeg soms mensen en gaan meestal roerende en onroerende goederen verloren. Vandaag de dag, wordt de brandveiligheid in gebouwen opgelegd door middel van normen. Het merendeel van deze normen zijn gebaseerd op ervaring en op resultaten van brandtesten voor bouwmaterialen. Door de recente ontwikkelingen van de moderne bouwtechnologie worden heden ten dage onconventionele structuren en ontwerpen gebouwd. De huidige normen zijn ontoereikend voor deze nieuwe materialen en ontwerpen. Daarom worden er nieuwe performantiële normen geïntroduceerd die het werkelijk risico en veiligheidsniveau voorschrijven in plaats van voorgeschreven vereisten, zoals bijvoorbeeld de minimale afstand tussen gebouwen. De nieuwe performantiële normen geven meer vrijheid aan de architect en bouwheer bij het ontwerp van het gebouw. Ze hebben wel als nadeel dat ze berekeningsmethoden vereisen om het risico te bepalen. Het is hier dat de brandmodellen hun rol spelen. De brandmodellen, meer specifiek de CFD-modellen worden momenteel reeds gebruikt voor het berekenen van rookevacuatie in sportstadia, treinstations, winkelcentra, ...

De geavanceerde brandmodellen kunnen eveneens gebruikt worden om de huidige prescriptieve normen te evalueren, en ze te voorzien met een meer wetenschappelijke basis. De modellen kunnen ook gebruikt worden bij het onderzoeken en analyseren van opgetreden branden, zoals bijvoorbeeld de brand in het Kings Cross metrostation in Londen. Ze geven dan inzicht in het mechanisme van ontstaan en groei van de brand. Als laatste, kunnen de brandmodellen een rol spelen bij productontwikkeling. In plaats van dure grootschalige testen kan het brandgedrag voorspeld worden met kleinschalige

goedkope testen gecombineerd met een brandmodel.

Beperkingen van de huidige modellen

De huidige brandmodellen (de drie categorieën) hebben als nadeel dat de brandhaard vooraf moet gedefinieerd worden. De groei van de brand ligt al voor de berekening of simulatie vast, en is dus onafhankelijk van de resultaten tijdens de berekening. Branduitbreiding voorspellen is meestal niet mogelijk en dit vormt een serieuze beperking. De huidige simulaties dienen zich meestal te limiteren tot lokale vuurhaarden.

Hoofdstuk 2: Mechanisme branduitbreiding

De ontsteking van en de branduitbreiding over een vast materiaal is cruciaal bij brand. Beiden bepalen de snelheid waarmee de brand zich ontwikkelt, de vrijgesteld warmte, de hoeveelheid rook, de betrokken materialen, enz.. Wanneer brand wordt gemodelleerd, moeten de onderliggende mechanisme in het model aanwezig zijn. Daarom zal het mechanisme van vlamvoortplanting hier kort worden beschreven.

Aangezien vlamuitbreiding kan gezien worden als een voortschrijdend ontstekingsfront zal het mechanisme van ontsteking eveneens besproken worden.

Ontsteking

Wanneer een vaste stof wordt opgewarmd door bijvoorbeeld een extern stralingspaneel of een hete luchtstroom, dan zal zijn temperatuur stijgen. In de meeste gevallen zal de maximum temperatuur aan het oppervlak optreden. Wanneer de warmtebron voldoende sterk is, loopt de temperatuur van de vaste stof zodanig hoog op dat pyrolysereacties optreden. Doorgaans neemt men aan dat de reacties starten zodra de vaste stof een kritische pyrolysetemperatuur heeft bereikt. Gedurende de pyrolysereacties wordt de maagdelijke vaste stof omgezet in vluchtige stoffen en een koollaag. De vluchtige stoffen diffunderen uit de vaste stof naar de gasfase, waar ze zich mengen met de lucht. De gasfase wordt voornamelijk opgewarmd door convectie en conductie via het hete oppervlak van de vaste stof en via convectie en eventueel straling van een externe warmtebron. Door deze warmte zullen de exotherme reacties in de gasfase intensifiëren, waardoor de temperatuur nog verder stijgt. Men veronderstelt de vaste stof ontstoken wanneer de reacties sterk toenemen. Dit gaat gepaard met de creatie van een vlam. De initiële ontsteking kan worden

veroorzaakt door warmte afkomstig van de vaste stof zelf (zelf-ontsteking) of door een externe bron (piloot-ontsteking). Afhankelijk van de condities in de gasfase kan de kleine reactie-zone zich uitbreiden over het hele oppervlak. Het kan echter ook gebeuren dat de initiële vlam onmiddellijk dooft door warmteverliezen (voornamelijk straling) of door volledige consumptie van de aanwezige gasvormige brandbare producten.

Het ontstekingsproces kan worden opgedeeld in 3 delen:

1. thermische degradatie van de vaste stof;
2. mengen van de brandbare vluchtige stoffen met de lucht of oxidant;
3. stijging van de verbrandingsreacties zodat het verbrandingsproces zichzelf onderhoudt.

De ontstekingstijd van een vaste stof bestaat dus uit de pyrolysetijd (deel 1) en uit een gas-inductietijd (deel 2 en 3). Afhankelijk van de manier van opwarmen kan ofwel de pyrolysetijd, ofwel de inductie tijd, ofwel beiden belangrijk zijn.

Branduitbreiding

Om de vlamvoortplanting te starten, moet er natuurlijk eerst een externe warmtebron aanwezig zijn. De ontsteking kan bestaan uit een externe stralingsbron (bijvoorbeeld een stralingspaneel in een brandtest), een pilootvlam (bijvoorbeeld een brandende lucifer) of een andere lokale warmtebron (bijvoorbeeld een kortsluiting). Wanneer een vlam is gevormd zullen de exotherme reacties in de gasfase de externe warmtebron meehelpen met het opwarmen van de vaste stof. Het merendeel van de energie gaat naar de pyrolysezone en de primaire opwarmzone, slechts een klein gedeelte gaat naar de secondaire, verder gelegen, opwarmzone. De initiële warmtebron kan nog steeds aanwezig zijn, maar in de meeste gevallen wordt de gevormde vlam de voornaamste warmtebron. De vlam zal zich enkel voortplanten wanneer er voldoende energie wordt gegeven aan de nog niet verbrande zones (primaire en secundaire verbrandingszones) zodat ook die zullen pyrolyseren.

Vlamvoortplanting over een vaste stof kan dus worden gezien als een voortschrijdend ontstekingsfront waarbij de lokale vlam zorgt voor zowel de warmte om de vaste stof te verhitten, als voor de pilootvlam in de gasfase. De primaire opwarmzone begint pas te pyrolyseren wanneer het de kritische temperatuur (pyrolysetemperatuur) bereikt. De pyrolysegassen van de primaire opwarmzone diffunderen dan naar het oppervlak van de vaste stof en mengen er zich met de lucht zodat een brandbaar gasmengsel wordt gevormd.

Dit mengsel zal direct worden ontstoken door de aanwezigheid van de vlam. Na de opwarmtijd (tot pyrolysetemperatuur) voor de primaire zone, zal het vlammenfront de afstand van de primaire opwarmzone zijn opgeschoven.

Afhankelijk van de condities in de vaste stof en de gasfase kan men vlamvoortplanting opdelen in drie verschillende categorieën:

1. mee- en tegenstroom uitbreiding;

2. uitbreiding over verkolende en niet verkolende vaste stoffen;

3. uitbreiding over thermische dikke en dunne vaste stoffen.

Het beschreven mechanisme van uitbreiding is bij alle categorieën aanwezig, maar sommige aspecten kunnen worden verwaarloosd.

Mee- en tegenstroom vlamuitbreiding

Bij tegenstroom vlamuitbreiding is de gasstroom tegengesteld aan de zin van vlamuitbreiding. De gasstroom duwt de vlam over de reeds brandende vaste stof, stroomafwaarts van het pyrolysefront. De maagdelijke vaste stof wordt opgewarmd door conductie en deels door straling. De vlamuitbreidingssnelheid is klein. Tegenstroomvlamuitbreiding treedt op als neerwaartse, laterale en horizontale uitbreiding bij vrije convectie.

Bij meestroomvlamuitbreiding wordt de vlam door de gasstroom voorwaarts geduwd. De vlam ligt dus voor het pyrolysefront, boven het maagdelijke materiaal. De warmte-overdracht (voornamelijk straling) van vlam naar vaste stof verloopt dus gemakkelijk en zorgt dus voor een snelle vlamuitbreiding. Meestroomvlamuitbreiding treedt op als opwaartse vlamuitbreiding.

Verkolende en niet-verkolende materialen

Bij niet-verkolende materialen brandt de vaste stof volledig af. Er wordt geen residu gevormd en dus vermindert de dikte van de vaste stof. Het pyrolysefront valt steeds samen met het oppervlak van de vaste stof.

Aan de andere kant, laten verkolende materialen wél een residu achter. De koollaag bouwt zich stelselmatig op en vormt een thermische weerstand tussen het oppervlak van de vaste stof en het pyrolysefront (dat zich nu ergens in de vaste stof bevindt). Hierdoor stroomt er minder energie naar het pyrolysefront wat een daling van de pyrolysereacties zal veroorzaken.

Thermische dik en dun

Voor thermische dunne materialen is de hoeveelheid warmte die naar de vaste stof wordt overgedragen eerder beperkt. Het materiaal kan veelal worden beschreven met slechts één enkele temperatuur. De vaste stof wordt snel gepyrolyseerd en de vlamuitbreiding is snel. Men kan aantonen dat de snelheid omgekeerd evenredig is met de dikte, er is immers minder materiaal dat op pyrolysetemperatuur moet gebracht worden.

Bij thermisch dikke materialen wordt een merkelijke hoeveelheid energie overgedragen. Het materiaal zal voor lange tijd branden (en pyrolyseren). De vlamuitbreidingssnelheid is zo goed als onafhankelijk van de dikte en ze is omgekeerd evenredig met de thermische inertie.

In een algemeen model voor vlamuitbreiding, zouden alle types (mee- en tegenstroom, verkolend en niet verkolend, thermische dik en dun) moeten kunnen worden voorspeld. Idealiter zou het model universeel moeten zijn en het soort vlamuitbreiding zelf voorspellen. Dit werk concentreert zich op vlamuitbreiding over verkolende materialen. Mee- en tegenstroom vlamuitbreiding, en thermisch dikke en dunne materialen moeten wel met het brandmodel kunnen worden voorspeld.

Hoofdstuk 3: Classificatie vlamuitbreidingsmodellen

In dit hoofdstuk worden de bestaande vlamuitbreidingsmodellen geclassificeerd. De opdeling is gebaseerd op twee belangrijke fysische processen die optreden tijdens vlamuitbreiding, namelijk de reactie/pyrolyse van de vaste stof en de warmte-terugkoppeling naar de vaste stof. Daarom is de classificatie gedaan volgens:

1. de aanwezigheid van een onafhankelijk model voor de pyrolyse van de vaste stof;

2. de warmte-terugkoppeling naar de vaste stof.

Deze twee criteria zijn onafhankelijk van elkaar en kunnen eveneens gezien worden als een classificatie volgens de vaste stof en de gasfase.

In de eerste classificatie, zie Figuur 3.1, wordt met het *verbrandingsmodel voor de vaste stof*, het model bedoeld dat de vrijstelling van de pyrolysegassen of energie beschrijft. Het model moet in staat zijn onafhankelijk te werken van de gasfase. Natuurlijk moeten dan geschikte randvoorwaarden

worden opgelegd. Voor de eerste klasse wordt de vrijstelling van pyrolysegassen bepaald uit experimentele resultaten, zoals bijvoorbeeld de Cone Calorimeter. In de tweede klasse wordt een thermische degradatie model gebruikt. Men kan deze klasse nog verder verdelen in modellen waarbij de reactiesnelheid van de pyrolysereacties oneindig en eindig is. Voor de oneindige reactiesnelheid zal het front bestaan uit een zone op constante temperatuur. Onder deze temperatuur komen geen reacties voor, terwijl erboven, de reacties steeds voltooid zijn. Voor de eindige snelheid zal de temperatuur over het pyrolysefront variëren. Meestal worden de reacties gemodelleerd met een eerste orde Arrhenius reactie. In de derde klasse van vlamuitbreidingsmodellen, wordt de vrijstelling van de pyrolysegassen beschreven door een algebraïsch model (of soms zelfs constant verondersteld). In het algemeen worden zulke modellen enkel gebruikt om de vlamuitbreidingssnelheid te bepalen. In de vierde en laatste klasse, wordt er geen pyrolysemodel gebruikt bij het vlamuitbreidingsmodel.

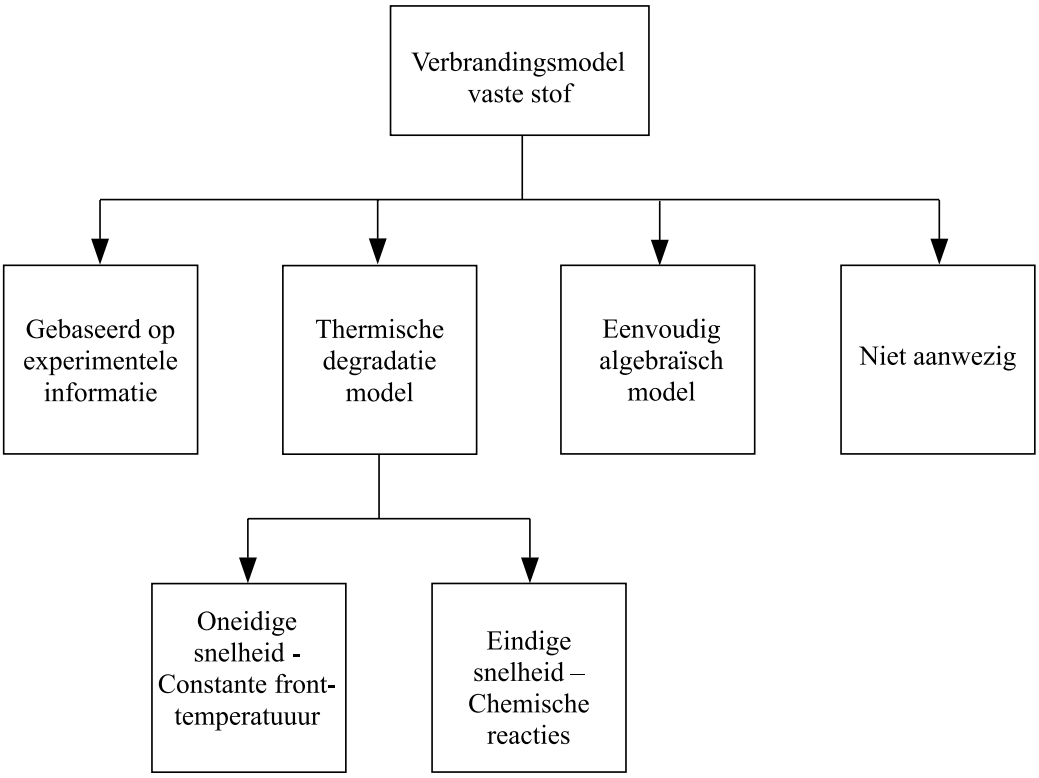

Figuur 3.1: Klassering volgens verbrandingsmodel voor de vaste stof

De vlamuitbreidingsmodellen kunnen eveneens worden geclassificeerd volgens de gasfase. Wanneer de gasfase volledig wordt gemodelleerd, zie de eerste klasse in Figuur 3.2, dan wordt de warmte-terugkoppeling berekend uit de gastemperaturen, de roetconcentraties, de stromingscondities, enz.. Het meest voor de handliggende model is natuurlijk een CFD-pakket, alhoewel er andere modellen bestaan. Wanneer de gasfase niet volledig gemodelleerd wordt, reduceert men de gasfase tot een vlam-representatie. De warmte-terugkoppeling kan volgen uit experimenten of kan worden berekend uit de eenvoudige vlam-representatie (bijvoorbeeld: vlam voostellen als een vlak op constante temperatuur).

In Hoofdstukken 4 t.e.m. 8 worden verschillende pyrolysemodellen uitvoerig besproken. De simulaties zijn niet gekoppeld met een gasfase model - er worden dus gepaste randvoorwaarden opgelegd. De modellen worden met elkaar vergeleken in Hoofdstuk 9. Het doel is de modellen te evalueren, alsook het model te identificeren dat het meest geschikt is om aan een CFD-pakket te koppelen.

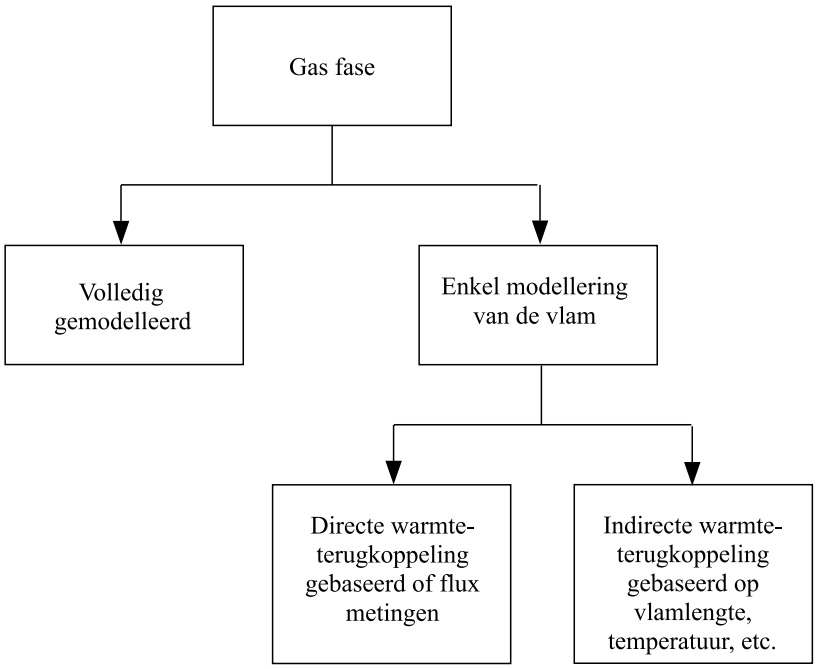

Figuur 3.2: Klassering volgens uitwerking van de gasfase

Hoofdstuk 4: Arrhenius model

In dit hoofdstuk wordt een pyrolysemodel ontwikkeld waarbij de pyrolysereacties beschreven worden door een Arrhenius-wet. De vaste stof bestaat in elk punt uit een mengeling van maagdelijk en verkoold materiaal en wordt gekarakteriseerd door de koolfractie. Aanvankelijk, dus voor opwarming, bestaat de vast stof volledig uit maagdelijk materiaal. Anderzijds, wanneer de vaste stof volledig is gepyrolyseerd, blijft er enkel nog puur verkoold materiaal over. Tussen deze twee toestanden bestaat de vaste stof uit een mengeling van verkoold en maagdelijk materiaal. De koolfractie verschilt naargelang de plaats.

De pyrolyse wordt beschreven door een één-staps-reactie:

$$\text{maagdelijk materiaal} \xrightarrow{+\text{ warmte}} \text{verkoold} + \text{pyrolyse gassen} \tag{1}$$

De reactiesnelheid wordt beschreven door onderstaande Arrhenius vergelijking:

$$k_{pyr} = A \cdot \exp\left(-\frac{E_a}{RT}\right) \tag{2}$$

Bij lage temperatuur reageert er bijna geen maagdelijk materiaal. Bij hogere temperatuur stelt er zich een evenwicht in tussen de toegevoerde energie en de endothermische pyrolysereacties.

De pyrolysegassen die geproduceerd worden in de vaste stof stromen onmiddellijk uit deze vaste stof. Er wordt dus verondersteld dat er zich geen gassen opstapelen in de stof. Bij hun tocht naar het oppervlak staan de pyrolysegassen steeds op dezelfde temperatuur als de vaste stof waar ze doorstromen. Dus, gedurende hun stroming van de pyrolysezone naar het oppervlak warmen de pyrolysegassen nog verder op.

De dichtheid, de thermische conductiecoëfficiënt en de warmte capaciteit zijn enkel functie van de koolfractie ξ_c:

$$\begin{aligned} \rho &= (1-\xi_c)\cdot\rho_v + \xi_c\rho_c \\ \lambda &= (1-\xi_c)\cdot\lambda_v + \xi_c\cdot\lambda_c c \\ c &= \frac{\rho_c\cdot c_c\cdot\xi_c + \rho_v\cdot c_v\cdot(1-\xi_c)}{(1-\xi_c)\cdot\rho_v + \xi_c\cdot\rho_c} \end{aligned} \tag{3}$$

Behoud van massa

De modelvergelijkingen worden afgeleid uit de controle volume techniek. Het behoud van massa voor een controle volume V met oppervlak S wordt

gegeven door:

$$\frac{\mathrm{d}}{\mathrm{d}t}\int_V \rho\,\mathrm{d}V = -\int_S \dot{\mathbf{m}}''_{pyr}\,\mathrm{d}\mathbf{S} \tag{4}$$

Met het divergentietheorema kan dit geschreven worden als een tijdsafgeleide van de koolfractie:

$$\frac{\partial \xi_c}{\partial t} = -\frac{\dot{m}'''_{pyr}}{\rho_c - \rho_v} \tag{5}$$

Aangezien de pyrolysegassen onmiddellijk uit de vaste stof stromen, geldt er:

$$\frac{\partial \dot{m}''_{pyr}}{\partial x} = -\dot{m}'''_{pyr} \tag{6}$$

De lokale productie van pyrolysegassen wordt beschreven door de Arrheniuswet:

$$\dot{m}'''_{pyr} = A \cdot \rho_v \cdot (1-\xi_c) \cdot \exp\left(-\frac{E_a}{RT}\right) \tag{7}$$

en hiermee kan Vergelijking 5 geschreven worden als:

$$\frac{\partial \xi_c}{\partial t} = -A \cdot \frac{\rho_v}{\rho_c - \rho_v} \cdot (1-\xi_c) \cdot \exp\left(-\frac{E_a}{RT}\right) \tag{8}$$

Behoud van energie

De pyrolysewarmte wordt uitgedrukt per kilogram gevormde pyrolysegassen. Ze kan worden bepaald uit:

$$\begin{aligned}&\rho_v\left(u_v(T_0) + \int_{T_0}^{T_{pyr}} c_v \mathrm{d}T\right) + \rho_v Q_{pyr}(T_{pyr}) \\ &\quad = \rho_c\left(u_c(T_0) + \int_{T_0}^{T_{pyr}} c_c \mathrm{d}T\right) + (\rho_v - \rho_c)\left(u_{pyr}(T_0) + \int_{T_0}^{T_{pyr}} c_{pyr}\mathrm{d}T\right)\end{aligned} \tag{9}$$

De vergelijking van het behoud van energie voor een volume V wordt bij verwaarlozing van de potentiële en kinetische energie, en van de volume-expansie gegeven door:

$$\frac{\mathrm{d}}{\mathrm{d}t}\int_V \rho u(T)\mathrm{d}V + \int_S u_{pyr}(T)\dot{\mathbf{m}}''_{pyr}\cdot\mathrm{d}\mathbf{S} = -\int_S \dot{\mathbf{q}}''\cdot\mathrm{d}\mathbf{S} \tag{10}$$

Deze vergelijking kan worden omgevormd naar:

$$\frac{\mathrm{d}}{\mathrm{d}t}\int_V \rho c T\mathrm{d}V + \int_S c_{pyr}T\dot{\mathbf{m}}''_{pyr}\cdot\mathrm{d}\mathbf{S} + \int_V Q_{pyr}\dot{m}'''_{pyr}\cdot\mathrm{d}V = -\int_S \lambda\frac{\partial T}{\partial \mathbf{n}}\mathrm{d}\mathbf{S} \tag{11}$$

Gediscretiseerde vergelijkingen

De eindige volume techniek wordt gebruikt om de vergelijkingen 6, 8 en 11 op te lossen. Een uniform ééndimensionaal rooster deelt de vaste stof op in N volumes. In elke volume wordt de temperatuur, de koolfractie, de massaflux pyrolysegassen, en de productie van pyrolysegassen bijgehouden. De tijdsdiscretisatie gebeurt met de hybride Cranck-Nicholson methode. Voor het convectieve deel in Vergelijking 10 wordt de "upwind" methode gebruikt, terwijl het rechterlid centraal wordt opgelost. De vergelijkingen worden iteratief opgelost met een Gauss-Seidel methode.

Simulaties

Aan het *Arrhenius model* zijn eenvoudige randvoorwaarden opgelegd die typisch zijn voor vlamuitbreiding. Bij de simulaties is het aantal volumes, de grootte van de tijdstap, en het aantal iteraties onderzocht. Bij gekoppelde berekeningen is het immers aangewezen om het aandeel van de rekentijd voor de reactie van de vaste stof tot een minimum te beperken. Samenvattend kan men stellen dat er 256 volumes nodig zijn bij een tijdstap van 0.5 s. Hierbij zijn per tijdstap een tiental iteraties voldoende. De rekentijd van deze methode is aan de hoge kant. Wanneer een te klein aantal volumes wordt gebruikt krijgt men oscillaties in de massaflux vrijgestelde pyrolysegassen

De temperatuur waarbij de pyrolysegassen worden vrijgesteld is afhankelijk van de Arrhenius constanten en van de wijze van opwarmen (snel op hoge temperatuur of traag op lage temperatuur). Analyse van pyrolysetemperatuur leerde dat de pyrolysegassen worden vrijgesteld in een tamelijk breed temperatuurinterval: tussen de 200 en 300 °C.

Hoofdstuk 5: Integraal model

De invloed van de temperatuur op de pyrolysereacties kan worden beschreven met een Arrhenius-wet, zoals is gedaan in het vorige hoofdstuk. Voor de meeste materialen is de activeringsenergie zodanig hoog dat ze enkel beginnen pyrolyseren als ze een kritische (pyrolyse)temperatuur bereiken. Boven deze temperatuur loopt de reactiesnelheid zeer snel op. Daarom wordt aangenomen dat de reactiesnelheid gelijk is aan nul voor een temperatuur lager dan de pyrolysetemperatuur, en oneindig voor een hogere temperatuur. Het pyrolysefront staat steeds op dezelfde temperatuur en wordt gereduceerd tot een oppervlak.

In het *Integraal model* wordt er een welbepaald temperatuurprofiel voor de vaste stof voorgesteld, bijvoorbeeld een kwadratische verloop. Met de be-

houdsvergelijkingen en de randvoorwaarden worden de ongekende coëfficiënten van het profiel bepaald.

Fasen

Het volledige pyrolyseproces kan worden opgedeeld in verschillende fasen. Afhankelijk van de positie van het warmtefront heeft men twee sequenties:

1. een inerte opwarmfase waarbij de vaste stof als half-oneindig wordt behandeld;
2. een pyrolysefase waarbij de vaste stof als half-oneindig wordt behandeld;
3. een pyrolysefase waarbij de vaste stof als eindig wordt behandeld;

of

1. een inerte opwarmfase waarbij de vaste stof als half-oneindig wordt behandeld;
2. een inerte opwarmfase waarbij de vaste stof als eindig wordt behandeld;
3. een pyrolysefase waarbij de vaste stof als eindig wordt behandeld;

Bijkomend kan nog een vierde fase worden gedefinieerd waarbij de overgebleven koollaag nog verder opwarmt.

Fundamentele modelvergelijkingen

De fundamentele modelvergelijkingen worden hier slechts gegeven voor de pyrolysefase waarbij de vaste stof als half-oneindig kan worden beschouwd. De andere fasen hebben gelijkaardige vergelijkingen.

De vaste stof wordt in deze fase verdeeld in drie gebieden: de koollaag, het pyrolysefront en de maagdelijke laag. De laatste wordt nog verder verdeeld in een laag die nog steeds op initiële temperatuur staat en een laag waar de invloed van de invallende warmteflux reeds te voelen is. Voor deze verschillende zones worden de behoudsvergelijkingen uitgeschreven.

Voor de koollaag levert het behoud van massa:

$$\dot{m}''_{pyr} = \rho_{pyr} v_{pyr} \tag{12}$$

en het behoud van energie:

$$\rho_c c_c \frac{\mathrm{d}}{\mathrm{d}t} \int_0^{\delta_c} (T - T_{pyr}) \, \mathrm{d}x = \dot{q}''_{net} - \dot{q}''_c \tag{13}$$

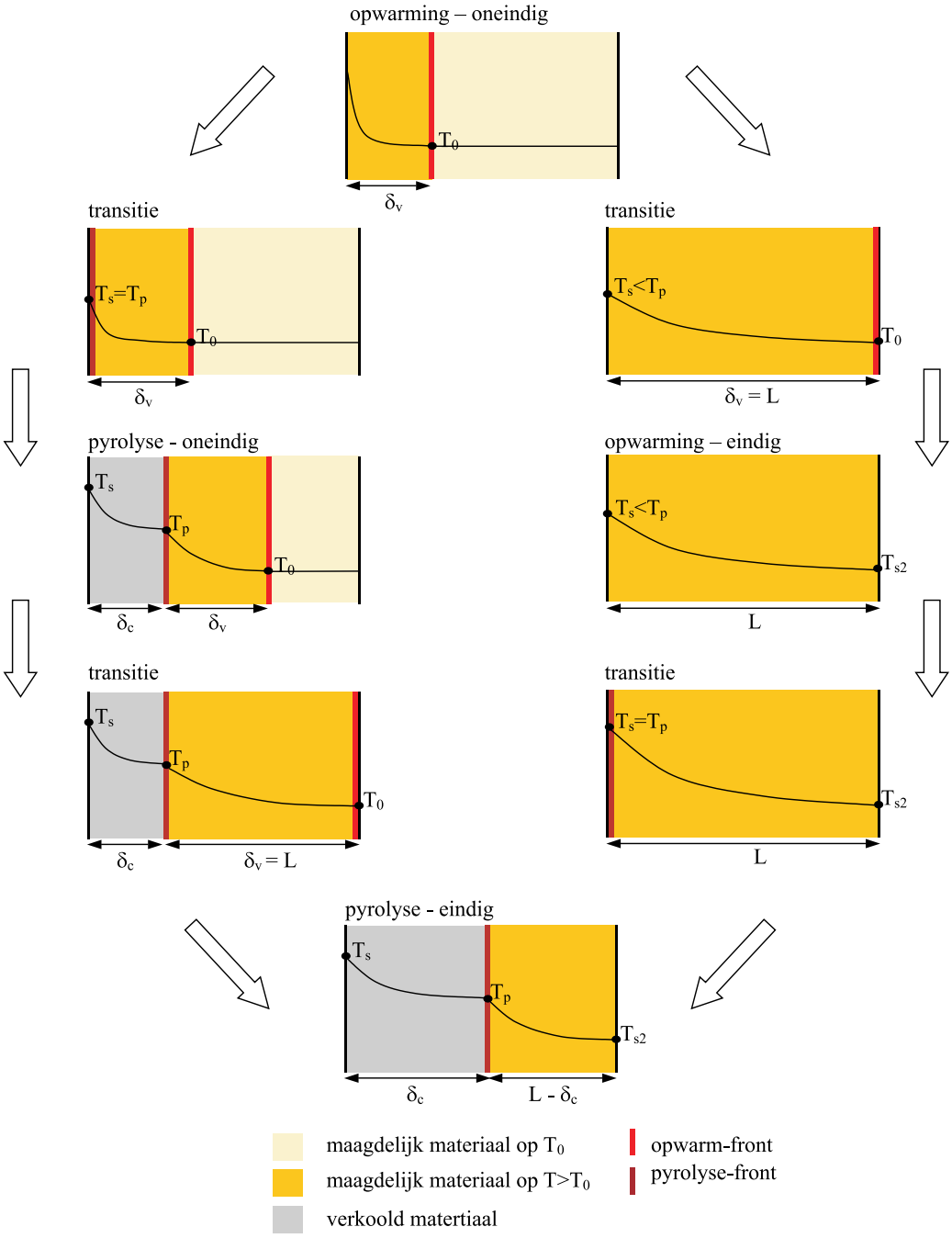

Figuur 5.1: Fasen in pyrolyseproces

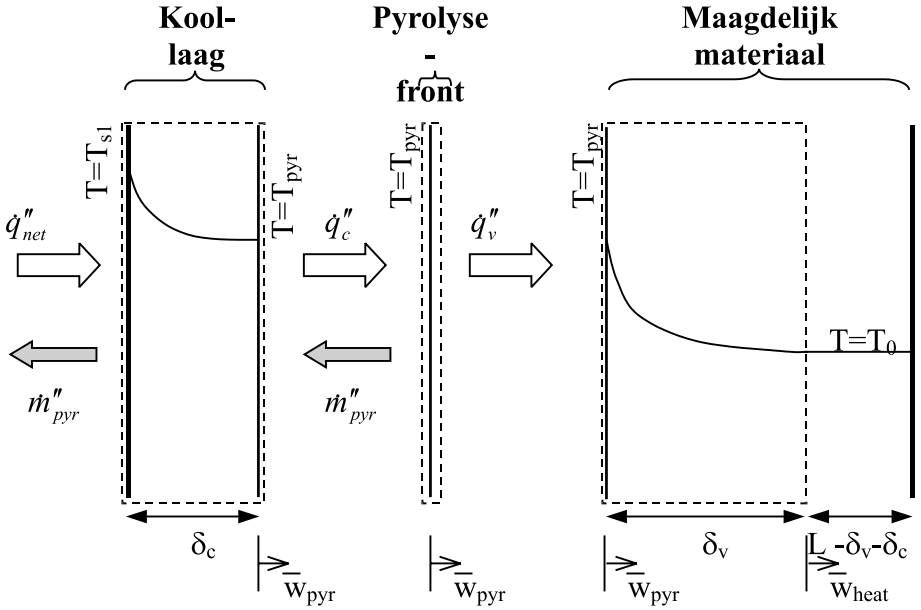

Figuur 5.3: Controle volumes voor pyrolyse - half-oneindig

De bijhorende randvoorwaarden zijn:

$$\begin{cases} -\lambda_c \left(\frac{\mathrm{d}T}{\mathrm{d}x}\right)_{x=0} &= \dot{q}''_{net} \\ -\lambda_c \left(\frac{\mathrm{d}T}{\mathrm{d}x}\right)_{x=\delta_c} &= \dot{q}''_c \\ \left(T\right)_{x=\delta_c} &= T_{pyr} \end{cases} \tag{14}$$

Voor het pyrolysefront geeft de vergelijking van behoud van massa:

$$(\rho_v - \rho_c) \cdot \frac{\mathrm{d}\delta_c}{\mathrm{d}t} = \dot{m}''_{pyr} \tag{15}$$

en het behoud van energie:

$$(\rho_v - \rho_c) \cdot \frac{\mathrm{d}\delta_c}{\mathrm{d}t} \cdot \Delta Q_{pyr}(T_{pyr}) \quad = \quad \dot{q}''_c - \dot{q}''_v \tag{16}$$

Voor het maagdelijk materiaal (beschouw enkel de zone waar de temperatuur verschillend is van de initiële temperatuur) is enkel het behoud van energie van belang, het behoud van massa geeft immers de identiteit:

$$\frac{\mathrm{d}}{\mathrm{d}t} \int_{\delta_c}^{\delta_c+\delta_v} (T - T_{pyr})\,\mathrm{d}x + T_{pyr}\frac{\mathrm{d}\delta_v}{\mathrm{d}t} + T_{pyr}\frac{\mathrm{d}\delta_c}{\mathrm{d}t} - T_0\frac{\mathrm{d}(\delta_c+\delta_v)}{\mathrm{d}t} = \frac{\dot{q}''_v}{\rho_v c_v} \tag{17}$$

met als randvoorwaarden:

$$\begin{cases} \left(T\right)_{x=\delta_c} & = & T_{pyr} \\ -\lambda_v \left(\frac{\mathrm{d}T}{\mathrm{d}x}\right)_{x=\delta_c} & = & \dot{q}''_v \\ \left(T\right)_{x=\delta_c+\delta_v} & = & T_0 \\ -\lambda_v \left(\frac{\mathrm{d}T}{\mathrm{d}x}\right)_{x=\delta_c+\delta_v} & = & 0 \end{cases} \tag{18}$$

Praktische modelvergelijkingen

Voor alle fasen wordt een kwadratische temperatuurprofiel gekozen. Voor de "half-oneindige pyrolysefase" worden de temperaturen in de kool en maagdelijke laag respectievelijk gegeven door:

$$\begin{aligned} T_c &= b_0 + b_1 \cdot (\delta_c - x) + b_2 \cdot (\delta_c - x)^2 \\ T_v &= c_0 + c_1 \cdot (x - \delta_c) + c_2 \cdot (x - \delta_c)^2 \end{aligned} \tag{19}$$

De drie energievergelijkingen voor de drie zones kunnen na enige berekeningen geschreven worden als:

$$\frac{\mathrm{d}\delta_c}{\mathrm{d}t} = \frac{1}{(\rho_v - \rho_c)\Delta H_{pyr} - \rho_v c_v (T_0 - T_{pyr})} \cdot \left(\dot{q}''_{net} - \rho_c c_c \frac{\mathrm{d}\theta_c}{\mathrm{d}t} + \frac{\rho_v c_v}{2} \cdot \frac{\mathrm{d}\theta_v}{\mathrm{d}t}\right) \tag{20}$$

$$\frac{\mathrm{d}\theta_c}{\mathrm{d}t} = 3 \cdot \alpha_c \cdot \left(\frac{1}{2} \cdot \frac{\dot{q}''_{net}}{\lambda_v} - \frac{\theta_c}{\delta_c^2}\right) \tag{21}$$

$$\frac{\mathrm{d}\theta_v}{\mathrm{d}t} = 2 \cdot (T_{pyr} - T_0) \cdot \left(\frac{4}{3} \cdot \frac{\alpha_v}{\theta_v} \cdot (T_{pyr} - T_0) + \frac{\mathrm{d}\theta_c}{\mathrm{d}t}\right) \tag{22}$$

Deze drie vergelijkingen geven δ_c, θ_c en θ_v waarbij de twee laatste variabelen de geïntegreerde temperaturen voorstellen, gedefinieerd als:

$$\begin{cases} \theta_c & = & \int_0^{\delta_c} (T - T_{pyr})\,\mathrm{d}x \\ \theta_v & = & \int_{\delta_v}^{\delta_v+\delta_c} (T - T_{pyr})\,\mathrm{d}x \end{cases} \tag{23}$$

De coëfficiënten van het temperatuurprofiel voor de koollaag worden gegeven door:

$$\begin{cases} b_0 & = & T_{pyr} \\ b_1 & = & 3 \cdot \frac{\theta_c}{\delta_c^2} - \frac{\dot{q}''_{net}}{2 \cdot \lambda_c} \\ b_2 & = & -\frac{3}{2} \cdot \frac{\theta_c}{\delta_c^3} + \frac{3}{4} \cdot \frac{\dot{q}''_{net}}{\delta_c \lambda_c} \end{cases} \tag{24}$$

en voor de maagdelijke laag door:

$$\begin{cases} c_0 &= T_{pyr} \\ c_1 &= 2 \cdot \frac{T_0 - T_{pyr}}{\delta_v} \\ c_2 &= \frac{T_{pyr} - T_0}{\delta_v^2} \end{cases} \tag{25}$$

Discretisatie

Het probleem is singulier wanneer de pyrolyse-fase start. Daarom is een impliciete methode gekozen. Voor de eerste pyrolyse-tijdstap wordt een volledige impliciete methode gebruikt, terwijl voor de andere stappen de Cranck-Nicholson methode wordt gebruikt.

De gediscretiseerde vergelijkingen worden direct opgelost door matrix inversie, maar een iteratielus is nog steeds aanwezig om gelineariseerd termen aan te passen. Een zuivere iteratieve methode waarbij de vergelijkingen sequentieel worden opgelost vergde te veel iteraties.

Validatie

De opwarmfase kan voor een constante invallende warmteflux vergeleken worden met analytische resultaten. Fouten in de oppervlaktetemperatuur waren ongeveer 8.5%. Voor andere randvoorwaarden kan de opwarmfase vergeleken worden met een eindige volume methode. Vergelijking van de resultaten leerde dat het "Integraal model" problemen heeft bij plotse verandering van de invallende warmteflux. In sommige gevallen werden zelfs temperaturen lager dan omgeving vastgesteld.

De pyrolysefase werd gevalideerd met het "Bewegend-rooster model" dat in het volgend hoofdstuk wordt besproken. Bij pyrolyse werden problemen gesignaleerd bij plotse verandering van de invallende warmteflux. Voor deze fase kan dit resulteren in negatieve vrijstelling van pyrolysegassen. De oorzaak van het falen van het "Integraal model" ligt in de onrealistisch snelle voortplanting van de randvoorwaarden naar de volledige vaste stof (hoe dik deze ook mag zijn). Een voordeel van het "Integraal model" is zijn korte rekentijd.

Hoofdstuk 6: Bewegend rooster

Het "Bewegend-rooster model" is gelijkaardig aan het "Integraal model". In feite waren het de beperkingen van het "Integraal model" die aanleid-

ing gaven tot dit nieuw pyrolysemodel. Met dit nieuw model zijn er geen beperkingen aangaande het temperatuurprofiel.

Ook in dit model zal het pyrolysefront gereduceerd worden tot één oppervlak op constante temperatuur.

Fasen

Voor het "Bewegend-rooster model" zijn er slechts drie fasen:

1. opwarming van zuiver maagdelijk materiaal;
2. pyrolyse;
3. opwarming van zuiver verkoold materiaal.

De fasen en de overgangen worden getoond in Figuur 6.1. Hier moet geen onderscheid gemaakt worden tussen eindig en half-oneindig, zoals het geval was voor het "Integraal model". Het aantal volumes in een laag blijft tijdens de simulatie constant. Dit impliceert een stilstaand rooster voor de opwarmfasen.

Modelvergelijkingen

De modelvergelijkingen worden enkel gegeven voor de pyrolysefase. De behoudsvergelijkingen zijn voor de koollaag en het pyrolysefront identiek aan die van het "Integraal model". De vergelijkingen voor de maagdelijke laag zijn echter verschillend.

Voor de koollaag krijgt men:

$$\begin{aligned} \frac{\mathrm{d}}{\mathrm{d}t}\int_0^{\delta_c}\Big(\rho_{pyr}\cdot c_{pyr}\cdot T+\rho_c\cdot c_c\cdot T\Big)\,\mathrm{d}x \quad &+ \quad \dot{m}''_{pyr}\cdot c_{pyr}\cdot T_s-\dot{m}''_{pyr}\cdot c_{pyr}\cdot T_{pyr} \\ + \quad \Big(\rho_{pyr}\cdot c_{pyr}\cdot T_{pyr}+\rho_c\cdot c_c\cdot T_{pyr}\Big)\cdot\Big(-\frac{\mathrm{d}\delta_c}{\mathrm{d}t}\Big) \quad &= \quad \dot{q}''_{net}-\dot{q}''_c \end{aligned} \tag{26}$$

Waarbij de randvoorwaarden worden gegeven door:

$$\begin{cases} -\lambda_c\left(\frac{\mathrm{d}T}{\mathrm{d}x}\right)_{x=0} &= \dot{q}''_{net}=\dot{q}''_{ext}-h(T_s-T_\infty)-\epsilon\sigma(T_s^4-T_\infty^4) \\ \quad \left(T\right)_{x=\delta_c} &= T_{pyr} \end{cases} \tag{27}$$

Voor het pyrolysefront geeft het behoud van massa:

$$(\rho_v-\rho_c)\frac{\mathrm{d}\delta_c}{\mathrm{d}t}=\dot{m}''_{pyr} \tag{28}$$

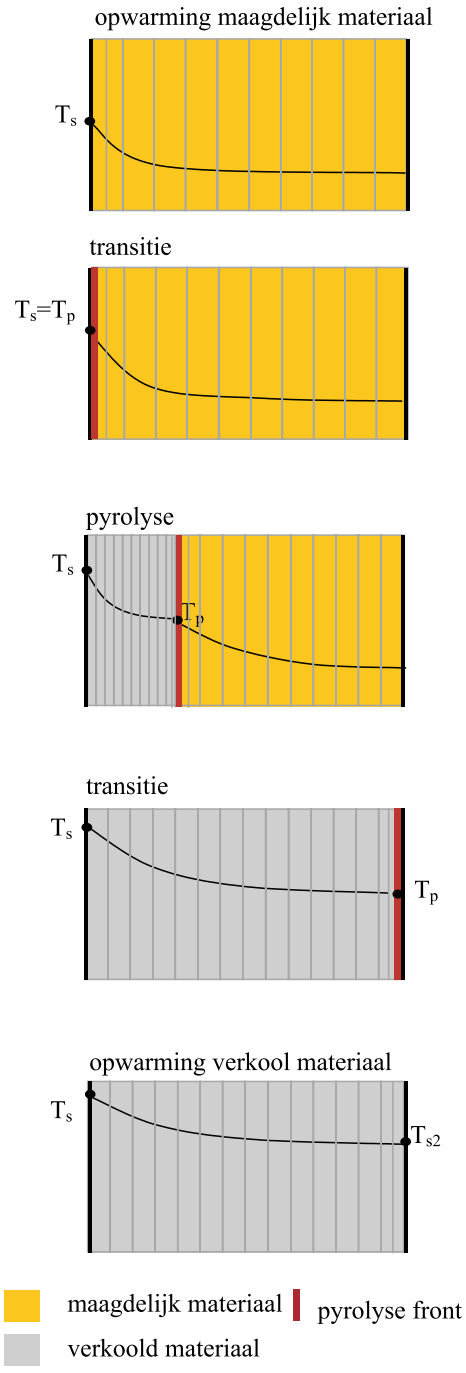

Figuur 6.1: Verschillende fasen voor “Bewegend-rooster model”

en het behoud van energie:

$$(\rho_v - \rho_c)\frac{\mathrm{d}\delta_c}{\mathrm{d}t}\Delta Q_{pyr}(T_{pyr}) \quad = \quad \dot{q}''_c - \dot{q}''_v \tag{29}$$

Voor de volledige maagdelijke laag geeft het behoud van energie:

$$\frac{\mathrm{d}}{\mathrm{d}t}\int_{\delta_c}^{L} \rho_v c_v T \,\mathrm{d}x - \rho_v c_v T_{pyr}\frac{\mathrm{d}\delta_c}{\mathrm{d}t} = \dot{q}''_v + \dot{q}''_{rear} \tag{30}$$

De randvoorwaarden voor deze laag zijn:

$$\begin{cases} \left(T\right)_{x=\delta_c} &= T_{pyr} \\ \lambda_v \left(\frac{\mathrm{d}T}{\mathrm{d}x}\right)_{x=L} &= \dot{q}''_{rear} \end{cases} \tag{31}$$

Discretisatie

Zoals gedaan werd voor de gehele koollaag en maagdelijke laag, kan men eveneens het behoud van energie voor een willekeurig volume i in een laag uitschrijven. Voor een volume in de koollaag geldt:

$$\begin{aligned} \frac{\mathrm{d}}{\mathrm{d}t}\int_{\Delta x_i} \rho_c c_c T \,\mathrm{d}x \quad &- \quad (\rho_c c_c)(w_{W,i}T_{W,i} - w_{E,i}T_{E,i}) \\ &+ \quad \dot{m}''_{pyr} c_{pyr}(T_{W,i} - T_{E,i}) \quad = \quad \dot{q}''_{E,i} - \dot{q}''_{W,i} \end{aligned} \tag{32}$$

Door de maagdelijke laag stromen geen pyrolysegassen, dus geldt er:

$$\begin{aligned} \frac{\mathrm{d}}{\mathrm{d}t}\int_{\Delta x_i} \rho_v c_v T \,\mathrm{d}x \quad &- \quad (\rho_v c_v)(w_{W,i}T_{W,i} - w_{E,i}T_{E,i}) \\ &= \quad \dot{q}''_{E,i} - \dot{q}''_{W,i} \end{aligned} \tag{33}$$

Ook bij dit model is de overgang van opwarmen naar pyrolyse singulier (de koollaag is nog onbestaande tijdens de opwarmfase). Daarom wordt er weer een impliciete methode gekozen, volledig impliciet voor de eerste tijdstap in de pyrolysefase en hybrid (Cranck-Nicholson) voor de andere tijdstappen.

De temperatuur op de grenzen van de volumes wordt centraal berekend, behalve voor de convectieve term met de pyrolysegassen waar "upwind" werd gebruikt (dit geeft een iets eenvoudigere uitwerking).

Twee roosters zijn onderzocht. In het eerste waren de roosters zowel in de maagdelijke als in de koollaag uniform, terwijl in het tweede het rooster in de maagdelijk laag niet-uniform was. Er werd afgeweken van het uniforme rooster omdat zo minder volumes konden worden gebruikt (en dus kortere

rekentijd). Enkel in de zone dicht bij het oppervlak of dicht bij het pyrolysefront zijn er sterk veranderende temperatuurgradiënten. Daarom werd het rooster daar fijner gekozen. In het progressieve rooster (niet-uniform) is de grootte van een volume gelijk aan de grootte van zijn voorganger vermenigvuldigt met een groeifactor. In de koollaag bleek het temperatuurprofiel gedurende de simulaties zo goed als lineair, zodat daar een uniform rooster voldoende was.

De temperaturen in een laag worden berekend met het Thomas algoritme (oplossen van tri-diagonale matrix). Uit de temperaturen in elke laag worden de warmtefluxen aan het pyrolysefront berekend, wat een nieuwe waarde voor de snelheid van het pyrolysefront geeft. Met deze nieuwe front snelheid worden opnieuw de temperaturen in de kool- en maagdelijke laag berekend. In de iteratieve methode wordt dus steeds de snelheid van het front aangepast totdat het energiebehoud van het pyrolysefront was voldaan.

Voor het uniforme rooster zijn er in de koollaag slechts 4 volumes nodig, terwijl er in de maagdelijke laag 64 vereist zijn. De berekening werden gedaan met een tijdstap van 0.1 s. Voor het niet-uniforme rooster in de maagdelijke laag waren er slechts 16 volumes nodig in die laag. De groeifactor bedroeg 1.3.

Hoofdstuk 7: Enthalpie model

Voor brandtoepassingen is het "Enthalpie model" nieuw. In het "Enthalpie model" wordt het scheidingsvlak van het pyrolysefront niet expliciet gevolgd, zoals in het "Integraal model" en het "Bewegend-rooster model". De methode is gebaseerd op de conservatieve vorm van het behoud van energie:

$$\int_t^{t+\Delta t} \frac{\mathrm{d}}{\mathrm{d}t} \left(\int_V E \mathrm{d}V \right) \mathrm{d}t \;=\; \int_t^{t+\Delta t} \int_S -\dot{\mathbf{q}}'' \cdot \mathbf{n} \, \mathrm{d}S \, \mathrm{d}t \tag{34}$$

Het voordeel van deze vorm is dat hij geldig blijft wanneer genomen over verschillende lagen en wanneer E of $\mathbf{q}$ sprongen vertoont. Voor de lokale differentiële vorm:

$$\frac{\partial}{\partial t} E + \nabla \cdot (\dot{\mathbf{q}}'') = 0 \tag{35}$$

is dit niet het geval.

Discretisatie

De eerste stap in de "Enthalpie methode" is reeds de discretisatie. De vaste stof wordt opgedeeld in een aantal gelijke volumes die niet van vorm veran-

deren tijdens de simulatie. De inhoud van een volume verandert van puur maagdelijk naar een gemengd volume, dat het pyrolysevolume voorstelt. Hier wordt dus afgestapt van de voorstelling van de pyrolysezone door een oppervlak. Het gemengde volume bestaat uit een mengeling van maagdelijk en verkoold materiaal op (constante) pyrolysetemperatuur. Het volume wordt gekarakteriseerd door de koolfractie.

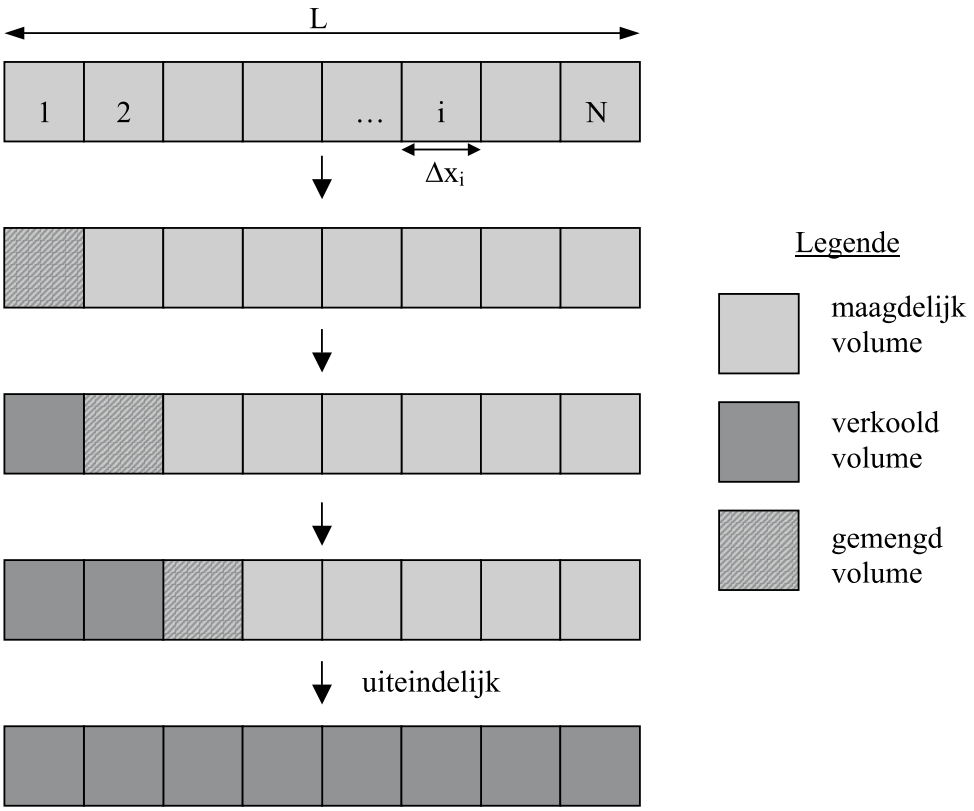

Figuur 7.1: Verplaatsing van het "gemengde volume"

Modelvergelijkingen

Het behoud van energie in conservatieve vorm is gegeven door:

$$\int_t^{t+\Delta t} \frac{\mathrm{d}}{\mathrm{d}t}\left(\int_V E \mathrm{d}V\right) \mathrm{d}t \;= \int_t^{t+\Delta t} \int_{\partial V} -\dot{\mathbf{q}}''_c \cdot \mathbf{n}\, \mathrm{d}S\, \mathrm{d}t \;+ \int_t^{t+\Delta t} \int_{\partial V} -\dot{\mathbf{q}}''_{pyr} \cdot \mathbf{n}\, \mathrm{d}S\, \mathrm{d}t \quad (36)$$

In discrete vorm wordt dit:

$$E_i^{n+1} = E_i^n + \frac{\Delta t}{\Delta x_i}\left[\left(\dot{q}''^{n+\theta}_{c,i-1/2} - \dot{q}''^{n+\theta}_{c,i+1/2}\right) + \left(\dot{q}''^{n+\theta}_{pyr,i-1/2} - \dot{q}''^{n+\theta}_{pyr,i+1/2}\right)\right] \quad (37)$$

De toestand van een volume, maagdelijk, gemengd of verkoold, wordt bepaald door de koolfractie. Voor een maagdelijk volume wordt de nieuwe koolfractie gegeven door:

$$\xi_i^n = 0 \quad \Longrightarrow \quad \xi_i^{n+1} = \max\left(0; \frac{E_i^{n+1}}{(\rho_v - \rho_c)\Delta Q_{pyr}}\right) \quad < 1 \quad (38)$$

Voor een gemengd volume wordt de nieuwe koolfractie gegeven door:

$$0 < \xi_i^n < 1 \quad \Longrightarrow \quad \xi_i^{n+1} = \max\left(\xi_i^n; \frac{E_i^{n+1}}{(\rho_v - \rho_c)\Delta Q_{pyr}}; 1\right) \quad (39)$$

Een verkoold volume blijft natuurlijk verkoold en dus verandert de koolfractie niet:

$$\xi_i^n = 1 \quad \Longrightarrow \quad \xi_i^{n+1} = 1 \quad (40)$$

De temperatuur van een maagdelijk volume volgt uit:

$$\xi_i^{n+1} = 0 \quad \Longrightarrow \quad T_i^{n+1} = T_{pyr} + \frac{E_i^{n+1}}{\rho_v c_v} \quad (41)$$

De temperatuur van een pyrolyserend gemengd volume is natuurlijk de pyrolysetemperatuur, dus:

$$\xi_i^{n+1} = \frac{E_i^{n+1}}{(\rho_v - \rho_c)\Delta Q_{pyr}} \quad \Longrightarrow \quad T_i^{n+1} = T_{pyr} \quad (42)$$

Wanneer het volume niet pyrolyseert (bijvoorbeeld bij afkoeling na afgebroken pyrolyse) dan geldt:

$$\xi_i^{n+1} > \frac{E_i^{n+1}}{(\rho_v - \rho_c)\Delta Q_{pyr}} \quad \Longrightarrow$$

$$T_i^{n+1} = T_{pyr} + \frac{E_i^{n+1} \; - \; \xi_i^{n+1}(\rho_v - \rho_c)\Delta Q_{pyr}}{\xi_i^{n+1}\rho_c c_c \; - \; (1 - \xi_i^{n+1})\rho_v c_v} \quad (43)$$

Voor een verkoold volume wordt de temperatuur berekend met:

$$\xi_i^{n+1} = 1 \quad \Longrightarrow \quad T_i^{n+1} = T_{pyr} + \frac{E_i^{n+1} - (\rho_v - \rho_c)\Delta Q_{pyr}}{\rho_c c_c} \quad (44)$$

De conductieve warmteflux in Vergelijking 37 wordt bepaald met de wet van Fourier:

$$\dot{q}''_{c,i-1/2} = -\frac{T_i - T_{i-1}}{R_{i-1/2}} \tag{45}$$

waar R de warmteweerstand gegeven door:

$$R_{i-1/2} = \frac{\frac{1}{2}\Delta x_{i-1}}{k_{i-1}} + \frac{\frac{1}{2}\Delta x_i}{k_i} \tag{46}$$

In de laatste vergelijking is k de effectieve conductiecoëfficiënt. Voor de berekening van de conductieve warmte-overdracht aan het gemengd volume, zijn er verschillende mogelijkheden om deze effectieve conductiecoëfficiënt in te vullen. Wanneer men in het gemengd volume een scheidingsoppervlak beschouwt, geldt:

$$\frac{1}{k_i} = \frac{\xi_i}{\lambda_c(T_i)} + \frac{(1-\xi_i)}{\lambda_v(T_i)} \tag{47}$$

Bij de "Enthalpie methode" is het niet meer noodzakelijk om een onderscheid te maken tussen verschillende fasen. Dit maakt de methode beduidend eenvoudiger. Voor de tijdsdiscretisatie wordt de Cranck-Nicholson methode gebruikt. De bekomen vergelijkingen werden iteratief opgelost.

Simulaties

De rekenresultaten vertonen ook voor een groot aantal volumes een massaflux pyrolysegassen die sterk oscilleerde. Het aantal oscillaties is gelijk aan het aantal volumes in de simulatie. Tussen opeenvolgende oscillaties valt de massaflux pyrolysegassen op nul. Een oplossing, onafhankelijk van het rooster, kan niet worden bekomen.

De verklaring van de oscillaties ligt in de temperatuur van het "gemengde volume". Zolang een volume "gemengd" is, dus aan het pyrolyseren, staat het op de constante pyrolysetemperatuur. Wanneer het volume volledig gepyrolyseerd is, zal het naastliggende volume nog steeds uit 100 % maagdelijk materiaal bestaan. De temperatuur van dit naastliggende volume is lager dan de pyrolysetemperatuur, want het volume wordt opgewarmd door conductie via het "gemengde volume" op pyrolysetemperatuur. Wanneer het pyrolysefront een volume verlaat, verdwijnt het even, of anders gezegd, staat het even stil tussen twee volumes. De massaflux pyrolysegassen valt dan op nul. Dit is een belangrijk nadeel van het anders eenvoudige "Enthalpie model".

Voor een tijdstap onafhankelijke oplossing, moeten kleine tijdstappen worden genomen, bijvoorbeeld voor 20 volumes tijdstappen van 0.05 s. Maar voor een grof rooster is de ruimtelijk discretisatiefout veel groter zodat de tijdstap kan worden vergroot naar 0.5 s. Men heeft voor dergelijk grof rooster natuurlijk een stapsgewijze vrijstelling van de pyrolysegassen. Voor 200 volumes moet de tijdstap kleiner zijn dan 0.05 s wegens stabiliteitsredenen.

Verbeteringen

De resultaten van het "Enthalpie model" zijn niet echt bevredigend wegens de oscillaties. Verschillende pogingen werden ondernomen om deze oscillaties te vermijden.

Als eerste werd het uitmiddelen in de tijd bekeken. Wanneer de hoeveelheid vrijgestelde pyrolysegassen bijvoorbeeld maar om de seconde vereist zijn, dan kan men de massaflux pyrolysegassen uitmiddelen over deze tijd.

$$\overline{\dot{m}''_{fl}} = \int_{\Delta t=1\,\mathrm{s}} \dot{m}''_{fl}(t)\mathrm{d}t \tag{48}$$

Natuurlijk moet de tijdstap in het "Enthalpiemodel" dan merkelijk kleiner zijn dan de uitmiddelingsperiode. Tevens moet het rooster fijn genoeg zijn zodat er verschillende of toch minstens één piek in de uitmiddelingsperiode zit. Er is nog steeds een groot aantal volumes nodig (minstens 640) wanneer gemiddeld wordt over 1 seconde. De gemiddelde afwijking in de massaflux bedroeg 10.8%.

Als tweede werd het uitmiddelen van resultaten van twee verschillende roosters bekeken. Het ene rooster was een half volume verschoven ten opzichte van het andere. Het zo bekomen resultaat was beter, maar vertoonde nog steeds oscillaties.

Als derde, werd voorgesteld om de berekeningen op verschillende (meer dan 2) maar grove roosters te doen. Elk rooster was net iets verschoven ten opzichte van de andere. Met 21 volumes en 10 roosters was er een gemiddelde fout in de massaflux van ongeveer 8%. De resultaten zijn dus merkelijk beter dan bij het uitmiddelen met slechts twee roosters, maar nog steeds waren kleine oscillaties aanwezig.

Als vierde werd een alternatieve berekening voor de conductie aan het "gemengd volume" voorgesteld. Dit bracht enkel op het einde van de simulatie bruikbare verbetering.

Als vijfde, en laatste, werd een variabel rooster geprobeerd. Hierbij wordt het rooster enkel in de buurt van het pyrolyserende volume verfijnd. Deze werkwijze werd gecombineerd met het uitmiddelen in de tijd. Deze methode gaf gelijkaardige resultaten als de eerste verbetering (enkel uitmiddelen in de

tijd) maar had merkelijk minder volumes nodig. Wanneer enkel werd uitgemiddeld in tijd waren bijvoorbeeld 1032 volumes nodig en was de rekentijd ongeveer tien keer langer dan bij de gecombineerde methode met variabel rooster (waar in totaal maar 122 volumes nodig waren).

Hoofdstuk 8: Twee-rooster model

Het "Twee-rooster model" is gebaseerd op het Arrhenius model van Hoofdstuk 4. Het concept van deze methode werd reeds beschreven in het werk van Yan en Holmstedt [126], de Ris & Yan [19] en Yan [125]. Het model bezit kenmerken van het "Arrhenius model", het "Bewegend-rooster model" en het "Enthalpie model".

In het standaard "Arrhenius model" is een heel fijn rooster nodig omdat anders oscillaties in de massaflux pyrolysegassen optreden. Feitelijk is dit fijne rooster enkel nodig in de buurt van de pyrolysezone omdat daar de densiteit op korte afstand sterk verandert. Dit was de aanleiding om een tweede rooster te introduceren.

Het model van de Ris & Yan [19] is geïmplementeerd maar met enkele kleine wijzigingen. De methode is geformuleerd in de koolfractie die in de voorgaande hoofdstukken ook is gebruikt. De temperatuur wordt op een grof rooster berekend, zie Figuur 8.1, met:

$$\frac{(\rho c T)_i^{n+1} - (\rho c T)_i^n}{\Delta t} \cdot \Delta x = \lambda_{i-1/2} \cdot \frac{T_{i-1}^{n+\theta} - T_i^{n+\theta}}{\Delta x} + \lambda_{i+1/2} \cdot \frac{T_{i+1}^{n+\theta} - T_i^{n+\theta}}{\Delta x} + Q_{pyr}(\rho_v - \rho_c) \left(\frac{\partial \xi}{\partial t}\right)^{n+\theta} \quad (49)$$

De koolfractie ξ wordt algemeen gegeven door:

$$\frac{\partial \xi}{\partial t} = (1 - \xi) \cdot f(T) \quad (50)$$

Wanneer een exponentiële reactiesnelheid wordt gebruikt is:

$$f(T) = A \cdot \exp\left(-\frac{E}{RT}\right) \quad (51)$$

Wanneer een gelineariseerde reactiesnelheid wordt gebruikt is:

$$f(T) = A_p \cdot (T - T_v) \quad (52)$$

waar A_p en T_v worden bepaald uit de gelineariseerde Arrheniuswet:

$$A_p = \frac{AE}{RT_{pyr}^2} \cdot \exp\left(-\frac{E}{RT_{pyr}}\right)$$
$$T_v = T_{pyr} \cdot \left(1 - \frac{E}{RT_{pyr}}\right)$$

In de energievergelijking kan men de bronterm (de laatste) term één tijdstap laten naijlen. Men kan dan het TDMA-algoritme gebruiken om de verschillende knooppuntstemperaturen direct te berekenen.

De koolfractie wordt berekend op het lokale verfijnde rooster, zie Figuur 8.2. Een linkse half volume van het grove rooster worden opgedeeld wanneer:

$$\xi_{links,i} \neq 1 \quad \text{en} \quad T_i > T_v \text{ of } T_{i-1} > T_v \tag{53}$$

een rechtse half volume:

$$\xi_{rechts,i} \neq 1 \quad \text{en} \quad T_i > T_v \text{ of } T_{i+1} > T_v \tag{54}$$

De berekening op het fijne rooster wordt gestopt wanneer:

$$\xi_{grof} > 1 - \epsilon$$

met ϵ een klein getal.

Simulatie

Voor de gelineariseerde reactiesnelheid vindt men bevredigende resultaten voor 80 grove en 2 fijne volumes (dus 1 grof volume wordt opgedeeld in 4 fijne volumes) met een tijdstap van 1 s. Voor de exponentiële reactiesnelheid waren er 10 fijne volumes nodige om eenzelfde nauwkeurigheid te bereiken. Bij de exponentiële reactiesnelheid waren er nog steeds kleine oscillaties (zelfs bij 80 fijne volumes). De tijdstap moet er ook iets kleiner worden genomen. De oorzaak is het naijlen van de bronterm in de energievergelijking. De berekeningstijd is voor de gelineariseerde reactiesnelheid ongeveer 80 maal sneller dan de exponentiële. Maar de exponentiële methode is op zijn beurt toch nog steeds twee maal sneller dan het "Arrhenius model" van Hoofdstuk 4.

Hoofdstuk 9: Validatie van pyrolysemodellen

In dit hoofdstuk worden de pyrolysemodellen beschreven in Hoofdstuk 4 tot 8 vergeleken met elkaar, en met experimenten. Het "Twee-rooster model"

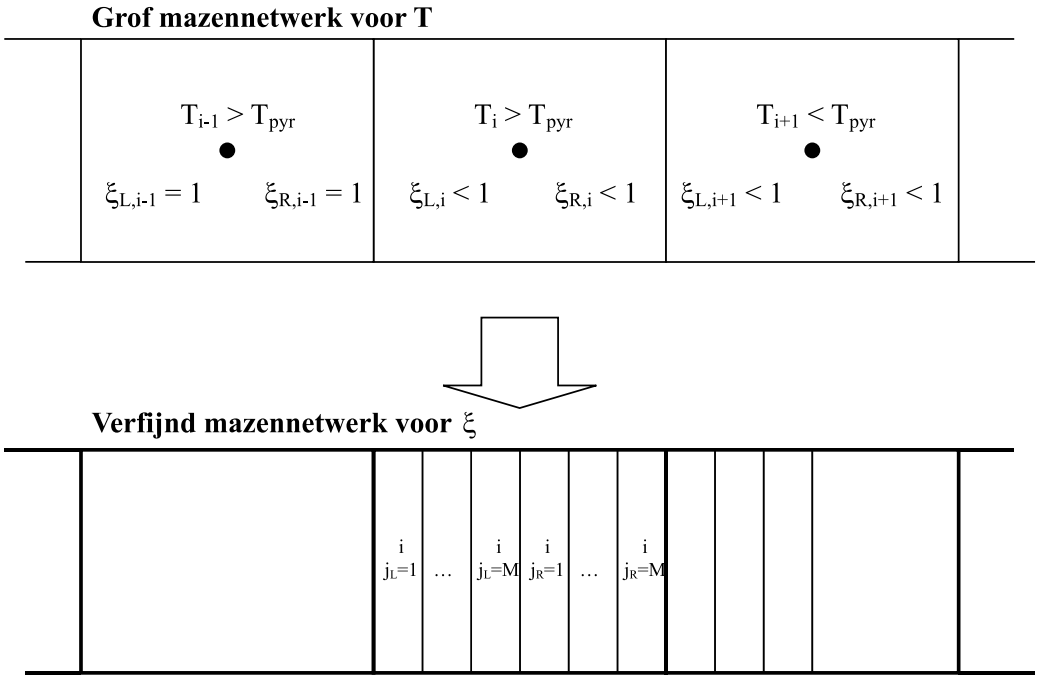

Figuur 8.1: Grof en verfijnd rooster

is hier niet opgenomen omdat de resultaten bijna identiek waren aan die van het "Arrhenius model". Voor het "Bewegend rooster" is steeds het niet-uniform rooster gebruikt. Voor het "Ethalpie model" bestaan er verschillende mogelijkheden om de stapsgewijze vrijstelling van pyrolysegassen te vermijden. Hier is geopteerd om te werken met twee roosters met elk 40 volumes, gecombineerd met tijdsmiddeling. Dit was een compromis tussen rekentijd en nauwkeurigheid.

Sensitiviteitsstudie

Gedurende de pyrolyse van verkolende materialen vertonen veel experimentele resultaten twee pieken in de vrijgave van pyrolysegassen. De tweede piek wordt veroorzaakt door het achterzijde-effect (*back effect*). Wanneer het pyrolysefront de geïsoleerde achterzijde van de vaste stof bereikt, zal er steeds minder energie van het pyrolysefront naar de maagdelijke stof stromen. Als deze daling groter is dan de daling van de energie die naar het front stroomt, zal er een tweede piek worden gevormd.

Sommige vlamuitbreidingsmodellen zijn enkel geldig voor thermische dunne of dikke materialen. De voorgestelde pyrolysemodellen worden verwacht beide regimes aan te kunnen. Simulaties tonen aan dat voor thermisch dikke materialen er zich twee pieken in de vrijstelling van pyrolysegassen kunnen vormen (*back effect*). Voor thermische dunne materialen is er slechts één piek, en kan een constante vrijgave van pyrolysegassen als benadering worden gebruikt.

Een vaste stof met dikte 1, 2, 5, 10, 20 en 50 mm werd gesimuleerd. Hieruit bleek dat het "Integraal model" soms een kortere ontstekingstijd voorspelde voor dikke materialen dan voor dunne. Wanneer de achterzijde volmaakt is geïsoleerd is dit echter onmogelijk. Deze fout in het model ligt in de overgang van de half-oneindige naar de eindige opwarmfase. Na deze overgang wordt de oppervlaktetemperatuur onderschat.

Wanneer de randvoorwaarde aan de achterzijde werd onderzocht (verschillende convectiecoëfficiënten werden opgelegd), werd voor het "Integraal model" bij de overgang van half-oneindige naar eindige pyrolysefase onrealistische resultaten vastgesteld. Alle modellen voorspellen het verdwijnen van de tweede piek wanneer de convectiecoëfficiënt aan de achterzijde vergroot.

De thermische materiaaleigenschappen voor het pyrolysemodel zijn veelal slecht gekend. De waarden in de literatuur voor bijvoorbeeld de densiteit van de koollaag lopen sterk uiteen, en zelfs voor de densiteit van de maagdelijke stof vindt men al merkelijke verschillen. Om de invloed van de verschillende materiaaleigenschappen op de vrijstelling van pyrolysegassen na te gaan, werd elke parameter 25% gewijzigd, terwijl de andere parameters

constant werden gehouden. De vier modellen geven gelijkaardige reactie bij verandering van de materiaaleigenschappen. De initiële piek in de vrijstelling van pyrolysegassen wordt voornamelijk bepaald door de pyrolysetemperatuur of de activeringsenergie. De oppervlaktetemperatuur van de vaste stof verandert slechts weinig bij het wijzigen van de materiaaleigenschappen.

Het wel of niet opwarmen van de pyrolysegassen bij hun stroming van pyrolysefront naar oppervlak werd eveneens onderzocht. Wanneer de pyrolysegassen warmte absorberen, voeren zij deze af naar de gasfase en duurt het langer om de vaste stof volledig te pyrolyseren. In het "Integraal model" kan de opwarming van de pyrolysegassen geïncorporeerd worden in de netto invallende warmteflux. In Figuur 9.1 blijkt duidelijk dat het "Integraal model" verschillend reageert dan de andere. Voor de dooftijd en de vrijstelling van pyrolysegassen is bijna geen verschil in tussen opwarming en geen opwarming. Dit komt omdat het "Integraal model" bij opwarming van de pyrolysegassen een lagere oppervlaktetemperatuur voorspelt dan de andere modellen. Door deze lagere temperatuur is het stralingsverlies kleiner en is er dus meer energie voorhanden voor de pyrolysereacties.

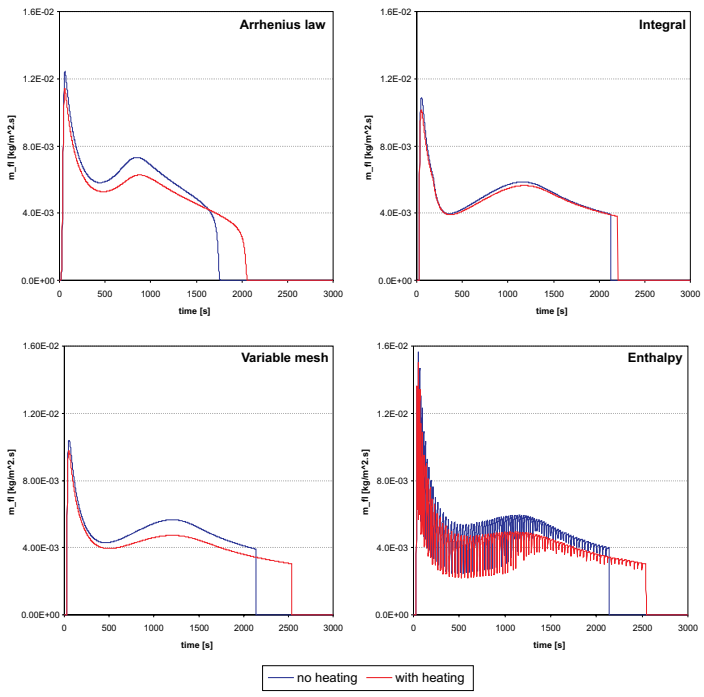

Figuur 9.1: Mass flux pyrolysegassen, met en zonder opwarming

Vergelijking met inert Cone Calorimeter proeven: multiplex

In het artikel van de Ris & Yan [19] vergelijken de auteurs hun pyrolysemodel met inerte Cone Calorimeter proeven. Multiplex werd blootgesteld aan een stralingsflux van $50\,\mathrm{kW/m^2}$ in een stikstof atmosfeer. De inerte atmosfeer verhindert de pyrolysegassen te ontsteken, en houdt de invallende warmteflux dus constant. De extra warmteflux van de vlam moet niet in rekening worden gebracht.

De thermische materiaaleigenschappen worden bepaald uit optimalisatie van de simulaties. Een voorbeeld van de bekomen vrijstelling van pyrolysegassen wordt gegeven in Figuur 9.2 voor het "Bewegend-rooster model".

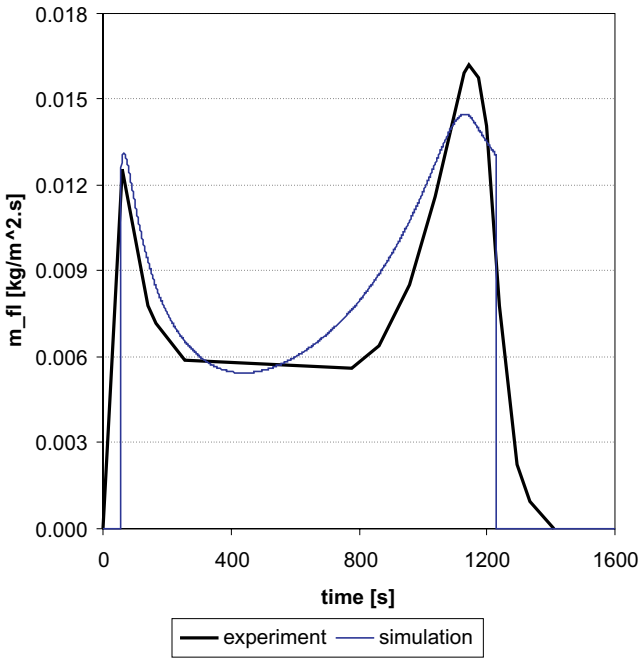

Figuur 9.2: Vrijstelling pyrolysegassen voor multiplex (inert atm)

Vergelijking met inerte Cone Calorimeter proeven: vezelplaat

Voor vezelplaat zijn de thermische eigenschappen uit de literatuur geëvalueerd. Twee reeksen eigenschappen, namelijk uit de Ris & Yan [19] en Novozhilov et *al.* [86] zijn gesimuleerd. De resultaten worden voorgesteld in Figuur

9.3 en 9.4. De resultaten (vrijstelling pyrolysegassen) met de eigenschappen van *de Ris & Yan* zijn aanvaardbaar. Die van *Novozhilov* zijn voor de eerste helft van de simulatie te laag, terwijl ze voor de tweede helft te hoog zijn. De oppervlaktetemperatuur is voor beide simulaties te hoog. Naast deze twee reeksen zijn eveneens geoptimaliseerde eigenschappen bepaald.

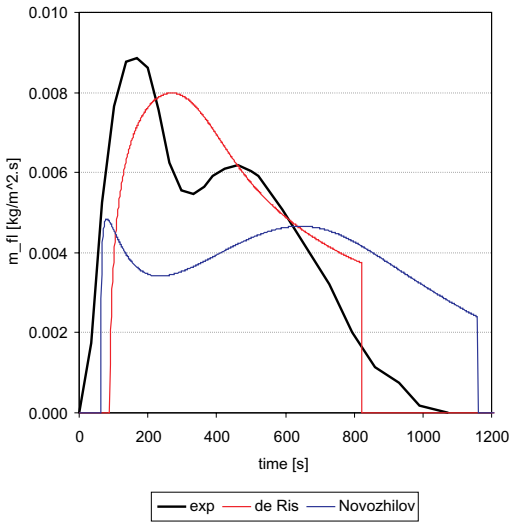

Figuur 9.3: Vrijstelling pyrolysegassen voor vezelplaat (inert atm)

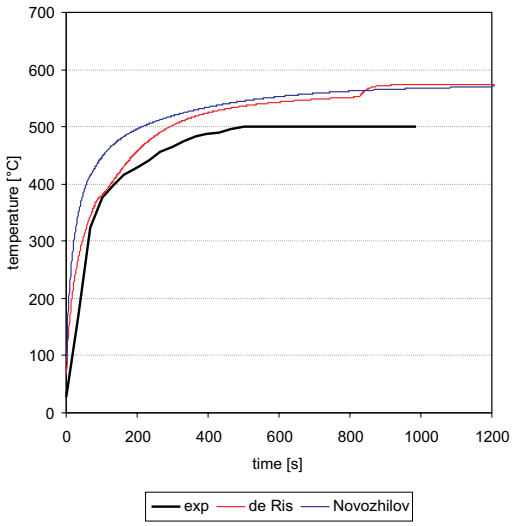

Figuur 9.4: Oppervlaktetemperatuur voor multiplex (inert atm)

Vergelijking met standaard Cone Calorimeter proeven: vezelplaat

Het "Bewegend-rooster model" is vergeleken met standaard Cone Calorimeter proeven, d.w.z. in een atmosfeer met 21% zuurstof. De experimentele resultaten van de Cone Calorimeter zijn niet gebruikt voor optimalisatie van de thermische eigenschappen (zoals gedaan in vorige sectie), omdat de randvoorwaarden voor het pyrolysemodel niet nauwkeurig gekend zijn. Immers, zodra de pyrolysegassen ontvlammen, moet de warmteflux van de vlam in rekening worden gebracht. Deze warmteflux moet worden gemodelleerd en over de waarde van de flux bestaat grote onzekerheid. Voor de eenvoud is hier met een constante warmteflux van $10\,\mathrm{kW/m^2}$ gewerkt.

Simulatie en experimenten zijn gedaan voor een externe warmteflux (= ingestelde Cone Calorimeter flux) van 25 en $50\,\mathrm{kW/m^2}$. Uit de resultaten bleek dat geen enkele reeks van de in de vorige sectie bepaalde thermische eigenschappen, beide testen nauwkeurig kon beschrijven.

Hoofdstuk 10: Eenvoudig vlamvoortplantingsmodel

In dit hoofdstuk wordt onderzocht:

1. of conductieve warmte-overdracht in de richting van de vlamuitbreiding in overweging moet worden genomen;

2. hoe groot de volumes in de richting van de vlamuitbreiding mogen zijn;

3. en hoe de terugkoppeling van de energie via de vlam (verbranding van pyrolysegassen) zich gedraagt.

Hiertoe zijn geschikte randvoorwaarden voor het pyrolysemodel (vaste stof) vereist. In dit stadium was het niet aangewezen de modellen reeds met een CFD-pakket te koppelen. Daarom is in de gasfase enkel de vlam gemodelleerd. Zowel directe als indirecte warmte-terugkoppeling zijn toegepast.

Voor de vaste stof wordt het "Arrhenius model" gekozen omdat dit één-, twee- en driedimensionale berekeningen toelaat. De conductieve warmteflux in een bepaalde richting kan worden verhinderd zodat een zogenaamde tweedimensionale berekening wordt opgebouwd uit een reeks onafhankelijke eendimensionale problemen.

Twee-dimensionale simulaties worden vergeleken met verticale vlamuitbreidingsexperimenten van Brehob en Kulkarni [9]. In hun experimenten werden stalen van 30 bij 120 cm door een lijnbrander ontstoken. Enkel de resultaten met vezelplaat worden gebruikt.

Geen terugkoppeling

Wanneer er geen terugkoppeling is van de vlam naar het pyrolysemodel, is de randvoorwaarde aan de vaste stof onafhankelijk van de resultaten in de simulatie. In de berekening van de op de vaste stof invallende warmteflux, zijn de snelheid van de vlamtip en pyrolysehoogte constant verondersteld. De warmteflux is aangepast zodanig dat hij overeenkwam met de experimenteel opgemeten waarden. Voor de zone buiten de pyrolysezone $x > x_{pyr}$:

$$\dot{q}''_{inc}(x,t) \;=\; \dot{q}''_{wo} \cdot \exp\left[C_0\left(\frac{x - v_p \cdot t + 0.35}{0.2}\right)\right] + \dot{q}''_{ext} + 20\,\mathrm{kW/m^2} \quad (55)$$

Voor de tweedimenionale berekening werden 10, 25, 50, 100, 200 en 400 volumes in de verticale richtingen genomen. De resultaten voor het grove rooster waren nog aanvaarbaar, maar ze waren niet rooster onafhankelijk.

Niet alle pyrolysemodellen ontwikkeld in Hoofdstukken 4 t.e.m. 8, laten tweedimensionale warmte-overdracht toe. De eendimensionale modellen kunnen echter toch gebruikt worden wanneer de conductieve warmte-overdracht in de vaste stof te verwaarlozen is. Uit de simulaties blijkt dat dit het geval is.

Wel terugkoppeling

In realiteit is de warmte-terugkoppeling afhankelijk van de reactie van de vaste stof. Wanneer de vaste stof veel pyrolysegassen afgeeft, zal dit in de gasfase voor een grote en hete vlam zorgen, en dus voor een verhoogde opwarming van de vaste stof (en omgekeerd). Fouten in de vrijstelling van pyrolysegassen kunnen dus worden versterkt. Daarom is een eenvoudig gasmodel met indirecte warmte-terugkoppeling aan het pyrolysemodel toegevoegd.

De randvoorwaarde wordt nu gegeven voor $x > x_p$ door:

$$\dot{q}''_w(x,t) \;=\; \dot{q}''_{wo} \cdot \exp\left[C_0 \left(\frac{x - x_p}{x_f - x_p}\right)\right] + \dot{q}''_{ext} - \dot{q}''_{rerad} \tag{56}$$

en voor $x < x_p$:

$$\dot{q}''_w(x,t) \;=\; \dot{q}''_{wo} \;+\; \dot{q}''_{ext} \;-\; \dot{q}''_{rerad} \tag{57}$$

De vlamlengte wordt berekend uit onderstaande correlatie:

$$x_f(t) - x_b(t) = K\left[\dot{Q}'(t) + H_c \cdot \int_{x_b(t)}^{x_p(t)} \dot{m}''_{pyr}\mathrm{d}x\right]^n \tag{58}$$

Voor grote vlamlengtes bleek deze correlatie niet toepasbaar.

De resultaten voor de een- en tweedimensionale berekening waren gelijkaardig en kwamen goed overeen met de experimenten, zie Figuur 10.1. De (terug)koppeling tussen gasmodel en pyrolysemodel is niet kritisch.

Hoofdstuk 11: Modellering van de gasfase

In dit hoofdstuk wordt het gasmodel besproken. Het gasmodel bestaat feitelijk uit een commercieel CFD-pakket, CFX. In de berekening komen turbulentie, verbranding, straling en roet-modellering aan bod. Voor elke "submodel" worden de belangrijkste technieken die bij brandberekening worden aangewend, bondig beschreven.

Naast de bespreking van het gasmodel wordt ook de koppeling tussen CFD-pakket en het pyrolysemodel uitgelegd. Het pyrolysemodel wordt via

gebruiker-routines (FORTRAN) geïmplementeerd. Het CFD-model geeft de netto invallende warmteflux door aan het pyrolysemodel. De resultaten van de pyrolyseberekeningen, dit zijn de oppervlaktetemperatuur en de hoeveelheid vrijgestelde pyrolysegassen wordt terug aan het CFD-model gegeven. Dit is schematisch voorgesteld in Figuur 11.1.

De transportvergelijkingen in CFX zijn van de vorm:

$$\int_V \frac{\partial \rho\phi}{\partial t} \mathrm{d}V \; + \; \int_S \rho \mathbf{U} \cdot \mathbf{n} \phi \mathrm{d}S \; - \; \int_S \Gamma \nabla \phi \cdot \mathbf{n} \mathrm{d}S \; = \; \int_V S \mathrm{d}V \tag{59}$$

Het rechterlid staat voor de bronterm en kan in de gebruikersroutines worden

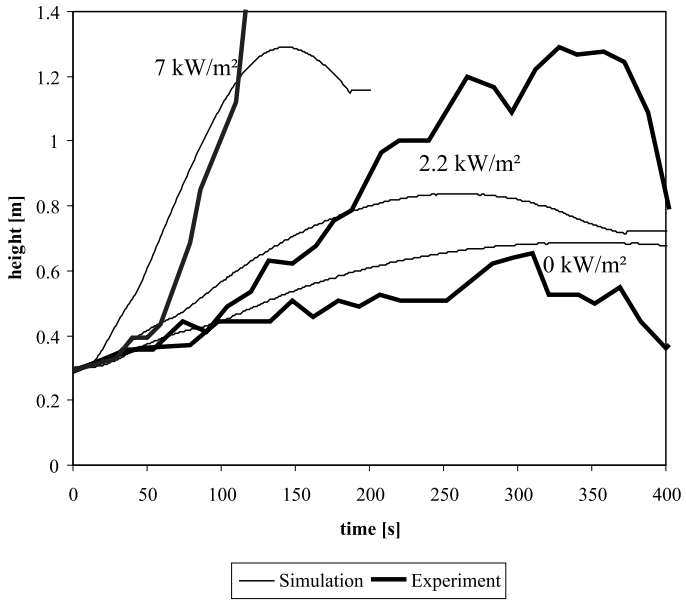

Figuur 10.1: Experimenteel en gesimuleerde vlamlengte

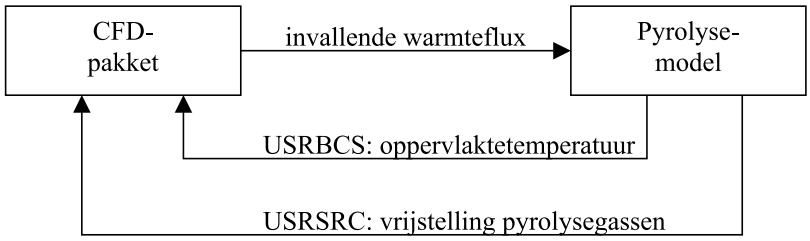

Figuur 11.1: Koppeling tussen CFX en pyrolysemodel

gedefinieerd. De brontermen worden gelineariseerd:

$$\int_V S \, \mathrm{d}V = S_u + S_p \cdot \phi \tag{60}$$

De pyrolysegassen die het berekeningsdomein van de gasfase binnenstromen worden gemodelleerd door het introduceren van brontermen in de gepaste volumes.

Massa in kg/s:

$$S_u = \dot{m}_{pyr} \tag{61}$$

Impuls loodrecht op de wand in kg.m/s^2 (u_{pyr} is nul voor de meeste berekeningen):

$$S_u = \dot{m}_{pyr} \cdot u_{pyr} \tag{62}$$

Energie in J/s:

$$S_u = \dot{m}_{pyr} \cdot m_f \cdot \left(H_{pyr} + \int_0^T c_p(T) \mathrm{d}T - \int_0^T c_{po}(T) \mathrm{d}T \right) \tag{63}$$

Mengfractie in kg/s:

$$S_u = \dot{m}_{pyr} \cdot F_{pyr} \tag{64}$$

Massa fractie brandstof in kg/s:

$$S_u = \dot{m}_{pyr} \cdot m_f \tag{65}$$

Hoofdstuk 12: Gekoppelde simulaties

In dit hoofdstuk worden gekoppelde simulaties vergeleken met twee experimenten uit de literatuur. Het eerste experiment (A) beschrijft de branduitbreiding in een kamerconfiguratie. Het experiment werd uitgevoerd door Sundström te SP in Zweden. Het tweede experiment (B) behandelt tweedimensionale verticale vlamuitbreiding. Het werd uitgevoerd door VTT in Finland.

Experiment A

De kamer heeft een diepte van 3.6 m, een breedte van 2.4 m, en een hoogte van 2.4 m. In het centrum van de korte wand was een deur van 2.0 m bij 0.8 m. De ontstekingsbron bestond uit een vierkante propaan-brander. Het vermogen van de brander bedroeg 100 kW. De zijwanden, de achterste wand en het plafond werden bekleed met vezelplaat.

Uit de simulaties van experiment A bleek dat de materiaaleigenschappen van de vezelplaat een belangrijke invloed hadden op de rekenresultaten. Dit werd aangetoond door de thermische warmtecapaciteit van het maagdelijke en verkoolde materiaal te veranderen (van 1300 naar 2000 J/kgK). Met deze "verbeterde" materiaaleigenschappen kwamen de rekenresultaten redelijk overeen met de experimenten. De gas en oppervlaktetemperaturen en de invallende warmteflux worden gegeven in Figuren 12.1 tot 12.3.

Ook door de roetfractie van de brander en de wanden aan te passen, kunnen de rekenresultaten merkelijk worden verbeterd. De resultaten na vlamoverslag bleken echter sterk te verschillen met de experimenten.

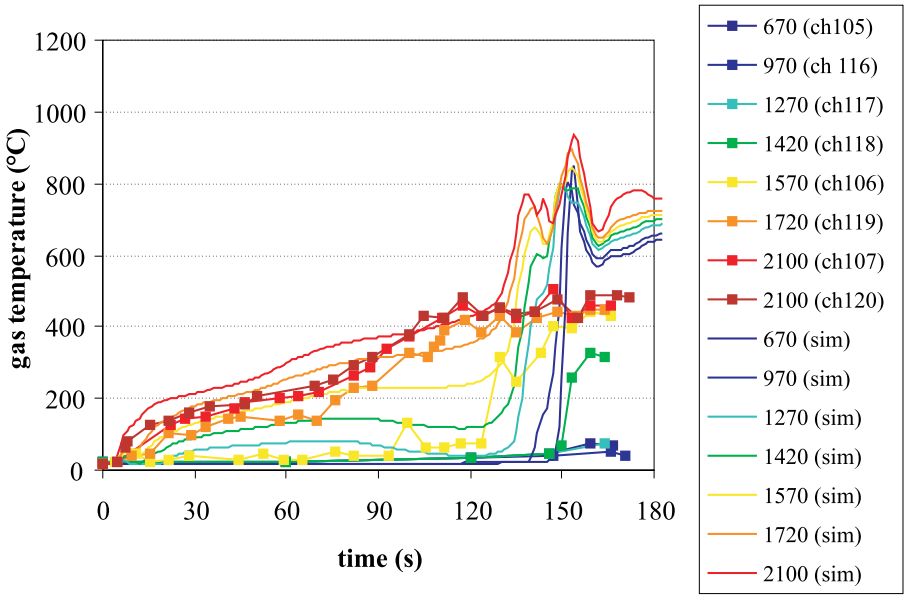

Figuur 12.1: Verticale gastemperaturen

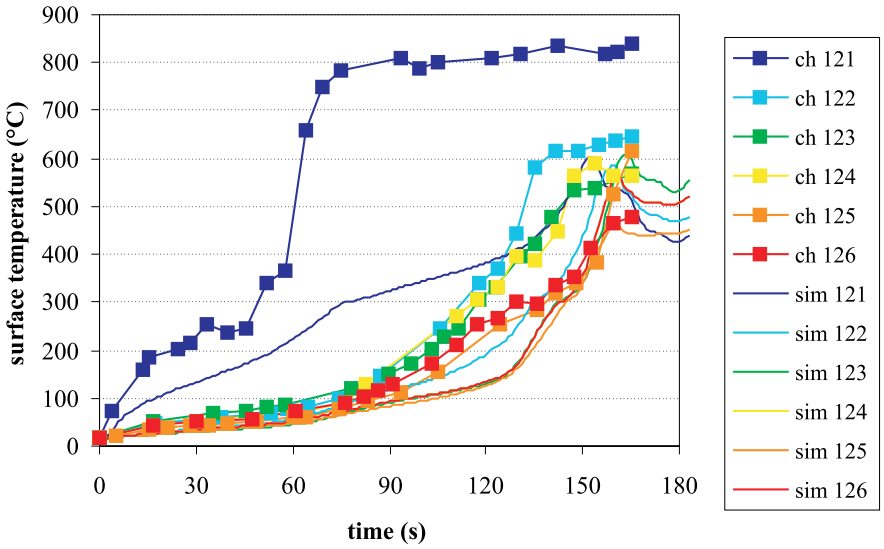

Figuur 12.2: Oppervlaktetemperaturen

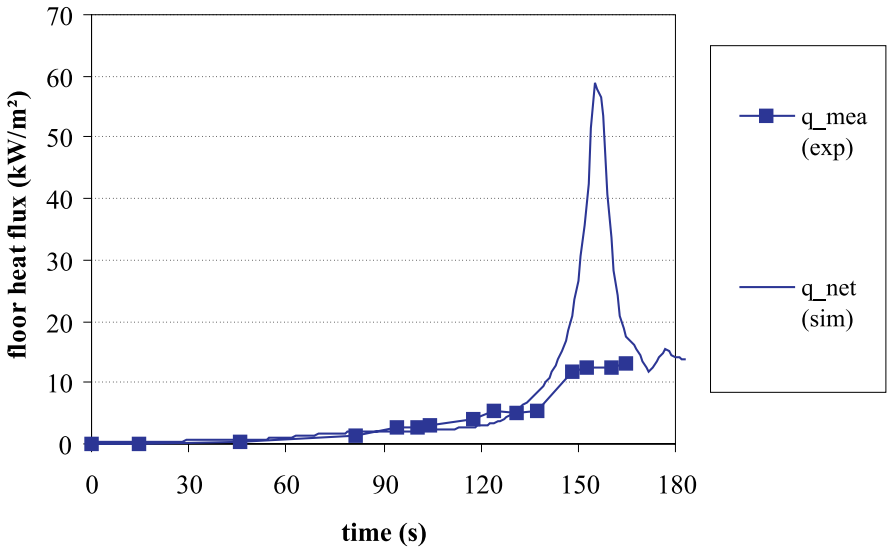

Figuur 12.3: Invallende warmteflux

Experiment B

Aangezien dit experiment tweedimensionaal was en gedetailleerdere metingen bezat dan het eerste experiment, werd het gebruikt om de fysische modellen te evalueren. In het experiment worden vezelplaten van 2.4 tot 7.5 m door een lijnbrander aan de voet van de platen ontstoken. Er trad verticale vlamuitbreiding op.

De eerste simulaties van experiment B waren niet bevredigend. Daarom werd eerste een eenvoudiger experiment bekeken, namelijk een inerte verticale wand met enkel de ontstekingsbrander. Simulaties van dit laatste experiment vertoonden steeds te hoge gastemperaturen en hoge snelheden. Deze worden vermoedelijk veroorzaakt door het turbulentie- en verbrandingsmodel. Anderzijds waren de opgemeten temperaturen aan de lage kant, en moeten er belangrijke correctiefactoren voor de experimentele waarden in rekening worden gebracht.

De kwantitatieve resultaten van de vlamuitbreiding over de vezelplaat waren dus teleurstellend. De kwalitatieve resultaten geven echter de belangrijke fenomenen weer. Op Figuur 12.4 ziet men het uitbreiden van de brand en het afnemen van de brandende zone. Dit komt goed overeen met de visuele schatting van de pyrolysehoogte tijdens de experimenten.

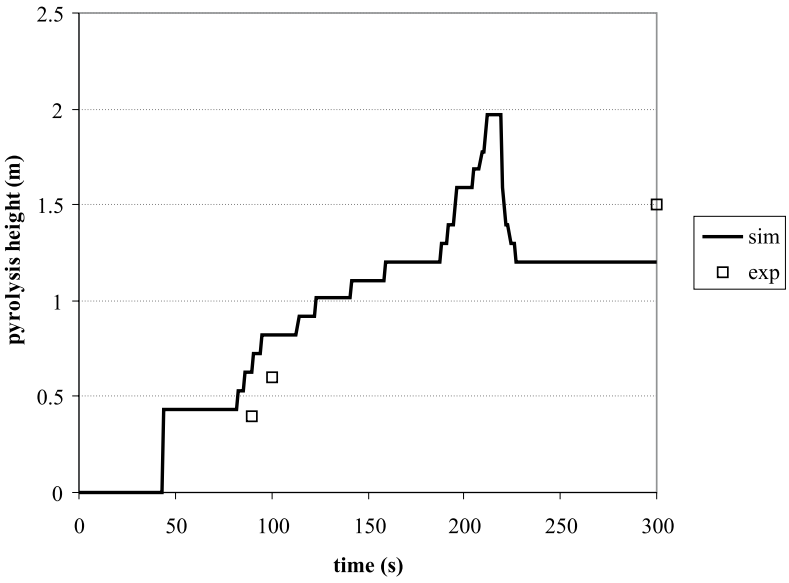

Figuur 12.4: Pyrolyse-hoogte

Hoofdstuk 13: Conclusies

Pyrloysemodellen

Er zijn vijf verschillende pyrolysemodellen onderzocht, namelijk:

1. Arrhenius model;
2. Integraal model;
3. Bewegend-rooster model;
4. Enthalpie model;
5. Twee-rooster model.

In al deze modellen beschrijft men de pyrolysereacties door een Arrheniuswet, ofwel veronderstelt men een oneindige snelle reactiesnelheid bij het bereiken van de *pyrolysetemperatuur*. Deze twee fysische representaties worden door de pyrolysemodellen verschillend opgelost. De oplossingsmethode heeft soms weerslag op het fysische model, bijvooorbeeld voor het "Enthalpie model" wordt het pyrolysefront voorgesteld met een eindig volume i.p.v. een oppervlak.

De verschillende modellen geven doorgaans gelijkaardige resultaten. Het "Arrhenius model" vraagt een zeer fijn rooster, en bijgevolg een lange rekentijd. Het kan wel eenvoudig worden uitgebreid naar twee of drie dimensies.

In het "Integraal model" is voorzichtigheid geboden bij parameterstudies. Wanneer in dit model wordt overgegaan van een half-oneindige fase naar een eindige fase treden er fouten op. Dit werd vastgesteld tijdens pure opwarming als tijdens pyrolyse. Een ander nadeel zijn de verschillende fasen (opwarming, pyrolyse, half-oneindig, eindig) die moeten worden opgesteld en gekoppeld. Een belangrijk voordeel is de korte rekentijd. Dit model is enkel eendimensionaal toepasbaar.

Het "Bewegend-rooster model" is voor brandtoepassingen nieuw. Het werd gebruikt om het "Integraal model" te evalueren. Het "Bewegend-rooster werkt ook met verschillende fasen die elkaar opvolgen, maar er zijn er wel minder dan in het "Integraal model". De rekentijd is korter voor een niet-uniform rekenrooster in de maagdelijke laag. Het model kan worden uitgebreid naar meerdere dimensies.

Ook het "Enthalpie model" is voor brandtoepassingen eveneens nieuw. Bij het "Enthalpie model" moeten voorzorgen worden genomen om oscillaties in de vrijgave van pyrolysegassen afkomstig van het rooster, te vermijden. Verschillende technieken werden geprobeerd. Het uitmiddelen in de tijd

gecombineerd met een variabel rooster bleek de beste oplossing. Het model kan eenvoudig worden uitgebreid naar meerdere dimensies.

Het "Twee-rooster model" gebruikt een grof rooster voor de temperatuur en een lokaal (aan het pyrolysefront) fijn rooster voor de dichtheid. De voorkeur wordt gegeven aan de gelineariseerde reactiesnelheid wegens zijn kortere rekentijd (grotere tijdstap, grover rooster).

Uit de vergelijking met experimenten blijkt duidelijk dat er een grote onzekerheid bestaat over de materiaaleigenschappen, zeker de eigenschappen voor de koollaag en het pyrolysefront. Simulaties met *standaard* waarden kunnen merkelijk verschillen met de realiteit. Veelal worden ongekende materiaaleigenschappen bepaald door optimalisatie van rekenresultaten met experimenten. Deze optimalisatie is echter niet eenduidig en sterk verschillende combinaties geven gelijkaardige resultaten.

Eenvoudig gasmodel

In verticale vlamuitbreiding wordt meestal verondersteld dat tweedimensionale warmte-overdracht overbodig is. Deze stelling is onderzocht met een eenvoudig vlamvoortplantingsmodel gekoppeld met het "Arrhenius model". De conductieve warmte-overdracht in de uitbreidingsrichting (verticaal) werd aan- en afgezet. Uit de resultaten bleek deze verticale warmte-overdracht verwaarloosbaar.

Uit deze gekoppelde simulaties volgt dat men relatief grote volumes kan gebruiken in de verticale richting. Dit is zeer belangrijk voor de berekeningen met CFD waar de rekentijd dient beperkt te houden.

CFD gasmodel

Werken met een commerciële code heeft voor- en nadelen. Voordelen zijn dat de code onmiddellijk beschikbaar is, dat ze verschillende fysische modellen (bijvoorbeeld voor turbulentie) en verschillende numerieke schema's bevat. Een belangrijk nadeel is natuurlijk dat de code gesloten is. Dit beperkt de gebruiker en compliceert dikwijls de simulaties. Men moet vindingrijk zijn om eigen code te implementeren.

Het "Bewegend-rooster model" werd gekoppeld met een commercieel CFD-pakket CFX. De gekoppelde simulaties werden vergeleken met twee experimenten uit de literatuur: branduitbreiding in een kamerconfiguratie en tweedimensionale verticale vlamuitbreiding.

De implementatie van het "Bewegend-rooster model" is omslachtig wegens de verschillende fases. Alle mogelijke overgangen van fases moeten wor-

den voorzien. De methode is vatbaarder voor fouten dan het “Arrhenius”, “Enthalpie” of “Twee-rooster model”.

Uit de simulaties van de kamerconfiguratie, kan men besluiten dat de materiaaleigenschappen een belangrijke invloed hebben op de rekenresultaten. Dit werd aangetoond door de thermische warmtecapaciteit en de roetfractie te wijzigen. De geöptimaliseerde materiaaleigenschappen vertonen goede overeenkomst met de experimenten. Echter in enkele meetpunten blijven er sterke verschillen bestaan.

De simulaties van de tweedimensionale verticale vlamuitbreiding waren niet bevredigend. Daarom werd eerst meer een eenvoudige simulaties van een inerte wand gedaan. Hierbij trad er geen vlamuitbreiding op, enkel de brander werd gemodelleerd. De berekende temperaturen en snelheden werden in deze simulaties sterk overschat. Anderzijds moet toch worden vermeld dat sommige experimentele resultaten in vraag konden worden gesteld. In elk geval, voor verder onderzoek, zijn gedetailleerdere en nauwkeurigere metingen noodzakelijk. Enkele fysische modellen werden gewijzigd (verbrandingsmodel, straling, grenslaag) maar weinig verbetering werd vastgesteld. De kwalitatieve resultaten zijn wel bevredigend.

Part I

Introduction

Chapter 1

Introduction

This thesis is situated in the fire safety domain. The goal is to perform flame spread simulations on solid, charring materials with the use of Computational Fluid Dynamics (CFD). Therefore a fire model is developed which comprises a solid combustion model for the solid phase, and a CFD and radiation package for the gas phase. It allows fire spread and fire growth calculations. The fire model is compared with experiments.

1.1 Classification of fire models

Deterministic fire models for enclosure fires can be divided into three categories [52]:

1. CFD models;
2. zone models;
3. and hand-calculations.

The CFD or 'field' models are the most sophisticated. They divide the enclosure into a very large number of small volumes. The basic conservation laws, i.e. mass, momentum and energy, are applied to the volumes. Calculations are complex and need a lot of computer power and time.

In zone models the enclosure is divided into a limited number of zones, often only three zones: an upper hot layer, a lower cold layer and a plume zone. Only the conservation of mass and energy is applied on the zones, the conservation of momentum is not used. The advantage of zone models is that they are simple to use and they are fast. Their restriction is limited accuracy, due to (over)simplified description of physical phenomena. Zone models become inadequate as fire problems become more complex.

The last category, the hand-calculations, are a collection of simple analytical solutions and empirical methods to calculate just one aspect of a fire, e.g. the flame height, the temperature or the mass flow of the fire plume, etc. They have a very limited application domain.

All three categories of models are very useful in fire safety engineering, but when new fire phenomena have to be examined, CFD models are the only valid tool. CFD models have a more fundamental basis and their application domain is much larger than that of zone models and hand-calculations. Together with the decreasing computer cost, this has led to an increasing use of CFD models in the fire community.

1.2 Application of fire models

Fire can be seen as an unwanted combustion process. It affects society and environment by loss of life and property. Nowadays public fire safety is provided through a number of prescriptive fire building codes and standards. Most of these codes are based on experience and test methods for construction products. Rapid developments in modern building technology in the last decades often have resulted in unconventional structures and design solutions. Because of new materials and new designs the prescriptive codes have become inadequate. Performance based codes are being introduced, where the actual risk and safety level of a building is quantified. These performance based codes leave more freedom in the design of a building, but need calculation methods to determine the safety level. Here fire models become involved. The building industry and regulators already use CFD models for smoke spread problems in complex geometries, e.g. train stations, sport stadia, tunnels, shopping malls, etc. The fire models can also be used to verify the adequacy of prescriptive codes and to provide them with scientific background. They can give insight in the mechanism of initiation and growth of a fire.

In fire investigations fire models can also be an important help, e.g. the Kings Cross fire in the subway of London [102].

Fire models can also play a role in product development: instead of performing expensive large-scale tests, the fire behaviour of a product can be predicted or improved using data from cheap and fast small-scale tests combined with fire models.

1.3 Limitations of present models

A drawback of most of the compartment fire models today is that the fire has to be predefined. The progress of the fire with time is defined before the calculation and is independent of the conditions in the enclosure during the simulation. No fire or flame spread is incorporated and simulations are restricted to localised fire sources.

Models that can predict the fire growth itself, from only an initiating fire (e.g. burning cigarette), would expand substantially the utility of field models in fire applications.

1.4 Charring versus non-charring materials

In a fire model, the pyrolysis process is of particular interest, since it plays a key role in the ignition, flame spread and burning processes during the early stages of fire growth. The pyrolysis behaviour of solid materials can be divided into two types:

- non-charring and;
- charring.

Non-charring materials burn away completely, leaving no residue, and are sometimes modelled in a similar way as flammable liquids. They often reach a more or less steady combustion regime [28].

In contrast, charring materials leave relatively significant amounts of residue when they burn. The pyrolysis of charring materials such as wood is a complex interplay of chemical reactions, heat and mass transfer. Charring materials must be modelled in terms of a pyrolysis front penetrating into the material with an increasing surface temperature and without a well-defined steady state.

In this thesis several existing pyrolysis models for charring materials will be examined and two new models [114] will be developed. The choice has been made to limit the models to charring materials. Many principles of the charring models are also applicable for non-charring models. In the future non-charring materials will be examined as well.

1.5 Vertical flame spread

In this work flame or fire spread is understood as actually surface fire spread over solid materials. This implies a moving flame in close proximity to the

Table 1.1: Order of magnitude of flame spread rates [89]

Phenomenon	Rate (cm/s)
Smoldering	10^{-3}–10^{-2}
Lateral or downward spread on thick solids	10^{-1}
Upward spread on thick solids	1–10^2
Horizontal spread on liquids	1–10^2
Pre-mixed flame speeds	
laminar deflagration	10–10^2
detonation	$3 \cdot 10^5$

source of its generation from a condensed phase. This to make the distinction between flame propagation in gases e.g. premixed fuel and air systems [89]. Flame spread in gases or over liquids is not treated.

The spread of a flame over the surface of a solid combustible is a subject of interest in fire safety because it strongly influences the initial fire development and the rate of heat release [15]. The modelling of wall fires in particular is important because wall fires spread upward rapidly and they can lead to rapid flashover in rooms [74]. Horizontal, lateral and downward flame spread is most often slower and therefore will contribute less to the fire growth than upward flame spread (see Table 1.1). Of course, the ventilation plays an important role. If the flow assists the flame spread (concurrent), horizontal flame spread can also be fast. The flame spread model developed in this work is valid for this kind of flame spread (fast) as well.

For sure, upward flame spread is a critical component in a growing fire [20]. Therefore the general pyrolysis models will be applied to vertical fire configurations.

1.6 Outline

In Chapter 2 the mechanism of flame spread is discussed in order to identify the important physical and chemical processes during pyrolysis. As flame spread can be seen as an advancing ignition front, the ignition of a solid material is treated as well. The factors affecting the flame spread process are summarized.

In Chapter 3 the most important existing models for vertical flame spread in literature are classified.

In Chapter 4 to Chapter 8 five different solid combustion models are presented. Three of these models, the "Arrhenius model" [24], the "Integral model" of e.g. Moghtaderi [77] and the "Linearised Arrhenius model" of Yan [125], are existing models, while the "Moving grid model" [114] and the "Enthalpy model" are new in fire research. In Chapter 3 some other solid combustion models are given that can be coupled to a computational fluid dynamics package (CFD), but most of them do not possess the same complexity as the models from Chapter 4 to Chapter 8.

In Chapter 9 the different solid combustion models are compared with each other and with experimental data found in literature. The model that was most suitable for coupling with CFD was chosen. This was the "Moving grid" model.

In Chapter 10 the "Arrhenius model" is incorporated in a simple flame spread model. The gas phase is not solved with a CFD model. Instead, flame length and flame temperature correlations are used to determine the heat feedback. These preliminary results reveal that more-dimensional solid combustion simulation can be solved by a series of independent one-dimensional calculations.

In Chapter 11 details are given for the modelling of the gas phase. The CFD model needs to deal with turbulence, combustion, radiation and soot. The implementation of the pyrolysis model in the CFD package is discussed.

In Chapter 12 the solid combustion model is coupled with the commercial CFD-code CFX. The coupled simulations are compared with two experiments described in literature. The first experiments concerned a room configuration, the second experiment concentrated on vertical two-dimensional flame spread.

In Chapter 13 the conclusions of this work are summarized.

Chapter 2

Mechanism of flame spread

The ignition of a combustible material and the flame spread over its surface are crucial in a fire. They both determine the rate of the fire development, the materials involved, the rate of heat release, the amount of smoke and toxic species released, etc. When modelling fire and fire spread, the fundamental processes should be understood. In this chapter the different processes will be described and the main parameters and influence factors will be identified.

Flame spread can be seen as an advancing ignition front. There are many similarities between the ignition of a solid and the flame spread over it. Therefore the ignition process will be discussed first.

2.1 Ignition [28, 26]

When a solid is heated by an external heat source, e.g. by a radiating surface, a hot air current or a flame, its temperature will rise. In most cases the maximum temperature will occur at the surface of the solid. The temperature profile in the solid is dependent of the amount of heat absorbed, the variation of the heat source in time, and the thermal properties of the solid. If the heat source is large enough, the temperature in the solid will be sufficient to start the thermal degradation or pyrolysis reactions. During this degradation, virgin material is transformed into volatiles, char and tar. The volatiles flow out of the solid and mix with the air or ambient oxidizer, adjacent to the solid. The gas layer is mainly heated by conduction and convection from the hot surface, and convection or radiation from an external heat source. Due to this heating the exothermal oxidation reactions in the gas phase (combustion reactions) will increase, which of course will further augment the temperature of the gas mixture and hence the exothermal reactions. When a run-away condition is attained, the solid is said to be ignited. This is characterized by a flame in the gas phase. The initial ignition can be triggered by the heat

provided by the solid only (spontaneous or auto ignition), or by an external element, a pilot. The pilot will locally increase the temperature and start the exothermic reactions. Dependent on the conditions in the gas phase, this small reaction zone can spread over the whole surface. Immediately after the flame has been produced, it can already extinguish due to heat losses (mainly radiation) or due to consumption of the combustible gases. A flash will appear at the surface. Only when sufficient combustible pyrolysis gases are continuously supplied, the flame can persist.

The ignition process can be divided into three subprocesses:

1. thermal degradation of the solid and production of combustible volatiles;
2. mixing of volatiles with air or oxygen;
3. rise in the combustion reactions rate until the process is self-supporting.

The ignition time of a solid exists of the solid pyrolysis time (subprocess 1) and the gas induction time (subprocess 2 and 3). The solid pyrolysis time is the time to heat up the solid and let it release pyrolysis gases, while the gas induction time is the time to let the pyrolysis gases mix with the oxygen and start the chemical combustion reactions in the gas phase. Dependent on the way of heating the solid pyrolysis time or induction time can sometimes be neglected.

For example when there is a pilot flame in the gas phase, the gas induction time will be strongly reduced. It can be neglected when compared with the pyrolysis time. Hence the ignition temperature (= surface temperature when the persistent flame is produced) is for pilot-ignition lower than for spontaneous ignition, for example for wood about 250 °C (critical surface temperature is 350 °C for pilot and 600 °C for spontaneous ignition [26]). Similar for the critical radiant heat flux (= heat flux that is just high enough to produce a persistent flame): for pilot ignition of wood it is about $12\,\mathrm{kW/m^2}$, while for spontaneous ignition it is $28\,\mathrm{kW/m^2}$ which is much higher.

On the other hand when the flow residence time is of the same order as the chemical reaction time, the induction time will be the most important part of the ignition time. This is the case when there is a strong fluid flow at the solid surface.

The relation between the ignition behaviour and flame spread is explained in Figure 2.1. In several tests, with a different external radiant heat flux, the time to ignition was measured. When the radiant flux decreases, ignition takes more time, which is represented by the right curve in Figure 2.1. Finally, at the critical radiant flux, ignition does not occur, even for long exposure times.

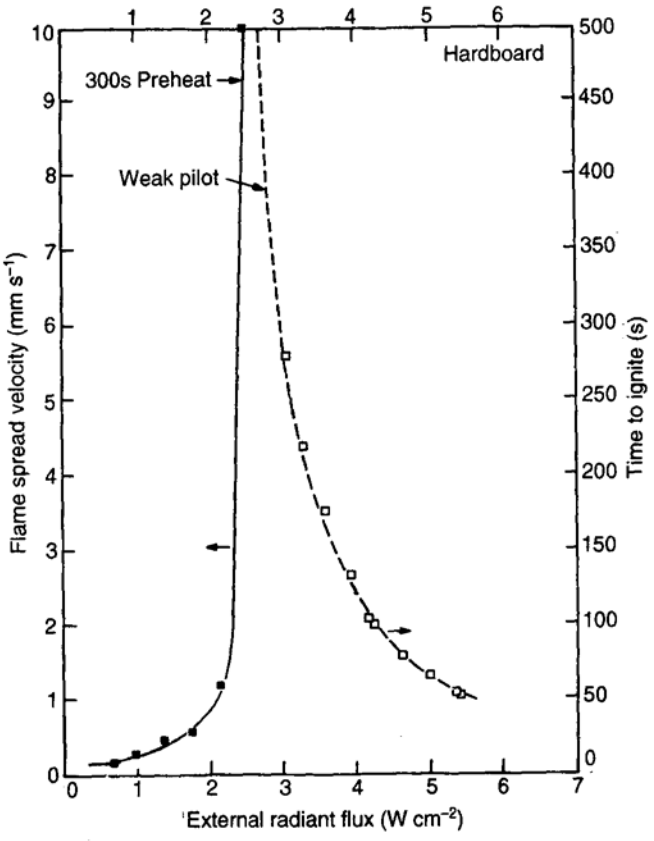

Figure 2.1: Variation of the pilot ignition time and lateral flame spread rate with the external radiant flux for hardboard sheets (from Cox [14])

For several external radiant heat fluxes belowe the critical heat flux, the lateral flame spread rate was measured. This is represented by the left curve in Figure 2.1. When the radiant flux increases, the flame spread will be faster. The spread rate is infinity when the external heat flux is equal to the critical value for the time to ignition. For this external flux the whole solid ignites at once which corresponds to an infinite spread rate.

2.2 Mechanism of flame spread [28]

To start the flame spread some external heat source must be available. The ignition of the solid can be invoked by external radiation (e.g. from remote flames or a radiant panel), a pilot flame (e.g. match) or by a local heat source (e.g. short-circuit or fault in electrical wiring). When a flame has been formed, the exothermic combustion reactions in the gas phase will assist the external heat source in heating up the solid by conduction, convection and radiation from the flame. Most of this energy goes in the pyrolysis and the primary preheating zone. Only a minor part of the flame energy will go to secondary preheating zone, see Figure 2.2. The initial external heat source can still be present, though in most cases the flame is from now on the main source of the heat feedback to the solid. The flame will only spread when the burning (= pyrolysis) zone supplies enough energy to the unburnt zone (= primary and secondary preheating zone) ahead of the flame so that this zone starts pyrolyzing. A schematic representation of the heat feedback is given in Figure 2.3.

Flame spread can thus be seen as an advancing ignition front where the local flame acts both as a heat source to heat up the solid and as pilot in the gas phase. When the material in the primary preheating zone attains a certain critical temperature, this zone will start to pyrolyse as well. The pyrolysis gases from the primary preheating zone flow to the surface of the solid, mix with the oxidising ambient and create a flammable mixture ahead of the pyrolysis zone. This mixture will be ignited by the flame. To sustain these exothermic combustion reactions, there must be appropriate conditions in the gas phase such as sufficient fuel and air, small heat losses, sufficient high temperature, etc.

It is assumed that no oxygen can diffuse to the solid in the pyrolysis zone during burning. The pyrolysis zone in the solid is thus an anaerobic zone [70] where no further oxidation is possible. Only when the flame in the gas phase has ceased, the char layer can be further oxidized

Dependent on the solid and gas phase conditions, three important classi-

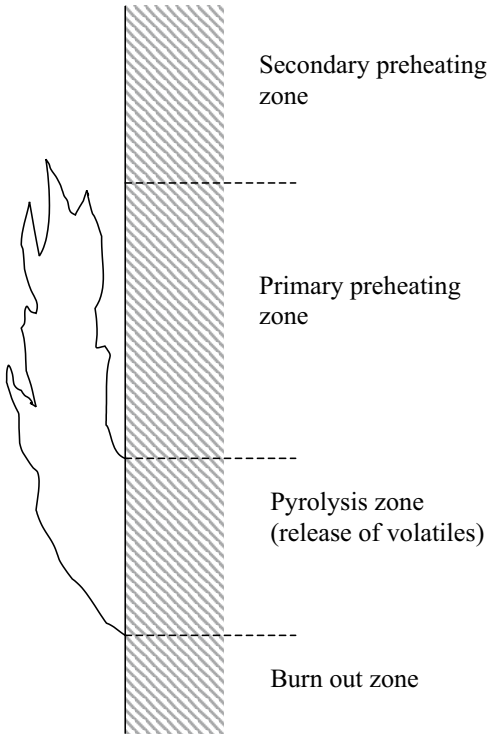

Figure 2.2: Zones in vertical flame spread [14]

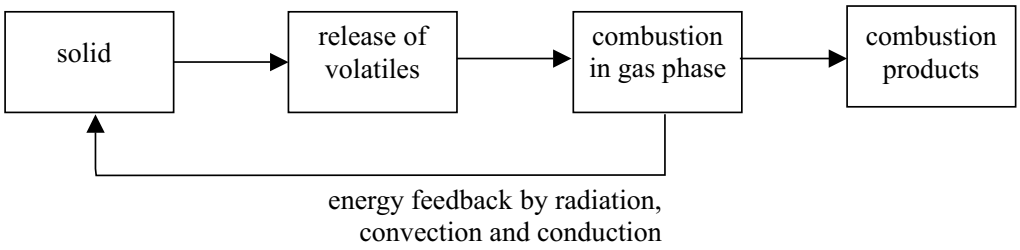

Figure 2.3: Schematic representation of solid combustion

fications of fire spread can be made:

- opposed and concurrent flame spread;
- flame spread over charring and non-charring materials;
- flame spread over thermal thick and thin materials.

The main mechanisms described in this section are present in all these cases, but some mechanisms will be more important while others can be neglected. From the viewpoint of model development this is important.

2.2.1 Opposed and concurrent flame spread

The flames can spread in the same direction as the airflow above the surface (concurrent) or in the opposite direction (opposed). The direction of spread is dependent on the orientation of the surface and on the flow characteristics [89].

In opposed flame spread the gas flow, either naturally induced or forced, opposes the direction of the flame spread, i.e. case (a) in Figure 2.4. In this configuration the gas flow pushes the flame over the already burning solid, downstream of the pyrolysis front. The heat is transferred to the virgin layer by conduction through the solid (slow) and by some radiation and conduction through the gas phase. Subsequent flame spread is low.

In natural convection flows, opposed flame spread occurs as downward, lateral or horizontal flame spread. Seldom this is the dominant way of fire growth.

In concurrent or wind-aided flame spread the flame is pushed forward by the gas or airflow. The flame is well ahead of the pyrolysis front and is laying directly over the virgin solid. The heat transfer to the solid is easy and makes the propagation fast. For laminar flames convection is the dominant way of heat transfer, while for larger, turbulent flames the heat transfer is mainly by radiation [28]. In natural convection flows, concurrent flame spread occurs as upward flame spread.

2.2.2 Flame spread of charring and non-charring materials

The flame spread or pyrolysis behaviour can also be divided into charring and non-charring.

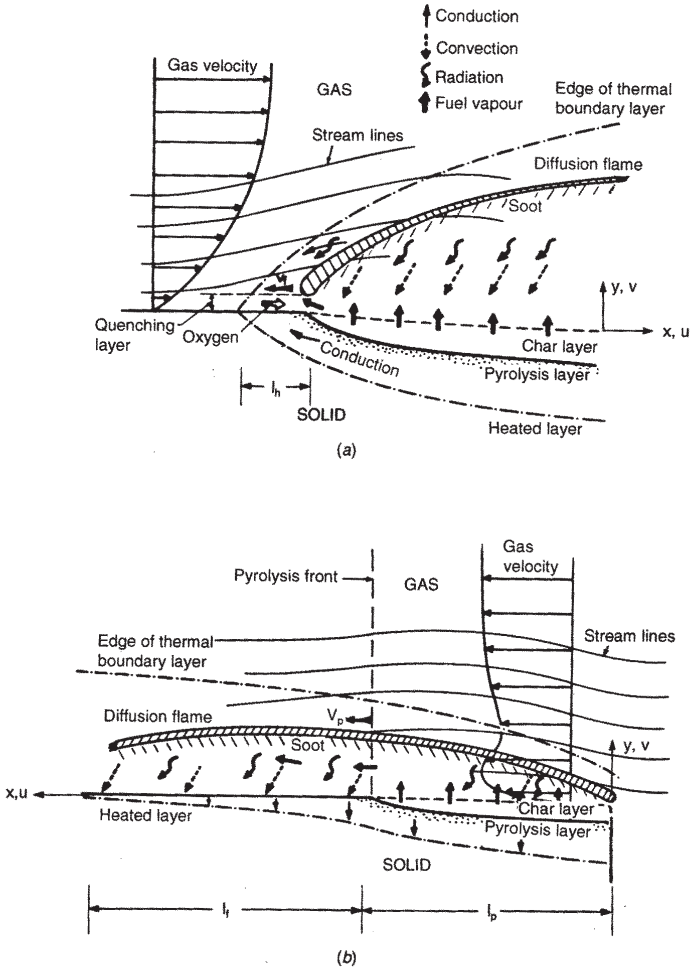

Figure 7 Schematic diagram of the spread of a flame over the surface of a solid combustible: (*a*) opposed flow; (*b*) concurrent flow.

Figure 2.4: Schematic diagram of the spread of a flame over the surface of a solid combustible: (a) opposed flow; (b) concurrent flow [14]

Non-charring materials burn away completely, leaving no residue or char layer. The solid surface is regressing inwards, see Figure 2.5. When the solid is sufficiently thick an almost steady state will be reached [109]. The melting behaviour of these types of materials can complicate the flame spread calculation.

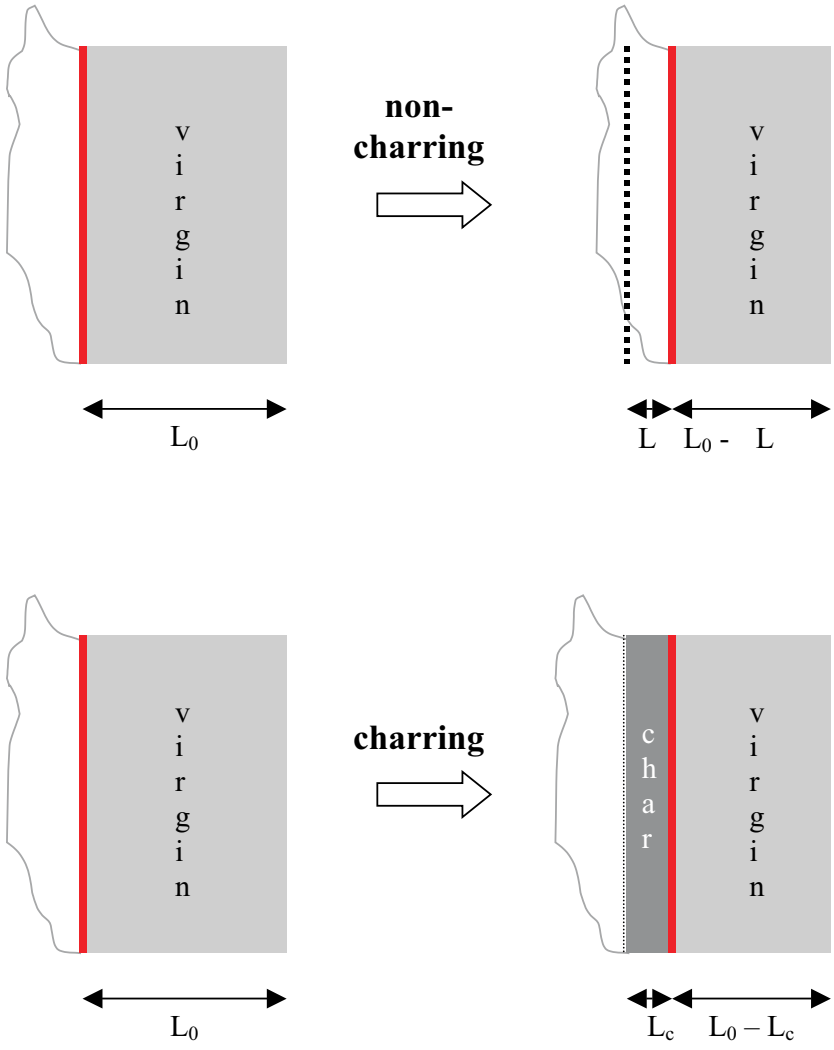

Figure 2.5: Combustion of non-charring and charring materials

On the other hand charring materials leave a considerable amount of residue (char) when they burn. This char layer gradually builds up as the

pyrolysis front is moving inwards the solid, see Figure 2.5. The layer forms an increasing thermal resistance between the exposed solid surface and the pyrolysis front and hence less heat will flow to the front. Still in some experiments [41] it was found that for certain materials with sufficient thickness, a more or less steady state can be obtained.

When all the volatiles have been exhausted, the flames extinguish and a solid char residue remains. The char continues to burn in a smouldering mode. Prior to this phase the char oxidation is usually minimal since the flame prevents diffusion of O_2 to the surface. Therefore, the heat release rate during the flaming phase is predominantly determined by the combustion of the released volatiles [108].

For certain materials, like for example wood, the char layer can shrink and small cracks appear on the surface due to pressure gradients in the material. The presence of these cracks allow volatiles to escape more easily. The cracks gradually widen as the char layer depends, leading to the characteristic "alligatoring" pattern.

2.2.3 Flame spread of thermally thick and thin materials

Yet another classification of fire spread can be done by the thickness of the solid: thermally thick and thin materials.

For thermally thin solids the heat transfer to the solid is small. The solid material is consumed very fast and a burn out front has to be considered. When the solid is thermally thin, it can be shown that the fire spread rate is inversely proportional with the thickness. There is less material to be brought at pyrolysis temperature and the solid can be treated with the lumped thermal capacity model. The flame spread rate is given by:

$$V_f \propto (\rho c L)^{-1} \tag{2.1}$$

On the other hand, for the thermally thick solids the heat transferred to the solid is important. The material will remain to burn and will contribute to the fire for long times. The spreading rate becomes independent of the thickness. The material acts as a semi infinite solid and the flame spread rate is inversely proportional with the thermal inertia:

$$V_f \propto (\rho c \lambda)^{-1} \tag{2.2}$$

The influence of the thermal inertia or thickness on the flame spread rate can be explained by the ignition theory. Many common materials thicker

than 1 mm may be assumed thermally thick for the length of time typically associated with upward flame spread [9].

In a general flame spread model it should be possible to simulate all the types of flame spread, i.e. concurrent/opposed, charring/non-charring, thick/thin. The model should be universal and should predict itself the type of flame spread that will occur. Therefore, the three types of heat transfer: radiation, convection and conduction, must be incorporated in the fire or flame spread model. Concurrent flame spread on charring, thick materials is the primary goal of this thesis.

2.3 Factors affecting the rate of flame spread

Beneath some factors are given that affect the rate of flame spread [26]. Some of them have already been discussed in the previous sections.

Chemical material properties:

- composition of solid;
- presence of fire retardants.

Physical material properties:

- initial temperature;
- direction of propagation;
- thickness;
- thermal properties;
- geometry.

Environmental factors:

- composition of atmosphere (inert, percentage O_2);
- pressure and temperature;
- external heat flux;
- air velocity;
- turbulence;
- gravity.

2.3.1 Direction of propagation

The flame spread rate is most often fastest for vertical upward spread. This can be explained by the heat feedback of the flame, which covers the heated material and enhances the heat transfer, see Section 2.2. The flame will tend to stick to the surface because of the entrainment of air at the non solid side of the flame. While for upward propagation this is very important, for the downward spread this phenomenon has little or no importance. Downward flame spread is much slower, see Table 1.1.

Notice that dependent on the ventilation, horizontal flame spread can also be fast. In concurrent horizontal flame spread (flame propagation in direction of gas flow), the gas flow pushes the flame over the solid material and the heat feedback is intense, as in vertical spread.

2.3.2 Geometry

The width of the solid has little or no influence on downward flame spread. For upward flame spread the rate will increase with width. This is due to the larger burning surface which will give larger flames. The heat transfer by radiation will enhance the spread rate. For example for a cotton fabric [26]:

$$V_f \propto (\text{width})^{0.5} \tag{2.3}$$

Flames propagate also faster over edges. An edge will act as a thermally thin material which has a low thermal capacity and will heat up very fast.

Also in corner configuration the flame spread is faster than on a flat surface. This is to be explained by the cross-radiation from each flame to the other surface.

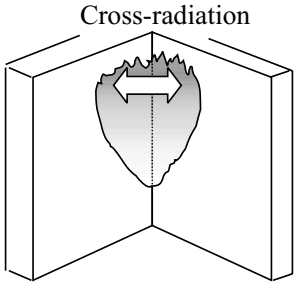

Figure 2.6: Corner configuration

2.3.3 Ambient factors

The *composition of the atmosphere* is important for the combustion in the gas phase. When insufficient oxidiser is present, due to consumption by the fire, the combustion reactions in the gas phase can cease and the flame spread will stop. Or, when the combustion reactions in the gas phase can still continue but less oxidiser is present, the flame temperature will be lower, heat feedback will be lower and subsequent the flame spread rate will be lower.

External radiation affects upward flame spread in two ways [9]. In the first way, the radiant heat flux adds to the heat feedback from the flame and causes the yet-unburned surface of the sample to heat up to the pyrolysis temperature more quickly. In the second way, the external radiation increases the pyrolysis reactions in the burning zone which in turn gives higher flames. Both effects of the external radiation accelerate the upward flame spread.

In general when the velocity of the *air flow* is increased, the flame spread will be enhanced due to better mixing of fuel and air in the gas phase. Above a critical velocity the flame spread will decrease due to cooling or flame blow off.

The *turbulence* in the gas phase can increase or decrease the heating (before pyrolysis), dependent on the way of heating (radiative or convective). In the gas phase a high turbulence will increase the mixing of fuel and oxidizer but on the other hand, it will cool down the mixture. The result is case dependent.

Chapter 3

Classification of models for flame spread

In this chapter an attempt is made to classify the present flame spread models. The main submodels of the flame spread models are identified. A few examples, each representing a class of flame spread models, will illustrate the different models.

The classification is done on the presence of submodels and flame spread mechanisms. The appearance of the flame spread like opposed versus concurrent, horizontal versus vertical, thermally thick versus thermally thin solid is not present in the classification.

3.1 Classification

There exist a lot of flame spread models. Classification is difficult because the distinction between the different models can be done for several aspects:

- Is the model analytical, algebraic or numerical?
- Is the thermal degradation of the solid incorporated via experiments or simulation?
- How are the combustion reactions or flames in the gas phase modelled?
- How is the heat feedback modelled?
- Is the model developed for charring or non-charring materials?
- Does the model need experimental results?
- ...

As the models vary from very simple to really complex, not all of the above questions are relevant for each model.

The classification given here, is based on the two important physical processes that occur during flame spread: the reaction of the solid phase, i.e. the solid combustion, and the heat feedback to the solid material. Therefore a classification is made according to:

1. the presence of an independent solid reaction model and
2. according to the calculation of the heat feedback.

These two criteria are independent of each other and can also be seen as a classification by the treatment of the solid and gas phase.

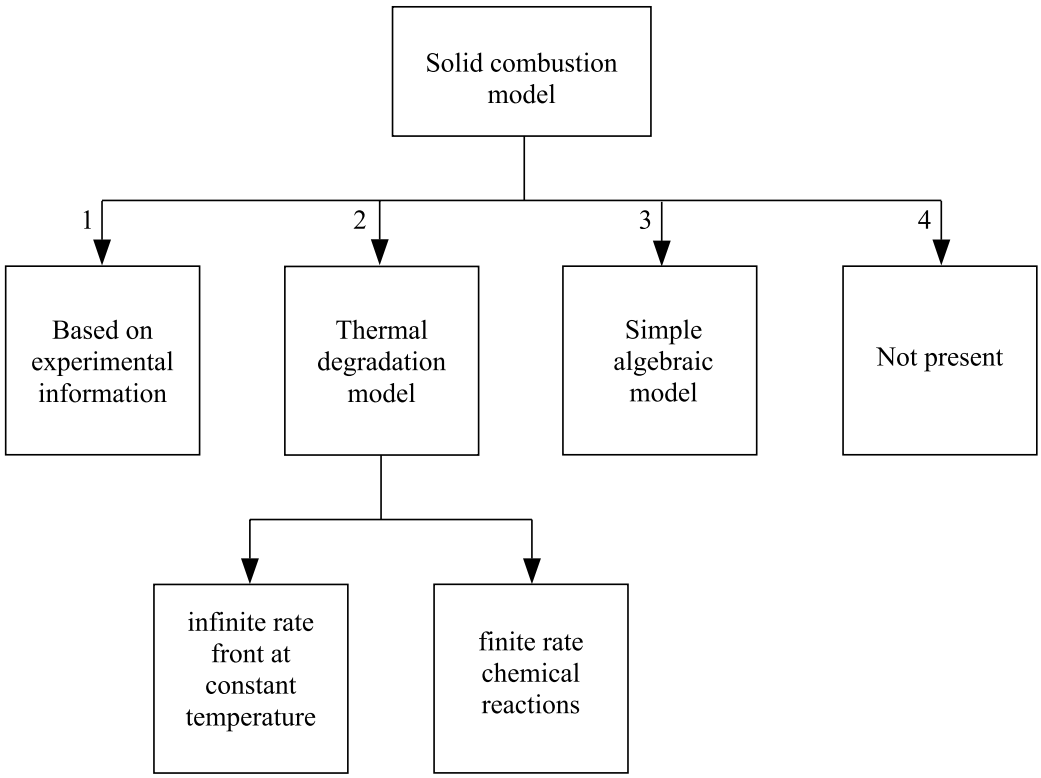

Figure 3.1: Classification of fire spread models by the solid reaction model

The first classification given in Figure 3.1 is done by the solid reaction model. The solid reaction model will describe the release of pyrolysis gases or energy by the solid and thus will generally give the mass loss rate of the solid. The

solid reaction model should be able to run as a stand-alone model, if of course suitable boundary conditions are provided. Such fundamental solid reaction model is independent of the flame spread configuration and the gas phase model. Different gas phase models can then be coupled to the solid reaction model to create a new model or a new combination of models.

In the first class of flame spread models (1 in Figure 3.1), the release of pyrolysis gases or energy is based on experimental results, e.g. Cone Calorimeter[1]. For certain test conditions, incident heat flux, orientation, etc. the mass loss of a sample is measured in time [117, 74].

In the second class of flame spread models (2 in Figure 3.1), a thermal degradation model is used. With the net heat flux on the solid, the models calculate the mass release and the solid temperature. The thermal degradation models can be divided further into finite rate and infinite rate. For the infinite rate models the thermal degradation front will be on a constant, known temperature [108, 77, 19]. Below that temperature no degradation reactions take place, while above that temperature the degradation reactions are already completely finished. The reaction rate at the pyrolysis temperature is thus assumed infinite. In the finite rate model the reaction rate of the thermal degradation reactions are always finite [24, 125]. The pyrolysis reactions proceed at different temperatures and are often modelled with a first order Arrhenius reaction.

In the third class of flame spread models (3 in Figure 3.1), the release of pyrolysis gases or heat output is predicted by simple algebraic equations or is even assumed constant [82, 56]. In general, the only purpose of these kinds of models is to predict the flame spread velocity. Sometimes the amount of volatiles released, does not intervene directly in the calculation, and the flame spread velocity is calculated by the general formula [90, 26, 89]:

$$\text{flame spread velocity} = \frac{\text{heated distance}}{\text{ignition time}} \tag{3.1}$$

This equation assumes that the not burning solid is heated by the flame only over a certain "heated distance", e.g. the primary heating zone in Figure 2.2. It will take the "ignition time" until this primary heated zone will ignite and burn. The flame front has then advanced the "heated distance" in a time given by the "ignition time". The subsequent flame velocity is this given by Equation 3.1. For the heated distance correlations are used, while the ignition time in Equation 3.1 is deduced from experiments, from an analytical expression, or from a numerical model.

In the fourth class (4 in Figure 3.1), no real solid combustion models is present in the sense that it predicts the release of pyrolysis gases or heat.

[1]More information on the Cone Calorimeter in Appendix A

For example the surface temperature is calculated until it reaches the ignition temperature. Afterwards, that part of the solid is no longer used in the calculation.

The flame spread models can also be classified by the modelling of the gas phase, see Figure 3.2. When the gas phase is fully modelled, the combustion reactions in the gas phase are present and the heat feedback is calculated from the soot concentration, temperature, etc. in the gas phase. The most obvious model is a computational fluid dynamics code where all modes of heat transfer, conduction, convection and radiation, are incorporated. Other models, though exist [97].

When the gas phase is not fully modelled, the gas phase is reduced to a flame representation. The heat feedback to the solid material can be taken from experiments [8, 60] or can be derived from a flame model. For the latter, the radiation and convective heat transfer are calculated from the flame geometry, length, temperature, ...

In literature a group of flame spread models is often identified as *thermal models*. In these models the ignition time of the solid is calculated with a pure thermal model, i.e. based on the conductive heat equation in the solid. The thermal degradation of the solid is not modelled and most often neither are the combustion reactions in the gas phase. The thermal models for surface fire spread are in general based on an ignition model.

3.2 Submodels for solid combustion

In this section some submodels are given that regularly appear in solid combustion models and hence in flame spread models.

3.2.1 Ignition time

Many flame spread models use the ignition time of the solid. This parameter is not a fundamental property of the material though, but depends on the way of heating, testing, apparatus, ...

Criteria for ignition
In experiments the first occurrence of (visible) flames is often taken as ignition criterion. For use in mathematical models several conditions for ignition can be used:

- a critical surface temperature;

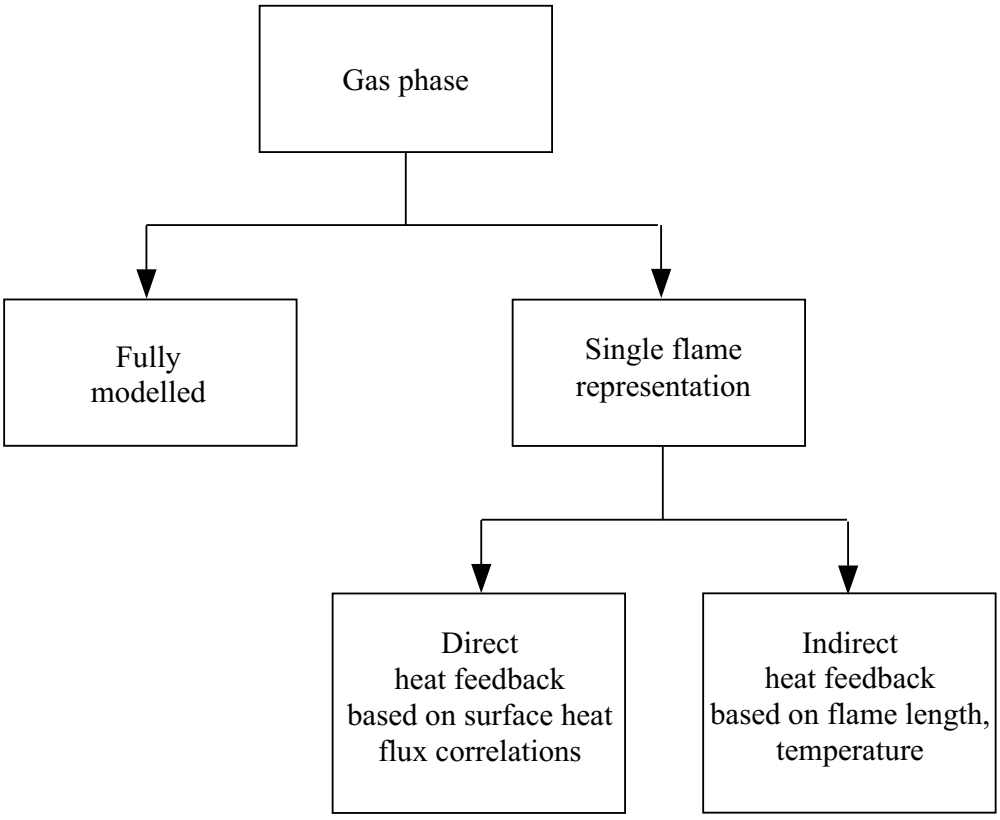

Figure 3.2: Classification of fire spread models by the solution of the gas phase

- a critical mean temperature of the solid;
- a critical pyrolysis rate;
- a critical rise in surface temperature;
- a critical rise in gas temperature;
- a change in temperature gradient at gas-solid interface.

For models of flame spread the surface temperature criterion is most used. It must be kept in mind that in reality a solid will start to decompose and release pyrolysis gases before the critical "ignition temperature" is reached [24].

Determination of the ignition time

As example, three simple models are given that predict the ignition time: the thermal ignition model for thermally thin and thick solids, and a general model. For all the models it is assumed that the net incident heat flux is known and constant.

For the thermally thin materials, the solid is assumed to have a uniform temperature throughout the heating process. The ignition time is determined as the time were the solid reaches the ignition temperature. This follows from conservation of energy and is given by [28]:

$$t_{ig} = \rho c L \frac{T_{ig} - T_0}{\dot{q}''_{net}} \tag{3.2}$$

For the thermally thick material, the surface temperature can be derived from the thermal theory for a semi infinite solid heated by a constant heat flux. The ignition time is given by the time for the surface to reach the ignition temperature [28]:

$$t_{ig} = \frac{\pi}{4} \lambda \rho c \frac{(T_{ig} - T_0)^2}{\dot{q}''^2_{net}} \tag{3.3}$$

In the third model the ignition time for a material is calculated with the conduction heat equation. For a simple one-dimensional model the heat equation is given by [26]:

$$\frac{\partial T}{\partial t} = \frac{\lambda}{\rho c} \frac{\partial^2 T}{\partial x^2} \tag{3.4}$$

with initial and boundary conditions:

$$\text{at t} = 0 \quad T = T_\infty \tag{3.5}$$

$$\text{for } x = 0 \quad \dot{q}''_{net} = -\lambda \frac{\partial T}{\partial x} \tag{3.6}$$

where $\dot{q}''_{net}$ is the total net incident heat flux at the surface. Once the surface temperature reaches the ignition temperature, ignition is started. The ignition temperature is again not a fundamental property of the material, and is determined experimentally.

The ignition time can also be determined by experiments. Care should be taken when using experimental ignition times in models as the variation of the heating of the solid is not included. Only when the incident heat flux during flame spread is the same as in the experiment, the ignition time will be valid.

3.2.2 Solid reaction: "heat of gasification"

This submodel of some flame spread models predicts the mass release of the solid from only the net incident heat flux. The heat feedback is derived with a gas phase model, for example with CFD [29]. The mass loss rate is in fact based on liquid burning, and is given by:

$$\dot{m}'' = \frac{\dot{q}''_{net}}{L_v} \tag{3.7}$$

Herein is L_v the heat of gasification as should not be confused with the pyrolysis heat. The heat of gasification is not a fundamental material property, but actually changes during heating. When the heat of gasification is used as solid combustion model, it is assumed to be constant. This simple solid combustion model is an example of the third class in Figure 3.1. For a steady state, the relation between the heat of gasification and the pyrolysis heat at steady state is given by [125]:

$$L_v = Q_{pyr} + \int_{T_0}^{T_{pyr}} c_v \mathrm{d}T \tag{3.8}$$

For non charring solids the heat of gasification is almost constant, while for charring materials the heat of gasification is a local and transient value and changes considerably during the pyrolysis process [125].

3.2.3 Solid reaction: based on experiments

3.2.3.1 Direct results

The mass loss rate or the release of pyrolysis gases can be derived from experiments. This represents the first category in Figure 3.1. For fire applications, the mass loss rate or heat release rate is often determined in the Cone Calorimeter. In this apparatus a sample is exposed to a constant external heat flux

from a radiating cone. During the test the mass loss is measured and the combustion gases are analysed. Typical Cone Calorimeter results are given in Figure 3.3.

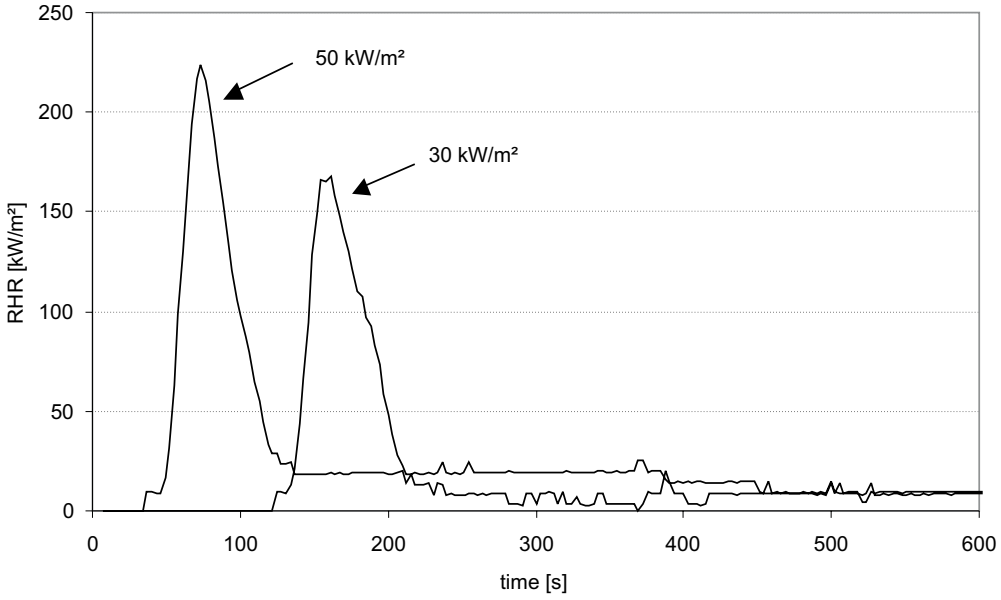

Figure 3.3: Rate of heat release rate from Cone Calorimeter experiments (for external heat flux of 30 and 50 kW/m^2)

A drawback of using experimental results is that the applicability is limited to the same or at least similar conditions (thickness, incident heat flux, ambient conditions, gas velocity, orientation, etc.) as in the experiment. In the Cone Calorimeter the external radiant heat flux is constant, while in a real fire the incident heat flux will vary in time, dependent on the growth of the fire, configuration, etc. The influence of a variable radiative heat flux in the Cone Calorimeter test, has not yet been fully examined, but even from tests with constant radiant heat flux it is clear that significant differences can occur. Figure 3.3 gives the results of a wall lining, being tested for a radiant heat flux of 30 and 50 kW/m^2. The heat release for the 30 kW/m^2 test, starts only when the heat release peak of the 50 kW/m^2 test is already finished. There is a time difference of about 90 s in the occurrence of the peak of heat release rate (HRR). The peak in the heat release rate is for the higher radiant heat flux also higher. Similar conclusions can be drawn from the mass loss rate.

Care should be taken when choosing a heat release or mass loss curve for the flame spread model. Van Hees [117] works with heat release rate curves that are taken at different radiant heat flux levels. During the simulation of the flame spread, the heat release of the solid will be taken from the heat release rate curve which was measured at the external heat flux closest to the present incident heat flux.

The Cone Calorimeter gives besides the heat release rate also the mass loss rate. From experiments it is known that the pyrolysis gases from common building materials do not have a constant heat of combustion. For the gas phase models the use of the measured heat release rate will be more appropriate than the heat release rate calculated from the mass loss rate and a constant assumed heat of combustion. Often the heat release rate is more practical because for example flame length correlations use the heat release rate of the fire and not the mass loss rate of the solid. Therefore in flame spread models based on experimental data, the HRR is used instead of the mass loss rate.

3.2.3.2 Scaled results

In a Cone Calorimeter a material is tested at a constant external heat flux. This heat flux is applied by radiation of the cone above the specimen. The heat flux can be adjusted at any level between 0 and 100 $\mathrm{kW/m^2}$ but during the experiment it is kept constant. The net incident heat flux at the solid will also include flame heat feedback, which is unknown.

In the method of Mitler [74] the mass loss rate of a material, exposed to a time dependent external heat flux, will be determined from several Cone Calorimeter tests done with constant external heat flux. The mass loss in case of the variable external heat flux is given by:

$$\dot{m}''_{pyr}(t) \;=\; \xi(t) \cdot \dot{m}''_{cone}(\tau) \tag{3.9}$$

Herein is $\dot{m}''_{cone}$ the mass loss rate measured in the Cone Calorimeter at the scaled time t. The scaled time τ is determined by:

$$\tau = \int_0^t \xi(t')\,\mathrm{d}t' \tag{3.10}$$

And $\xi(t)$ is the change of the pyrolysis rate due to the net heat flux incident on the material being greater or smaller than the one during the Cone Calorimeter test:

$$\xi(t,\tau) = \frac{\dot{q}''_{net}(t)}{\dot{q}''_{net,cone}(\tau)} \tag{3.11}$$

From experiments it is known that the cone heat flux is nearly constant so that the ξ is only dependent on t and not, or weakly, on τ. The net heat flux in the Cone Calorimeter exists of the external heat flux, the flame heat flux and the reradiation:

$$\dot{q}''_{net,cone} = \epsilon \cdot \dot{q}''_{ext} + \dot{q}''_{flame} - \dot{q}''_{rerad} \tag{3.12}$$

The scaling technique was originally developed for the heat release rate by Smith [105].

3.2.4 Solid reaction: thermal degradation with infinite rate

This type of solid combustion models will predict the time-dependent mass loss rate of the solid. The chemical energy that is incorporated in these gases is calculated with a constant heat of combustion of the pyrolysis gases.

The models calculate the temperature in the solid. When the solid reaches a critical temperature, the "ignition temperature" of Section 3.2.1, a pyrolysis front will be created. This front advances into the solid and keeps a constant temperature. The front temperature is the pyrolysis temperature and equals the "ignition temperature". The rate of the transformation reaction of virgin material into char is assumed to be infinite. So all the net heat that is provided to the pyrolysis front will be used for the endothermic reactions, and thus the heat provided determines the mass loss rate. Virgin material is immediately transformed into char, there are no intermediate products.

Integral models

A beautiful solid combustion model which calculates the thermal degradation at infinite rate, are the "Integral model"[2] of Moghtaderi [77] and of Spearpoint & Quintiere [109]. "Integral models" can be used for non-charring materials [20, 96] as well as for charring materials [109].

"Integral models" assume that the temperature distribution depends on the space variable x in some particular fashion (linear, quadratic or exponential). The temperature profile is combined with the boundary conditions and the conservation of mass and energy to obtain a set of three coupled differential equations. The solution of the differential equations gives the temperature in the solid and the mass loss rate in function of time. Further information on "Integral models" is given Chapter 5.

[2]Quotes are used for the whole solid combustion model with infinite thermal degradation rate, when no quotes are used the numerical technique is intended.

3.2.5 Solid reaction: thermal degradation with finite rate

The models where the thermal degradation is described with a finite rate, are often called fundamental models. They make less simplifications and try to reproduce reality more closely.

The rate of thermal degradation is calculated with an Arrhenius equation [63]:

$$k = A \cdot \exp\left(-\frac{E_a}{R_u T}\right) \tag{3.13}$$

where k is the specific reaction-rate, A the Arrhenius factor, R_u universal gas constant, E_a the activation energy, and T the temperature.

The thermal degradation schemes are almost always one-step models and either include a one single reaction [125, 19, 129, 86]:

$$\text{solid} \xrightarrow{\text{k}} \text{volatiles} + \text{char} \tag{3.14}$$

or two different reactions as in [24]:

$$\begin{cases} \text{solid} \xrightarrow{k_1} \text{volatiles} \\ \text{solid} \xrightarrow{k_2} \text{char} \end{cases} \tag{3.15}$$

There are also two-step models with the active solid as intermediate state, and two reactions as in [19]:

$$\text{solid} \xrightarrow{k_1} \text{active solid} \begin{cases} \xrightarrow{k_2} \text{tar} \\ \xrightarrow{k_3} \text{gas} + \text{char} \end{cases} \tag{3.16}$$

Of course more complicated schemes are possible, but so far they bring little improvement.

In most models it is assumed that the pyrolysis gases that are produced in the solid, flow immediately out of the solid, without any resistance. In the work of Di Blasi [23] the flow of the pyrolysis gases in the solid is described by the pressure gradients and gravity forces. Volatiles can thus accumulate in the solid. The simulations were done for a square shaped section of the solid. The flow of the pyrolysis gases was predominantly corresponding to the temperature gradients in the solid. In most practical cases though, the thickness of the solid is small with regard to the length and width. Subsequent the resistance to the flow in the lateral direction will be much higher

than in the direction of the depth. For practical cases, the assumption of unimpeded flow is accepted [125].

When the chemical degradation reactions are modelled, no ignition temperature is needed. In fact the ignition temperature can be derived from the simulation, dependent on the criterion assumed (see Section 3.2.1). At first sight one needs one input parameter less, the ignition temperature, but by modelling the thermal degradation reactions at least two extra parameters are introduced: the activation energy E_a and the Arrhenius factor A. The pyrolysis reactions now proceed at any temperature. At low temperatures the reaction rate will be very low and the reaction is insignificant. On the other hand, at very high temperature the reaction rate will be very high and an infinite rate can be accepted. In between there is a temperature interval were degradation reactions will occur at temperature dependent rates. The pyrolysis front will not be infinitely thin as in the infinite rate model, but will have a finite thickness. The transition from virgin material to char is not abrupt but happens in a continuous way.

The equations for the solid phase by Di Blasi [24] are given as an example: The thermal degradation scheme is as follows:

$$\begin{cases} solid \xrightarrow{k_1} \text{volatiles} \\ solid \xrightarrow{k_2} \text{char} \end{cases} \tag{3.17}$$

The assumptions made are:

- no swelling or surface regression;
- local thermal equilibrium between the solid and the volatiles;
- negligible accumulation of volatiles in the solid;
- volatiles flow without any resistance to solid surface.

Conservation of virgin material:

$$\frac{\partial \rho_s}{\partial t} = -(k_1 + k_2)\rho_s \tag{3.18}$$

Conservation of char:

$$\frac{\partial \rho_c}{\partial t} = k_2 \rho_s \tag{3.19}$$

Conservation of volatiles:

$$\frac{\partial m}{\partial y} = k_1 \rho_s \tag{3.20}$$

Conservation of energy:

$$c_s \frac{\partial \rho_s (T_s - T_0)}{\partial t} + c_c \frac{\partial \rho_c (T_s - T_0)}{\partial t} + c_p \frac{\partial m (T_s - T_0)}{\partial t} = \frac{\partial}{\partial x}(\lambda_s \frac{\partial T_s}{\partial x}) + \frac{\partial}{\partial y}(\lambda_s \frac{\partial T_s}{\partial y}) + k_1 \rho_s \Delta h_{s1} + k_2 \rho_s \Delta h_{s2} \tag{3.21}$$

with:

$$k_k = A_k \exp(-\frac{E_k}{R T_s}) \qquad \text{with} \quad k = 1, 2$$

$$m = \int_0^y k_1 \rho_s \mathrm{d}y$$

the thermal conduction coefficient

$$\lambda_s = \eta \lambda_v + (1 - \eta) \lambda_c$$

$$\eta = \rho_s / \rho_{s0}$$

3.3 Submodels for the gas phase

3.3.1 Gas phase: direct heat feedback

The flame and the gas phase are not really required here. Only the heat feedback to the solid is determined.

Delichatsios [20] uses a constant heat flux of $30\,\mathrm{kW/m^2}$ for the zone covered by the flame. Outside the flaming zone the heat flux is assumed zero. When implemented into a flame spread model, a stepwise flame propagation will be the result.

Brehob [8] uses a variable forward heat flux. The net incident heat flux for vertical wall flames is based on measured data. The correlation is given by:

$$\dot{q}''_w(x,t) = \dot{q}''_{wo} \exp\left(C_0 \frac{x - x_p}{x_f - x_p}\right) + \dot{q}''_{ext} - \dot{q}''_{rerad} \tag{3.22}$$

where $\dot{q}''_{wo}$ is material dependent. This expression is used for the forward heat flux in the heating zones. For the pyrolyzing zone, no heat flux is given.

The application of the heat flux correlations is limited to the same flame spread configuration as in the experiments.

3.3.2 Gas phase: indirect heat feedback

These type of gas phase models calculate the heat feedback with a simplified flame representation. The feedback is strongly dependent on the type of flame spread and therefore different equations and formulas are needed when predicting opposed, concurrent or horizontal, vertical flame spread.

As an example the gas phase model by Van Hees [117] will be given. The flame is represented by a surface with uniform temperature, see Figure 3.4. The chemical reactions in the gas phase are not taken into account. The net incident heat flux on the surface of a solid volume i is given by the sum of several heat fluxes:

$$\dot{q}''_{net} = \dot{q}''_{f,i} + \dot{q}''_{ext,i} + \dot{q}''_{conv,i} + \dot{q}''_{cond,i} - \dot{q}''_{r,i} \tag{3.23}$$

where:

- $\dot{q}''_{net}$ the total net incident heat flux at the surface of volume i (W/m^2);
- $\dot{q}''_{f,i}$ the radiation heat flux of the flame (W/m^2);
- $\dot{q}''_{ext,i}$ the external radiation, for example from a hot gas layer (W/m^2);
- $\dot{q}''_{conv,i}$ the convective heat flux at the surface of volume i (W/m^2);
- $\dot{q}''_{cond,i}$ the conductive heat transmitted from the flame to the solid i (W/m^2);
- $\dot{q}''_{r,i}$ the radiation heat losses at the surface of volume i (W/m^2).

To determine each term in the equation of the total net incident heat flux the following elements have to be modelled.

- the geometry of the flame (length, shape, ...);
- the emissivity of the flame;
- the temperature of the flame;
- the external heat flux;
- the convection coefficient or the convective heat loss or gain;
- the conduction in the gas phase (dependent on flame configuration whether negligible or not);

- the radiation loss to the environment.

For each element several formulas are available. Here only some options for the flame length calculation will be given.

The flame length is always correlated with the released heat output. A well-known correlation for wall-flame height is the one of Hasemi [91]

$$x_f = \beta_1 (\dot{Q}')^{2/3} \tag{3.24}$$

Markstein [72] gave a slight different equation:

$$x_f = \beta_2 (\dot{Q}')^{1/3} \tag{3.25}$$

Van Hees [117] used yet an other empirical formula that is more general applicable:

$$\frac{x_f}{D} = 3.7 \left(\frac{\dot{Q}}{\rho c_p T_\infty \sqrt{gD} D^2} \right)^{2/5} - 1.02 \tag{3.26}$$

where x_f the flame length, and D the equivalent diameter of the flame determined by the surface area:

$$(x_p - x_b) \cdot B \tag{3.27}$$

with x_p the pyrolysis height, x_b the burnout height, and B the width of the plume.

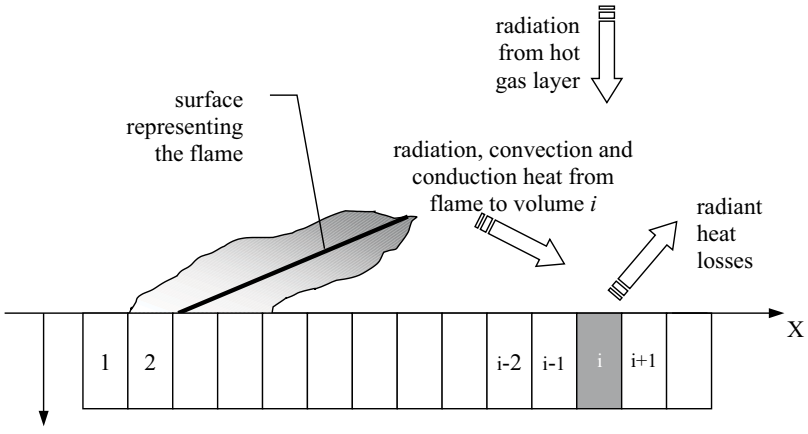

Figure 3.4: Heat fluxes for thermal model

In experiments often a burner is used to onset the flame spread. Once the solid is ignited the flames of the burner and the flames of the burning solid will merge. It is impossible to make a distinction between the flames originating from the burner and those from the burning solid, they will act as one flame. Little guide exists, how this flame can be modelled. Mitler [73] suggests:

$$x_f = 0.14\sqrt{\dot{Q}'_{burner} + \dot{Q}'_{wall}} \tag{3.28}$$

While Brehob and Kulkarni [8] propose:

$$x_f - x_b = K\left[\dot{Q}'_{burner} + H_c \int_{x_p}^{x_b} \dot{m}'' \mathrm{d}x\right]^n \tag{3.29}$$

3.3.3 Gas phase: fully modelled

A more detailed representation of the gas phase can be given by computational fluid dynamics programs. The flame will now be fully calculated dependent on the conditions in the gas phase (velocities, temperature, oxygen concentration, ...). The basis of a CFD code are the conservation of mass, momentum and energy. These coupled partial differential equations are most often solved with a finite volume technique. For turbulent combustion, submodels are required that deal with turbulence, combustion, soot, radiation, ... More information is given in Chapter 11.

As example the model of Di Blasi [24] developed for laminar gas flow is given. It is only valid for small scale flame spread. The gas phase equations exists of conservation equations for mass, momentum, species and energy. The formulation is quasi-steady so the processes in the gas phase are described by a series of successive steady states. Indeed the boundary conditions for the gas phase change slowly, and the characteristic time in the gas phase is much lower than for the solid. Therefore the equations can be written in steady form and no transient terms are present.

Conservation of mass:

$$\frac{\partial(\rho u)}{\partial x} + \frac{\partial(\rho v)}{\partial y} = 0 \tag{3.30}$$

Conservation of momentum in the vertical direction:

$$\frac{\partial(\rho u u)}{\partial x} + \frac{\partial(\rho u v)}{\partial y} = -\frac{\partial p}{\partial x} + \mu\left(\frac{\partial^2 u}{\partial x^2} + \frac{\partial^2 u}{\partial y^2}\right) + \frac{\mu}{3}\frac{\partial}{\partial x}\left(\frac{\partial u}{\partial x} + \frac{\partial v}{\partial y}\right) - g(\rho_0 - \rho)$$

(3.31)

Conservation of momentum in the horizontal direction:

$$\frac{\partial(\rho uv)}{\partial x}+\frac{\partial(\rho vv)}{\partial y}=-\frac{\partial p}{\partial y}+\mu\left(\frac{\partial^2 v}{\partial x^2}+\frac{\partial^2 v}{\partial y^2}\right)+\frac{\mu}{3}\frac{\partial}{\partial y}\left(\frac{\partial u}{\partial x}+\frac{\partial v}{\partial y}\right) \quad (3.32)$$

Conservation of species:

$$\frac{\partial(\rho uY_i)}{\partial x}+\frac{\partial(\rho vY_i)}{\partial y}=w_i+\frac{\partial}{\partial x}\left(\rho D\frac{\partial Y_i}{\partial x}\right)+\frac{\partial}{\partial y}\left(\rho D\frac{\partial Y_i}{\partial y}\right) \qquad i=F,O \quad (3.33)$$

where the source or sink terms in the species equations due to chemical reaction, are given by:

$$w_i=-A\exp\left(-\frac{E}{RT}\right)Y_O Y_F \rho^2 \frac{\nu_i M_i}{M_f} \qquad i=F,O \quad (3.34)$$

with Y_i the mass fraction for fuel (F) or oxygen (O).

Conservation of energy:

$$\frac{\partial(\rho uT)}{\partial x}+\frac{\partial(\rho vT)}{\partial y}=\dot{q}''_{combustion}+\dot{q}''_{rad}+\lambda\left(\frac{\partial^2 T}{\partial x^2}+\frac{\partial^2 T}{\partial y^2}\right) \quad (3.35)$$

where the source term in the energy equation are given by:

$$\dot{q}''_{combustion}=-w_F\Delta H_c \quad (3.36)$$

$$\dot{q}''_{rad}=-4K_p\sigma T^4 \quad (3.37)$$

with K_p the Planck absorption coefficient. The equations form a set of coupled non-linear differential equations and must be solved with numerical methods.

State equation

$$\rho T=\text{constant} \quad (3.38)$$

3.4 Examples of flame spread models

Some examples of flame spread models are given to illustrate some extra mechanisms and techniques which are not presented in the models for solid combustion and the gas phase of Section 3.2 and 3.3. The examples give a survey of the different levels of complexity in fire spread models and should allow the reader to place this work in the fire research domain. It is clear that beside the methodology that will be followed in this work (predicting the reaction of the solid material with a pyrolysis model), other possibilities exist.

3.4.1 Example: de Ris

In this example an algebraic flame spread model is described which does not have a solid combustion model and which uses direct heat feedback in the gas phase. This simple flame spread model was developed by de Ris [18] for opposed flame spread, see Figure 3.5.

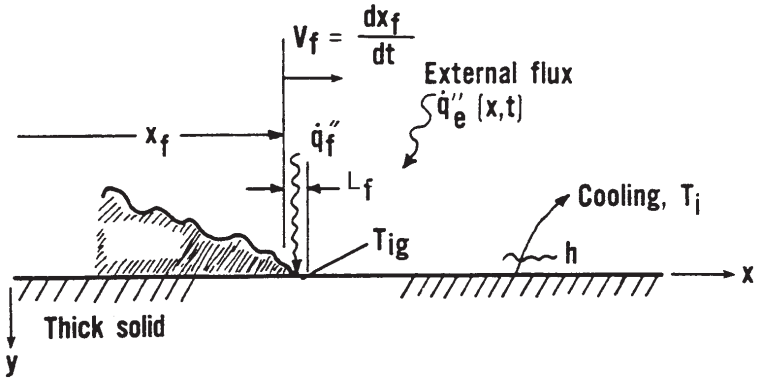

Figure 3.5: Opposed flame spread [56]

The flame spread rate is given by the general Equation 3.1:

$$V_f = \frac{l_f}{t_{ig}} \tag{3.39}$$

The flame spread is thus seen as an advancing ignition front. The solid is heated over the flame length l_f with a constant assumed flame heat flux. The heated solid will ignite after an exposure to the flame heat flux for a time equal to the ignition time t_{ig}. Once the new solid is ignited it will heat up the solid over again the flame length.

For thermally thick solids, the heating will only be noticeable to a certain penetration depth:

$$\Delta = \left(\frac{\lambda t_{ig}}{\rho c}\right)^{1/2} \tag{3.40}$$

With a rather rude conservation of energy:

$$\rho \cdot c \cdot \Delta \cdot V_f \cdot (T_{ig} - T_s) = \dot{q}''_f \cdot l_f \tag{3.41}$$

the flame spread velocity becomes:

$$V_f = \frac{l_f}{\lambda \rho c} \cdot \frac{\dot{q}''_f}{(T_{ig} - T_s)^{1/2}} \tag{3.42}$$

The result is a simple algebraic equation for the flame spread velocity. No information on the mass loss rate is provided. The flame length and flame heat flux are input parameters, obtained for experiments.

3.4.2 Example: Mowrer and Williamson

The model that will be described here, was initially developed for upward flame spread by Mowrer and Williamson [82]. A similar model has been proposed for concurrent horizontal flame spread by Van Hees [117]. The solid reaction model assumes a constant heat release rate and the flame is represented by direct heat feedback.

In Figure 3.6 the solid is pyrolyzing for $0 < x < x_p$. The variation of the distance x_p determines the flame spread rate. It is assumed that once the solid is pyrolyzing a flame exists in the gas phase. The flame is extending to a length x_f and heats up the solid with an assumed constant heat flux. The solid receives from 0 to x_{po} a constant external heat flux from the ignition source.

The flame spread velocity is here seen as the velocity of the pyrolysis front. The front is identified by the location where the solid temperature equals the ignition temperature. For thin materials a burn-out front will be introduced when the solid is totally consumed. For thick charring materials the char layer acts as a thermal isolator. The pyrolysis rate can drop under the critical value to sustain a flame and a burn-out front is formed, although not all the solid is consumed.

The following assumptions are made:

- the heat flux of the flame is constant for the flaming zone $x < x_f$; outside this zone it is zero;
- the external or ignition heat flux is constant for the zone $0 < x < x_{po}$;
- the flame length follows from the heat release rate by the relation:

$$\frac{x_f}{x_p} = k_f \dot{E}'' \tag{3.43}$$

where x_f the length of the flame (m), x_p the pyrolysis distance (m), k_f a constant dependent on configuration (m^2/kW), in literature often a value 0.01 m^2/kW is used and; $\dot{E}''$ the heat release rate of the material (kW/m^2). A more general correlation is given by:

$$x_f = k_f (\dot{Q}')^n \tag{3.44}$$

where Q' is the total heat release rate per unit width.

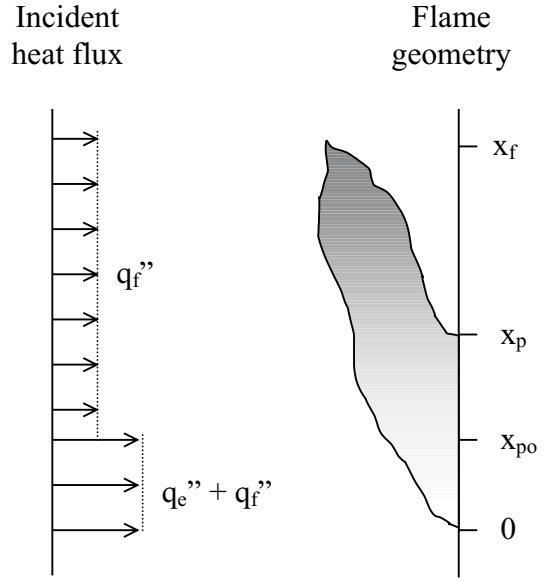

Figure 3.6: Heat fluxes in model

The flame can spread with or without burn-out front. For the first period when no burn out front exists, the velocity of the pyrolysis front is given by:

$$\frac{\mathrm{d}x_p}{\mathrm{d}t} \approx \frac{x_p(t+t_{ig}) - x_p(t)}{t_{ig}} = \frac{x_f(t) - x_p(t)}{t_{ig}} \tag{3.45}$$

Again this is based on Equation 3.1. For the second period the burn out front has to be included:

$$v_p(t) - v_b(t) = \frac{\mathrm{d}}{\mathrm{d}t}\Big(x_p - x_b\Big) = \left(\frac{x_f(t) - x_p(t)}{t_{ig}}\right) - \left(\frac{x_f(t) - x_p(t)}{t_{bo}}\right) \tag{3.46}$$

When a constant heat release rate is assumed, Equations 3.45 and 3.46 have an analytical solution.
For $0 < t < t_{bo}$:

$$x_p = x_{po} \cdot \exp\left(\frac{(k_f \dot{E}'' - 1)t}{t_{ig}}\right) \tag{3.47}$$

While for $t > t_{bo}$:

$$x_p - x_b = (x_{p1} - x_{po}) \cdot \exp\left[\left(k_f \dot{E}'' - \frac{t_{ig}}{t_{bo}} - 1\right)\frac{t - t_{bo}}{t_{ig}}\right] \tag{3.48}$$

Important parameters in this model are:

- the constant k_f ;
- the heat release rate of the solid;
- the ignition time t_{ig};
- and the burn out time t_{bo}.

When the experimental heat release rate is used, the equations can not be solved analytically and numerical methods have to be applied. To simplify the problem and to avoid the use of numerical methods, a mean value from the experimental results of the Cone Calorimeter can be used. Also when an exponential decaying function for the heat release rate is assumed, $\dot{q}'' = \dot{q}''_{max} \cdot \exp(-t/\tau)$, Equations 3.45 and 3.46 can be solved analytically. The results of the Cone Calorimeter are dependent on the radiation level. Most often the experiments are done for a (constant) radiation level of $25\,\mathrm{kW/m^2}$, though in reality the flame heat flux will change during the burning of the solid. The ignition time t_{ig} and the burn out time t_{bo} are determined with the Cone Calorimeter as well. And often the parameters in the model described above, are fitted to the experimental results of flame spread to obtain better correspondence.

3.4.3 Example: di Blasi

The fundamental solid combustion model of Section 3.2.5 can be coupled to the fundamental gas phase model of Section 3.3.3 to obtain a flame spread model as was done by di Blasi [24]. The coupling of the solid and gas model is done by the boundary conditions. For the species fuel and oxygen the convective and diffusive mass flux in the gas phase must be equal to the mass flux generated at the surface (by the solid model). When it is assumed that only fuel (F) and no oxygen (O) is generated by the solid then:

$$\rho D \frac{\partial Y_F}{\partial y} = m_s(Y_F - 1) \tag{3.49}$$

$$\rho D \frac{\partial Y_O}{\partial y} = m_s Y_O \tag{3.50}$$

with $m_s = \int_0^{L_s} K_1 \rho_s \mathrm{d}y$ the volatiles produced by the solid.

At the interface the gas temperature is equal to the solid temperature:

$$T_{\text{gas, interface}} = T_{\text{solid, interface}} \tag{3.51}$$

The conservation of energy at the interface is given by:

$$\underbrace{-\lambda\frac{\partial T}{\partial y}}_{fluid} = \underbrace{-\lambda_s\frac{\partial T_s}{\partial y}}_{solid} - q_{rs} + q_{rgs} \tag{3.52}$$

with q_{rs} the reradiation or the radiation loss of the surface

$$q_{rs} = \varepsilon\sigma(T_s^4 - T_0^4) \tag{3.53}$$

and q_{rgs} the absorbed radiation energy of the flame in the gas phase [75]

$$q_{rgs} = 2\varepsilon\sigma\int_{L_s}^{L_g} K_p T^4 \mathrm{d}y \tag{3.54}$$

Convection is here neglected.

3.5 Survey of input parameters

The input parameters for the fire spread models can be divided into fundamental properties and global characteristics [56]. The fundamental properties are further subdivided into those describing the chemical composition, the thermal properties and the combustion properties. The properties are independent on the method used to measure them. The global characteristics, on the other hand, do vary with the method used to measure them.

Fundamental properties

- Chemical composition
  - elementary composition
  - moisture content
  - properties of both solids and gasified products
- Thermal properties
  - thermal conductivity
  - heat capacity
  - density
  - emissivity
  - mass diffusivity

  - porosity

- Combustion properties
  - heat of combustion
  - heat of pyrolysis
  - kinetics of combustion
  - extinction coefficient of fuel vapours
  - kinetics of pyrolysis

Global characteristics

- rate of mass release
- rate of heat release
- radiative fraction of heat release
- regression rate
- ignition temperature
- effective thermal inertia
- surface spread of flame
- smoke generation
- species generation
- dripping, sparking
- mechanical behaviour: deformation, delamination, shrinking, cracking

Lots of the present flame spread models need global characteristics. In general they need the yield of pyrolysis gases or the heat release rate per unit area under exposure. The only standard method producing data in the required form for all the parameters is the Cone Calorimeter [38]. The Cone Calorimeter has already successfully been used as a source of data by modellers everywhere in the world.

Not all the properties that are given here must be present in a flame spread model. Dependent on the assumptions and simplifications certain properties will be redundant. For example when the rate of mass release is calculated by the solid combustion model, the global characteristic “rate of

mass release" is redundant. Of course, when less global characteristics are used, the model will be more universal.

An example of the determination of the ignition temperature and the effective thermal inertia is given in Appendix B

3.6 Prescribed fire growth

In a special set of models the flame spread is prescribed. These models are called *fire growth* models instead of *flame spread* models. Fire growth is seen as a global process where several surfaces and materials are involved, while flame spread is limited to a single surface. For a steady fire the heat release rate is dependent on the ventilation factor, while for transient fires the heat release is dependent on the time. The fire is modelled as a whole, with no details about the flame front and flame velocity. The fuel is pseudo-homogenous, though it consists of different materials.
From experimental results the heat release rate for vertical growth is given by:

$$\dot{Q} \propto t^3 \tag{3.55}$$

For horizontal growth:

$$\dot{Q} \propto t^2 \tag{3.56}$$

In some case, for example counter current flame spread, a linear growth law can be possible:

$$\dot{Q} \propto t \tag{3.57}$$

When the fire is fully developed, the heat release rate is in most fires determined by the amount of air that can be supplied to the fire: the fire is ventilation controlled. The amount of air supplied is constant in time and depends on the geometrical configuration (width and height of windows), so:

$$\dot{Q} = \text{constant} \tag{3.58}$$

t^2-fire
Work by the National Bureau of Standard, (NFPA 92B) [83] based upon a series of fire test and analysis has provided a basis for evaluating the growth of various types of fire which can be approximated by a simple equation of the form:

$$\dot{Q} = \alpha \cdot t^2 \tag{3.59}$$

Table 3.1: Categories of T-squared fires [83]

Description	Typical materials	Intensity coefficient (kW/s^2)
Slow	-	0.0029
Moderate	Cotton/polyester sprungmattress	0.012
Fast	Plastic foam, stacked timber pallets, full mail bags	0.047
Ultra-fast	Methyl alcohol pool fire, fast burning upholstered furniture	0.19

where $\dot{Q}$ the heat release rate in kW, α the intensity coefficient in kW/s^2 and t the time in s. The equation is commonly known as a T-squared fire. The intensity coefficient varies with the type of materials present and the configuration of the fire room. Whilst no two fires are ever identical, four basic categories of fire have been defined which are considered to form a good basis for design purposes.

The heat release rate predicted by the T-squared law can be incorporated in many different ways in the fire model. For example, in a computational fluid dynamics program the heat can be released in a volume, through a surface, as a heat source or as a fuel component. [64, 124]

Part II

Solid combustion models

The reaction of the solid phase to an incident heat flux can be modelled in several ways. In this part of the thesis several solid combustion models are examined:

- Arrhenius law model;
- Integral model;
- Moving mesh model;
- Enthalpy model;
- Dual mesh model.

Each model is treated in a separate chapter. In the last chapter of this part, the solid combustion models are compared with each other and with experiments.

The goal of this part is to reveal the predicting capabilities of the models as well as to evaluate their calculation speed. The last is especially important when the solid combustion model is coupled with a CFD code. Therefore, a rather extensive study is done of the time step, the cell size, the number of iterations, the convergence criteria, etc. The most suitable models for coupling to a CFD code will be chosen.

In most of the simulations in this part, the models are run as stand-alone model. This means that no gas phase model is used. The boundary condition thus the net incident heat flux at the solid surface, is given by the user. In Chapter 9 some direct heat feedback gas phase models are used, dependent on the experiment.

Chapter 4

Reaction of solid material: Arrhenius law

4.1 Description of the model

In this chapter a solid combustion model is developed where the reaction rate of the pyrolysis reactions is described by an Arrhenius law [61, 62]. The transformation of virgin material into char is gradual, which gives the pyrolysis front a finite thickness. The pyrolysis gases, that are produced in the solid, are assumed to flow immediately out of the solid. The solid model is based on work done by Di Blasi [22] and Ritchie [97].

The solid material is considered to exist of a mix of virgin and char material. At the start, before pyrolysis, the whole solid exists of pure virgin material. When the solid is fully pyrolyzed, only pure char is left. In between, the solid exists of this mix of char and virgin material. The local ratio is given by the char volume fraction.

During the pyrolysis reactions, the solid is converted from virgin material into char and pyrolysis gases in a continuous way. The degradation of the solid is described by a one-step reaction [24]:

$$\text{virgin} \xrightarrow{+\text{ heat}} \text{char} + \text{pyrolysis gases} \tag{4.1}$$

The reaction rate is described by an Arrhenius equation:

$$k_{pyr} = A \cdot \exp\left(-\frac{E_a}{RT}\right) \tag{4.2}$$

As a consequence, the pyrolysis reactions "take off" above a certain temperature (see further). At low temperatures the pyrolysis reactions are negligible.

When the temperature rises, the pyrolysis reactions grow such as the available heat allows. The pyrolysis reaction are endothermic and thus absorb sensible heat. So during the pyrolysis process the local temperature of the solid is kept low by these endothermic reactions. Once all the virgin material in a location is fully consumed, the temperature will rise again.

The pyrolysis gases, produced in the solid, flow immediately out of the solid. No gases are stored in the solid. Thus the driving pressure gradients are not modelled. On their way to the surface of the solid (i.e. interface solid / fluid) it is assumed that the gases will be at the same temperature as the solid material they are flowing through [88]. In this way the pyrolysis gases will heat up during their movement from the place produced, to the place where they are released in the fluid (front surface).

It is assumed that the density, the conduction coefficient and the heat capacity of the solid material (virgin and char material as well) do not depend on temperature. They are, though, function of the composition of the solid, determined by the char volume fraction ξ_c.

The model equations are derived with the control volume technique. There is no surface regression, the geometry and the solid boundaries are fixed in time.

4.1.1 Conservation of mass

In the solid material we consider a steady control volume with volume V and surface S. It is assumed that the pyrolysis gases $\dot{m}''_{pyr}$ will flow only in the direction perpendicular to the solid / fluid interface. The conservation of mass gives (see Figure 4.1) [63]:

$$\frac{\mathrm{d}}{\mathrm{d}t}\int_V \rho \,\mathrm{d}V = -\int_S \dot{\mathbf{m}}''_{pyr}\,\mathrm{d}\mathbf{S} \tag{4.3}$$

The density of the solid ρ is given by

$$\rho = \xi_v \cdot \rho_v + \xi_c \cdot \rho_c = (1-\xi_c)\cdot\rho_v + \xi_c \cdot \rho_c \tag{4.4}$$

where ρ_c the density of the char material, ρ_v the density of pure virgin material, and ξ_c the char volume fraction. Equation 4.4 can be determined from:

$$\begin{aligned} & m = m_v + m_c \\ & \Rightarrow \frac{m}{V} = \frac{m_v}{V} + \frac{m_c}{V} \\ & \Rightarrow \rho = \frac{m_v}{V_v}\cdot\frac{V_v}{V} + \frac{m_c}{V_c}\cdot\frac{V_c}{V} \\ & \Rightarrow \rho = \rho_v \cdot \xi_v + \rho_c \cdot \xi_c \end{aligned} \tag{4.5}$$

The divergence theorem is applied to Equation 4.3 and the result is combined with Equation 4.4 to obtain:

$$\frac{\partial \xi_c}{\partial t} = -\frac{\nabla \cdot (\dot{m}''_{pyr})}{\rho_c - \rho_v} \tag{4.6}$$

As the produced pyrolysis gases are immediately evacuated out of the solid, the pyrolysis mass flux can be related to the pyrolysis mass production per volume unit by:

$$\nabla \cdot (\dot{m}''_{pyr}) = -\dot{m}'''_{pyr} \tag{4.7}$$

The pyrolysis gases flow only in the direction perpendicular to the solid/gas interface, so this reduces to:

$$\nabla \cdot (\dot{m}''_{pyr}) = \frac{\partial \dot{m}''_{pyr}}{\partial x} = -\dot{m}'''_{pyr} \tag{4.8}$$

The rate of the production of pyrolysis gases is given by the Arrhenius law:

$$\dot{m}'''_{pyr} = A \cdot \rho_v \cdot (1 - \xi_c) \cdot \exp\left(-\frac{E_a}{RT}\right) \tag{4.9}$$

And Equation 4.6 becomes:

$$\frac{\partial \xi_c}{\partial t} = -A \cdot \frac{\rho_v}{\rho_c - \rho_v} \cdot (1 - \xi_c) \cdot \exp\left(-\frac{E_a}{RT}\right) \tag{4.10}$$

Remark: The density of the pure char is in reality not a constant. It is dependent on the incident and the critical heat flux or in other words on the local temperature history of the solid material [108]. For wood, for example, it was found that more char is produced when the incident heat flux is lower (for same critical heat flux). As a consequence the solid model should have a sort of a variable density. But because the dependent parameters for the char fraction are not clearly known, a constant value is used.

4.1.2 Conservation of energy

4.1.2.1 Specific heat capacity

The specific heat capacity of the solid is determined by the following reasoning. Consider a solid volume at temperature T. The volume consists of a homogenous mix of char and virgin material, (a) in Figure 4.2, but it can

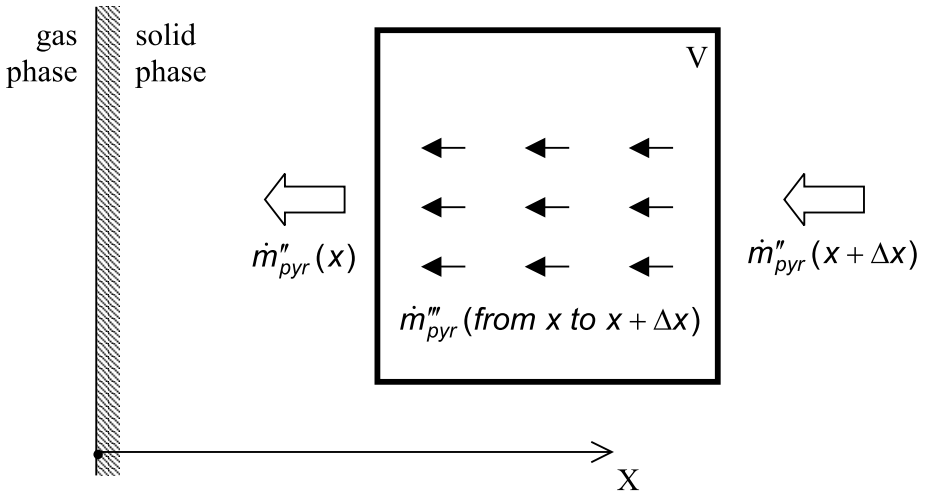

Figure 4.1: Flow of pyrolysis gases

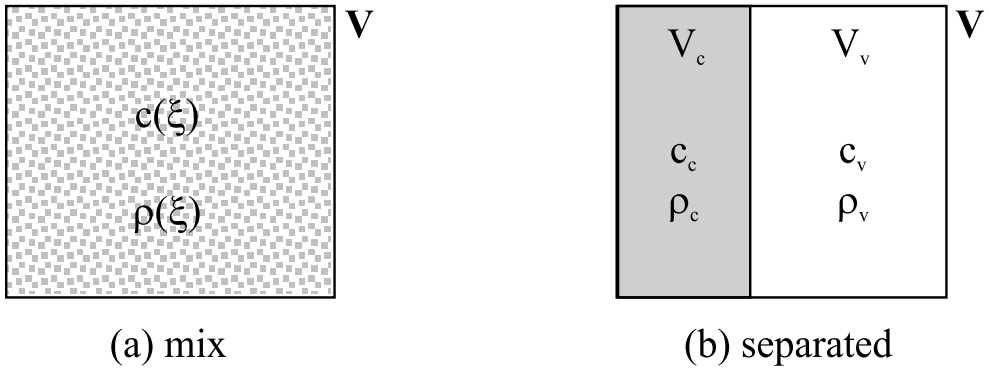

Figure 4.2: Calculation of heat capacity

also be seen as composed of two pure components, see (b) in Figure 4.2. The heat stored in both cases should be the same, thus:

$$m \cdot (u_0 + c \cdot T) = m_c \cdot (u_{0,c} + c_c \cdot T) + m_v \cdot (u_{0,v} + c_v \cdot T) \tag{4.11}$$

This determines the solid specific heat capacity:

$$c(\xi) = \frac{\rho_c c_c \xi_c + \rho_v c_v (1 - \xi_c)}{\rho_c \xi_c + \rho_v (1 - \xi_c)} \tag{4.12}$$

and

$$u_0(\xi) = \frac{\rho_c c_{c,0} \xi_c + \rho_v c_{v,0} (1 - \xi_c)}{\rho_c \xi_c + \rho_v (1 - \xi_c)} \tag{4.13}$$

4.1.2.2 Pyrolysis heat

In the solid the following single step pyrolysis reaction takes place:

$$\text{virgin} \xrightarrow{+ \text{ heat of pyrolysis}} \text{char} + \text{volatiles} \tag{4.14}$$

The heat of pyrolysis is expressed in Joules per kilogram *volatiles* and it can be determined with the char, virgin and volatile energies [125]. Consider an amount of virgin material at a temperature T_{pyr} that is transformed entirely into char material and pyrolysis gases by the absorption of energy. There is only enough energy supplied for the endothermic reactions, so no further heating will be present. Conservation of energy for this transformation can be written as

$$\begin{aligned} &\rho_v \left(u_v(T_0) + \int_{T_0}^{T_{pyr}} c_v \mathrm{d}T \right) + \rho_v Q_{pyr}(T_{pyr}) \\ &\quad = \rho_c \left(u_c(T_0) + \int_{T_0}^{T_{pyr}} c_c \mathrm{d}T \right) + (\rho_v - \rho_c) \left(u_{pyr}(T_0) + \int_{T_0}^{T_{pyr}} c_{pyr} \mathrm{d}T \right) \end{aligned} \tag{4.15}$$

When the reference temperature T_0 and the pyrolysis temperature T_{pyr} are taken 0 °C, and when the heat capacities are assumed constant, than:

$$\rho_v u_v(T_0) + (\rho_v - \rho_c) Q_{pyr}(T_0) = \rho_c u_c(T_0) + (\rho_v - \rho_c) u_{pyr}(T_0) \tag{4.16}$$

Note that T_0 is the reference temperature, typical 0 °C, and is different from the initial temperature of the solid. The heat of pyrolysis is thus dependent on the temperature at which the pyrolysis reaction will proceed. The heat

of pyrolysis at a temperature $T_{pyr,1}$, i.e. $Q(T_{pyr,1})$, can be determined from $Q(T_{pyr,2})$ from:

$$(\rho_v - \rho_c)Q_{pyr}(T_{pyr,1}) - (\rho_v - \rho_c)Q_{pyr}(T_{pyr,2}) = \rho_c\left(\int_{T_{pyr,1}}^{T_{pyr,2}} c_c \mathrm{d}T\right) + (\rho_v - \rho_c)\left(\int_{T_{pyr,1}}^{T_{pyr,2}} c_{pyr}\mathrm{d}T\right) - \rho_v\left(\int_{T_{pyr,1}}^{T_{pyr,2}} c_v \mathrm{d}T\right) \tag{4.17}$$

4.1.2.3 Conservation of energy

For the conservation of energy the following energy flows are considered:

1. conduction in the solid;
2. convection of pyrolysis gases through the solid;
3. heat accumulation in the solid.

Again we consider a control volume with volume V and surface S. When the change in potential and kinetic energy is neglected and when there is no volume expansion considered, the conservation of energy is then given by:

$$\frac{\mathrm{d}}{\mathrm{d}t}\int_V \rho u(T)\mathrm{d}V + \int_S u_{pyr}(T)\dot{\mathbf{m}}''_{pyr}\cdot\mathrm{d}\mathbf{S} = -\int_S \dot{\mathbf{q}}''\cdot\mathrm{d}\mathbf{S} \tag{4.18}$$

When a distinction is made between the pyrolysis gases $\dot{m}''_{fl}$ which are flowing through the volume and originate from deeper solid, and the pyrolysis gases $\dot{m}''_{vol}$ that are produced in the volume itself, Equation 4.18 becomes:

$$\frac{\mathrm{d}}{\mathrm{d}t}\int_V \rho\Big(u(T_0) + c(T-T_0)\Big)\mathrm{d}V + \int_S \Big(u_{pyr}(T_0) + c_{pyr}\cdot(T-T_0)\Big)\dot{\mathbf{m}}''_{vol}\cdot\mathrm{d}\mathbf{S} + \int_S \Big(u_{pyr}(T_0) + c_{pyr}\cdot(T-T_0)\Big)\dot{\mathbf{m}}''_{fl}\cdot\mathrm{d}\mathbf{S} = -\int_S \dot{\mathbf{q}}''\cdot\mathrm{d}\mathbf{S} \tag{4.19}$$

Over half of the surface $\dot{\mathbf{m}}''_{fl}\cdot\mathrm{d}\mathbf{S}$ is positive and over the other half it is negative (but with the same absolute value) as the gas is just flowing through. This means that the term $u_{pyr}(T_0)$ in the fl-term will cancel or:

$$\frac{\mathrm{d}}{\mathrm{d}t}\int_V \rho c(T-T_0)\mathrm{d}V + \int_S c_{pyr}(T-T_0)\dot{\mathbf{m}}''_{vol}\cdot\mathrm{d}\mathbf{S} + \int_S c_{pyr}(T-T_0)\dot{\mathbf{m}}''_{fl}\cdot\mathrm{d}\mathbf{S} + \frac{\mathrm{d}}{\mathrm{d}t}\int_V \rho u(T_0)\mathrm{d}V + \int_S u_{pyr}(T_0)\dot{\mathbf{m}}''_{vol}\cdot\mathrm{d}\mathbf{S} = -\int_S \dot{\mathbf{q}}''\mathrm{d}\mathbf{S} \tag{4.20}$$

With Equation 4.4, Equation 4.6, Equation 4.16 and the divergence theorem, this can be written as:

$$\frac{\mathrm{d}}{\mathrm{d}t}\int_V \rho c(T-T_0)\mathrm{d}V + \int_S c_{pyr}(T-T_0)\dot{\mathbf{m}}''_{vol}\cdot\mathrm{d}\mathbf{S} + \int_S c_{pyr}(T-T_0)\dot{\mathbf{m}}''_{fl}\cdot\mathrm{d}\mathbf{S} + \int_S Q_{pyr}(T_0)\dot{\mathbf{m}}''_{vol}\cdot\mathrm{d}\mathbf{S} = -\int_S \dot{\mathbf{q}}''\mathrm{d}\mathbf{S} \quad (4.21)$$

where the two separate flows $\dot{\mathbf{m}}''_{vol}$ and $\dot{\mathbf{m}}''_{fl}$ can be added again. When the reference temperature T_0 is taken zero, and when the law of Fourier is applied for the conductive heat fluxes, then for an interior volume:

$$\frac{\mathrm{d}}{\mathrm{d}t}\int_V \rho cT\mathrm{d}V + \int_S c_{pyr}T\dot{\mathbf{m}}''_{pyr}\cdot\mathrm{d}\mathbf{S} + \int_V Q_{pyr}\dot{m}'''_{pyr}\cdot\mathrm{d}V = -\int_S \lambda\frac{\partial T}{\partial \mathbf{n}}\mathrm{d}\mathbf{S} \quad (4.22)$$

or

$$\frac{\partial}{\partial t}(\rho cT) - \nabla\cdot(\dot{m}''_{pyr}c_{pyr}T) + Q_{pyr}\dot{m}'''_{pyr} = \nabla\cdot(\lambda\nabla T) \quad (4.23)$$

4.2 Discretized equations

The finite volume technique is used to solve the set of partial differential equations given by Equations 4.8, 4.10 and 4.22. A uniform steady one-dimensional grid is used which divides the solid into N grid cells. In each cell the temperature T, the char volume fraction ξ_c, the pyrolysis mass flux $\dot{m}''_{pyr}$ and volume pyrolysis mass production $\dot{m}'''_{pyr}$ is stored. For the time discretization the Crank-Nicholson hybrid method is used. For the convective part in Equation 4.22 the first order upwind method is used. In an iterative method the equations are solved one by one with the Gauss Seidel method.

The pyrolysis mass production for a volume i is given by:

$$\dot{m}'''_{pyr,i} = (1-\xi_{c,i})\cdot\rho_v\cdot A\cdot\exp\left(-\frac{E}{RT_i}\right) \qquad i = 1\ldots N \quad (4.24)$$

with N the number of nodes. The pyrolysis mass flux at the left boundary of volume i (see Figure 4.3) is given by:

$$\dot{m}''_{pyr,i} = \dot{m}''_{pyr,i+1} + \dot{m}'''_{pyr,i}\cdot\Delta x \quad (4.25)$$

It is assumed that no pyrolysis gases flow into or out of the solid at the rear boundary or:

$$\dot{m}''_{pyr,N+1} = 0 \quad (4.26)$$

For the discretization of the *mass* equation, a hybrid (Crank Nicholson) method is used. The subscript m indicates the iteration number during a time step, while n indicates the value of the variable at the previous time step. Discretization of Equation 4.10:

$$\frac{\xi_i^{m+1} - \xi_i^n}{\Delta t} = \theta \cdot RHS_i^{m+1} + (1-\theta) \cdot RHS_i^n \tag{4.27}$$

The parameter θ is a variable controlling the type of difference scheme. If $\theta = 0$ the method reduces to the explicit method, if $\theta = 1$ it reduces to the fully implicit method. The RHS in Equation 4.27 given by:

$$RHS_i = A \cdot \frac{\rho_v}{\rho_v - \rho_c} \cdot (1 - \xi_{c,i}) \cdot \exp\left(-\frac{E_a}{RT_i}\right) \tag{4.28}$$

The temperature in the RHS on $m+1$ will be approximated by the temperature on m, the variable ξ is written on $m+1$.

After some modifications:

$$\xi_i^{m+1} = \xi_i^n + \frac{c_{relax}}{1 + \theta \cdot \Delta t \cdot RHS_i^n}\Big((\xi_i^n - \xi_i^m) + \theta \cdot \Delta t \cdot RHS_i^m \; + \; (1-\theta) \cdot \Delta t \cdot RHS_i^n\Big) \tag{4.29}$$

With c_{relax} a coefficient smaller than 1 to ensure stability during the iterations. This can be seen as an explicit pseudo-step in time, where the calculated change of the variable can be reduced for stability reasons.

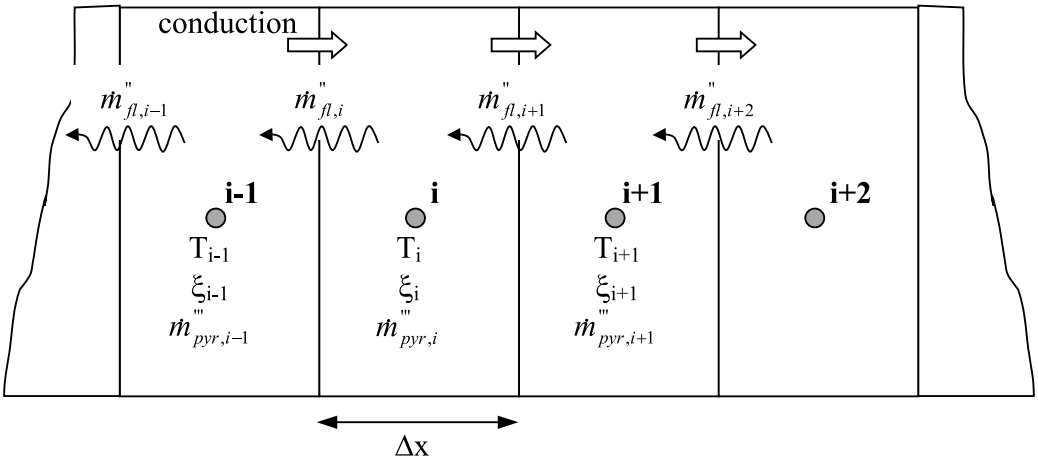

Figure 4.3: Storage of variables in grid

Equation 4.28 is substituted into this equation, care must be taken that the same expression is used for the calculation of the production of pyrolysis gases. When this is not the case, there is no correct conservation of mass and values for the char volume fraction higher than 1 are possible.

The conservation of *energy* of Equation 4.23 is discretized in a similar way:

$$\frac{(\rho cT)_i^{m+1} - (\rho cT)_i^n}{\Delta t} = \theta\ RHS_i^{m+1} + (1-\theta)\ RHS_i^n \tag{4.30}$$

Again after some modifications:

$$T_i^{m+1} = T_i^m + \frac{c_{relax}}{\Theta}\Bigg[\Big((\rho cT)_i^n - (\rho cT)_i^m\Big)\frac{\Delta x}{\Delta t} + \theta\ RHS_i^{m+1} + (1-\theta)\ RHS_i^n\Bigg] \tag{4.31}$$

with

$$RHS_i = (\dot{m}''_{pyr}c)_{i+1/2}^m T_{i+1}^m - (\dot{m}''_{pyr}c)_{i-1/2}^m T_i^m + \lambda_{i+1/2}^m \frac{T_{i+1}^{m+1} - T_i^m}{\Delta x} - \lambda_{i+1/2}^m \frac{T_i^m - T_{i-1}^{m+1}}{\Delta x} + Q_{pyr}\dot{m}'''_{pyr}\Delta x + Q_{boundary}$$

$$\Theta = (\rho c)_i^m \frac{\Delta x}{\Delta t} + \theta\Big((\dot{m}''_{pyr}c)_{i-1/2}^m + \lambda_{i+1/2}^m \frac{1}{\Delta x} + \lambda_{i-1/2}^m \frac{1}{\Delta x}\Big) + Q_{boundary}$$

The temperature T_{i+1} and T_{i-1} are, dependent on the iteration loop over the cells, known or unknown. If the iteration is started at the top or the left, the temperature at cell $i-1$ will be known. Similar, if we start at the bottom or the right, the temperature of cell $i+1$ will be known. $Q_{boundary}$ incorporates the boundary conditions. For the front cell this is the incident heat flux; for the rear cell this is a fixed heat flux and/or heat convection. The coefficient c_{relax} in the equation is smaller than 1 to ensure stability during the iterations.

4.3 Solution of discretized equations

The solution procedure is given in Figure 4.4. The thermal properties are

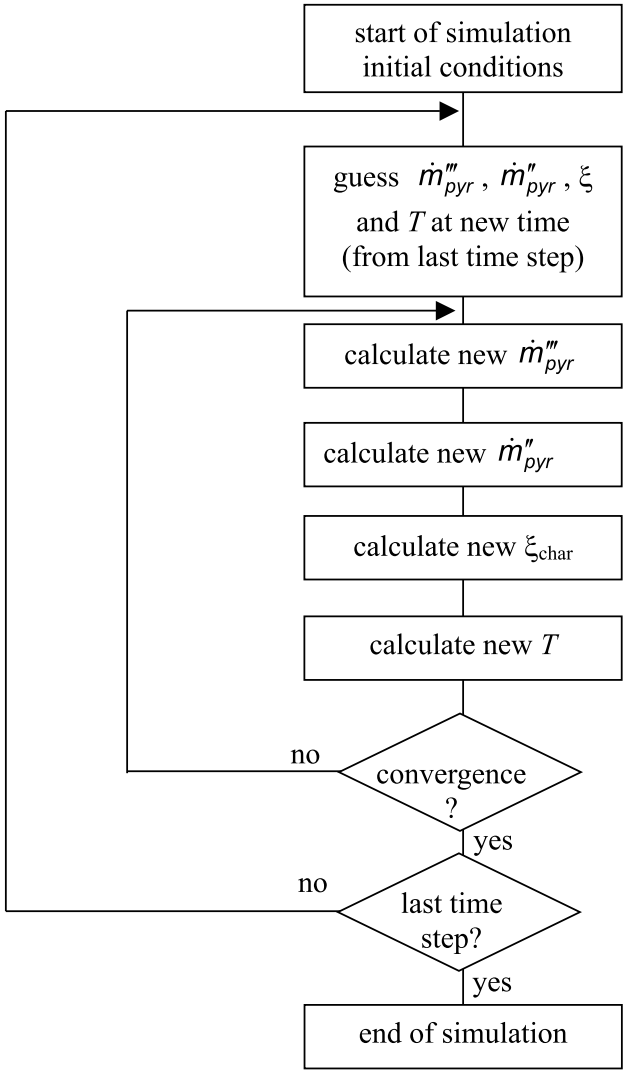

Figure 4.4: Scheme for solution of equations

calculated with the char volume fraction:

$$\begin{aligned} \rho &= \xi_v \cdot \rho_v + \xi_c \cdot \rho_c \\ &= (1-\xi_c) \cdot \rho_v + \xi_c \rho_c \\ \lambda &= \xi_v \cdot \lambda_v + \xi_c \cdot \lambda_c \\ &= (1-\xi_c) \cdot \lambda_v + \xi_c \cdot \lambda_c c \\ c &= \frac{\rho_c \cdot c_c \cdot \xi_c + \rho_v \cdot c_v \cdot (1-\xi_c)}{(1-\xi_c) \cdot \rho_v + \xi_c \cdot \rho_c} \end{aligned} \tag{4.32}$$

The pyrolysis mass production per volume is a strong function on temperature. At the start the temperature and the char volume are low and almost no gases are produced. Once the temperature is high enough, pyrolysis starts in a sort of run-away condition. The solid is pyrolyzed fast and as a consequence a pyrolysis *wave* will flow through the solid.

4.4 Determination of time step and cell size

In this paragraph three parameters important for the numerical solution are examined:

1. the number of time steps or the length of a time step;
2. the number of nodes or size of a cell;
3. the number of iterations per time step.

As boundary condition on the front surface, a constant incident heat flux is taken. This is not realistic because when the surface temperature rises the heat losses to the surrounding will rise as well, and the net incident heat flux will lower. But for simplicity a constant net incident heat flux is taken. The material properties that were used, are given in Table 4.1. The rear surface is assumed to be perfectly insulated.

4.4.1 "The solution"

First a grid and time converged solution, further called "the solution", is calculated on a very fine grid with very small time steps and enough iterations. This solution is compared with the solution on a more coarse grid, calculated with larger time steps in order to determine maximum grid and time step sizes. The solution for a constant incident heat flux of $50\,\mathrm{kW/m^2}$ is given in Figure 4.5. The thick black curve represents the solution for 1024 cells and a time step of 0.005 s.

Table 4.1: Material properties [53]

Property	Value	Units
ρ_v	650	kg/m^3
ρ_c	350	kg/m^3
c_c	1257	J/kgK
c_v	1257	J/kgK
λ_v	.1257	W/mK
λ_c	.1257	W/mK
E_a	1.257 10^5	kJ/kmol
A	10^{10}	1/s
Q_{pyr}	7.54 10^5	J/kg

The mass flux of pyrolysis gases rises quickly to a maximum at about 10 s. When the pyrolysis front is moving inwards, the char layer gradually builds up, and the mass flux decreases and reaches a more or less steady value [108]. When all the virgin material is consumed the mass flux drops to zero and the surface temperature rises more quickly because of the lack of the endothermic pyrolysis reactions. When the pyrolysis front reaches the rear surface, two effects that determine the mass release rate are present: the increasing thermal resistance of the char layer which will lower the heat flux to pyrolysis front, and on the other hand the insulated rear surface. Because of the insulation, the virgin material will thus continuously heat up, and thus less energy (in the limit only the energy for the endothermic reactions thus no sensible heat) will be needed to complete the pyrolysis reactions. This of course speeds up the pyrolysis reactions and gives a larger mass flux of pyrolysis gases. The combination of both effects is known as the "back effect" [109].

4.4.2 Cell size

To determine the optimal parameters (cell size, time step and iterations) - one parameter is changed from "the solution". First the cell size is gradually augmented until the error fell under the wanted precision. In this way the maximum cell size in similar simulation can be determined. Then, the time step is gradually augmented which will give the maximum time step where the solution is stable and has the wanted precision.

When the number of solid cells is decreased, the mass flux of pyrolysis gases is intermittent, see Figure 4.5. If we compare with "the solution" it is

clear that those oscillations are unwanted and have no physical meaning. We can explain those oscillations when we look in more detail at the results. The variables of two neighbouring cells are tracked in time in Figure 4.6. The important results here are the temperature, the char volume fraction and the volume production of pyrolysis gases. When in cell i the temperature reaches about 500 K, it is seen on the volume production of pyrolysis gases graph that the pyrolysis reactions start to become significant. Meanwhile the temperature of cell $i+1$ is still too low to allow any pyrolysis reactions. After some time we see that the pyrolysis reactions in cell i reach a maximum, but still there are no pyrolysis reactions in the neighbouring cell $i+1$ due to the low temperature. The pyrolysis reactions in cell i, will now decrease because of the lack of virgin material. As there are still no pyrolysis reactions in the other cells but in i, the pyrolysis mass flux at the surface will have the same shape as the pyrolysis volume production in i. Only when the temperature in cell $i+1$ is high enough (about 500 K) the pyrolysis reactions in the solid, in cell $i+1$, start again.

The number of oscillations in the mass release rate at the surface during a whole simulation, should be equal to the amount of cells used, at least if the pyrolysis front reaches the rear surface in the simulation. In Figure 4.5 we can see 16 oscillations which is expected for 16 cells.

We notice in Figure 4.6 that the peak in volume production of pyrolysis

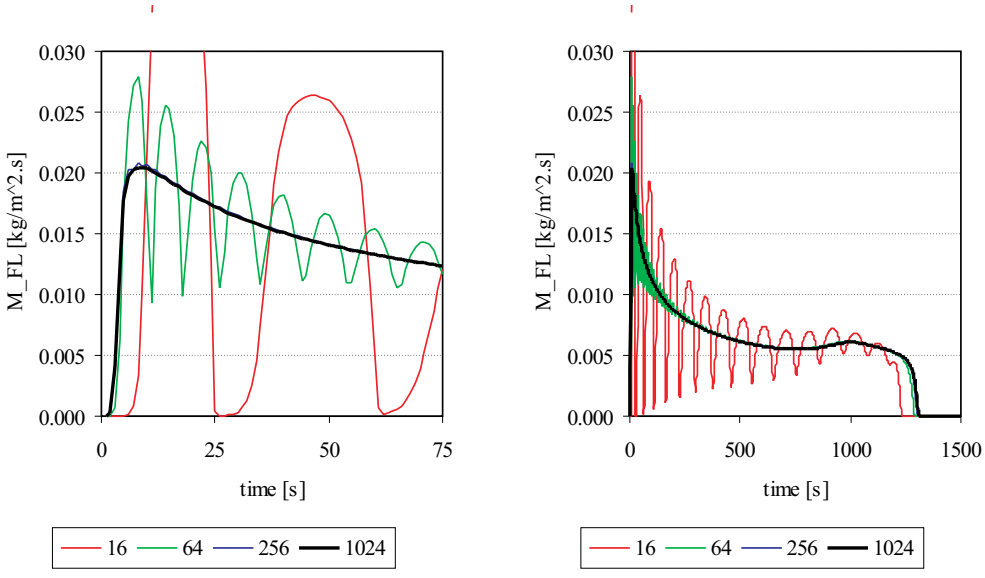

Figure 4.5: Mass flux of pyrolysis gases for several grids

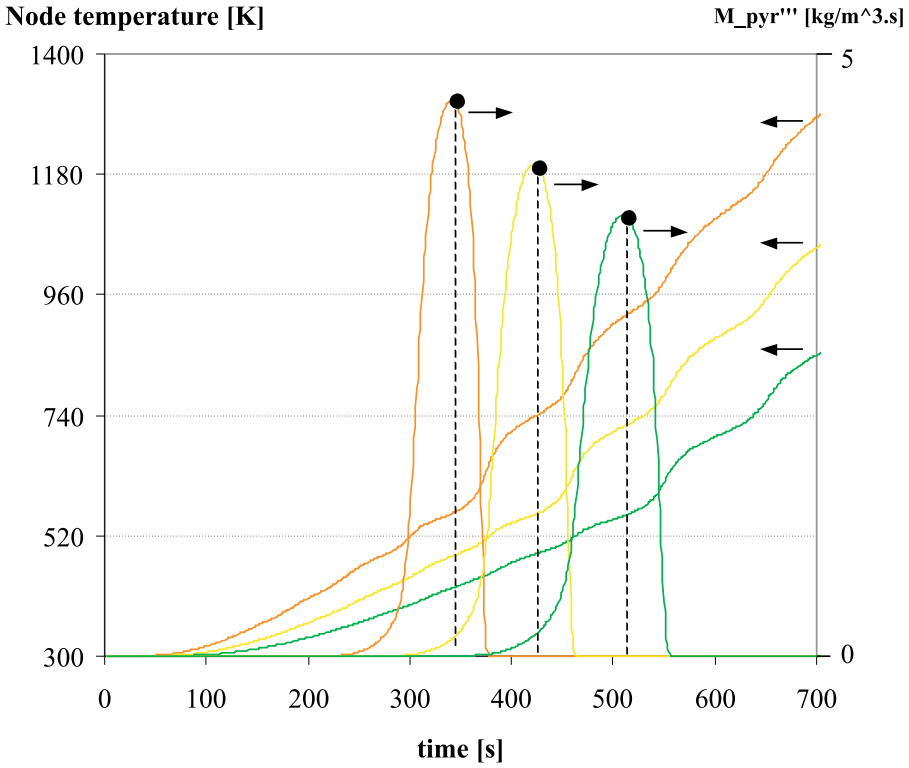

Figure 4.6: Temperature, ξ and $\dot{m}'''_{pyr}$ for three neighbouring nodes

Table 4.2: Error percentage for $\dot{m}''_{pyr,max}$, t_{max} and t_{cease}

Number of nodes	$\dot{m}''_{pyr,max}$ (kg/m^{2}s)	t_{max} (s)	t_{cease} (s)
16	112	79	6
32	72	25	3
64	37	9	1
128	13	14	1
256	2	8	4
512	0.4	0.5	0.1
1024	0	0	0

gases $\dot{m}'''_{pyr}$, is lower for "deeper" cells. These cells will heat up at a lower rate than the cells close to the surface. As a consequence, for a certain temperature, the char volume fraction will be already higher for the deeper cells, as there was more time available to pyrolyse the solid; the $\dot{m}'''_{pyr}$ curve will be smeared out in time and the peak will be lower.

The error in the maximum mass release rate ($\dot{m}''_{pyr,max}$), the time of this maximum (t_{max}) and the time of extinghuisment where $\dot{m}''_{pyr,max}$ drops to zero, is given for several numbers of nodes in Table 4.2. It is clear that the "Arrhenius law" model needs a lot of cells in order to have an oscillation free mass release rate.

4.4.3 Time step size

For the fine grid the time step size was varied from fine (= 0.005 s) to large (= 2 s). From the mass flux of pyrolysis gases, see Figure 4.7, we conclude that time steps of 2 s are too large because strong oscillations are introduced. The amplitude of these oscillations decreases with time what can be expected as we more or less reach a steady state. With a time step size of 1 s there are still oscillations, but only at the peak in the mass flux of pyrolysis gases. These oscillations are of course of a different nature than the oscillations that were introduced by increasing the cell size. When the boundary conditions (incident heat flux) are less severe, e.g. a step function that is less high, a step size of 1 s will probably be sufficient. To be on the safe side, though, a time step of 0.1 s is taken.

When a too large time step size is taken, unrealistic values for the char volume fraction (> 1) can be obtained. An example is the simulation with 1024 cells with a 2 s time step, where without precautions values of the char volume fraction higher than 1 are noticed. In those and in further simulations the char volume fraction was bounded between 0 and 1.

4.4.4 Optimal combination of cell and time step size

Next, the interaction of the cell size and time step is investigated. This is done by a simulation where the maximum accepted cell size and time step is used. The error for the maximum mass release rate is larger than the sum of the cell and time step size error separately as is observed by comparing Table 4.2 and 4.3. When the time step size is small, the main error is still produced by the cell size. Results with 256 nodes and time step size 0.5 s could be accepted, though there are still small oscillations.

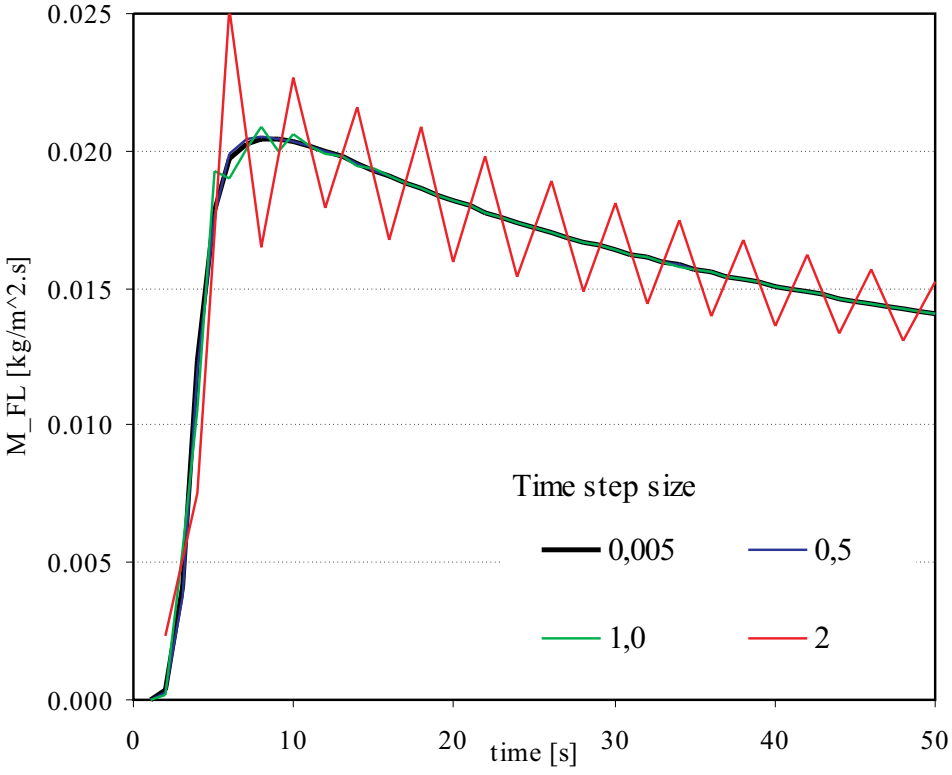

Figure 4.7: Influence of time step size.

Table 4.3: Error percentage for $\dot{m}''_{pyr,max}$, t_{max} and t_{cease}

Time step s	$\dot{m}''_{pyr,max}$ kg/m^2	t_{max} s	t_{cease} s
0.005	0.0	0.0	0.0
0.01	0.0	0.0	0.8
0.02	0.0	0.1	1.6
0.04	0.0	0.1	2.6
0.1	0.0	0.4	3.8
0.2	0.0	0.4	3.8
0.5	0.0	6.7	4.2
1	2.1	6.7	4.2
2	23.1	30.0	4.4

Table 4.4: Error percentage for $\dot{m}''_{pyr,max}$, t_{max} and t_{cease}

Number of nodes	Time step size	$\dot{m}''_{pyr,max}$	t_{max}	t_{cease}
1024	0.05	0.0	0.0	0.0
128	0.5	12.5	10.9	4.5
128	0.2	12.6	14.4	4.4
256	0.5	2.6	6.7	4.6
256	0.2	2.2	9.0	4.1

4.4.5 Number of iterations

As last the number of iterations per time step is examined. It is obvious that when the time step size is reduced, the amount of iterations per time step needed to obtain a certain precision will be smaller. When the amount of computer time is about the same, preference is given to simulations with smaller time steps as these will have smaller errors. The number of iterations is mainly determined by the size of the time step, the cell size has minor influence. For 256 nodes and a time step of 0.5 s, 5 iterations seemed insufficient (errors up to 11% caused by time lagging compared with simulation with 50 iterations), but 10 iterations give already satisfactory results (errors about 1%).

4.5 Further analysis

4.5.1 Location of the pyrolysis front

The location of the pyrolysis front is determined by the location where the char volume fraction ξ_c is equal to 0.99 for the top of the front, and to 0.01 for the bottom of the front. This is an arbitrary definition that will give an idea of the thickness of the pyrolysis front. The front location follows from linear interpolation between nodes. As the shape of the front is non-linear as can be seen in Figure 4.8 where the pyrolysis front is given for several times, there will be an error in the calculation the location. This is explained in Figure 4.9. In this figure a non-linear front moves with constant speed from left to right. The top location of the front, calculated with linear interpolation, is drawn in the figure. When the speed of the real front is constant, and the shape of the front is not changing in time, the location of the front - determined by a char volume fraction of 0.99, should be a linear function of time. Due to the linear interpolation and the shape of the front it can be

seen that this is not the case. The arrows on the X-axis show the location of the pyrolysis front in time. They should be evenly separated when the front velocity is constant. We see that when the front is close to the cell i, the calculated speed of the front will be lower than when the front is close to the cell $i+1$. When the cell size gets smaller the shape of the front between two nodes will be closer to a linear shape. So for small cells the error is small.

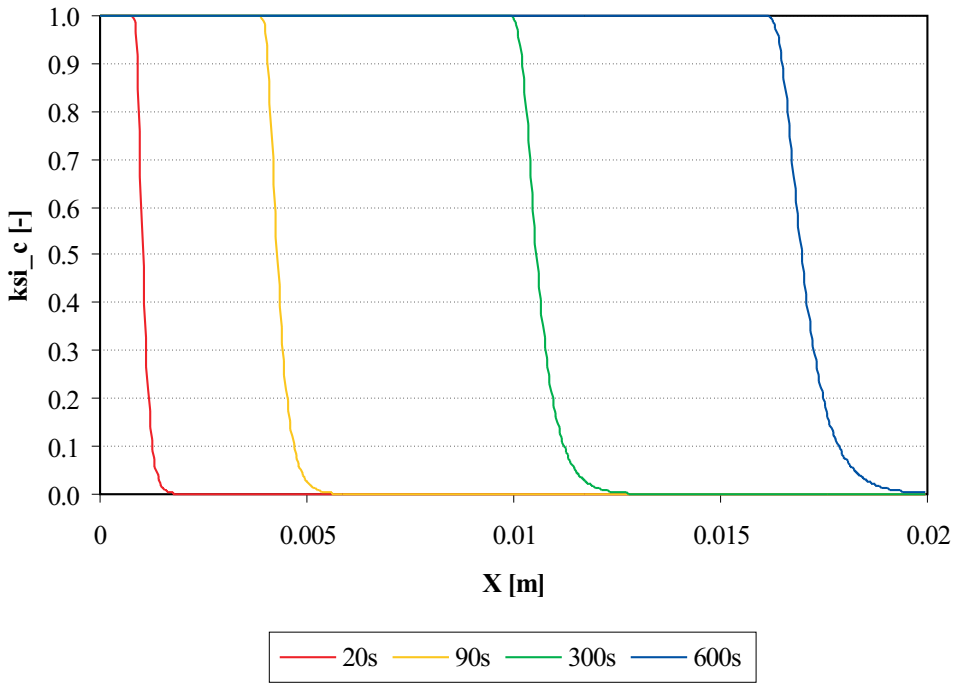

Figure 4.8: Slice of char volume fraction for 20, 90, 300 and 600s

In Figure 4.10 the front locations and temperature is given for a simulation with 1024 and 16 cells. As the front advances in the solid, the thickness of the front - defined by the char volume fractions 0.99 and 0.01 - grows. For the simulation with 1024 cells, the front temperatures are almost constant, while for the case with 16 cells, the temperatures of the front have large variations.

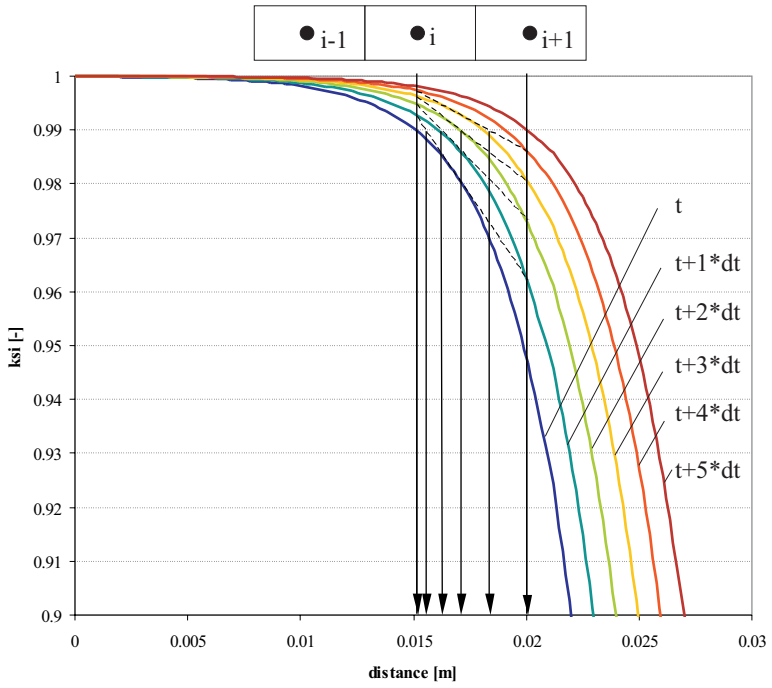

Figure 4.9: Location of pyrolysis front ($\xi = 0.9$) by linear interpolation for front with constant speed

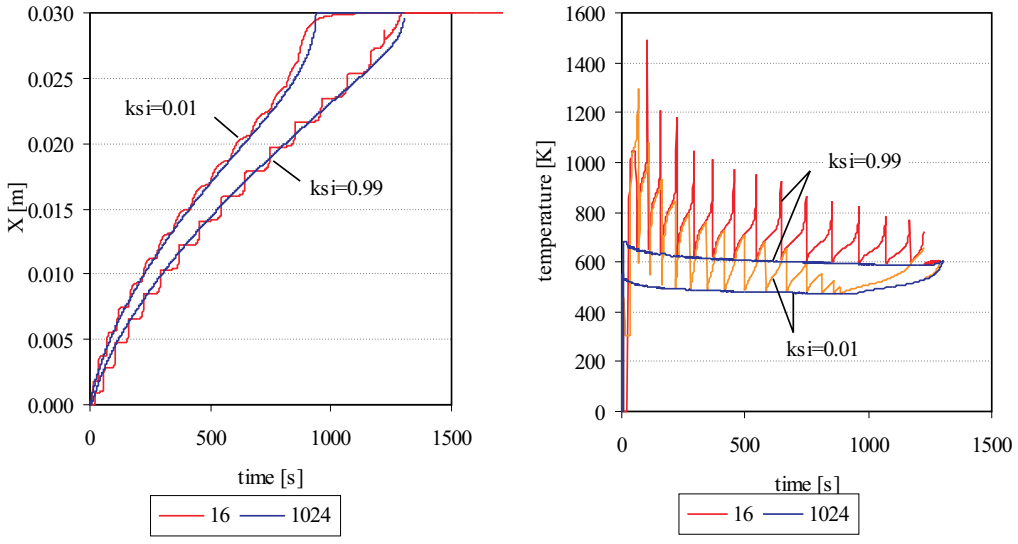

Figure 4.10: Front location and temperature

4.5.2 Analysis of the heat fluxes

In this paragraph the present heat fluxes are analysed in order to determine:

1. the driving force of the pyrolysis process;
2. if the convection of pyrolysis gases are an important heat sink in a cell;
3. the proportion between conduction and heat absorption by pyrolysis;

For a cell in the middle of the solid ($i = N/2$) the conduction heat, convective heat (or the heating of pyrolysis gases when they migrate to the surface), the change of the energy content of the solid and the absorbed pyrolysis heat is stored for each time step. The results are given in Figure 4.11. Results are dependent on the thermal properties, but similar results are expected for other building materials.

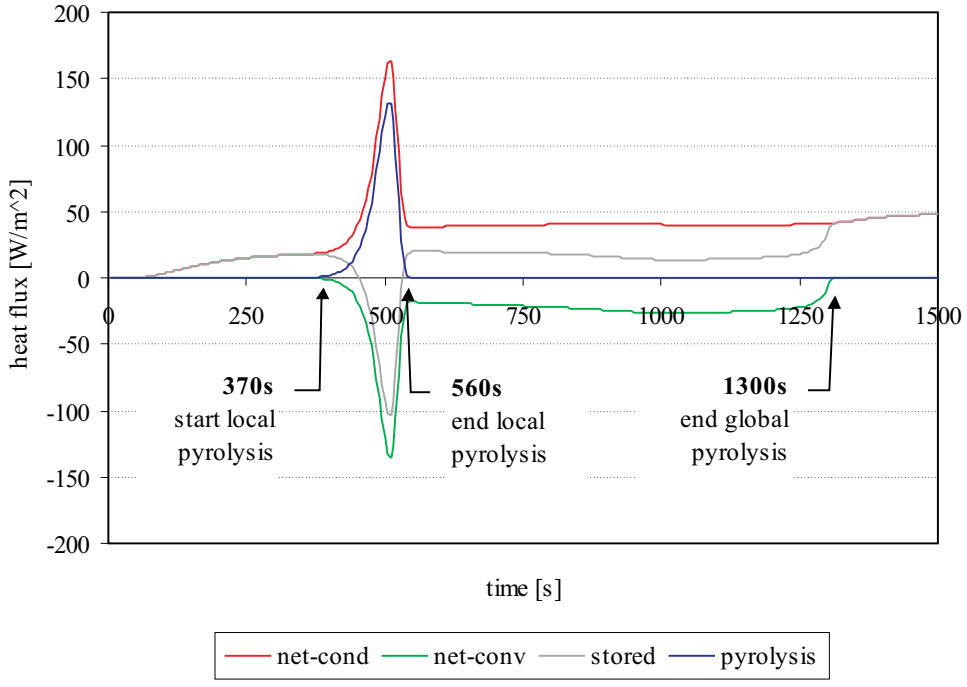

Figure 4.11: The heat flows for cell in the middle of the solid

At the start of the simulation the node in the middle of the solid is almost not influenced by the incident heat flux. Only after 65 s the solid in the middle is heating up and conductive heat fluxes are present. When the

pyrolysis front has not yet passed the zone in the solid, the net conduction heat (= conduction heat in at x minus the conduction heat out at $x + \Delta x$) is equal to the internal energy change of the solid. At about 370 s, when the pyrolysis front starts passing the zone, all the heat that is available in that zone, is absorbed by the pyrolysis process. The stored internal energy drops as a consequence of the changing density and specific heat capacity. The temperature, on the other hand, always rises. In the pyrolyzing zone the rise of the temperature is of course rather low. When the front has passed, at about 560 s, pyrolysis gases originating from deeper solid, flow through the zone. These gases will be heated up by the local hotter solid. During this process, the net conduction heat is the largest heat flow. The convective heat flow and the change of the energy content are equally important and are both in absolute value about half of the net conductive heat flow. So half of the energy that is supplied to a zone by conduction, is used for heating up the pyrolysis gases, while the other half is stored internally in the solid. At about 1300 s the pyrolysis front has reached the end surface of the solid, and pyrolysis reactions in the whole solid cease. No pyrolysis gases flow through the zone anymore, and the net conduction heat is totally used for the change of the internal energy.

4.5.3 Analysis of the pyrolysis reaction temperature

With the temperatures at which the pyrolysis gases are produced, a spectrum of pyrolysis gases is determined. As can be seen on Figure 4.12 the pyrolysis products are released for solid temperatures between 150 and 350 °C. For temperatures lower than 150 °C the reactions are not fast enough to be of any importance and above 350 °C the solid will be locally already transformed into char. The maximum release rate of pyrolysis products is at about 248 °C. Of course, this maximum is dependent on the parameters in the Arrhenius equation, but also on the way of heating and on the thermal properties. If, under some conditions, the material is kept for a very long time at a low temperature, say 150 °C, eventually all material will pyrolyse at that temperature. With the Arrhenius description, even at room temperature the material is still decomposing, only it takes very long times to be noticeable (e.g. $\dot{m}'''_{pyr} = 2.5\,10^{-10}$ kg/m^3.s at room temperature).

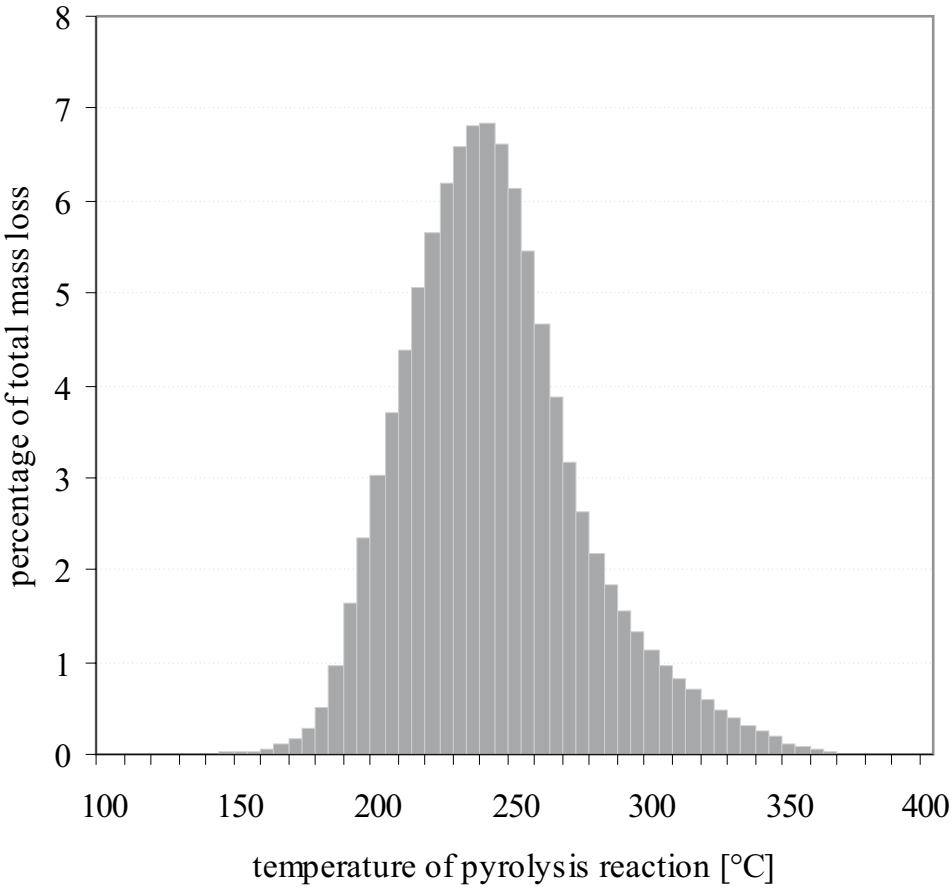

Figure 4.12: Temperature distribution of production of pyrolysis gases

4.6 The two and three-dimensional model

In the one-dimensional model it is assumed that the conduction perpendicular to the fluid/solid interface is predominant to the conduction in the direction of the interface. The solid is only influenced by the incident heat flux at its boundaries, and not by the solid laying above or under it (in the vertical situation of Figure 4.1).

In the two-dimensional model, conduction of heat perpendicular and parallel to the surface is allowed. The pyrolysis gases still flow perpendicular to the solid/fluid interface and therefore they will not be influenced by the extra dimension, see Figure 4.13. Hence, only in the discretized energy equation appears an extra conduction term.

Again, after some modifications Equation 4.31 becomes:

$$T_i^{m+1} = T_i^m + \frac{c_{relax}}{\Theta}\left[\left((\rho cT)_i^n - (\rho cT)_i^m\right)\frac{\Delta V}{\Delta t} + \theta \cdot RHS_i^m + (1-\theta)\cdot RHS_i^n\right] \quad (4.33)$$

with

$$\begin{aligned} RHS = {} & (\dot{m}''_{pyr}c)^m_{i+1/2}T^m_{i+1/2}\Delta A_x - (\dot{m}''_{pyr}c)^m_{i-1/2}T^m_{i-1/2}\Delta A_x \\ + {} & \lambda^m_{i+1/2}\frac{T^{m+1}_{i+1}-T^m_i}{\Delta x}\Delta A_x - \lambda^m_{i-1/2}\frac{T^{m+1}_i - T^m_{i-1}}{\Delta x}\Delta A_x \\ + {} & \lambda^m_{j+1/2}\frac{T^{m+1}_{j+1}-T^m_j}{\Delta y}\Delta A_y - \lambda^m_{j-1/2}\frac{T^{m+1}_j - T^m_{j-1}}{\Delta y}\Delta A_y \\ & + Q_{pyr}\dot{m}'''_{pyr}\Delta V + Q_{boundary} \end{aligned}$$

$$\begin{aligned} \Theta = {} & (\rho c)^m_i\frac{\Delta V}{\Delta t} + \theta\Big[(\dot{m}''_{pyr}c)^m_{i-1/2}\Delta A_x + \\ & \frac{\Delta A_x}{\Delta x}\left(\lambda^m_{i+1/2}+\lambda^m_{i-1/2}\right) + \frac{\Delta A_y}{\Delta y}\left(\lambda^m_{j+1/2}+\lambda^m_{j-1/2}\right) + Q'_{boundary}\Big] \end{aligned}$$

The solution procedure is similar to the one-dimensional case. Only the iterative loop for solving the mass and energy equation is a little different, as the loop has to be expanded to two dimensions. A lexicographic ordering is used, where dependent on the iteration number the loop through the cell will be one of the patrons as in Figure 4.14. The solution procedure is the same as for the one-dimensional model.

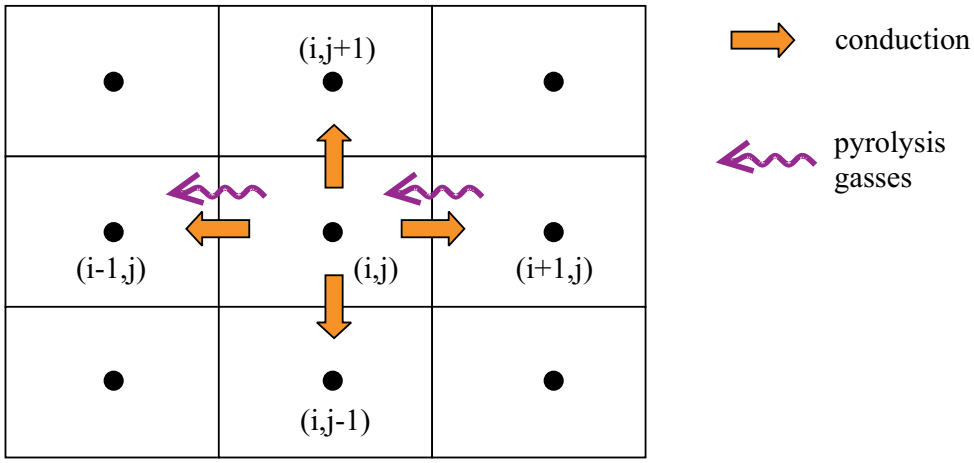

Figure 4.13: Energy fluxes in two-dimensional model

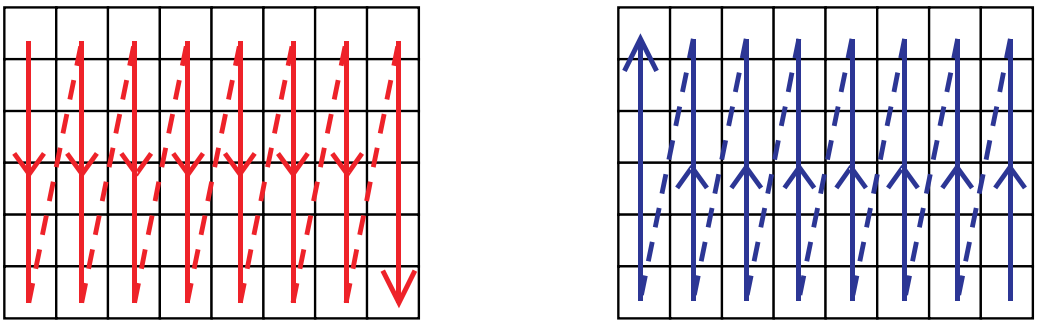

Figure 4.14: Lexicographic ordering

If the cell size in the direction of the gas/solid interface has to be of the same size as perpendicular to the surface, it will be difficult to use this model for two and three-dimensional problems because a very large number of cells will be needed. For example for a solid of 3 cm thick, 30 cm wide and 30 cm high at least $200 \times 2000 \times 2000 = 8\ 10^8$ cells are needed. This is from practical considerations - computer power - unacceptable.

Therefore, the question arises whether the cell size in the direction of the fire spread, i.e. parallel to the surface can be increased. This depends on the variation of the incident heat flux on the surface. To examine this the net incident heat flux from a real solid flame and the speed of the spreading of the flame over the solid surface is required. This will be examined in Chapter 10. In that chapter the two-dimensional solid reaction model based on Arrhenius law will be coupled to a simple empirical gas phase model. In this way a realistic variation of the boundary condition with time, caused by the spreading of the flame in the gas phase, can be modelled. The size of the cells in the direction of the solid/gas interface is examined, as well as the difference of one and two-dimensional simulations.

4.7 Improved pyrolysis production calculation?

Instead of calculating the pyrolysis production for one cell with only one temperature, an attempt has been made to integrate the pyrolysis production over the depth of the solid using an interpolated temperature profile. This idea was thought to be successful because the temperature distribution is rather good predicted by a coarse grid. With a temperature interpolation and with an integration of the mass release rate of pyrolysis gases, results without oscillations were expected. Calculation can then be done on a coarse grid which should be much faster. For the calculation of the temperature and the char volume fraction a coarse, fast mesh is used. For the calculation of the volume pyrolysis production a fine grid is used, as shown in Figure 4.15. The calculation of the total mass of pyrolysis product is given by:

$$\begin{aligned} \int_{\Delta x_i} \dot{m}'''_{pyr} \mathrm{d}x &= \int_{\Delta x_i} A \frac{\rho_v}{\rho_v - \rho_c} (1 - \xi_i) \exp\left(-\frac{E_a}{RT_i}\right) \mathrm{d}x \\ &\approx \sum_{i,j} A \frac{\rho_v}{\rho_v - \rho_c} (1 - \xi_{i,j}) \exp\left(-\frac{E_a}{RT_{i,j}}\right) \Delta x_{i,j} \end{aligned} \tag{4.34}$$

Herein are the variables $\xi_{i,j}$ and $T_{i,j}$ the interpolated values of the char volume fraction and temperature respectively; the index j is the loop in the subdivision of the original mesh.

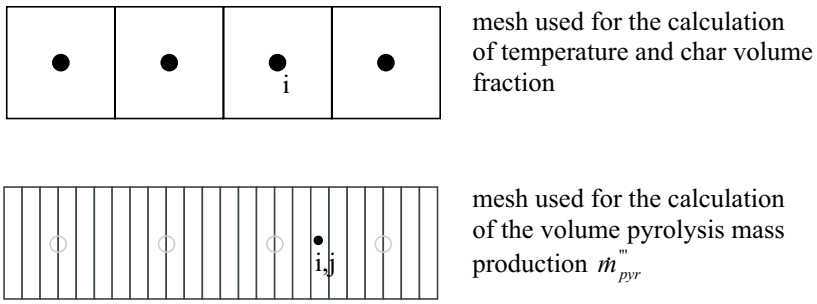

Figure 4.15: Fine and coarse grid for calculation of production of pyrolysis gases

Linear and tangent hyperbolic interpolation schemes have been used for a fine representation of the char volume fraction, while for the temperature always a linear interpolation scheme was used. Neither of these schemes was successful. A quadratic or higher order interpolation is not thought to improve the results.

The interpolation/integration approach for $\dot{m}''_{pyr}$ must be stopped (set to zero) as the char volume fraction in the normal grid reaches the value 1. This is needed to satisfy mass conservation. When we interpolate the char volume fraction, we see that when $\xi_i = 1$ and $\xi_{i+1} < 1$, and linear interpolation is used, there is a part of the local pyrolysis reactions in cell i. A part of the cell would release pyrolysis gases (in the subgrid), though this is prohibited because in the coarse grid $\xi_i = 1$, and there is no more virgin material to pyrolyse. The problem is caused by wrong front modelling. The dips in the surface mass release rate $\dot{m}''_{pyr}$ are created at the locations where $\xi_i = 1$ but $\xi_{i,j} < 1$.

In Chapter 8 this idea is resumed and with succes. The main difference is that in Chapter 8 a dual mesh is used: a coarse grid for the temperature and a fine grid for the char fraction [125]. The calculation of the char fraction in the fine grid is now fully decoupled of the coarse grid. No limitations such as $\xi_i = 1$ are required then.

4.8 Applications

Of course, the model can be used for fully coupled simulation with a CFD code. The CFD code calculates the conditions in the fluid phase and determines the incident heat flux on the solid model. With this incident heat flux the solid reaction model calculates a new surface temperature and the mass

flux of pyrolysis gases. The results are used as boundary conditions in the fluid model. In short, the CFD code will calculate the flame and incident heat flux on the solid surface, while the solid model calculates the surface temperature and the heat or chemical source terms for the fluid phase. This solid reaction model can of course also be coupled to several other gas phase models that are based for example on correlations and empirical formulas.

Different variable boundary conditions can be examined and simulated. A database with the rate of mass release of pyrolysis gases can be developed, similar as is done with Cone Calorimeter results (see Section 3.2.3 in Chapter 3). The database can be used to give the surface temperature and the amount of pyrolysis gases released during a CFD simulation, without the need to simulate the full solid phase during the simulation. The instantaneous incident heat flux and its history could be used for classification.

The solid reaction model can be used to predict ignition times of solid materials. A fluid model can be coupled with the solid model and dependent on the ignition criteria, the ignition time can be calculated. If the temperature or minimum amount of pyrolysis gases is used, no fluid model is necessary. The induction time in the fluid is then neglected. The extra effort of calculating the pyrolysis reactions is, in this application, not always required. A simple conduction model without the modelling of the pyrolysis reactions, will give similar results because pyrolysis reactions are weak before ignition.

The current model is not immediately applicable or extendable to non-charring materials. For non-charring materials there is no char layer and therefore the thermal parameters can not be calculated. In the non-charring models the thermal characteristics remain those of the virgin material and there is no transition into char. The thickness of the solid changes with time and this feature is not present in the model.

4.9 Further improvements

Numerical improvement can be obtained by an adaptive mesh. The pyrolysis zone is represented with a fine mesh, while the char and virgin zones can be represented by a coarse mesh. The number of meshes could for the present case be reduced by a factor of about four when only the pyrolysis front is refined.

Further physical improvements to the Arrhenius law model could include:

- A description of the gas flow instead of assuming that the gases flow immediately out of the solid. This can be useful when thick materials are pyrolyzed. In this work though, only thin solids are considered

where one direction, the thickness, is a lot smaller compared with the length and the width of the surface.

- In-depth absorption of radiation with the law of Beer;
- Char oxidation;
- Material deformation, swelling, delamination, ...;
- ...

Because this solid combustion model is more fundamental than the solid combustion models in the following chapters, this model is more suitable to "add-on" extra physical detail.

4.10 Conclusion

In this chapter a solid reaction model based on the Arrhenius law was developed and tested. Typical cell and time step sizes were determined. Oscillations in the mass flux of pyrolysis gases for large cell size were explained.

This model can be used to predict flame spread in several ways. It can be coupled with a CFD code (fully modelling of gas phase) or with a simplified gas phase model based on correlations.

The input parameters for this model are the conduction coefficient, the heat capacity, and the density for both virgin and char material, the heat of pyrolysis and the two Arrhenius constants (A and E_a).

Chapter 5

Reaction of solid material: "Integral model"

The integral method, which uses a prescribed variable profile, was first used by von Karman and Pohlhausen [49] to solve approximately boundary layer momentum and energy equations. The method, however, is equally attractive for solving any problem governed by a diffusion type equation, such as unsteady heat conduction problems in solids.

Here the technique will be used to predict the reaction of a solid to an incident heat flux, as was done by Moghtaderi *et al.* [77] and Spearpoint and Quintiere [108, 109, 110]. The influence of the temperature on the rate of pyrolysis can be described by an Arrhenius equation, as was done in Chapter 4. For most materials though, the activation energy is so high that they start to pyrolyse only when they reach their so-called pyrolysis temperature. In this model, below this temperature no pyrolysis reactions are possible, while once the pyrolysis temperature has been attained, the heat absorbing pyrolysis reactions will proceed at a rate that keeps the local temperature constant. Only when locally all the material has been pyrolyzed the temperature can rise again. Therefore in the "Integral model" the pyrolysis front is reduced to a single surface, where the pyrolysis reaction will proceed at infinite rate.

In the "Integral model" a certain temperature profile is proposed (e.g. quadratic). With the conservation equations and the boundary conditions the unknown coefficients of the profile can be determined.

5.1 Phases

The sequence of events occurring in a solid when it is exposed to a fire environment can be divided into different phases [77]. Before the surface

temperature has reached the pyrolysis temperature, the solid exists entirely of virgin material. No pyrolysis reactions are present, and the solid is in the heating phase. As soon as the surface temperature has reached the pyrolysis temperature the solid enters the pyrolysis phase. Dependent on the location of the "heat wave"[1] in the virgin layer, three different phases can be defined:

1. the heating phase or "inert heating" with solid treated as semi-infinite;
2. the pyrolysis phase with the solid treated as semi-infinite;
3. the pyrolysis phase with the solid treated as finite;

or

1. the heating phase or "inert heating" with solid treated as semi-infinite;
2. the heating phase or "inert heating" with solid treated as finite;
3. the pyrolysis phase with the solid treated as finite.

A final fourth phase can be defined, where the pyrolysis reactions have ended and the char layer is further heated. The two ways of pyrolysis, with the sequence of the different phases is given in Figure 5.1.

In the first phase, the heating phase with the solid treated as semi-infinite, the solid exists entirely of virgin material and the density of the solid is uniform. A part of the incident heat flux is transferred to the interior of the solid by conduction, while the remaining part will be reradiated or convected to the surroundings. In the "Integral model" the temperature profile in the solid is prescribed, e.g. by a linear, quadratic or exponential temperature profile [20]. The temperature rise is confined in a layer with thickness δ, which is called the thermal penetration depth or the thermal layer. The location where $x = \delta$ corresponds with the "thermal front" or "heat wave". The ratio of the thermal penetration depth δ to the thickness of the material L determines whether the solid acts as thermally thick ($\delta < L$), intermediate ($\delta \approx L$) or thermally thin ($\delta > L$). Although, for thermally thin materials a thermal penetration depth can not longer be defined. As heating continues there are two possibilities: or the surface temperature reaches the pyrolysis temperature, or the thermal wave hits the rear surface of the solid ($\delta = L$). If pyrolysis starts before the wave front hits the rear surface, the pyrolysis phase is treated as semi-infinite. When during the semi-infinite pyrolysis phase the heat wave hits the rear surface, the finite pyrolysis phase commences. The

[1] heat wave = location where the influence of the incident heat flux is felt $\Rightarrow$ the temperature starts to rise; before the temperature was still equal to the initial temperature.

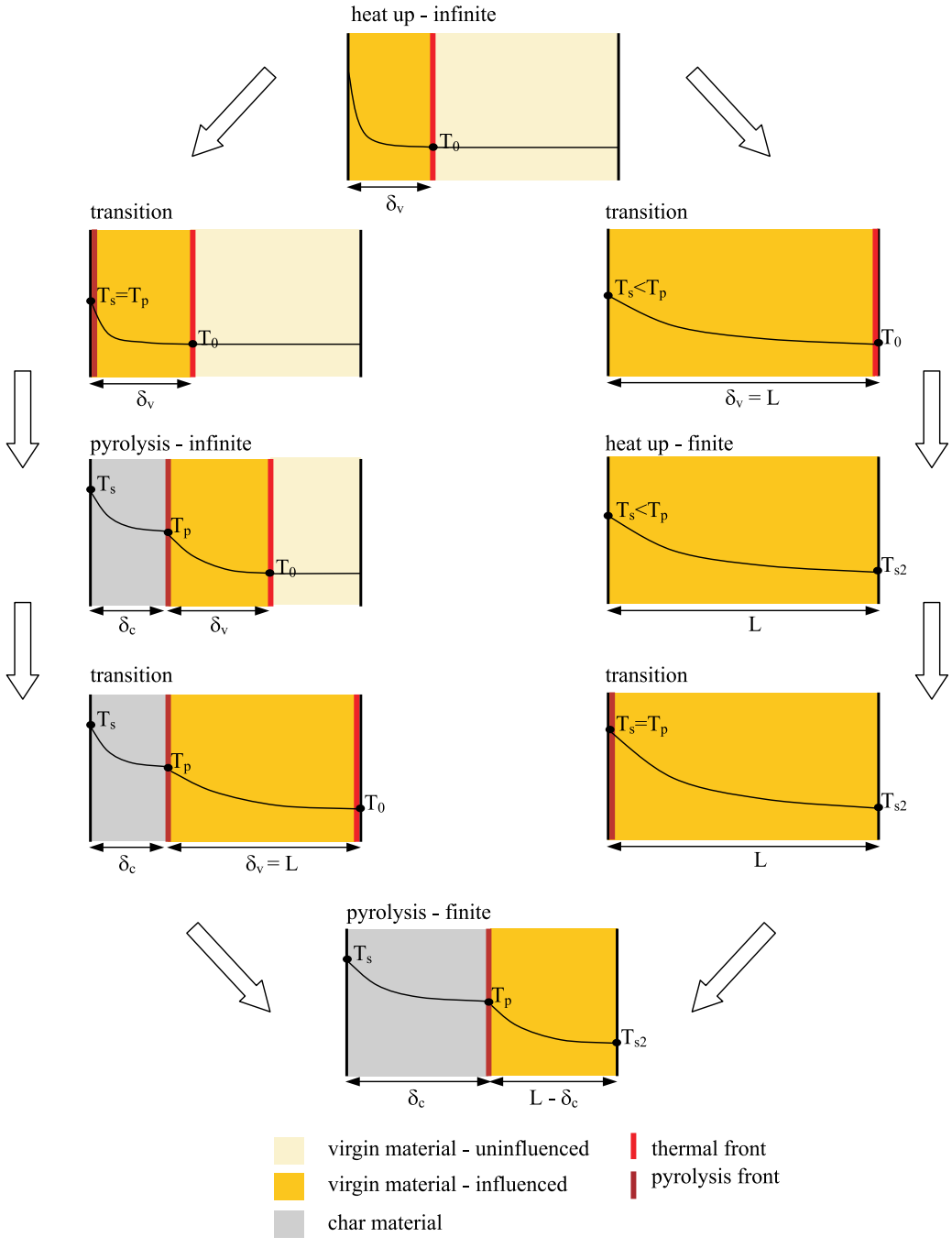

Figure 5.1: Stages in pyrolysis process

temperature is now affected by the boundary conditions on the front and rear surface.

It is of course also possible that the wave front already hits the rear surface before the surface temperature reaches the pyrolysis temperature. The heating phase where the solid is treated as semi-infinite, transforms then into finite. Eventually this heating phase will be succeeded by the finite pyrolysis phase.

Is it possible to extend the "Integral model" with a cooling phase. When the heat flux to the pyrolysis front is insufficient to keep it at the pyrolysis temperature, the pyrolysis reaction will stop. For that phase, the location of the front (no longer a pyrolysis front but rather an interface char/virgin) is fixed and its temperature is variable and of course below the pyrolysis temperature.

5.2 Fundamental model equations

Originally the integral method was developed for the heating of semi-infinite materials. For this case there are three boundary conditions to obtain the unknown coefficients of the temperature profile: one for the boundary conditions at $x = 0$ (incident heat flux) and two for the boundary conditions at the thermal wave front at $x = d$ (the temperature must be equal to the initial temperature T_0 and the heat transfer at the end of the thermal penetration zone is zero). These conditions are called the *natural conditions*. When for instance a quadratic temperature profile is proposed, there are enough conditions to determine the unknown coefficients of the temperature profile. If a higher order polynomial is proposed for the temperature profile, there are insufficient equations to determine all the unknown coefficients. Additional derived boundary conditions can be imposed by assuming that the higher derivatives are zero at the end of the thermal penetration zone ($x = \delta$). These assumptions are called the *smoothing* or *derived conditions*. They make the assumed profile to go smoothly into the undisturbed initial temperature at $x = \delta$ and provide enough conditions to determine the coefficients of the temperature profile [98, 49].

In the following, the model equations for the different phases will be derived. They consist of:

1. heat up phase – semi-infinite;

2. heat up phase – finite;

3. pyrolysis phase – semi-infinite;

4. pyrolysis phase – finite.

The equations are all one-dimensional. The temperature profiles in the figures are illustrative and not based on any calculations. The equations are based on work by Spearpoint [108] and Moghtaderi [77].

For the char layer and the virgin material a temperature profile is prescribed, e.g. a quadratic polynomial with dependent x, the depth in the solid. The char layer is confined by the front surface and the pyrolysis front. The virgin layer is confined by the pyrolysis front and the thermal front. The rest of the virgin material (i.e. $\delta_v + \delta_c < x < L$) is unaltered and thus still on initial temperature. The coefficients in the temperature profile are unknown and vary with time. They can be determined with the conservation equations of mass and energy that are integrated over the different zones together with the application of the boundary conditions.

5.2.1 Conservation equations on a moving volume

Consider a moving volume V with surface S such as drawn in Figure 5.2

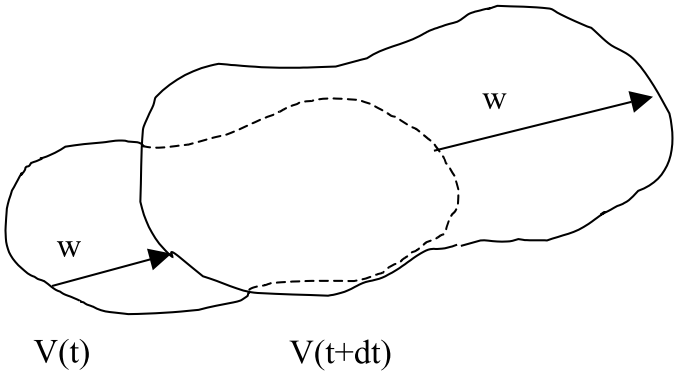

Figure 5.2: Moving control volume

The velocity of the control volume w is variable along the surface S. After a time dt the volume $V(t)$ has transformed into $V(t + dt)$, which may be larger, equal or smaller than the original volume.

The conservation equation for mass on the moving volume V can be written as [63]:

$$\frac{\mathrm{d}}{\mathrm{d}t}\int_V \rho \,\mathrm{d}V + \int_S \rho(\mathbf{v} - \mathbf{w}) \cdot \mathrm{d}\mathbf{S} = 0 \tag{5.1}$$

For solid material where the density is constant and where there is no material flowing out of the control volume, the left hand side is identically zero. It is trivial that the conservation of mass in a solid does not provide a new useful equation.

The conservation equation for energy on the moving volume V can be written as [63]:

$$\frac{\mathrm{d}}{\mathrm{d}t}\int_V \rho E \,\mathrm{d}V + \int_S \rho E(\mathbf{v}-\mathbf{w})\cdot\mathrm{d}\mathbf{S} = \int_V \dot{q}'''\mathrm{d}V - \int_S \dot{\mathbf{q}}''\cdot\mathrm{d}\mathbf{S} - \int_S p\mathbf{v}\cdot\mathrm{d}\mathbf{S} + \Phi \quad (5.2)$$

The first term in the LHS represents the rate of change of the internal energy, the second term in the LHS the energy transfer over the moving boundaries. The first term in the RHS represents the energy production in the volume, the second term the energy transfer by conduction, and the last two terms the pressure work and the viscous dissipation.

The kinetic and potential energy can be neglected so that:

$$E = u + E_{kin} + E_{pot} \approx u$$

When the pressure work and the viscous dissipation are neglected [108], Equation 5.2 can be written as:

$$\frac{\mathrm{d}}{\mathrm{d}t}\int_V \rho u \mathrm{d}V + \int_S \rho u(\mathbf{v}-\mathbf{w})\cdot\mathrm{d}\mathbf{S} = -\int_S \dot{\mathbf{q}}''\cdot\mathrm{d}\mathbf{S} \quad (5.3)$$

5.2.2 Heat up phase - semi-infinite model

In the semi-infinite model the heat wave ($x = d$) has not yet reached the rear surface. The different parameters for the heat-up phase are given in Figure 5.3. A control volume is drawn in Figure 5.3 with the dashed line. The front surface at the interface solid/fluid is fixed, while the thermal front ($x = \delta_v$) moves with a velocity w_{heat} which is given by:

$$w_{heat} = \frac{\mathrm{d}\delta_v}{\mathrm{d}t} \quad (5.4)$$

If we assume that $u = c \cdot T$, the specific heat capacity and density constant, then Equation 5.3 for the one-dimensional case becomes:

$$\frac{\mathrm{d}}{\mathrm{d}t}\int_0^{\delta_v} \rho_v c_v T \,\mathrm{d}x - \rho_v c_v T_0 \frac{\mathrm{d}\delta_v}{\mathrm{d}t} = \dot{q}''_{net} - 0 \quad (5.5)$$

With the Leibnitz formula for differentiating an integral, we find the *heat-balance integral* or *energy integral equation* [49]:

$$\rho_v c_v \frac{\mathrm{d}}{\mathrm{d}t}\int_0^{\delta_v} (T - T_0)\,\mathrm{d}x = \dot{q}''_{net} \quad (5.6)$$

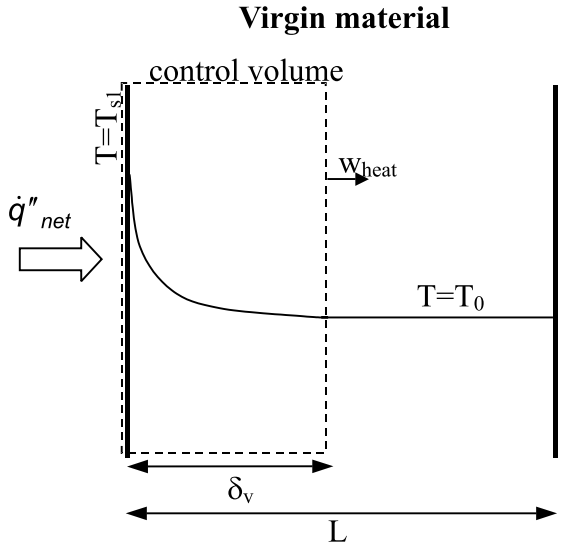

Figure 5.3: Control volume for heat up phase (semi-infinite)

With a new variable, the integrated temperature θ_{heat}:

$$\theta_{heat} = \int_0^{\delta_v} (T - T_0)\,\mathrm{d}x \tag{5.7}$$

the energy integral can be written as:

$$\frac{\mathrm{d}\theta_{heat}}{\mathrm{d}t} = \frac{\dot{q}''_{net}}{\rho_v c_v} \tag{5.8}$$

The net incident energy flux consists of an external heat flux, a convective and a radiative heat loss:

$$\dot{q}''_{net} = \dot{q}''_{ext} - h(T_{s1} - T_0) - \epsilon\sigma(T_{s1}^4 - T_\infty^4) \tag{5.9}$$

In the work of Moghtaderi [77] the external heat flux is constant in time and the convective and radiative heat flux are lumped together in an equivalent heat transfer coefficient, and hence

$$\dot{q}''_{net} = \dot{q}''_{ext} - h(T_s - T_\infty) - \epsilon\sigma(T_s^4 - T_\infty^4) = \dot{q}''_{ext} - h_{eq}(T_s - T_\infty) \tag{5.10}$$

Notice that the external heat flux is totally absorbed by the solid. The net heat flux would be more correct when the external heat flux is multiplied by the absorptivity of the solid surface. As this model will be compared with

results from Moghtaderi [77], the same expression for the net heat flux is used. As most of the time the emissivity is unity or nearly unity the error is not too large.

The emissivity will change during heating. Initially we have the value of the virgin material, but due to the thermal exposure the surface will darken and char will be formed. A value of one is a good assumption. The law of Kirchoff (emissivity equals absorptivity) is valid for most materials and temperature intervals [108].

The natural boundary conditions for the problem are given by the heat flux at the boundaries and the temperature at the thermal front:

$$\begin{cases} -\lambda_v \left(\frac{\mathrm{d}T}{\mathrm{d}x}\right)_{x=0} &= \dot{q}''_{net} \\ \lambda_v \left(\frac{\mathrm{d}T}{\mathrm{d}x}\right)_{x=\delta} &= 0 \\ \left(T\right)_{x=\delta} &= T_0 \end{cases} \tag{5.11}$$

5.2.3 Heat up phase - finite model

In the finite model the thermal front ($x = \delta$) has reached the rear surface. The different parameters for the heat-up phase where the model must be treated as a finite solid, are given in Figure 5.4. Since δ_v is no longer a

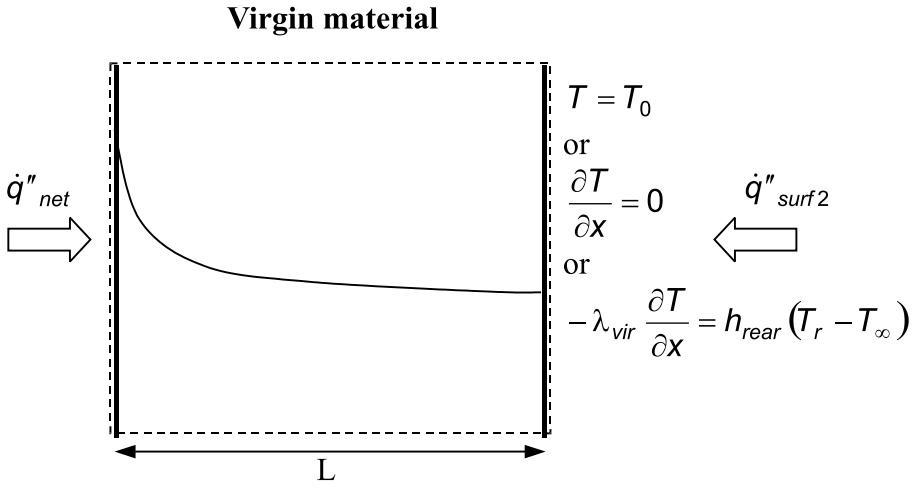

Figure 5.4: Control volume for heat up phase (finite)

dependent variable, only the coefficients of the quadratic temperature profile are unknown. There are now three equation to determine these unknowns: two natural boundary conditions (instead of three in the semi-infinite case)

and the energy equation. The boundary condition for the front surface (left surface in Figure 5.4) is:

$$-\lambda_v \left(\frac{\mathrm{d}T}{\mathrm{d}x}\right)_{x=0} = \dot{q}''_{net} \tag{5.12}$$

For the rear surface the equation is dependent on the boundary condition chosen. If the rear temperature is constant then:

$$\big(T\big)_{x=L} = T_0 \tag{5.13}$$

If the rear surface is perfectly insulated then:

$$-\lambda_v \left(\frac{\mathrm{d}T}{\mathrm{d}x}\right)_{x=L} = 0 \tag{5.14}$$

If convection is assumed at the rear surface then:

$$-\lambda_v \left(\frac{\mathrm{d}T}{\mathrm{d}x}\right)_{x=L} = \dot{q}''_{rear} = h_{rear}(T_\infty - T_{s2}) \tag{5.15}$$

The energy equation is given by:

$$\rho_v c_v \frac{\mathrm{d}}{\mathrm{d}t} \int_0^L T \,\mathrm{d}x = \dot{q}''_{net} + \dot{q}''_{rear} \tag{5.16}$$

As the integration is done over a constant interval (0 to L), this can be written as:

$$\rho_v c_v \frac{\mathrm{d}}{\mathrm{d}t} \int_0^L (T - T_0) \,\mathrm{d}x = \dot{q}''_{net} + \dot{q}''_{rear} \tag{5.17}$$

Or with the integrated temperature:

$$\frac{\mathrm{d}\theta_{heat}}{\mathrm{d}t} = \frac{1}{\rho_c c_v}(\dot{q}''_{net} + \dot{q}''_{rear}) \tag{5.18}$$

5.2.4 Pyrolysis phase - semi-infinite model

When pyrolysis reactions are occurring, we divide the solid into three zones: the char layer, the pyrolysis front and the virgin material layer. For the semi-infinite model the thermal front has not yet reached the rear surface, so we can further subdivide the virgin zone in a heated zone and an unheated zone, still at initial temperature. The different parameters for the pyrolysis phase where the model can be treated as a semi-infinite solid, are given in Figure 5.5. In the general equation for conservation of mass (Equation 5.1) and energy (Equation 5.3) the boundary velocity is $\mathbf{w_{pyr}} = \mathrm{d}\delta_c/\mathrm{d}t$ at the pyrolysis front; and $\mathbf{w_{heat}} = (\mathrm{d}\delta_v + \mathrm{d}\delta_c)/\mathrm{d}t$ at the thermal front.

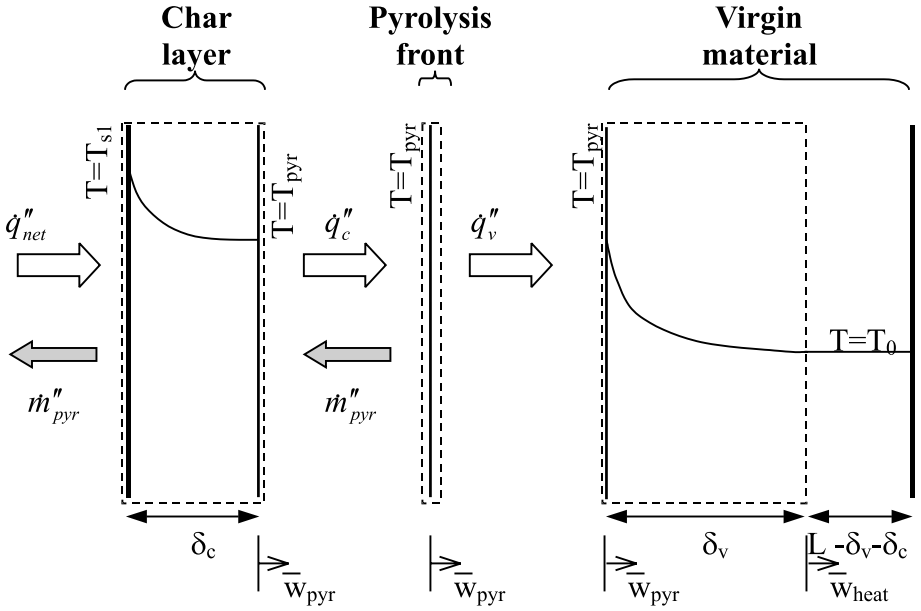

Figure 5.5: Control volume for burning model (infinite pyrolysis model)

5.2.4.1 Char layer

Conservation of mass: The char layer exists of char and volatiles. It is assumed that there is no accumulation of volatiles in the solid. The integral in the mass conservation equation is taken over the char layer, hence:

$$\frac{\mathrm{d}}{\mathrm{d}t}\int_0^{\delta_c}(\rho_{pyr}+\rho_v)\,\mathrm{d}x+\rho_{pyr}\left(\left(v_{pyr}\right)-\left(v_{pyr}+\frac{\mathrm{d}\delta_c}{\mathrm{d}t}\right)\right)+\rho_c\left(\left(0\right)-\left(0+\frac{\mathrm{d}\delta_c}{\mathrm{d}t}\right)\right)=0 \tag{5.19}$$

As the density of the char material and the pyrolysis gases are assumed constant, and there is no accumulation of gases in the solid, Equation 5.19 is always fulfilled. The mass flux at the front surface is given by:

$$\dot{m}''_{pyr}=\rho_{pyr}v_{pyr} \tag{5.20}$$

As there is no accumulation of volatiles, the density $\rho_{pyr}=0$. As the volatiles flow immediately out of the solid, the velocity $v_{pyr}=\infty$, but the product $\rho_{pyr}\cdot v_{pyr}\neq 0$ and is finite.

Conservation of energy: With Equation 5.20 the general form of conservation of energy, Equation 5.3, can be written for the char layer as:

$$\begin{aligned} \frac{\mathrm{d}}{\mathrm{d}t}\int_0^{\delta_c}\Big(\rho_{pyr}u_{pyr}(T)+\rho_c u_c(T)\Big)\mathrm{d}x \quad &+ \quad \dot{m}''_{pyr}h_{pyr}(T_s)-\dot{m}''_{pyr}h_{pyr}(T_{pyr}) \\ + \quad \Big(\rho_{pyr}u_{pyr}(T_{pyr})+\rho_c u_c(T_{pyr})\Big)\Big(-\frac{\mathrm{d}\delta_c}{\mathrm{d}t}\Big) \quad &= \quad \dot{q}''_{net}-\dot{q}''_c \end{aligned} \tag{5.21}$$

The pressure and the viscous dissipation terms for the pyrolysis gases have been neglected (see [108]). The heating of the pyrolysis gases in the char layer will at first not be taken into account as was done by Moghtaderi [77]. In other words the gases leave the solid at the same temperature as they have entered the char layer. Later on, the heating of the gases is included. When there is no heating of the pyrolysis gases in the solid:

$$\rho_c c_c \frac{\mathrm{d}}{\mathrm{d}t}\int_0^{\delta_c}(T-T_{pyr})\,\mathrm{d}x = \dot{q}''_{net}-\dot{q}''_c \tag{5.22}$$

In the pyrolysis phase the integrated temperatures θ_c and θ_v are defined as:

$$\begin{cases} \theta_c &= \int_0^{\delta_c}(T-T_{pyr})\,\mathrm{d}x \\ \theta_v &= \int_{\delta_v}^{\delta_v+\delta_c}(T-T_{pyr})\,\mathrm{d}x \end{cases} \tag{5.23}$$

The relation between the integrated temperature during pyrolysis and heat-up phase is given by:

$$\theta_v = \theta_{heat}-\delta_v\cdot(T_{pyr}-T_0) \tag{5.24}$$

where δ_v is taken at the transition from heat-up to pyrolysis phase. Hence the energy integral for the char layer, Equation 5.22 becomes:

$$\frac{\mathrm{d}\theta_c}{\mathrm{d}t} = \frac{1}{\rho_c c_c}\cdot(\dot{q}''_{net}-\dot{q}''_c) \tag{5.25}$$

The natural boundary conditions for the char layer are:

$$\begin{cases} -\lambda_c\left(\frac{\mathrm{d}T}{\mathrm{d}x}\right)_{x=0} &= \dot{q}''_{net} \\ -\lambda_c\left(\frac{\mathrm{d}T}{\mathrm{d}x}\right)_{x=\delta_c} &= \dot{q}''_c \\ \big(T\big)_{x=\delta_c} &= T_{pyr} \end{cases} \tag{5.26}$$

5.2.4.2 Pyrolysis front

For the pyrolysis front the volume is theoretically zero, but still the conservation equations apply.

Conservation of mass: The conservation of mass on the pyrolysis front control volumes gives:

$$\rho_{pyr} \cdot \left(v_{pyr} + \frac{\mathrm{d}\delta_c}{\mathrm{d}t} \right) - \rho_c \cdot \left(0 - \frac{\mathrm{d}\delta_c}{\mathrm{d}t} \right) + \rho_v \cdot \left(0 - \frac{\mathrm{d}\delta_c}{\mathrm{d}t} \right) = 0 \tag{5.27}$$

In the first term only $\rho_{pyr} \cdot v_{pyr} \neq 0$ should be considered, because no volatiles are stored in the char layer. Or by assuming the density of the pyrolysis gases small compared with the density of the char and virgin material, this can be written as:

$$(\rho_v - \rho_c) \cdot \frac{\mathrm{d}\delta_c}{\mathrm{d}t} = \dot{m}''_{pyr} \tag{5.28}$$

Conservation of energy: The conservation of energy on the pyrolysis front control volumes gives:

$$\rho_{pyr} \cdot u_{pyr} \cdot \left(v_{pyr} + \frac{\mathrm{d}\delta_c}{\mathrm{d}t} \right) + \rho_c \cdot u_c \cdot \left(0 + \frac{\mathrm{d}\delta_c}{\mathrm{d}t} \right) + \rho_v \cdot u_v \cdot \left(0 - \frac{\mathrm{d}\delta_c}{\mathrm{d}t} \right) = \dot{q}''_c - \dot{q}''_v \tag{5.29}$$

Here again, only the velocity of the volatiles should be considered in the first term. Therefore:

$$\dot{m}''_{pyr} \cdot u_{pyr}(T_{pyr}) + \frac{\mathrm{d}\delta_c}{\mathrm{d}t} \cdot \Big(\rho_c \cdot u_c(T_{pyr}) - \rho_v \cdot u_v(T_{pyr}) \Big) = \dot{q}''_c - \dot{q}''_v \tag{5.30}$$

which can be written as:

$$(\rho_v - \rho_c) \cdot \frac{\mathrm{d}\delta_c}{\mathrm{d}t} \cdot \Delta Q_{pyr}(T_{pyr}) = \dot{q}''_c - \dot{q}''_v \tag{5.31}$$

Here is ΔQ_{pyr} the heat of pyrolysis or the heat of vaporisation.

$$\Delta Q_{pyr} = u_{pyr}(T_{pyr}) + \frac{\rho_c \cdot u_c(T_{pyr}) - \rho_v \cdot u_v(T_{pyr})}{\rho_v - \rho_c} \tag{5.32}$$

With Equation 5.28, the following equation is obtained:

$$\dot{m}''_{pyr} \cdot \Delta Q_{pyr}(T_{pyr}) = \dot{q}''_c - \dot{q}''_v \tag{5.33}$$

If the equations of conservation of energy for the char, virgin and pyrolysis front are added, they will give the conservation of energy over the whole solid.

There exist models where the heat of pyrolysis is written per kilogram virgin material. In literature the heat of pyrolysis is not always clearly defined. It should be defined as the chemical converting energy associated with unit mass of volatile products [125].

5.2.4.3 Virgin material

Conservation of mass: For the virgin material the conservation of mass gives:

$$\frac{\mathrm{d}}{\mathrm{d}t}\int_{\delta_c}^{\delta_c+\delta_v}\rho_v \mathrm{d}x \;-\; \rho_v \cdot \left(0 + \frac{\mathrm{d}\delta_v}{\mathrm{d}t}\right) = 0 \tag{5.34}$$

which gives no extra equation. Trivial, as there is no mass flow in this zone.

Conservation of energy: Application of Equation 5.3 gives:

$$\frac{\mathrm{d}}{\mathrm{d}t}\int_{\delta_c}^{\delta_c+\delta_v}\rho_v u_v(T)\,\mathrm{d}x + \rho_v u_v(T_{pyr})\frac{\mathrm{d}\delta_c}{\mathrm{d}t} - \rho_v u_v(T_0)\frac{\mathrm{d}(\delta_c+\delta_v)}{\mathrm{d}t} = \dot{q}_v'' \tag{5.35}$$

When the specific heat capacity and density are assumed constant:

$$\frac{\mathrm{d}}{\mathrm{d}t}\int_{\delta_c}^{\delta_c+\delta_v}(T-T_{pyr})\,\mathrm{d}x + T_{pyr}\frac{\mathrm{d}\delta_v}{\mathrm{d}t} + T_{pyr}\frac{\mathrm{d}\delta_c}{\mathrm{d}t} - T_0\frac{\mathrm{d}(\delta_c+\delta_v)}{\mathrm{d}t} = \frac{\dot{q}_v''}{\rho_v c_v} \tag{5.36}$$

With the integrated temperature defined in Equation 5.23, this becomes:

$$\frac{\mathrm{d}\theta_v}{\mathrm{d}t} - \left(\frac{\mathrm{d}\delta_v}{\mathrm{d}t} + \frac{\mathrm{d}\delta_c}{\mathrm{d}t}\right)\cdot(T_{pyr}-T_0) = \frac{\dot{q}_v''}{\rho_v c_v} \tag{5.37}$$

The natural boundary conditions for the virgin material layer are:

$$\begin{cases} \left(T\right)_{x=\delta_c} &= T_{pyr} \\ -\lambda_v\left(\frac{\mathrm{d}T}{\mathrm{d}x}\right)_{x=\delta_c} &= \dot{q}_v'' \\ \left(T\right)_{x=\delta_c+\delta_v} &= T_0 \\ -\lambda_v\left(\frac{\mathrm{d}T}{\mathrm{d}x}\right)_{x=\delta_c+\delta_v} &= 0 \end{cases} \tag{5.38}$$

5.2.5 Pyrolysis phase - finite model

When the thermal wave reaches the rear surface of the solid, the finite pyrolysis model must be used. The different parameters are given in Figure 5.6.

For the char layer and the pyrolysis front we have the same equations as for the infinite pyrolysis model. For the virgin material the energy equation is different due to the influence of the rear surface boundary condition.

Conservation of mass: For the virgin material the conservation of mass reduces to the identity:

$$\frac{\mathrm{d}}{\mathrm{d}t}\int_{\delta_c}^{L}\rho_v\,\mathrm{d}x-\rho_v\cdot\left(0+\frac{\mathrm{d}\delta_v}{\mathrm{d}t}\right)=0 \tag{5.39}$$

Conservation of energy: The conservation of energy of Equation 5.3 gives:

$$\frac{\mathrm{d}}{\mathrm{d}t}\int_{\delta_c}^{L}\rho_v c_v T\,\mathrm{d}x-\rho_v c_v T_{pyr}\cdot\left(0+\frac{\mathrm{d}\delta_c}{\mathrm{d}t}\right)=\dot{q}''_v+\dot{q}''_{rear} \tag{5.40}$$

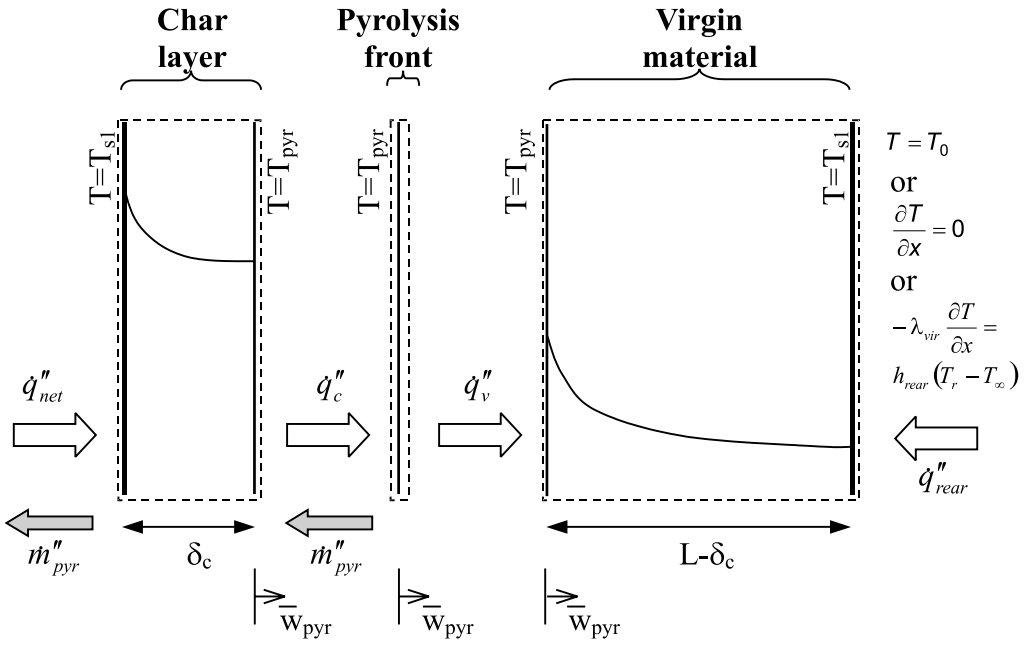

Figure 5.6: Control volume for burning model (finite pyrolysis model)

When a constant density and specific heat capacity are assumed, this can be written as:

$$\frac{\mathrm{d}\theta_v}{\mathrm{d}t} = \frac{1}{\rho_v c_v} \cdot (\dot{q}''_v + \dot{q}''_{rear}) \tag{5.41}$$

The natural boundary conditions for the virgin material layer are:

$$\begin{cases} \left(T\right)_{x=\delta_c} & = & T_{pyr} \\ -\lambda_v \left(\frac{\mathrm{d}T}{\mathrm{d}x}\right)_{x=\delta_c} & = & \dot{q}''_v \\ -\lambda_v \left(\frac{\mathrm{d}T}{\mathrm{d}x}\right)_{x=\delta_c+\delta_v} & = & -\dot{q}''_{rear} \end{cases} \tag{5.42}$$

5.3 Practical model equations

Before a temperature profile can be proposed, it is necessary to examine the natural and smoothing conditions because they will determine the maximum allowable number of unknowns in the profile. For the semi-infinite heat-up phase there are three natural conditions; further smoothing conditions can be supplied by requiring that second and higher order derivatives at the end of the thermal penetration depth are zero. Any order of polynomial for the temperature profile can be proposed, see Appendix C. For the semi-finite heat-up phase we have only two natural conditions: the heat flux at the two surfaces. There is no longer a thermal penetration depth and the smoothing conditions can not be applied. A quadratic temperature profile is the highest order that can be used. In the semi-infinite pyrolysis phase we have for the char layer three natural conditions: two heat fluxes at the char boundaries and the pyrolysis temperature at the end of the char layer. For the virgin material we have four natural conditions: two heat fluxes at the boundaries $(\dot{q}''_v)_{x=\delta_c}$ and $(\dot{q}''_v)_{x=\delta_c+\delta_v} = 0$, and two temperature $(T_v)_{x=\delta_c} = T_{pyr}$ and $(T_v)_{x=\delta_c+\delta_v} = T_0$. Further conditions are $\left(\frac{\mathrm{d}T_c}{\mathrm{d}t}\right)_{x=\delta_c}$ and $\left(\frac{\mathrm{d}T_v}{\mathrm{d}t}\right)_{x=\delta_c} = 0$. For the virgin layer smoothing conditions can be applied at the thermal front. Any order can be used for the temperature profile in the virgin layer. For the char layer only a polynomial of maximum third order is possible. In the finite pyrolysis phase there are three natural conditions for both the virgin and char layer: two heat fluxes at their boundaries and the pyrolysis temperature at the pyrolysis front. For both layers we have $\left(\frac{\mathrm{d}T_c}{\mathrm{d}t}\right)_{x=\delta_c}$ and $\left(\frac{\mathrm{d}T_v}{\mathrm{d}t}\right)_{x=\delta_c} = 0$ so that for both temperature profiles maximum a third order polynomial is possible. Because in the finite heat up phase only a second order polynomial is possible, it is suggested to use a second order temperature profile for all the phases and layers.

5.3.1 Heat up phase - semi-infinite model

When a quadratic profile for the temperature is assumed, three unknown coefficients a_0, a_1 and a_2 are introduced:

$$T(x,t) = a_0(t) + a_1(t) \cdot (\delta_v - x) + a_2(t) \cdot (\delta_v - x)^2 \tag{5.43}$$

The energy integral (Equation 5.8) gives the integrated temperature θ_{heat} from:

$$\frac{\mathrm{d}\theta_{heat}}{\mathrm{d}t} = \frac{\dot{q}''_{net}}{\rho_v c_v} \tag{5.44}$$

with initial condition that $\theta_{heat} = 0$ for $t = 0$.

From the natural boundary conditions (Equation 5.11):

$$\begin{cases} a_0 &= T_0 \\ a_1 &= 0 \\ a_2 &= \dot{q}''_{net}/2\lambda_v\delta_v \end{cases} \tag{5.45}$$

The thermal penetration depth is calculated from the integrated temperature, Equation 5.7, where Equation 5.43 is substituted for the temperature profile:

$$\delta_v = \sqrt{\frac{6 \cdot \lambda_v \cdot \theta_{heat}}{\dot{q}''_{net}}} \tag{5.46}$$

The net incident heat flux is calculated from:

$$\dot{q}''_{net} = \dot{q}''_{ext} - h(T_{s1} - T_\infty) - \epsilon\sigma(T_{s1}^4 - T_\infty^4) \tag{5.47}$$

where T_{s1} is the left surface temperature or $T(x = 0, t)$. These equations are valid until $\delta_v = L$ or $T_{s1} = T_{pyr}$.

It is already clear that the "Integral model" is only valid for heating cases where the temperature profile will resemble a quadratic profile. The model is also not applicable when the net incident heat flux becomes zero.

5.3.2 Heat up phase - finite model

We assume a similar quadratic temperature profile as in the semi-infinite model, only the thermal penetration is replaced by the thickness L of the solid:

$$T(x,t) = a_0(t) + a_1(t) \cdot (L - x) + a_2(t) \cdot (L - x)^2 \tag{5.48}$$

The energy integral (Equation 5.18) gives the integrated temperature θ_{heat} from:

$$\frac{\mathrm{d}\theta_{heat}}{\mathrm{d}t} = \frac{1}{\rho_v c_v}(\dot{q}''_{net} + \dot{q}''_{rear}) \tag{5.49}$$

where the initial condition for θ_{heat} follows from the semi-infinite calculation.

From the natural boundary conditions:

$$\begin{cases} a_0 &= T_0 + \frac{\theta_{heat}}{L} - \frac{L}{6\cdot\lambda_v}(\dot{q}''_{net} - 2\cdot\dot{q}''_{rear}) \\ a_1 &= \frac{\dot{q}''_{rear}}{\lambda_v} \\ a_2 &= \frac{1}{2L\lambda_v}(\dot{q}''_{net} + \dot{q}''_{rear}) \end{cases} \tag{5.50}$$

For this phase there is no need to calculate the thermal penetration depth, as it is not defined. The net incident heat flux is calculated from:

$$\dot{q}''_{net} = \dot{q}''_{ext} - h(T_{s1} - T_\infty) - \epsilon\sigma(T_{s1}^4 - T_\infty^4) \tag{5.51}$$

For the rear surface only a convective boundary is assumed, which gives:

$$\dot{q}''_{rear} = h(T_0 - T_{s2}) \tag{5.52}$$

The heat up phase with the finite model is also valid for the heating of the remaining char layer when the pyrolysis reaction are finished.

5.3.3 Pyrolysis phase - semi-infinite model

The temperature profiles in the char and in the virgin layer will both be described by a quadratic relation:

$$\begin{aligned} T_c &= b_0 + b_1\cdot(\delta_c - x) + b_2\cdot(\delta_c - x)^2 \\ T_v &= c_0 + c_1\cdot(x - \delta_c) + c_2\cdot(x - \delta_c)^2 \end{aligned} \tag{5.53}$$

After some calculation the equation for conservation of energy over the pyrolysis front can be written as:

$$\frac{\mathrm{d}\delta_c}{\mathrm{d}t} = \frac{1}{(\rho_v - \rho_c)\Delta H_{pyr} - \rho_v c_v(T_0 - T_{pyr})}\cdot\left(\dot{q}''_{net} - \rho_c c_c\frac{\mathrm{d}\theta_c}{\mathrm{d}t} + \frac{\rho_v c_v}{2}\cdot\frac{\mathrm{d}\theta_v}{\mathrm{d}t}\right) \tag{5.54}$$

The conservation of energy in the char layer gives:

$$\frac{\mathrm{d}\theta_c}{\mathrm{d}t} = 3\cdot\alpha_c\cdot\left(\frac{1}{2}\cdot\frac{\dot{q}''_{net}}{\lambda_v} - \frac{\theta_c}{\delta_c^2}\right) \tag{5.55}$$

And the conservation of energy in the virgin layer gives:

$$\frac{\mathrm{d}\theta_v}{\mathrm{d}t} = 2 \cdot (T_{pyr} - T_0) \cdot \left(\frac{4}{3} \cdot \frac{\alpha_v}{\theta_v} \cdot (T_{pyr} - T_0) + \frac{\mathrm{d}\theta_c}{\mathrm{d}t} \right) \tag{5.56}$$

Equations 5.54 to 5.56 will give δ_c, θ_c and θ_v. The coefficients in the temperature profiles are calculated with the boundary conditions (Equation 5.26) and the equations for the integrated temperature (Equation 5.23). For the char layer:

$$\begin{cases} b_0 &= T_{pyr} \\ b_1 &= 3 \cdot \frac{\theta_c}{\delta_c^2} - \frac{\dot{q}''_{net}}{2 \cdot \lambda_c} \\ b_2 &= -\frac{3}{2} \cdot \frac{\theta_c}{\delta_c^3} + \frac{3}{4} \cdot \frac{\dot{q}''_{net}}{\delta_c \lambda_c} \end{cases} \tag{5.57}$$

And for the virgin layer:

$$\begin{cases} c_0 &= T_{pyr} \\ c_1 &= 2 \cdot \frac{T_0 - T_{pyr}}{\delta_v} \\ c_2 &= \frac{T_{pyr} - T_0}{\delta_v^2} \end{cases} \tag{5.58}$$

When the coefficients are substituted in the temperature profile, the integrated temperature of the virgin layer gives:

$$\delta_v = \frac{3}{2} \cdot \frac{\theta_v}{T_0 - T_{pyr}} \tag{5.59}$$

The net incident heat flux on the front surface can be modified to include the extra heat flux of a flame:

$$\dot{q}''_{net} = \dot{q}''_{ext} - h(T_{s1} - T_\infty) - \epsilon\sigma(T_{s1}^4 - T_\infty^4) + \dot{q}''_{flame} \tag{5.60}$$

When the pyrolysis gases are heated by the char layer, the net incident heat is subtracted with the sensible heated absorbed by the gases. As the conservation of energy is written out for the whole char zone at once, the heat absorbed by the pyrolysis gases can easily be lumped in the net incident heat.

$$\dot{q}''_{net} = \dot{q}''_{ext} - h(T_{s1} - T_\infty) - \epsilon\sigma(T_{s1}^4 - T_\infty^4) - \dot{m}''_{pyr}(T_{s1} - T_{pyr}) \tag{5.61}$$

The surface temperature is given by

$$T_{s1} = T_c(x = 0) \tag{5.62}$$

From conservation of mass over the pyrolysis zone, the mass flux of pyrolysis gases is given by:

$$\dot{m}''_{pyr} = (\rho_v - \rho_c)\frac{\mathrm{d}\delta_c}{\mathrm{d}t} \tag{5.63}$$

5.3.4 Pyrolysis phase - finite model

The temperature profiles in the char and in the virgin layer will be again described by a quadratic relation:

$$\begin{aligned} T_c &= b_0 + b_1 \cdot (\delta_c - x) + b_2 \cdot (\delta_c - x)^2 \\ T_v &= c_0 + c_1 \cdot (x - \delta_c) + c_2 \cdot (x - \delta_c)^2 \end{aligned} \tag{5.64}$$

After some calculation the equation for conservation of energy over the pyrolysis front can be written as:

$$\frac{\mathrm{d}\delta_c}{\mathrm{d}t} = \frac{1}{(\rho_v - \rho_c)\Delta H_{pyr}} \cdot \left(\dot{q}''_{net} - \rho_c c_c \frac{\mathrm{d}\theta_c}{\mathrm{d}t} - \rho_v c_v \cdot \frac{\mathrm{d}\theta_v}{\mathrm{d}t} + \dot{q}''_{rear} \right) \tag{5.65}$$

The conservation of energy in the char layer gives:

$$\frac{\mathrm{d}\theta_c}{\mathrm{d}t} = 3 \cdot \alpha_c \left(\frac{1}{2} \cdot \frac{\dot{q}''_{net}}{\lambda_c} - \frac{\theta_c}{\delta_c^2} \right) \tag{5.66}$$

And the conservation of energy in the virgin layer gives:

$$\frac{\mathrm{d}\theta_v}{\mathrm{d}t} = 3 \cdot \alpha_v \left(\frac{1}{2} \cdot \frac{\dot{q}''_{rear}}{\lambda_v} - \frac{\theta_v}{\delta^2} \right) \tag{5.67}$$

with $\delta = L - \delta_c$. The coefficients in the temperature profiles are calculated with the boundary conditions and equation for the integrated temperature. For the char layer:

$$\begin{cases} b_0 &= T_{pyr} \\ b_1 &= 3 \cdot \frac{\theta_c}{\delta_c^2} - \frac{\dot{q}''_{net}}{2 \cdot \lambda_c} \\ b_2 &= -\frac{3}{2} \cdot \frac{\theta_c}{\delta_c^3} + \frac{3}{4} \cdot \frac{\dot{q}''_{net}}{\delta_c \lambda_c} \end{cases} \tag{5.68}$$

For the virgin layer:

$$\begin{cases} c_0 &= T_{pyr} \\ c_1 &= 3 \cdot \frac{\theta_v}{\delta^2} - \frac{\dot{q}''_{rear}}{2 \cdot \lambda_v} \\ c_2 &= -\frac{3}{2} \cdot \frac{\theta_v}{\delta^3} + \frac{3}{4} \cdot \frac{\dot{q}''_{rear}}{\delta \lambda_v} \end{cases} \tag{5.69}$$

The net incident heat flux on the left surface is given by:

$$\dot{q}''_{net} = \dot{q}''_{ext} - h(T_{s1} - T_\infty) - \epsilon\sigma(T_{s1}^4 - T_\infty^4) - \dot{m}''_{pyr}(T_{s1} - T_{pyr}) \tag{5.70}$$

while on the right surface flux, only convection is considered:

$$\dot{q}''_{rear} = h(T_\infty - T_{s2}) \tag{5.71}$$

The surface temperatures are given by:

$$\begin{cases} T_{s1} &= T_c(x=0) \\ T_{s2} &= T_v(x=L) \end{cases} \tag{5.72}$$

The mass flux of pyrolysis gases is given by:

$$\dot{m}''_{pyr} = (\rho_v - \rho_c)\frac{\mathrm{d}\delta_c}{\mathrm{d}t} \tag{5.73}$$

When the pyrolysis reactions have finished, and $\delta_c = L$, the remaining char will further heat up. Equations are similar to the finite heat up model for the virgin material. No char oxidation is taken into account.

5.3.5 Heat up phase - composite char/virgin

When the incident heat flux is insufficient to sustain the endothermic pyrolysis reactions a new phase must be introduced: a heat up phase of the composite char/virgin. The pyrolysis front has a temperature lower than the pyrolysis temperature. The char thickness is fixed because pyrolysis reactions have ceased. This phase was not described by Moghtaderi [77] nor by Spearpoint [108].

On first sight it may appear that this special heat up phase of virgin/char will only occur when the net incident heat flux is negative or thus when the solid is cooling down, for example, when the external heat flux disappears. When we look closer to the equations, it becomes clear that even with a positive net incident heat flux the virgin/char heat up phase can appear. When the heat flux from the pyrolysis front to the virgin material is greater than the heat flux from the char layer to the pyrolysis front, the endothermic reaction can no longer proceed. The front has to cool down and its temperature must be lower than the pyrolysis temperature.

As this phase is not probable to occur during vertical flame spread and as there are no experimental results available to validate this phenomenon or phase, the heat up phase for virgin/char (at the same time) is not described here. The finite and semi-infinite heating phases were included in the code and preliminary simulations revealed that a zero net heat flux causes problems for the semi-infinite phase.

5.3.6 Higher order polynomials

Higher order polynomials (e.g. cubic) can be used for the virgin layer. Extra unknown coefficient are introduced, and thus extra equations are required to

solve for these unknowns. For the semi-infinite case, smoothing conditions can be applied, but for the finite case these conditions are no longer available. For the finite model an extra equation can be derived for an isothermal rear surface. The temperature of the rear surface will not change in time, which with the general heat equation, gives that the second derivative must be zero at the rear surface. For an insulated rear surface or a convection boundary it is not possible to generate derived or smoothing boundary conditions. An extra condition is then not available.

5.4 Discretization

As the problem is stiff and singular when pyrolysis starts, an implicit method has been chosen. For the heating phase a second order (Cranck-Nicholson) implicit method is used. For the first time step in the pyrolysis phase a second order method can not be used because the model is singular. At the start of pyrolysis the pyrolysis depth and integrated temperature are non-existent and the char layer must still be created. To circumvent this problem the first step is taken fully implicit, while for the other time steps the Cranck-Nicholson method was used.

The discretized equations are only given for the pyrolysis phase. The equations for the semi infinite pyrolysis phase are:

$$\frac{\delta_c^{m+1} - \delta_c^n}{\Delta t} = \frac{1}{(\rho_v - \rho_c)Q_{pyr} + \rho_v c_v (T_{pyr} - T_0)} \cdot \left[\theta \cdot \dot{q}''^{m+1}_{net} + (1-\theta) \cdot \dot{q}''^{n}_{net} - \rho_c c_c \cdot \frac{\theta_c^{m+1} - \theta_c^n}{\Delta t} + \frac{\rho_c c_v}{2} \cdot \frac{\theta_v^{m+1} - \theta_v^n}{\Delta t} \right] \tag{5.74}$$

$$\frac{\theta_c^{m+1} - \theta_c^n}{\Delta t} = 3 \cdot \alpha_c \cdot \left[\frac{\theta \cdot \dot{q}''^{m+1}_{net} + (1-\theta) \cdot \dot{q}''^{n}_{net}}{2\lambda_c} - \theta \cdot \frac{\theta_c^{m+1}}{(\delta_c^m)^2} - (1-\theta) \cdot \frac{\theta_c^n}{(\delta_c^n)^2} \right] \tag{5.75}$$

$$\begin{aligned}\frac{\theta_v^{m+1}-\theta_v^n}{\Delta t} &= \frac{8}{3}\cdot\alpha_v\cdot(T_{pyr}-T_0)^2\cdot \\ &\left[\theta\cdot\frac{1}{\theta_v^n}+(1-\theta)\cdot\frac{1}{\theta_v^n}+\theta\cdot\left(\frac{1}{\theta_v^n}-\frac{1}{(\theta_v^m)^2}\cdot(\theta_v^{m+1}-\theta_v^n\right)\right] \\ &+2\cdot(T_{pyr}-T_0)\cdot\frac{\delta_c^{m+1}-\delta_c^n}{\Delta t}\end{aligned} \tag{5.76}$$

The first term in the RHS of the θ_v equation is linearized:

$$\frac{1}{\theta_v^{m+1}}\approx\frac{1}{\theta_v^m}+\frac{1}{(\theta_v^m)^2}(\theta_v^{m+1}-\theta_v^m) \tag{5.77}$$

In the second term in the θ_c equation, the δ_c is not linearized; it stays behind one iteration. For a fully implicit method $\theta = 1$, while for the Cranck-Nicholson method $\theta = 1/2$. For the finite pyrolysis phase the discretized equations are given by:

$$\begin{aligned}\frac{\delta_c^{m+1}-\delta_c^n}{\Delta t} = \frac{1}{(\rho_v-\rho_c)Q_{pyr}}\Bigg[&\theta\cdot\dot{q}''^{m+1}_{net}+(1-\theta)\cdot\dot{q}''^{n}_{net} \quad + \\ \theta\cdot\dot{q}''^{m+1}_{rear}+(1-\theta)\cdot\dot{q}''^{n}_{rear} \quad &- \quad \rho_c c_c\frac{\theta_c^{m+1}-\theta_c^n}{\Delta t} \quad + \quad \rho_v c_v\frac{\theta_v^{m+1}-\theta_v^n}{\Delta t}\Bigg]\end{aligned} \tag{5.78}$$

$$\begin{aligned}\frac{\theta_c^{m+1}-\theta_c^n}{\Delta t} &= 3\cdot\alpha_c\cdot\theta\cdot\left(\frac{\dot{q}''^{m+1}_{net}}{2\lambda_c}-\frac{\theta_c^{m+1}}{(\delta_c^m)^2}\right) \\ &+ \quad 3\cdot\alpha_c\cdot(1-\theta)\cdot\left(\frac{\dot{q}''^{n}_{net}}{2\lambda_c}-\frac{\theta_c^{n}}{(\delta_c^n)^2}\right)\end{aligned} \tag{5.79}$$

$$\begin{aligned}\frac{\theta_v^{m+1}-\theta_v^n}{\Delta t} &= 3\cdot\alpha_v\cdot\theta\cdot\left(\frac{\dot{q}''^{m+1}_{rear}}{2\lambda_v}-\frac{\theta_v^{m+1}}{(\delta_v^m)^2}\right) \\ &+ \quad 3\cdot\alpha_v\cdot(1-\theta)\cdot\left(\frac{\dot{q}''^{n}_{rear}}{2\lambda_v}-\frac{\theta_v^{n}}{(\delta_v^n)^2}\right)\end{aligned} \tag{5.80}$$

5.5 Solution of discretized equations

For the heating phases (virgin infinite, virgin finite and char finite) the differential equations are discretized with the Cranck-Nicholson method. A simple

iterative method, pseudo-time stepping, is used to solve the equation. The solution is straightforward and therefore not mentioned here.

In the finite and infinite pyrolysis phase there are three linear algebraic equations. These are solved simultaneously by matrix inversion of a 3×3 matrix. When the equations are solved sequentially, many iterations were needed to converge, most probably due to the cross influence. With the matrix inversion still an iteration loop is present to deal with the update of $\dot{q}''_{net}$ and δ_c^m instead of δ_c^{m+1}.

The initial guess for pyrolysis depth in the first pyrolysis time step is given by:

$$\delta_{guess} = \frac{\dot{q}''_{net}}{(\rho_v - \rho_c)Q_{pyr}} \cdot \frac{\Delta t}{10} \tag{5.81}$$

When the initial guess was poor, sometimes no solution could be obtained for the first pyrolysis step. With the guess from above no problems were encountered.

5.5.1 Time step size

The converged solution is obtained by diminishing the time step until no changes appeared in the results. Following time steps were tested: 0.001, 0.01, 0.1 and 1 s. The largest acceptable time step was 0.1 s. When larger time steps were taken, the start of pyrolysis was delayed, see Figure 5.7. The end of pyrolysis (extinguishment) was predicted well for all time steps. The material properties and boundary conditions that were used for the calculation in Figure 5.7, were the same as in Section 4.4 of Chapter 4.

5.5.2 Convergence criteria

Form the converged solution the convergence criteria in a time step were relaxed. A time step was said to be converged when the change between successive iterations in the integrated temperature was smaller than a fixed percentage of its value. For the pyrolysis phases, convergence was tested on the integrated temperature of the virgin and char material and for the pyrolysis depth. A difference of 10^{-6} percent in succeeding iterations is still acceptable (for the three variables) for the results at the peak of the mass release rate, but not acceptable for the results after that. Dependent on the time step about 50 to 175 iterations per time step were necessary, where the larger values were required at the pyrolysis peak and near the end of pyrolysis (extinguishment).

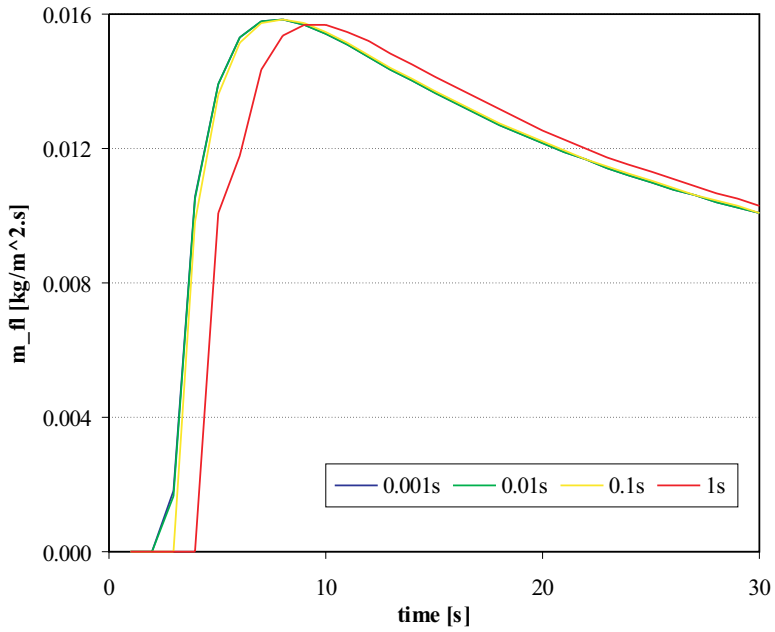

Figure 5.7: Mass flux of pyrolysis gases for different time steps

5.6 Validation of heat up phase

The heat up phase can easily be compared with analytical or numerical results. The finite and infinite heating phases are compared with numerical results for a constant net incident heat flux, as well as for a step function in the heat flux. The last, to simulate the sudden increase of the incident heat flux due to the ignition of the pyrolysis gases in the gas phase.

5.6.1 Constant net incident heat flux

When the net incident heat flux on the surface is constant and when the solid can be treated as semi-infinite, an analytical solution can be obtained [11]. The solution for the surface temperature is given by:

$$T_v(x=0,t) = T_0 + \sqrt{\frac{4}{\pi}} \cdot \frac{\dot{q}''_{net}}{\lambda_v} \cdot \sqrt{\alpha t} \tag{5.82}$$

For these conditions, i.e. constant net incident heat flux and semi-infinite solid, the "Integral model" for the semi-infinite heat-up phase also gives an analytical solution for the surface temperature. Equation 5.44 can be integrated and hence Equation 5.46 gives:

$$\delta_v = \sqrt{6 \cdot \alpha_v \cdot t} \tag{5.83}$$

When this is substituted into the equations for the coefficients of the temperature profile, Equation 5.45, the surface temperature becomes:

$$T_v(x=0,t) = T_0 + \sqrt{\frac{3}{2}} \cdot \frac{\dot{q}''_{net}}{\lambda_v} \cdot \sqrt{\alpha t} \tag{5.84}$$

The temperature rise of the left surface, predicted by the "Integral model" is about 8,5 % higher than the analytical one. ($\sqrt{3/2}$ / $\sqrt{4/\pi} = 1.085$).

The non-dimensional temperature rise in function of the non-dimensional depth is given in Figure 5.8. The temperature rise is made non-dimensional with the analytical, correct temperature rise. The depth is made non-dimensional by the penetration depth of the "Integral model". For the case of a constant incident heat flux, these non-dimensional temperature profiles are valid for any time. The "Integral model" overestimates the temperature at the solid/fluid interface. It gives correct results for a non-dimensional depth of about 0.5. Deeper in the solid, the "Integral model" underestimates the temperature. For $x > \delta$ there is no temperature rise predicted in the "Integral model", which is not correct because of the parabolic character of the heat equation.

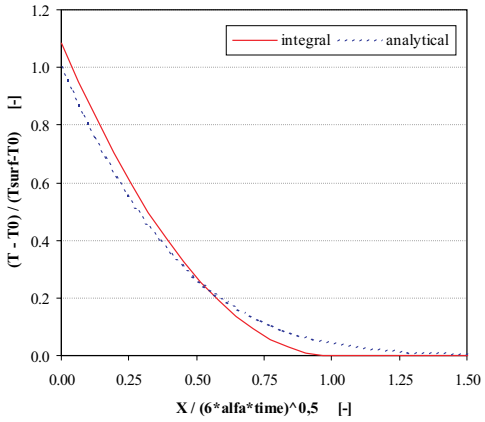

Figure 5.8: Temperature rise versus depth

5.6.2 Variable net incident heat flux

When the net incident heat flux is not constant, there are no simple analytical results available to validate the model. The results of the "Integral model" can be compared with numerical results, e.g. finite element or finite volume technique. Here the results will be compared with results from a one-dimensional finite volume method of which the derivation can be found in every heat transfer textbook.

A few cases that can be important for the simulation of flame spread, have been simulated:

- constant external heat flux ($\neq$ constant incident heat flux);
- step function for external heat flux in semi-infinite model;
- step function for external heat flux in finite model.

5.6.2.1 Constant external heat flux

In these simulation no pyrolysis was allowed simply by assuming a very high pyrolysis temperature. The following thermal properties are used: density $\rho = 650\,\mathrm{kg/m^3}$, specific heat capacity $c = 1257\,\mathrm{J/kgK}$ and the thermal conductivity $\lambda = 0.1257\,\mathrm{W/mK}$. The emissivity is taken 1 and the convection coefficient at the solid/fluid interface is $15\,\mathrm{W/m^2.K}$. The external heat flux is constant and equal to $10\,\mathrm{kW/m^2}$. The net incident heat flux is not constant because radiative and convective heat losses are included at the solid/fluid interface.

As can be seen in Figures 5.9 the results of the "Integral model" resemble very good the "correct" values of the finite volume calculation. The maximum error in the surface temperature rise is about 10 % and appears just after the start of the simulation. As time goes on, the error decreases to about 1 % (after 2 minutes).

For the finite phase the surface temperature is now underestimated. Again there is a point in the solid where the "Integral model" equals the "correct" solution. At the rear surface the "Integral model" overestimates the temperature.

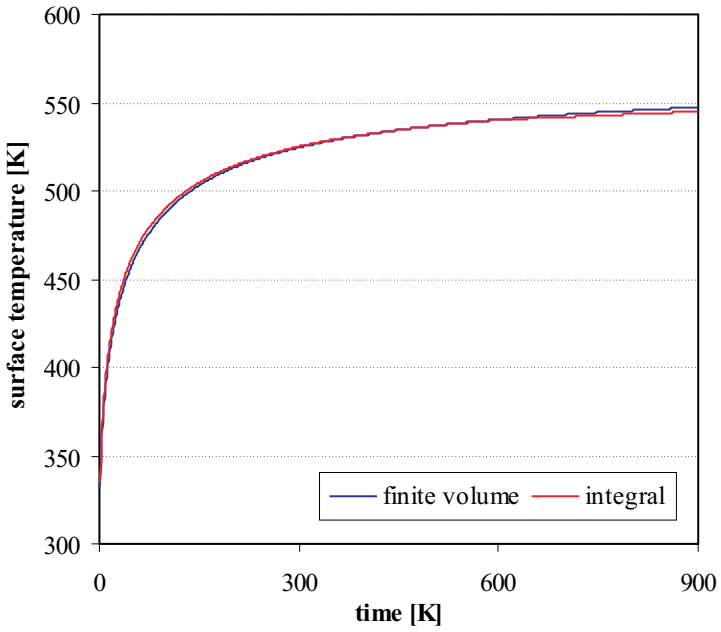

Figure 5.9: Surface temperature for an external heat flux of 10 kW/m^2

5.6.2.2 Step function for external heat flux in semi-infinite phase

In this case the external heat flux has a step function at 60 s where its value goes from 10 to 15 kW/m^2. The step function occurs for the "Integral model" in the semi-infinite model.

For the "Integral model" there is a sudden rise in the surface temperature, see Figure 5.10. The temperature changes discontinuously and is overestimated at the step in the external heat flux. The difference between the

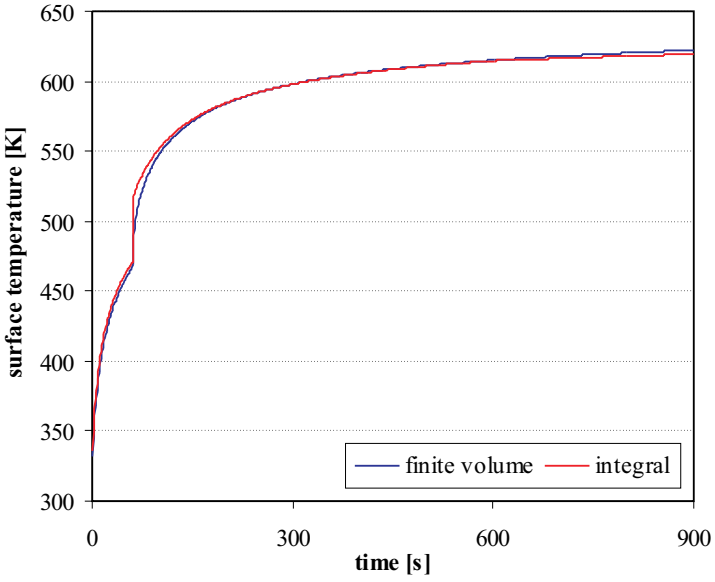

Figure 5.10: Comparison of "Integral model" with finite volume method

surface temperatures predicted by the two models, decreases for some time until both give the same surface temperature. After that, the "Integral model" will give lower surface temperatures as is also noticed for the constant external heat flux. The discontinuity is also visible in Figure 5.11 where the thermal penetration depth predicted by the "Integral model" is given. The thermal penetration depth is directly dependent on the net heat flux, so that a discontinuity in the net heat flux will result in a discontinuity in the thermal penetration depth.

The maximum error in the surface temperature, which is most important for the start of pyrolysis, is about 18 % at the step.

5.6.2.3 Step function for external heat flux in finite phase

In this case the external heat flux has a step function in the finite model at 700 s, and again the external heat flux goes from 10 to 15kW/m^2.

The maximum error in the surface temperature rise is now about 21 % which is larger than in the semi-infinite case.

The temperature profile at 705 s, i.e. 5 s after the step function, in Figure 5.12 is peculiar. The surface temperature at the rear boundary ($x = 0.03$ m) is lower than the ambient surface temperature. This is incompatible with the

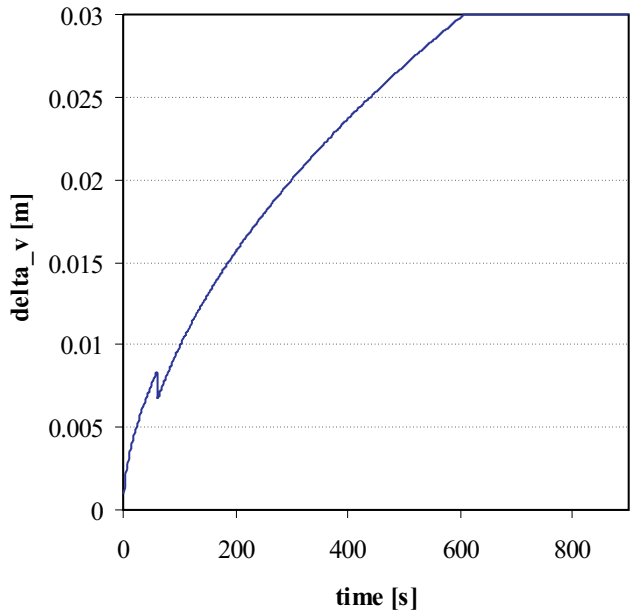

Figure 5.11: Thermal penetration depth for "Integral model"

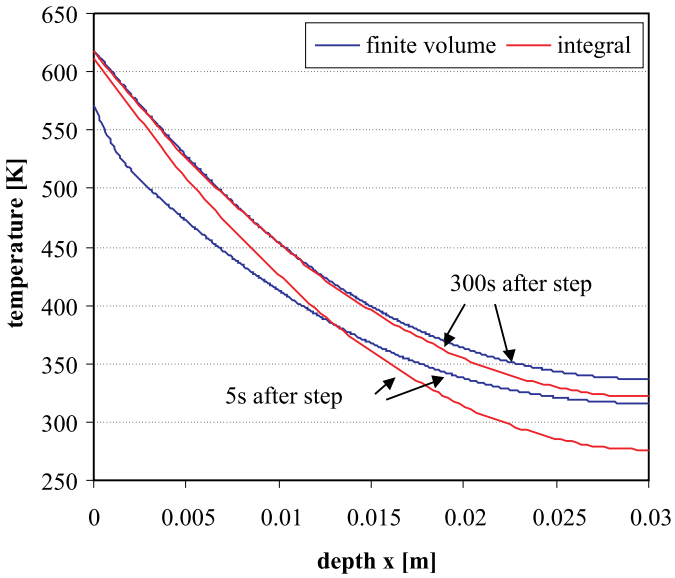

Figure 5.12: Temperature profile 5 and 300 s after step

second law of thermodynamics. This flaw in the "Integral model" is caused by the assumption of a prescribed temperature profile. The only way to fulfil the conservation of energy and the boundary conditions with a quadratic temperature profile, is to lower the rear surface temperature.

The boundary conditions on the front and rear surface will have a strong influence on the whole temperature profile. Just after the step in the external heat flux, the surface temperature at the front surface is directly dependent on the rear boundary condition. Though the heat equation is parabolic, such a strong dependency on such small time increment (any Δt after step) and over such large distance (L), is unrealistic.

5.7 Validation of pyrolysis phase

The pyrolysis phase can be validated with the "Moving grid" model of Chapter 6. Both models possess the same model equations but have different numerical solutions. The "Moving grid" model though, makes no assumptions on the temperature profile and will converge to the correct solution of the physical model equations. Such a comparison has been done by Theuns *et al.* [114]. The main results will be given here.

The "Integral model" has already been compared with experimental data by Moghtaderi [77] and by Spearpoint & Quintiere [109]. These comparisons, though, are hampered by the modelling of the experiment itself because the net incident heat flux must always be modelled somehow. Therefore, the difference in the experimental results and the simulation can be due to the "Integral model" itself or due to the representation of the experiment (or modelling of boundary condition of the solid). When the "Integral model" is compared with the "Moving mesh" method, a true numerical comparison or validation can be done, without evaluating the influence of the different material properties.

5.7.1 Case 1

When the pyrolysis starts and combustible volatiles are released (in the "Moving mesh" model at 12 s) the external heat flux is raised form 30 to 50 $\mathrm{kW/m^2}$. The constant heat flux of 30 $\mathrm{kW/m^2}$ represents the radiation from remote flames or from test radiation panels. The increase in the incident heat flux represents the ignition of the combustible volatiles in the gas phase and can be seen as a persistent flame. The induction time to obtain an ignitable mixture in the gas phase, is neglected. The rise in the external heat flux is triggered by the first release of pyrolysis gases, this is when the

surface temperature reaches the critical pyrolysis temperature.

Both models give similar results, as is shown in Figure 5.13. There are minor differences in the peak of mass flux of pyrolysis gases and the time at which this peak occurs.

5.7.2 Case 2

For enclosed fires flashover[2] can occur. When flashover takes place, all exposed combustible items in the enclosure get involved. This phenomenon is here modelled as a sudden rise in the external heat flux some time after the start of pyrolysis. In this case the rise in the external heat flux happens on a fixed time (60 s after start). In reality, the time of flashover will be dependent on the enclosure conditions.

The peak in the release of pyrolysis gases is much lower than in case 1, because of the insulating effect of the char layer. When the external heat flux rises, the char layer is much thicker than in case 1, which allows less heat to flow to the pyrolysis front.

The "Integral model" shows some peculiar behaviour: immediately after the rise of the external heat flux the mass flux of pyrolysis gases drops sharply, see Figure 5.13. In some cases even negative mass fluxes where noted. The reason is the unrealistic, direct influence of the net incident heat flux on the whole temperature profile. This sudden decrease in the mass flux of pyrolysis gases is not present in case 1 as the change in the external heat flux occurs at the start of pyrolysis.

5.7.3 Case 3

In this case a sudden rise and fall of the external heat flux is examined. The rise in the external heat flux starts at the beginning of pyrolysis, while the fall is at a fixed time. The fall in the external heat flux can represent the extinghuisment of the flames in the gas phase due to e.g. lack of oxygen, or the effect of an activated sprinkler installation.

Here the "Integral model" shows again a bad prediction just after the fall of the external heat flux, see Figure 5.14. There is a sudden short rise in the mass flux of pyrolysis gases, but less than a second later, the mass flux is back normal.

[2]flashover = the rapid transition to a state of total surface involvement in a fire of combustible material within an enclosure [51]

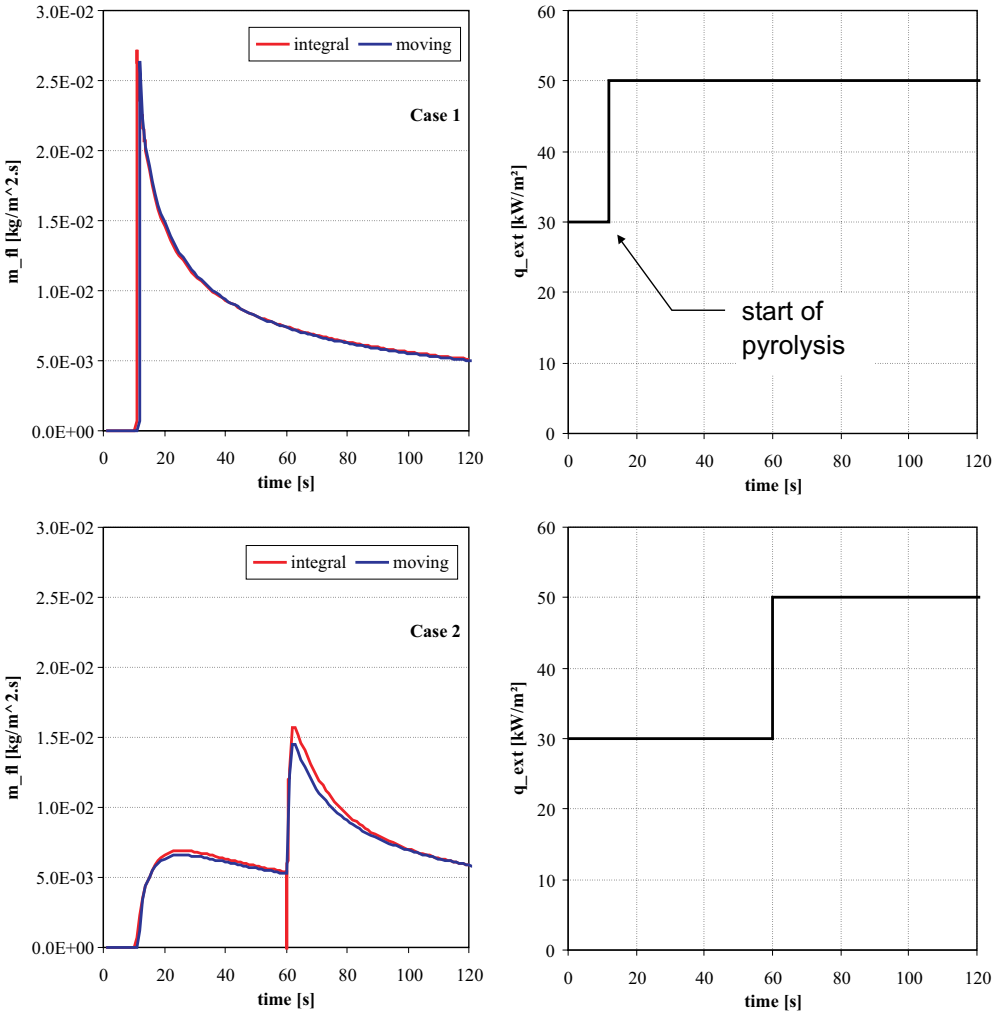

Figure 5.13: Validation of Integral model: Case 1 and 2

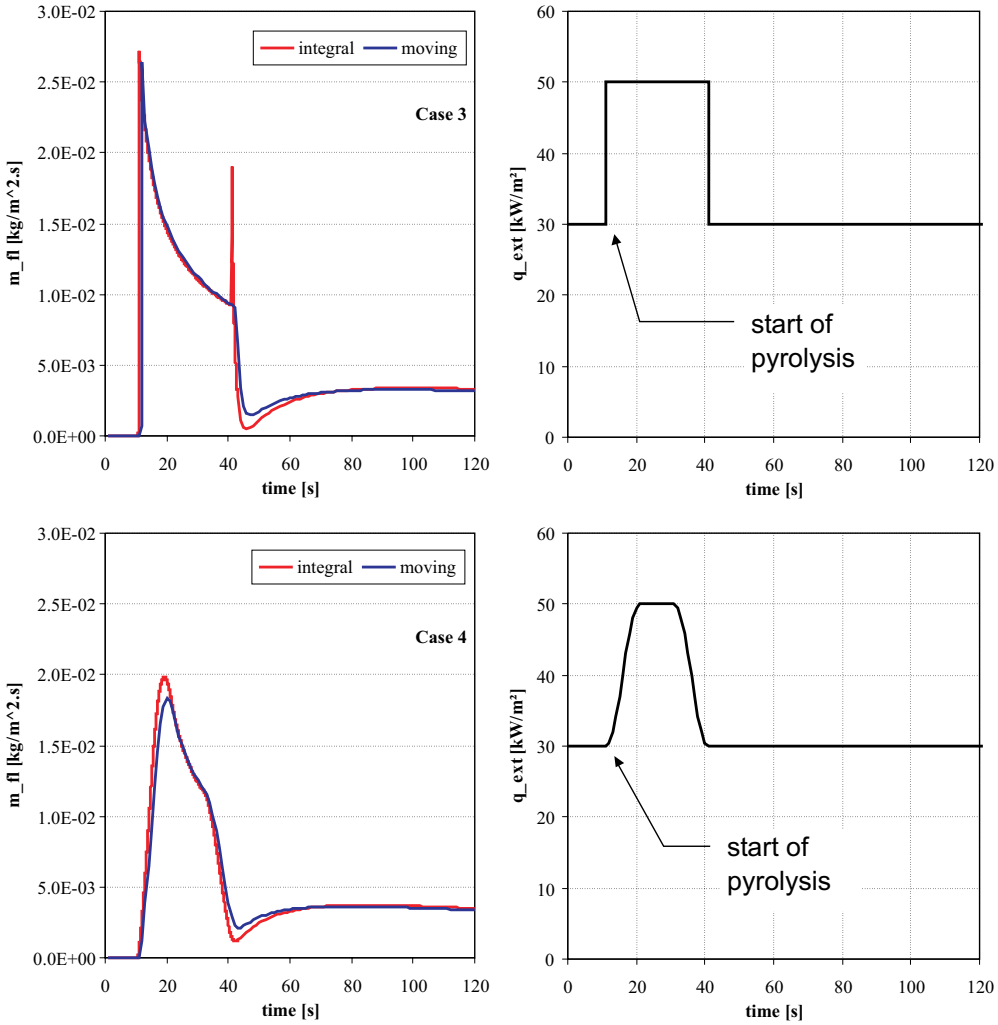

Figure 5.14: Validation of Integral model: Case 3 and 4

5.7.4 Case 4

It is clear that the "Integral model" has problems with sudden changes in the external heat flux. Therefore, in this case, the external heat flux is varied smoothly (sinusoidal for the variation between 30 and 50 kW/m^2).

As can be seen in Figure 5.14, when a smooth variation in the external heat flux is applied, the "Integral" and "Moving meshes" model show good agreement.

When calculation times are compared, the "Integral model" is in general about 5 times faster than the "Moving mesh" model. When a finer mesh and smaller time steps are taken, the calculation time of the "Moving mesh" model will of course increase.

5.7.5 Deficiencies of "Integral model"

The "Integral model" performs very well when the boundary conditions are constant or changing slowly. Sudden changes in the net incident heat flux, though, are transmitted immediately and unrealistically high through the whole solid. The model is therefore less adeaquate for predicting flashover.

As the temperature is prescribed (e.g. quadratic), the "Integral model" can only be valid for those types of heating which will result in that prescribed temperature profile. In flame spread simulations the incident heat flux can suddenly rise due to for example ignition of the pyrolysis gases in the gas phase, but it can also suddenly fall due to for example lack of oxygen in the gas phase. This kind of heating can result in temperature profiles that are different from the quadratic ones.

The "Integral model" has not the capability to refine and as a consequence will always give an approximate solution of the model equations.

In the "Integral model" only one-dimensional heat transfer is allowed and thus a more dimensional pyrolysis problem has to be solved as a series of independent one-dimensional problems, as wil be done in Section 10.2.3.2.

5.8 Further developments

The "Integral model" is applicable for non-charring materials. The char layer is omitted and the boundary conditions, i.e. the net heat flux, is applied at the pyrolysis front. The moving solid/gas interface now coincides with the pyrolysis front for the whole pyrolysis phase.

It is possible to incorporate a water vaporisation front in the "Integral model". The virgin material is then divided into three zone: a zone where the water has been vaporized, a second zone where the temperature is lower

than the water vaporization temperature and a third last zone where the virgin material has still the initial temperature. There are three fronts in the model, namely the pyrolysis, the water vaporization and the heat wave front. When the moisture content of the solid is low the water vaporization front may be omitted. But even for high moisture contents the model with one front can perform well. The latent heat of water vaporisation is than sort of included into the pyrolysis heat. In literature almost all of the solid combustion modelling is done without considering the moisture content explicitly.

Maybe improvement could be made by splitting the pyrolysis front in two fronts: one at low temperature and one at high pyrolyzing temperature. For example the activation energies for the appearance of the different gaseous products from the pyrolysis of e.g. cellulose fall into two bands [103]. A model with two fronts would be more appropriate for these kind of materials. The transformation of virgin material into char goes over an intermediate component:

$$\text{virgin} \longrightarrow \text{intermediate} \longrightarrow \text{char}$$

The "Integral model" could be adapted to include temperature dependent properties, though this is cumbersome and sometimes impossible.

5.9 Conclusion

The validation of the "Integral model" with the pure conduction calculation revealed that in most cases the "Integral model" gives acceptable results. Sudden changes of the boundary conditions though, are immediately and unrealistically felt throughout the whole solid. So when the net incident heat flux is changing a lot, it is not advised to use the "Integral model".

The "Integral model" is one-dimensional. It can not be expanded to two or three dimensions. More dimensional problems can be solved by a series of one-dimensional "Integral models", as will be shown in Section 10.2.3.2.

A disadvantage of the "Integral model" are the different phases. Unlike the "Arrhenius law" model, separate model equations must be developed for each phase. This makes the implementation more difficult and more prone to errors. For example when sudden changes in the boundary conditions are combined with a change of heating or pyrolysis phase.

Chapter 6

Reaction of solid material: Moving meshes

6.1 Introduction

The "Moving meshes model" is similar to the "Integral model" of Chapter 5. In fact, it were the limitations of the "Integral model", i.e. the prescribed temperature profile, that gave the idea for the variable or "'Moving meshes" method. In the new method any temperature profile can be predicted dependent of course on the number of cells that will be used. As the pyrolysis zone is modelled as an infinitely thin front, it is expected that fewer cells will be necessary than in the "Arrhenius law model" of Chapter 4. In that model a large number of cells was needed for an accurate description of the pyrolysis front.

In this chapter variable meshes will be used to calculate the reaction of the solid to an incident heat flux [114]. The char layer is growing, while the virgin layer is shrinking. Variable meshes are applied to both the char and virgin layer, as shown in Figure 6.1

6.2 Phases in simulation

For the variable meshes method only three different phases are defined:

1. heat up of virgin material;

2. pyrolysis;

3. heat up of char material;

The phases and the transitions are shown in Figure 6.2. There is no need to make a distinction between finite or semi-infinite phases, as was done for the "Integral model". The number of cells in a layer is constant during a phase and thus in the heat up phases the meshes are fixed.

In the first phase the solid exists entirely of virgin material and the grid is steady. When the surface temperature reaches the pyrolysis temperature the pyrolysis phase starts. From now on, there is an expanding char zone and a shrinking virgin zone, which are separated by the infinitely thin pyrolysis front. The meshes in the char and virgin zone are thus variable. The pyrolysis phase ends when the pyrolysis front reaches the rear surface and all the virgin material is consumed. The remaining inert char will be further heated up by the external heat flux.

Dependent on the boundary conditions, a fourth phase is possible: a heat up phase of a composite solid of char and virgin material. This phase can only exist when pyrolysis has already started but comes to a standstill because of insufficient heat supply. The external heat flux must thus be changing with time. The transition between the pyrolysis phase and the char/virgin heat up phase is determined by the heat flux from the char layer to the pyrolysis front. When this heat flux is equal or lower than the heat flux from the pyrolysis

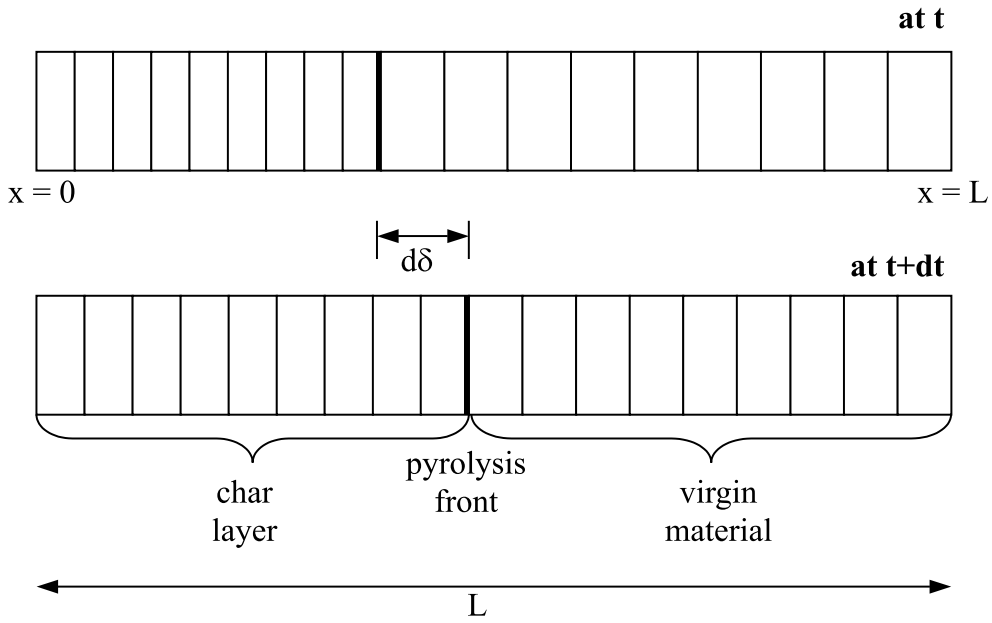

Figure 6.1: Variable meshes at time t and t+dt

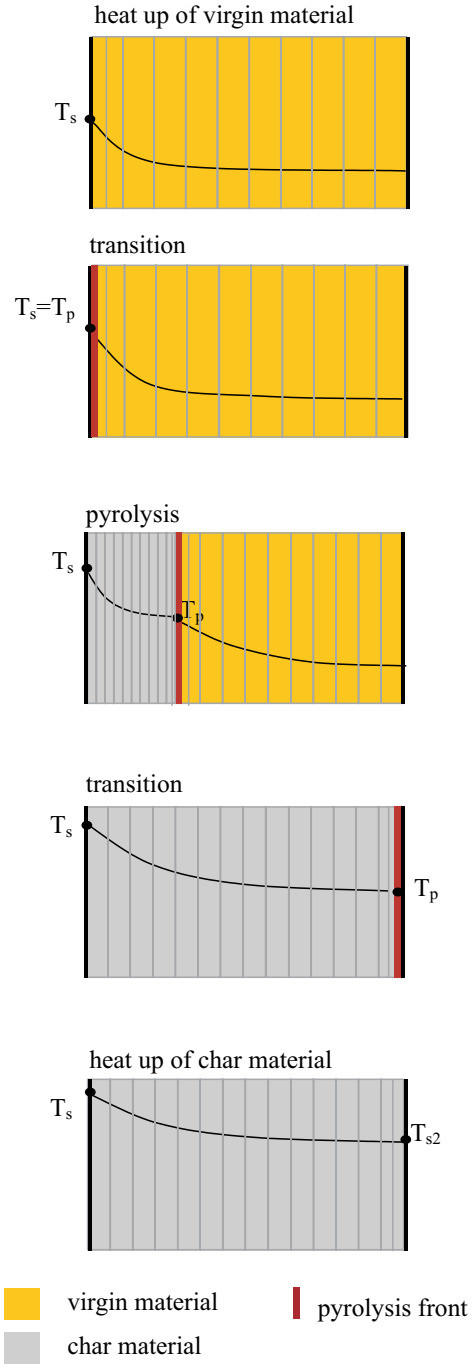

Figure 6.2: Different phases for variable meshes model

front to the virgin layer, there is insufficient energy to maintain the pyrolysis reactions. The solid will then react as a normal composite of char and virgin material where the temperature of the interface char/virgin is lower than the pyrolysis temperature. When the external heat flux is rising again, such that it heats up the char layer, the pyrolysis phase will continue again when the front or interface char/virgin temperature reaches the pyrolysis temperature. The phases are defined as follows:

- the virgin heat up phase last as long as the surface temperature is lower than the pyrolysis temperature;
- the pyrolysis phase last until the thickness of the char layer equals the solid thickness **or** until the heat flux from the char layer to the pyrolysis front is smaller than the heat flux from the pyrolysis front to the virgin layer;
- the heat up char/virgin phase last as long as the interface char/virgin temperature is lower than the pyrolysis temperature;
- the char heat up phase starts when the thickness of char layer equals the total thickness.

The criteria to switch between phases can easily be derived from the definitions above.

6.3 Model equations

During the **heating phase** there are no pyrolysis reactions and hence the conservation of mass is redundant. The temperature in the solid is determined by the conservation of energy:

$$\frac{\mathrm{d}}{\mathrm{d}t}\int_V \rho c T \,\mathrm{d}V = -\int_S \dot{\mathbf{q}}'' \cdot \mathrm{d}\mathbf{S} \tag{6.1}$$

The density and specific heat capacity are or pure virgin, or pure char material.

For the **pyrolysis phase** the solid is divided into three zones: the char layer, the pyrolysis front and the virgin material layer. The general equation of conservation of energy can be applied to the three zones.

6.3.1 Char layer

For the char layer, the pyrolysis gases that flow from the pyrolysis front to the front surface ($x = 0$) can be considered. It is assumed that the volatiles are in thermal equilibrium with the char they are passing through [88]. As no gases are produced in the char layer and as there is no accumulation of gases, the amount of pyrolysis gases that is entering the layer is equal to the amount of gases leaving the front surface.

The conservation of energy, Equation 5.3, is applied to the whole char layer:

$$\begin{aligned} \frac{\mathrm{d}}{\mathrm{d}t}\int_0^{\delta_c}\Big(\rho_{pyr}\cdot u_{pyr}(T)+\rho_c\cdot u_c(T)\Big)\,\mathrm{d}x \quad &+ \quad \dot{m}''_{pyr}\cdot u_{pyr}(T_s)-\dot{m}''_{pyr}\cdot u_{pyr}(T_{pyr}) \\ + \quad \Big(\rho_{pyr}\cdot u_{pyr}(T_{pyr})+\rho_c\cdot u_c(T_{pyr})\Big)\cdot\Big(-\frac{\mathrm{d}\delta_c}{\mathrm{d}t}\Big) \quad &= \quad \dot{q}''_{net}-\dot{q}''_c \end{aligned} \tag{6.2}$$

With $u = u(T_0) + c \cdot T$, it becomes:

$$\begin{aligned} \frac{\mathrm{d}}{\mathrm{d}t}\int_0^{\delta_c}\Big(\rho_{pyr}\cdot c_{pyr}\cdot T+\rho_c\cdot c_c\cdot T\Big)\,\mathrm{d}x \quad &+ \quad \dot{m}''_{pyr}\cdot c_{pyr}\cdot T_s-\dot{m}''_{pyr}\cdot c_{pyr}\cdot T_{pyr} \\ + \quad \Big(\rho_{pyr}\cdot c_{pyr}\cdot T_{pyr}+\rho_c\cdot c_c\cdot T_{pyr}\Big)\cdot\Big(-\frac{\mathrm{d}\delta_c}{\mathrm{d}t}\Big) \quad &= \quad \dot{q}''_{net}-\dot{q}''_c \end{aligned} \tag{6.3}$$

The boundary conditions are:

$$\begin{cases} -\lambda_c\left(\frac{\mathrm{d}T}{\mathrm{d}x}\right)_{x=0} &= \dot{q}''_{net}=\dot{q}''_{ext}-h_{s1}(T_{s1}-T_\infty)-\epsilon\sigma(T_{s1}^4-T_\infty^4) \\ \left(T\right)_{x=\delta_c} &= T_{pyr} \end{cases} \tag{6.4}$$

6.3.2 Pyrolysis front

For the pyrolysis front the conservation of mass, Equation 5.1, gives:

$$(\rho_v-\rho_c)\frac{\mathrm{d}\delta_c}{\mathrm{d}t}=\dot{m}''_{pyr} \tag{6.5}$$

The conservation of energy gives:

$$\begin{aligned} \rho_{pyr}\cdot u_{pyr}\cdot\left(v_{pyr}+\frac{\mathrm{d}\delta_c}{\mathrm{d}t}\right)-\rho_c\cdot u_c\cdot\left(0-\frac{\mathrm{d}\delta_c}{\mathrm{d}t}\right)+\rho_v\cdot u_v\cdot\left(0-\frac{\mathrm{d}\delta_c}{\mathrm{d}t}\right) \\ = \quad \dot{q}''_c-\dot{q}''_v \end{aligned} \tag{6.6}$$

or

$$\dot{m}''_{pyr} \cdot u_{vol}(T_{pyr}) \quad + \quad \frac{\mathrm{d}\delta_c}{\mathrm{d}t} \cdot \Big(\rho_c \cdot u_c(T_{pyr}) - \rho_v \cdot u_v(T_{pyr})\Big) \\ = \quad \dot{q}''_c - \dot{q}''_v \quad (6.7)$$

or with Equation 4.16 and 6.5:

$$(\rho_v - \rho_c)\frac{\mathrm{d}\delta_c}{\mathrm{d}t}\Delta Q_{pyr}(T_{pyr}) \quad = \quad \dot{q}''_c - \dot{q}''_v \quad (6.8)$$

6.3.3 Virgin layer

No gases flow in the virgin material layer, so there is no need to consider the conservation of mass in this zone. The conservation of energy for the whole layer is given by:

$$\frac{\mathrm{d}}{\mathrm{d}t}\int_{\delta_c}^{L} \rho_v \cdot u_v(T)\,\mathrm{d}x - \rho_v \cdot u_v(T_{pyr}) \cdot \frac{\mathrm{d}\delta_c}{\mathrm{d}t} = \dot{q}''_v + \dot{q}''_{rear} \quad (6.9)$$

or with $u = u(T_0) + c \cdot T$:

$$\frac{\mathrm{d}}{\mathrm{d}t}\int_{\delta_c}^{L} \rho_v c_v T\,\mathrm{d}x - \rho_v c_v T_{pyr}\frac{\mathrm{d}\delta_c}{\mathrm{d}t} = \dot{q}''_v + \dot{q}''_{rear} \quad (6.10)$$

The boundary conditions are:

$$\begin{cases} \big(T\big)_{x=\delta_c} &= T_{pyr} \\ \lambda_v \left(\frac{\mathrm{d}T}{\mathrm{d}x}\right)_{x=L} &= \dot{q}''_{rear} \end{cases} \quad (6.11)$$

6.4 Discretisation

Only for the pyrolysis phase the equations will be given. The virgin, char and char/virgin heating phase are straightforward and will not be discussed.

6.4.1 Mesh

During the pyrolysis phase the front temperature is of course known. As the virgin and the char layer both end at that front, half a cell is taken so that the a node can be placed at the front or boundary of the zone [16]. An example of the subsequent mesh is given in Figure 6.3. Notice that the cell size in the char zone is different from in the virgin zone. As a result of the

half cell at the front, the mesh for the heating up of the virgin material also has a half cell at the boundary surface. The same mesh is used, because this avoids interpolation at the transition from heat up to pyrolysis phase. Similar, the mesh in the char heat up phase will end with a half cell at the rear boundary surface.

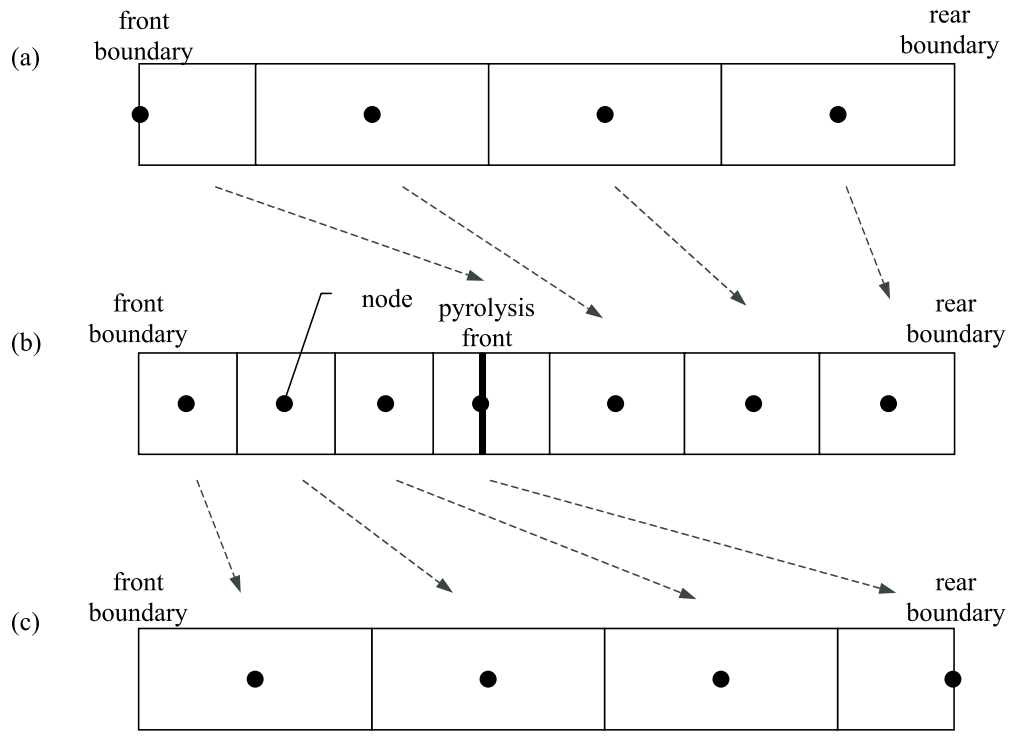

Figure 6.3: Mesh during (a) virgin heat up, (b) pyrolysis, (c) char heat up

6.4.2 Space and time discretization

Consider a one-dimensional, rectangular grid as in Figure 6.4.

Similar as was done in Section 6.3 for the whole char and virgin layer, the conservation of energy can be written for one volume of the mesh in the char and virgin zone. For a single char cell i:

$$\begin{aligned} \frac{\mathrm{d}}{\mathrm{d}t}\int_{\Delta x_i} \rho_c c_c T \,\mathrm{d}x \quad &- \quad (\rho_c c_c)(w_{W,i}T_{W,i} - w_{E,i}T_{E,i}) \\ &+ \quad \dot{m}''_{pyr} c_{pyr}(T_{W,i} - T_{E,i}) \quad = \quad \dot{q}''_{E,i} - \dot{q}''_{W,i} \end{aligned} \tag{6.12}$$

and for a virgin cell:

$$\frac{\mathrm{d}}{\mathrm{d}t}\int_{\Delta x_i} \rho_v c_v T \,\mathrm{d}x \quad - \quad (\rho_v c_v)(w_{W,i}T_{W,i} - w_{E,i}T_{E,i}) \\ = \quad \dot{q}''_{E,i} - \dot{q}''_{W,i} \quad (6.13)$$

where T_W and T_E are the temperatures, w_W and w_E the boundary velocities and $\dot{q}''_W$ and $\dot{q}''_E$ the conductive heat fluxes at the west and east boundary respectively.

At the transition from virgin heating to the pyrolysis phase, the model equations are singular because the char zone does not yet exist. This singularity for the first time step, is simply overcome by taking a fully implicit time step (first order). For the subsequent time steps, the second order accurate Cranck-Nicolson method is used. Heating of the pyrolysis gases by the char layer is included. To calculate a new time step at $n+1$, Equation 6.12 is written out at a time level $n+\theta$:

$$\rho_c c_c \frac{T_i^{n+1}\Delta x_i^{n+1} - T_i^n \Delta x_i^n}{\Delta t} \; + \; \rho_c c_c \left(T_{W,i}^{n+\theta} w_{W,i}^{n+\theta} - T_{E,i}^{n+\theta} w_{E,i}^{n+\theta}\right) \\ + \; \dot{m}''^{n+\theta}_{pyr} c_{pyr}\left(T_{W,i}^{n+\theta} - T_{E,i}^{n+\theta}\right) \; = \; \lambda_c \left(\frac{\mathrm{d}T}{\mathrm{d}x}\right)_{W,i}^{n+\theta} \; - \; \lambda_c \left(\frac{\mathrm{d}T}{\mathrm{d}x}\right)_{E,i}^{n+\theta} \quad (6.14)$$

For the virgin layer Equation 6.13 becomes:

$$\rho_v c_v \frac{T_i^{n+1}\Delta x_i^{n+1} - T_i^n \Delta x_i^n}{\Delta t} \; + \; \rho_v c_v \left(T_{W,i}^{n+\theta} w_{W,i}^{n+\theta} - T_{E,i}^{n+\theta} w_{E,i}^{n+\theta}\right) \\ = \; \lambda_v \left(\frac{\mathrm{d}T}{\mathrm{d}x}\right)_{W,i}^{n+\theta} \; - \; \lambda_v \left(\frac{\mathrm{d}T}{\mathrm{d}x}\right)_{E,i}^{n+\theta} \quad (6.15)$$

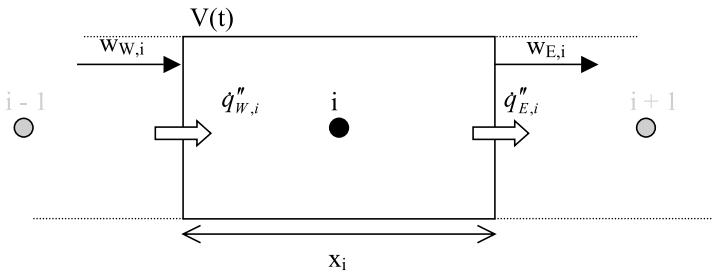

Figure 6.4: One volume of the mesh

For the first pyrolysis time step, which is fully implicit, θ should be taken unity (backward Euler method), otherwise it is 0.5 (Cranck-Nicholson).

The temperature at the boundaries of the interior cells is determined with a central differencing scheme. Central is preferred above upwind as the mesh velocity is small and as there is no real strong convective flow. The temperature at the west boundary W in between time steps can be written as

$$\begin{aligned} T_{W,i}^{n+\theta} &= \left(T_i^{n+\theta} + T_{i-1}^{n+\theta}\right)/2 \\ &= \theta \cdot \left(T_i^{n+1} + T_{i-1}^{n+1}\right)/2 \;+\; (1-\theta) \cdot \left(T_i^{n} + T_{i-1}^{n}\right)/2 \end{aligned} \tag{6.16}$$

And similar for the east boundary E:

$$\begin{aligned} T_{E,i}^{n+\theta} &= \left(T_i^{n+\theta} + T_{i+1}^{n+\theta}\right)/2 \\ &= \theta \cdot \left(T_i^{n+1} + T_{i+1}^{n+1}\right)/2 \;+\; (1-\theta) \cdot \left(T_i^{n} + T_{i+1}^{n}\right)/2 \end{aligned} \tag{6.17}$$

The derivative of the temperature at the west boundary W is given by:

$$\begin{aligned} \left(\frac{\mathrm{d}T}{\mathrm{d}x}\right)_{W,i}^{n+\theta} &= \frac{T_i^{n+\theta} - T_{i-1}^{n+\theta}}{\Delta x^{n+\theta}} \\ &= \theta \cdot \frac{T_i^{n+1} - T_{i-1}^{n+1}}{\Delta x^{n+1}} \;+\; (1-\theta) \cdot \frac{T_i^{n} - T_{i-1}^{n}}{\Delta x^{n}} \end{aligned} \tag{6.18}$$

And similar for the east boundary E:

$$\begin{aligned} \left(\frac{\mathrm{d}T}{\mathrm{d}x}\right)_{E,i}^{n+\theta} &= \frac{T_{i+1}^{n+\theta} - T_i^{n+\theta}}{\Delta x^{n+\theta}} \\ &= \theta \cdot \frac{T_{i+1}^{n+1} - T_i^{n+1}}{\Delta x^{n+1}} \;+\; (1-\theta) \cdot \frac{T_{i+1}^{n} - T_i^{n}}{\Delta x^{n}} \end{aligned} \tag{6.19}$$

For the convective term, the heating of the pyrolysis gases, an upwind method is used:

$$\begin{aligned} &\dot{m}''^{n+\theta}_{pyr} \cdot c_{pyr} \cdot \left[T_W^{n+\theta} + T_E^{n+\theta}\right] \;= \\ &\dot{m}''^{n+\theta}_{pyr} \cdot c_{pyr} \cdot \left[\left(\theta \cdot T_W^{n+1} + (1-\theta) \cdot T_W^{n}\right) - \left(\theta \cdot T_E^{n+1} + (1-\theta) \cdot T_E^{n}\right)\right] \end{aligned} \tag{6.20}$$

For the first char cell (at the solid/fluid interface) there is no conductive heat flux from the left side. This flux must be replaced with the net surface heat

flux:

$$\begin{aligned}\theta \cdot \dot{q}''^{n+1}_{net} + (1-\theta) \cdot \dot{q}''^{n}_{net} \quad &= \\ \theta \cdot \left[\dot{q}''^{n+1}_{ext} + h^{n+1}_{eq} \cdot \left(T_\infty - (1.5 \cdot T^{n+1}_{c,i=1} - 0.5 \cdot T^{n+1}_{c,i=2}) \right) \right] \\ + (1-\theta) \cdot \left[\dot{q}''^{n}_{ext} + h^{n}_{eq} \cdot \left(T_\infty - (1.5 \cdot T^{n}_{c,i=1} - 0.5 \cdot T^{n}_{c,i=2}) \right) \right]\end{aligned} \tag{6.21}$$

A variable equivalent heat transfer coefficient h_{eq} is used, so that the influence of the net heat flux on the first two nodes is directly implemented:

$$h_{eq} = h_{s1} + \epsilon \cdot \sigma \cdot (T_\infty + T_{s1}) \cdot (T^2_\infty + T^2_{s1}) \tag{6.22}$$

with h_{s1} the convective coefficient at the gas/solid interface.

For the last virgin cell (at the back surface) there is no conductive heat flux from the right side. This flux must be replaced with the net back surface heat flux. For a convective boundary:

$$\begin{aligned}\theta \cdot \dot{q}''^{n+1}_{rear} + (1-\theta) \cdot \dot{q}''^{n}_{rear} \quad &= \\ \theta \cdot h^{n+1}_{rear} \cdot \left(T_\infty - (1.5 \cdot T^{n+1}_{v,i=N_v} - 0.5 \cdot T^{n+1}_{v,i=N_v-1}) \right) \\ + (1-\theta) \cdot h^{n}_{rear} \cdot \left(T_\infty - (1.5 \cdot T^{n}_{v,i=N_v} - 0.5 \cdot T^{n}_{v,i=N_v-1}) \right)\end{aligned} \tag{6.23}$$

The temperature of the pyrolysis front is known so that:

$$T^n_{c,i=N_c+1} = T^{n+1}_{c,i=N_c+1} = T_{pyr} \tag{6.24}$$

and

$$T^n_{v,i=0} = T^{n+1}_{v,i=0} = T_{pyr} \tag{6.25}$$

The method that is derived above will be applied to the virgin and char layer. For these layers the velocity of the mesh boundaries is not yet known; it will follow from the velocity of the pyrolysis front.

6.4.3 Mesh velocity

The char layer is made of several moving volumes (meshes) that are equidistant. The velocity of the mesh boundaries is determined by the velocity of the pyrolysis front. For volume i (numbering start at 1 for the first volume):

$$\begin{cases} w^{n+\theta}_W &= \frac{1}{N} \cdot \left(\frac{\mathrm{d}\delta_c}{\mathrm{d}t} \right)^{n+\theta} \cdot (i-1) \\ w^{n+\theta}_E &= \frac{1}{N} \cdot \left(\frac{\mathrm{d}\delta_c}{\mathrm{d}t} \right)^{n+\theta} \cdot (i) \end{cases} \tag{6.26}$$

The left front surface of the zone (i.e. at $x = 0$) is assumed to be steady.

For the virgin material the mesh cells are taken equidistant. The velocity of the mesh boundaries is determined by the velocity of the pyrolysis front. For volume i (numbering start at 1 for first volume)

$$\begin{cases} w_W^{n+\theta} &= \frac{1}{N_v} \cdot \left(\frac{\mathrm{d}\delta_c}{\mathrm{d}t}\right)^{n+\theta} \cdot (N_v - i + 1) \\ w_E^{n+\theta} &= \frac{1}{N_v} \cdot \left(\frac{\mathrm{d}\delta_c}{\mathrm{d}t}\right)^{n+\theta} \cdot (N_v - i) \end{cases} \tag{6.27}$$

The right surface of the zone ($x = L$) is assumed to be steady.

6.4.4 The pyrolysis front.

The front velocity is determined from the conservation of energy over the pyrolysis front:

$$\begin{aligned} W^{n+\theta} &= \left(\frac{\mathrm{d}\delta_c}{\mathrm{d}t}\right)^{n+\theta} \\ &= \frac{1}{(\rho_v - \rho_c \cdot \Delta H_{pyr}(T_{pyr})} \cdot \left((\dot{q}_c'')^{n+\theta} - (\dot{q}_v'')^{n+\theta}\right) \end{aligned} \tag{6.28}$$

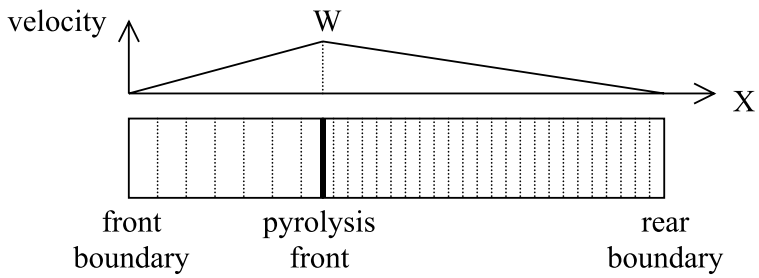

Figure 6.5: Velocity of the cell boundaries for variable meshes

where the heat fluxes $(\dot{q}''_c)^{n+\theta}$ and $(\dot{q}''_v)^{n+\theta}$ in the RHS are derived from the conservation of energy of the half cells neighbouring the pyrolysis front:

$$\begin{aligned}
\dot{q}''^{n+\theta}_c &= -\frac{\rho_c c_c}{2\,\Delta t}\cdot T_{pyr}\cdot\left(\Delta x_c^{n+1}-\Delta x_c^{n}\right)\\
&- \rho_c c_c\Bigg[\left(\frac{N_c}{N_c+0.5}\cdot W^{n+\theta}\right)\cdot\\
&\left(\frac{T_{pyr}+\theta\cdot T^{n+1}_{c,i=N_c}+(1-\theta)\cdot T^{n}_{c,i=N_c}}{2}\right)-W^{n+\theta}\cdot T_{pyr}\Bigg]\\
&- \lambda_c\left[\theta\cdot\frac{T_{pyr}-T^{n+1}_{c,i=N_c}}{\Delta x_c^{n+1}}+(1-\theta)\cdot\frac{T_{pyr}-T^{n}_{c,i=N_c}}{\Delta x_c^{n}}\right]
\end{aligned}\tag{6.29}$$

and

$$\begin{aligned}
\dot{q}''^{n+\theta}_v &= -\frac{\rho_v c_v}{2\,\Delta t}\cdot T_{pyr}\cdot\left(\Delta x_v^{n+1}-\Delta x_v^{n}\right)\\
&- \rho_v c_v\Bigg[W^{n+\theta}\cdot T_{pyr}-\\
&\left(\frac{N_v}{N_v+0.5}\cdot W^{n+\theta}\right)\cdot\left(\frac{T_{pyr}+\theta\cdot T^{n+1}_{v,i=1}+(1-\theta)\cdot T^{n}_{v,i=1}}{2}\right)\Bigg]\\
&- \lambda_v\left[\theta\cdot\frac{T^{n+1}_{v,i=1}-T_{pyr}}{\Delta x_v^{n+1}}+(1-\theta)\cdot\frac{T^{n}_{v,i=N_v}-T_{pyr}}{\Delta x_v^{n}}\right]
\end{aligned}\tag{6.30}$$

The mass flux of pyrolysis gases is calculated with:

$$(\dot{m}''_{fl})^{n+\theta}=(\rho_v-\rho_c)\left(\frac{\mathrm{d}\delta_c}{\mathrm{d}t}\right)^{n+\theta}\tag{6.31}$$

6.5 Solution of discretized equations

6.5.1 Heating phases

The char, virgin, and char/virgin heat up phase are all done on a steady mesh. A direct method, the Thomas algorithm for solving a tri-diagonal system of equations [2], is used for calculating the unknown temperatures. Still an iteration is present to allow for the adaptation of the equivalent heat transfer coefficient in Equation 6.21, which is dependent on the surface temperature.

6.5.2 Pyrolysis phase

A direct method is used to determine the temperatures for a certain front velocity. First an iterative method was implemented, but this needed a lot of iterations to converge. The Thomas algorithm for solving a tri-diagonal system of equations [2] is used for calculating the unknown temperatures. Only when few iterations are sufficient, the iterative method will be faster than the direct method.

In succeeding iterations, the front velocity is adjusted until energy conservation over the pyrolysis front is fulfilled, see Figure 6.6. The criterion to stop the iterations, is based on the temperature difference in between iterations. If the temperature change falls under a certain percentage, the time step is assumed converged.

For the first pyrolysis step, a fully implicit method is used for the char layer. This only makes use of the variables at the new time step. At the start of pyrolysis there are no char cells and no char temperatures, the char zone is then non-existent.

When heating of pyrolysis gases is included, the convective heat flow is discretized with an upwind method. For the half char cell near the pyrolysis front no heating is considered. For the cell next to the fluid/solid interface, the temperature of the out flowing gases is taken the surface temperature instead of the temperature in the first node.

6.6 Determination of time step and cells size

The same physical properties are used as in Section 4.4 of Chapter 4.

6.6.1 "The solution"

The "correct" or grid and time step converged solution is obtained when the results of the simulation do not change anymore after grid refinement and time step size reduction.

The number of iterations is here not an issue as during the simulation the number of iterations is determined by a convergence criterion. For the outer iterations, where the front velocity is adjusted each iteration, the criterion for convergence was the difference in temperature for succeeding iterations that needed to be smaller than 10^{-14} of the local node value. This is about machine precision as the simulations where done with double precision. For the inner iteration, for which the front velocity was fixed but the equivalent heat transfer coefficient at the solid/fluid interface could vary, the criterion was less stringent. Here the difference in temperature for succeeding inner

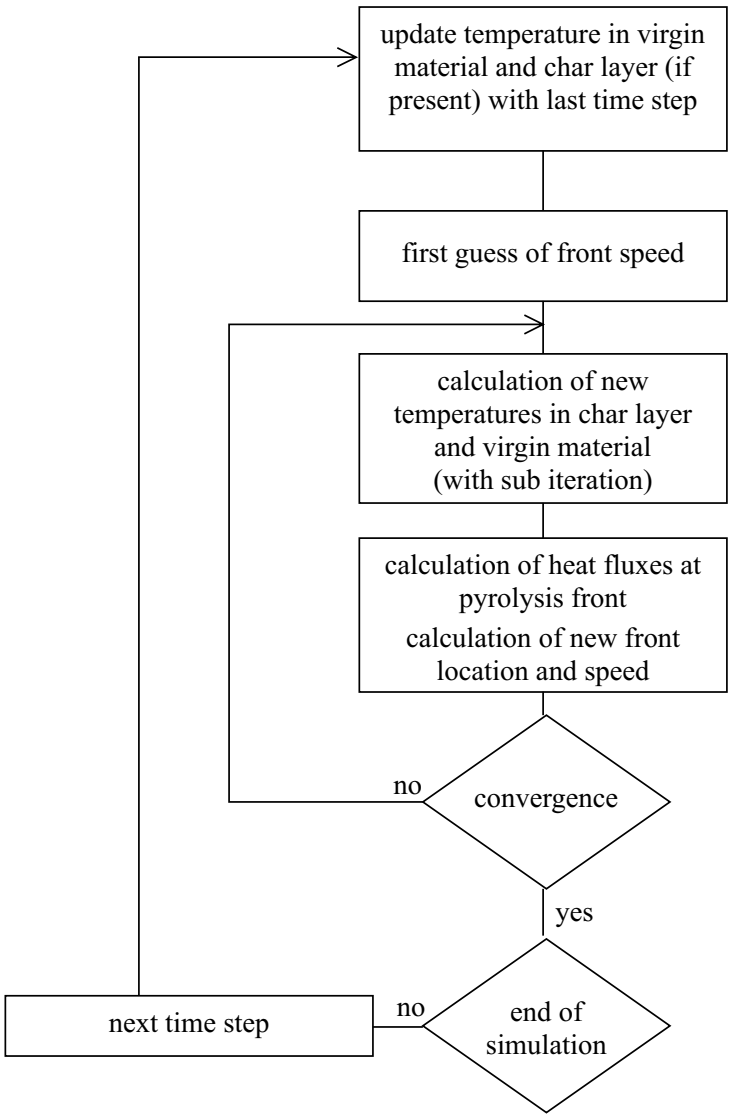

Figure 6.6: Solution scheme for the pyrolysis phase

iterations was smaller than 10^{-8} of the local node value. During the simulation it was noticed that only one or two inner iterations where needed. When the surface temperature and thus the non-linear boundary condition changes smoothly, the inner iteration cycle can probably be removed. The inner iterations are retained to ensure that correct temperatures are obtained after an outer iteration. When this is not the case, convergence can be difficult to obtain. This was noticed when the equations where solved with an iterative method.

When the grid and time step are refined, care should be taken that the numerical representation of the variables (temperatures) is accurate enough. When pyrolysis starts the char zone is very small, and when the time step size limits to zero the char zone will also go to zero thickness, due to the singularity at the start of the pyrolysis phase. As a results the difference of the temperatures of the nodes will reduce, as well will the size of the char cells. When calculating the heat flux problems of numerical accuracy can arise. In the simulation the variables were therefore stored with double precision and for the time step and cell sizes examined, no problems of numerical accuracy came across.

For the "correct solution" 128 of char cells, 128 of virgin cells and a time step size of 0.01 s was used.

6.6.2 Cell size

For a time step of 0.01 s the amount of cells is systemically reduced, typically dived by 2. The following combinations have been simulated:

N_c	4	8	16	32	64	128
N_v	4	8	16	32	64	128

So, in each simulation the number of cells in char and virgin zone were equal.

From Figure 6.7 it can be seen that when the number of cells in the virgin and char layer is reduced, the sharp peak in the mass flux of pyrolysis gases at the start of the simulation is not properly predicted. Reducing the number of cells gives a higher peak at later times. After the peak the mass flux is predicted quiet well for all the combinations. Even the cease time when the front reaches the rear surface is not strongly influenced by the number of cells.

When predicting the surface temperature or the start of pyrolysis, the number of cells should be higher than 32. Fewer cells give a delayed start of pyrolysis (about 15 s delay for 4 cells). A non-uniform grid will allow simulations with fewer cells, see further.

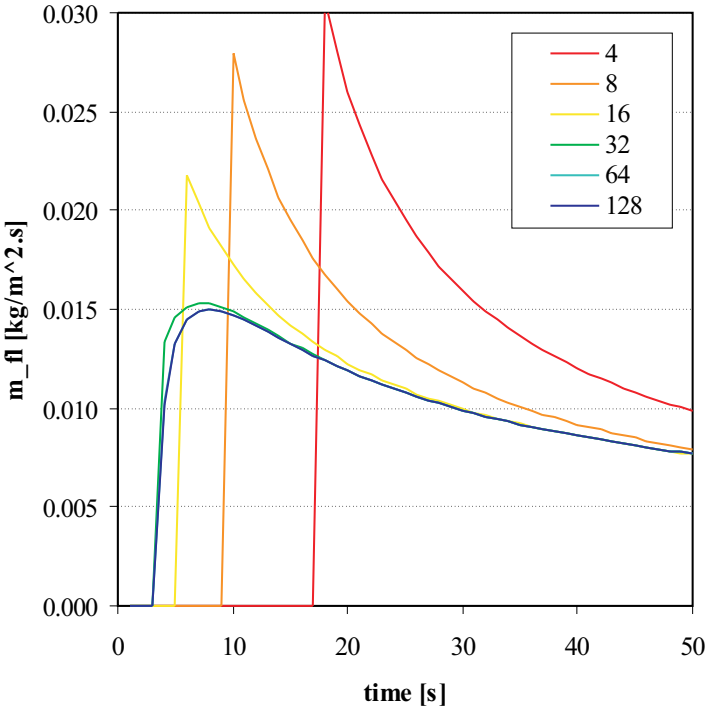

Figure 6.7: Mass flux of pyrolysis gases for different numbers of char and virgin cells

6.6.3 Time step size

For a mesh with 128 cells for the virgin as for the char zone, the time steps is systemically augmented. The following time step sizes have been simulated:

Δt (s)	0.01	0.05	0.1	0.5	1	2

If the time step size is increased too much, the peak in the mass flux of pyrolysis gases is not represented well, see Figure 6.8. For the results after the peak in the mass flux, the size is less critical. Similar conclusions can be drawn for the surface temperature. A time step of 0.1 s seems reasonable.

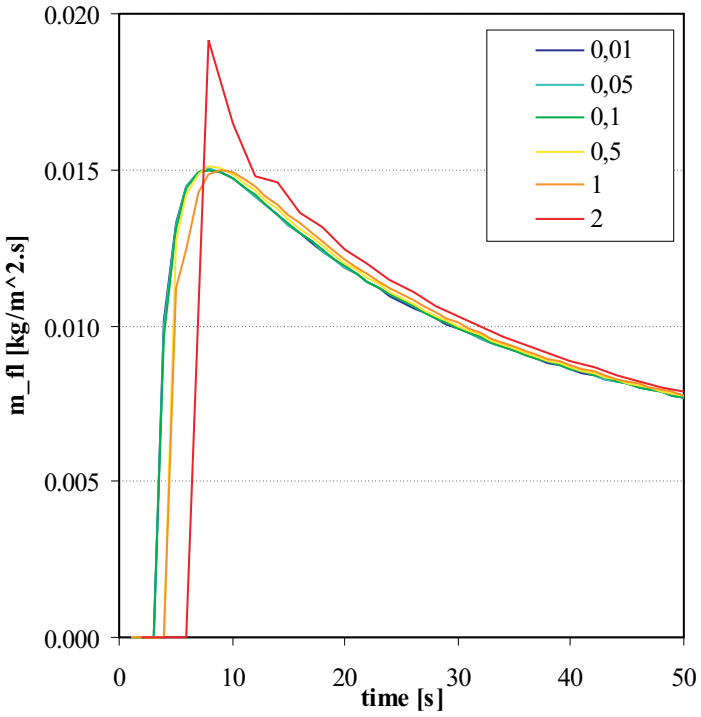

Figure 6.8: Mass flux of pyrolysis gases for different time step sizes

6.6.4 Optimal combination of cell and time step size

For the optimal combination of parameters, the number of cells for the char and virgin material are taken different. The temperature distribution in the char layer is more or less linear during the simulation (the solid/fluid boundary rises slowly in time due to the radiative cooling, while the other boundary is constant at pyrolysis temperature). This can be seen in Figure 6.9 where a typical temperature profile in the solid is given for the pyrolysis phase. Thus fewer cells can be taken for the char layer. For the virgin layer more cells are necessary because the mesh must be able to predict the sharp temperature gradient at the surface at the start of the simulation. A non-equidistant grid will make it possible to use even fewer cells in the virgin layer, as will appear further. The following combinations were simulated and compared:

N_v	32	32	64	64	64	64
N_c	16	16	4	8	16	32
Δt	0.1	0.01	0.1	0.1	0.1	0.1

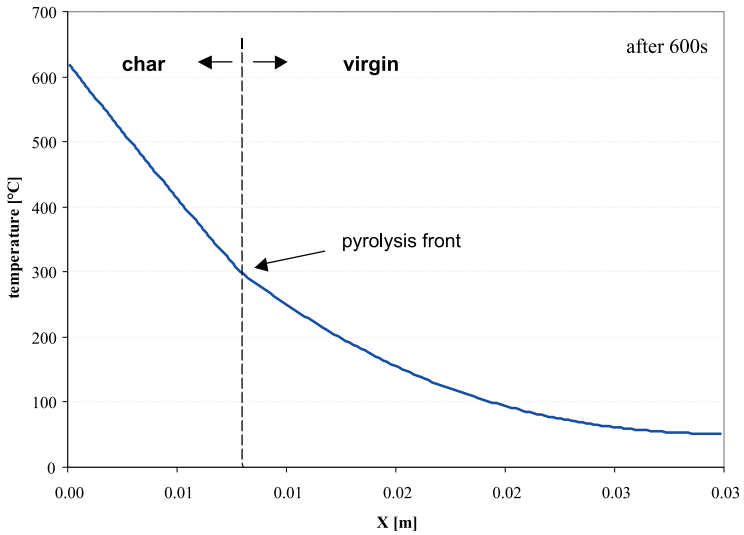

Figure 6.9: Temperature profile during pyrolysis for "Moving mesh"

From the results in Figure 6.10 it is clear that more cells must be taken in the virgin layer than in the char layer. The number of cells in the virgin layer seems to be critical while the number of cells in the char layer seems to have minor influence. Even with four cells in the char layer an acceptable converged solution is obtained, this is of course due to the almost linear temperature profile.

6.6.5 Convergence criteria

To obtain a solution an iterative method is used. In successive iterations the velocity of the pyrolysis front is corrected until the heat flux balance for the front is satisfied. Even when there is no pyrolysis, an iterative method is necessary as the left boundary condition is non-linear, caused by the radiation.

The test for convergence is done on all node temperatures. When the difference of the node temperatures in successive (outer) iterations is smaller than a prescribed percentage of the actual node value, the time step is assumed to be converged. Differences should certainly be smaller than 10^{-5}

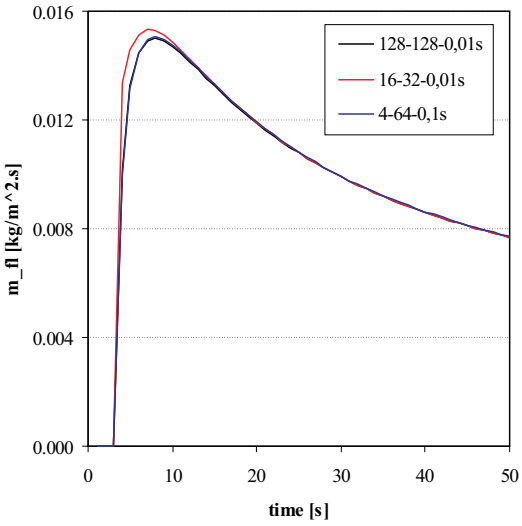

Figure 6.10: Optimal combination of cell sizes and time step

percent of the node value. If larger, the cease time is predicted wrongly. The peak in the mass flux of pyrolysis gases is still predicted well for a 10^{-2} percent convergence criterion, but the cease time is strongly overestimated. Dependent on the application of the results, severe or loose convergence criteria can be applied. If only the first minutes are of interest, the convergence criterion can be taken maximum 10^{-3} percent. If the extinguishment time is important, it should be reduced to 10^{-8}. For a time step of 0.01 s and 0.1 s about 10 outer iterations per time step are necessary.

6.7 Non-equidistant mesh

In the virgin material, the temperature is initially rising only in a small zone. The rest of the virgin material is almost unaffected by the boundary condition (net heat flux for the heating phase and the pyrolysis temperature for the pyrolysis phase). In the "Integral model" this unaffected zone was defined as the zone beyond the thermal penetration depth.

When an equidistant grid is used in the variable char and virgin layers, there are a lot of cells in the unaffected zone. Therefore a non-equidistant grid will perform better with the same amount of cells. The cells are taken finer near the front surface, where the strongest temperature gradient exists.

6.7.1 The progressive mesh

A progressive mesh is used where the length of a cell is equal to the length of the previous cell multiplied by a growth factor:

$$\Delta x_i = a^{i-1} \cdot \Delta x_1 \tag{6.32}$$

The growth factor is constant and the same for all cells. It is given by:

$$a = \left(\frac{\Delta x_1}{\Delta x_{N_v}} \right)^{1/(N_v-1)} \tag{6.33}$$

The ratio of the last cell to the first virgin cell is called the "ratio":

$$\text{ratio} = \frac{\Delta x_1}{\Delta x_{N_v}} \tag{6.34}$$

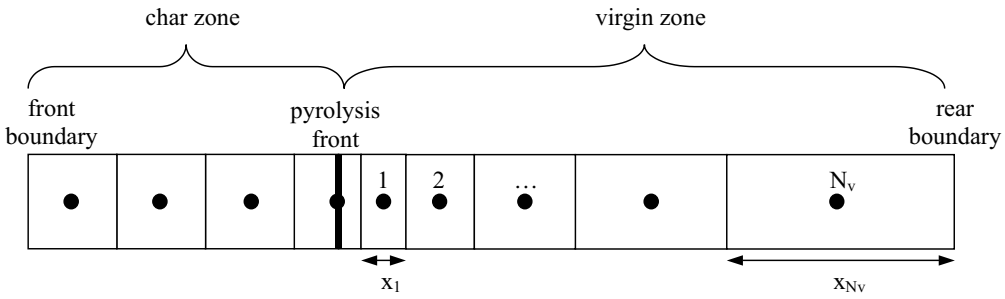

Figure 6.11: Non-equidistant mesh

The velocity of the mesh boundaries in the virgin zone is again determined by the velocity of the pyrolysis front and the location of the mesh boundaries. For volume i (numbering start at 1 for the first volume) the velocity at the west boundary is given by:

$$w_{W,i}^{n+\theta} = 2 \cdot \left(\frac{\mathrm{d}\delta_c}{\mathrm{d}t} \right)^{n+\theta} \cdot \frac{a^{i-1} - a^{N_v}}{3 - a - 2a^{N_v}} \tag{6.35}$$

and for the east boundary

$$w_{E,i}^{n+\theta} = 2 \cdot \left(\frac{\mathrm{d}\delta_c}{\mathrm{d}t} \right)^{n+\theta} \cdot \frac{a^{i} - a^{N_v}}{3 - a - 2a^{N_v}} \tag{6.36}$$

Notice that the mesh velocities are only dependent on the front velocity and the constant growth factor. The thickness of the virgin material nor the location of the pyrolysis front intervene. The mesh in the char zone is the same as in Section 6.4.3.

6.7.2 Results

The results that follow are obtained with an equidistant grid for the char layer, with for each simulation 128 cells (so that this number has no influence on the results anymore), and a progressive grid for the virgin material. The number of cells in the virgin material and the ratio of the length of the first cell to the last cell are varied. Only the first fifty seconds are presented in the figures, which includes the peak in the mass release rate of pyrolysis gases. The rest of the simulation did not contain any extra information.

From the mass release rate of pyrolysis gases in Figure 6.12 it can be seen that the results improve remarkably by introducing a non-equidistant mesh. The equidistant results are for ratio = 1. As the number of cells in the virgin layer decreases, the ratio of the first and last cell has to be increased. If the ratio is too high (for example 80 for case with 16 cells) the results are worse than for a lower ratio (e.g. 40).

In Table 6.1 the error in the prediction of the peak in the mass release rate of pyrolysis gases is given. The cases where the error in the peak of mass flux of pyrolysis gases was lower than 1 % are underlined once, the case were the error was minimal but larger than 1 % are underlined twice. When the number of cells is too low, e.g. the case with 4 and 8 cells, the temperature profile can not be represented accurate enough. Discrepancies occur that cannot be removed by changing the dimensions of the grid (by increase of the ratio). The error is not only located at the peak, but spreads out in time.

The growth factor can be taken very high. Values up to about 1.3 are still tolerable for 16 cells in the virgin layer. When the growth factor is too high, the discretization errors become visible, e.g. the case with 8 nodes and ratio 80.

6.8 Further developments

If this model is expanded into two or three dimensions, the discretization can no longer be done on a rectangular grid. The cell sizes in neighbouring rows or cells perpendicular to the fluid/solid boundary is different. The grid can be transformed into a rectangular grid or the heat flux can be discretized on a non-rectangular grid. Another option is using a unstructured grid.

The variable meshes model can be easily adapted for non-charring materials. The boundary condition, net heat flux, is then directly applied at the fluid/solid interface. The total thickness of the solid is then equal to the thickness of the virgin material.

Swelling of the char material could be incorporated in the model with,

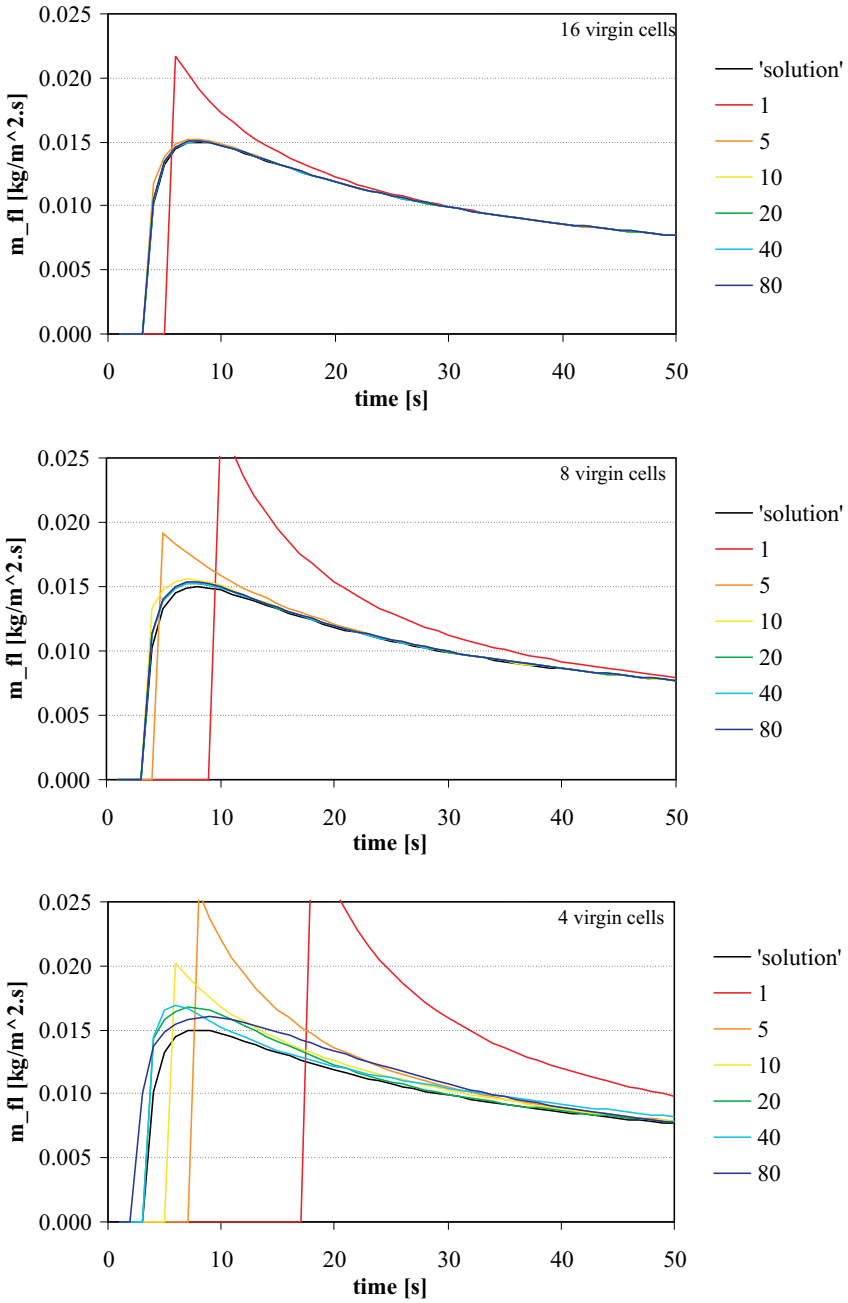

Figure 6.12: Mass flux of pyrolysis gases for 16, 8 and 4 virgin cells and for ratios of 1, 5, 10, 20 ,40 ,80

Table 6.1: Error in the peak in mass release rate of pyrolysis gases (%) (column: number of cells virgin; rows: ratio)

	4	8	16	32	64
1	118.4	91.2	47.8	2.2	0.2
5	75.9	27.9	1.2	0.2	0.005
10	75.9	3.9	0.5	0.1	-
20	11.6	2.1	0.4	0.1	-
40	12.3	2.0	0.4	0.1	-
80	6.6	2.7	0.6	0.1	-

for example, a simple constant expansion coefficient.

6.9 Conclusion

The "Moving meshes model" is similar to the "Integral model". The physical equations that describe the two models, i.e. the two coupled Stefan problems [1], are identical. Only the solution of these models is different. The "Moving meshes model" gives a correct solution of these physical equations (when grid converged), while the "Integral model" always gives approximate results. The "Moving meshes model", hence, can be used to validate the "Integral model" as was already done in Chapter 5.

When using the "Moving meshes model", a non-equidistant mesh should be used in the virgin zone. This grid needs much less cells and thus calculation time. The growth factor for the mesh can be taken up to 1.3.

Chapter 7

Reaction of solid material - Enthalpy model

7.1 Introduction

In the "Enthalpy method" the explicit tracking of the pyrolysis front, i.e. the interface between the virgin and the char layer is bypassed. The front is not forced on the solution of the char and virgin layer, as was done in the "Integral" and "Moving grid" model of Chapter 5 and 6, but is obeyed automatically as a "natural boundary condition".

The enthalpy solution approach is based on the energy conservation law in primitive form:

$$\int_t^{t+\Delta t} \frac{\mathrm{d}}{\mathrm{d}t} \left(\int_V E \mathrm{d}V \right) \mathrm{d}t \;=\; \int_t^{t+\Delta t} \int_S -\dot{\mathbf{q}}'' \cdot \mathbf{n} \, \mathrm{d}S \, \mathrm{d}t \tag{7.1}$$

where E is the energy density (per unit volume) and $-\dot{\mathbf{q}}'' \cdot \mathbf{n}$ is the heat flux into the volume V across its boundary S. The distinct advantage of this primitive form is that it is valid irrespective of layer, and even if E and $\dot{\mathbf{q}}''$ experience jumps. It is more general than the localized differential form:

$$\frac{\partial}{\partial t} E + \nabla \cdot (\dot{\mathbf{q}}'') = 0 \tag{7.2}$$

For smooth E and $\dot{\mathbf{q}}''$ Equations 7.1 and 7.2 are equivalent, but at the pyrolysis front the partial differential Equation 7.2 can only be interpreted in the classical point wise sense inside each phase separately. The conservation across the interface must be imposed explicitly as an additional interface or boundary condition, making front-tracking necessary [1]. The original problem is then separated in two coupled Stefan problems.

In the "Enthalpy method" the conservation of energy will be applied across the pyrolysis front. Only the one-dimensional formulation will be given. The expansion to two and three dimensions is straightforward.

7.2 Discretization

The first step in the "Enthalpy method" is already the space discretization. The solid is divided into a finite number of control volumes V_i which remain steady during the calculation. A volume changes from virgin over "mushy" into char, see Figure 7.1. The virgin or char volumes contain respectively pure virgin or char material. A mushy cell exists of a mix of virgin and char material, and contains the "interface" or the pyrolysis front. It can be seen as a pyrolysis zone with finite thickness. The mushy control volume is assumed at pyrolysis temperature. It can move maximum one cell per time step. As the pyrolysis zone in this method is described by a whole cell, i.e. the mushy cell, the results of the method will strongly be dependent on the grid chosen.

Instead of a "front-tracking" scheme, the method becomes "volume-tracking". The movement of the mushy front is showed in Figure 7.1.

7.3 Models equations

7.3.1 Conservation of energy

The heat flux term in the general energy equation is divided into a conductive and a convective term:

$$\int_t^{t+\Delta t} \frac{\mathrm{d}}{\mathrm{d}t}\left(\int_V E \mathrm{d}V\right)\,\mathrm{d}t \;=\; \int_t^{t+\Delta t}\int_{\partial V} -\dot{\mathbf{q}}''_{cond}\cdot\mathbf{n}\,\mathrm{d}S\,\mathrm{d}t \;+\; \int_t^{t+\Delta t}\int_{\partial V} -\dot{\mathbf{q}}''_{pyr}\cdot\mathbf{n}\,\mathrm{d}S\,\mathrm{d}t \quad (7.3)$$

The convective term represents the transport of the pyrolysis gases to the surface, while the conductive terms represent the pure conductive heat fluxes. The energy conservation is applied for each control volume V_i. Each equation is discretized at $n+\theta$ which gives the new energy density E_i^{n+1}:

$$E_i^{n+1} = E_i^n + \frac{\Delta t}{\Delta x_i}\left[\left(\dot{q}''^{n+\theta}_{cond,i-1/2} - \dot{q}''^{n+\theta}_{cond,i+1/2}\right) + \left(\dot{q}''^{n+\theta}_{pyr,i-1/2} - \dot{q}''^{n+\theta}_{pyr,i+1/2}\right)\right] \quad (7.4)$$

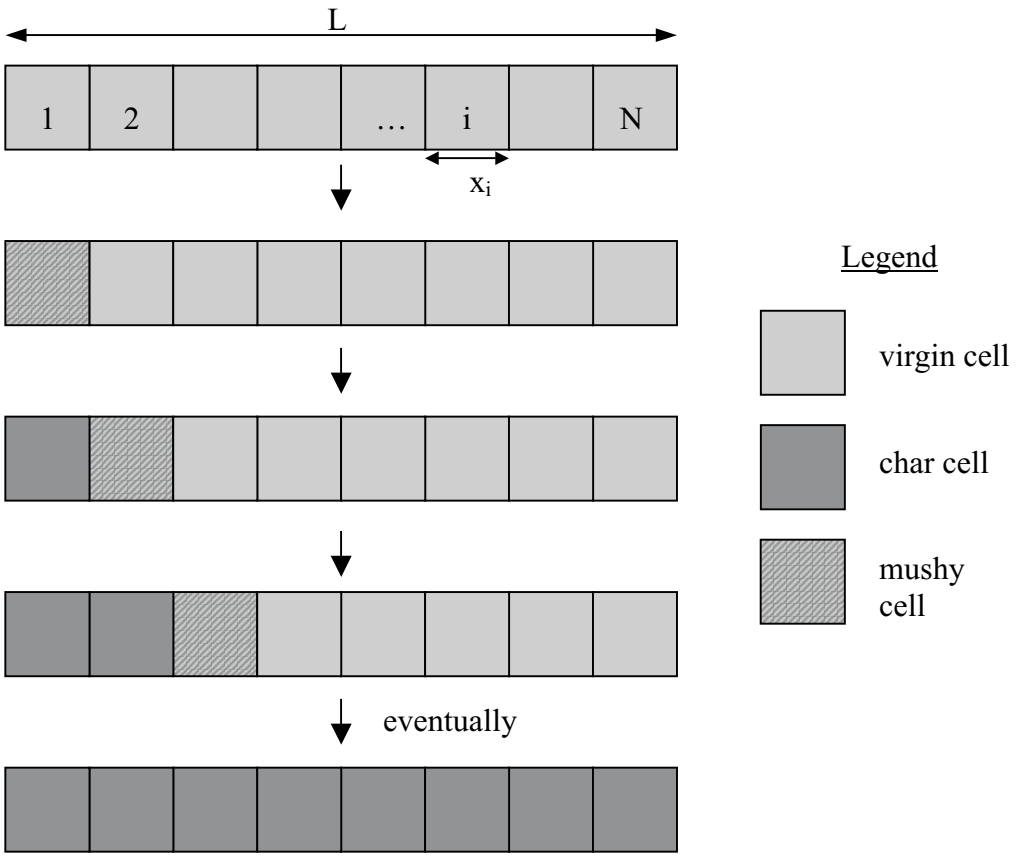

Figure 7.1: Movement of mushy front

7.3.2 State equation

The equation of state determines whether a volume is virgin, mushy, or char. For modelling the pyrolysis process with the "Enthalpy method", care must be taken in the equation of state. The "Enthalpy method" as proposed by Alexiades [1] was developed for melting processes. The transition from solid to liquid is reversible, while for the pyrolysis process it is irreversible: once char has been formed it can not be transformed again into virgin material. On Figure 7.2 the vertical line (at T_{pyr}) represents the pyrolysis process. This is a one way reaction, the energy density will rise monotonous. While for the heating of the char and virgin material, energy can rise and fall dependent on the heating conditions.

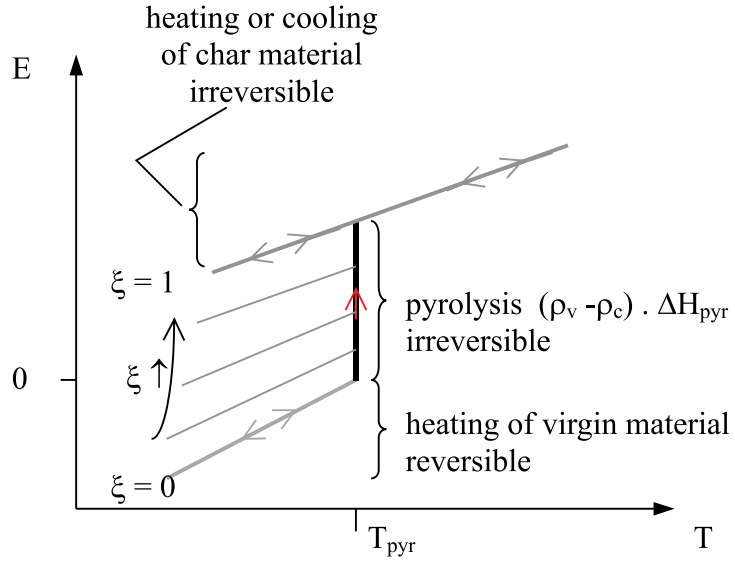

Figure 7.2: Relation energy density and temperature

The state of a volume is described by the char volume fraction ξ_i:

If $\xi_i = 0$	$\Longrightarrow$	a pure virgin cell
If $0 < \xi_i < 1$	$\Longrightarrow$	a mushy cell (contains char, virgin and interface)
If $\xi_i = 1$	$\Longrightarrow$	a pure char cell

For a virgin cell where the pyrolysis front has just entered, the enthalpy of the cell is given by:

$$E_i = 0 \quad \Longrightarrow \quad \xi_i = 0$$

while for a cell where the pyrolysis front has just left, the enthalpy of the cell is given by:

$$E_i = (\rho_v - \rho_c) \cdot \Delta Q_{pyr} \quad \Longrightarrow \quad \xi_i = 1$$

Both cells are at pyrolysis temperature. For a mushy cell the char volume fraction is determined by:

$$\xi_i = \frac{E_i}{(\rho_v - \rho_c) \cdot \Delta Q_{pyr}}$$

The char fraction is calculated from the energy density E_i^{n+1}. If in the previous time step the volume was a virgin cell, then the new char fraction is given by:

$$\xi_i^n = 0 \quad \Longrightarrow \quad \xi_i^{n+1} = \max\left(0; \frac{E_i^{n+1}}{(\rho_v - \rho_c)\Delta Q_{pyr}}\right) \quad < 1 \tag{7.5}$$

The new value ξ_i^{n+1} must be smaller than 1 because it is assumed that in a single time step a cell can not be transformed from virgin into char. Each cell must undergo the "mushy phase". In the code it is checked that the new char fraction does not exceed unity.

Once char has been formed in a volume, it can not be transformed into virgin again. When a mushy cell is cooling down, this implies that the temperature is lower than the pyrolysis temperature, the char fraction will remain equal. When the mushy cell is at pyrolysis temperature and its internal heat is increasing, the char fraction will of course increase:

$$0 < \xi_i^n < 1 \quad \Longrightarrow \quad \xi_i^{n+1} = \min\left(\xi_i^n; \frac{E_i^{n+1}}{(\rho_v - \rho_c)\Delta Q_{pyr}}; 1\right) \tag{7.6}$$

Once a volume has become pure char, it remains pure char, so:

$$\xi_i^n = 1 \quad \Longrightarrow \quad \xi_i^{n+1} = 1 \tag{7.7}$$

7.4 Temperature calculation

The energy density E is defined as the sum of the sensible energy and the pyrolysis energy. Zero energy density is defined by virgin material at pyrolysis temperature, so the energy density for virgin material is given by:

$$E_i = \int_{T_{pyr}}^{T_i} \rho_v c_v(T) \mathrm{d}T \qquad \text{with} \quad T_i < T_{pyr} \tag{7.8}$$

For the char material it is given by:

$$E_i = \int_{T_{pyr}}^{T_i} \rho_c c_c(T)\mathrm{d}T \ + \ (\rho_v - \rho_c) \cdot \Delta Q_{pyr} \tag{7.9}$$

And for a mushy cell, the energy density E_i is given by the sum of the energy of the virgin and char material:

$$E_i = \xi_i \cdot \left(\int_{T_{pyr}}^{T_i} \rho_c c_c(T)\mathrm{d}T \ + \ (\rho_v - \rho_c) \cdot \Delta Q_{pyr} \right) + (1 - \xi_i) \cdot \left(\int_{T_{pyr}}^{T_i} \rho_v c_v(T)\mathrm{d}T \right) \quad T_i \leq T_{pyr} \tag{7.10}$$

The temperature of a volume is determined by both the energy density and the char fraction. When a constant heat capacity is assumed, the temperature can be determined immediately out of Equations 7.8 and 7.10. When the heat capacity is variable, an implicit equation must be solved.

When constant heat capacity is assumed, the temperature for a virgin volume is given by:

$$\xi_i^{n+1} = 0 \quad \Longrightarrow \quad T_i^{n+1} = T_{pyr} + \frac{E_i^{n+1}}{\rho_v c_v} \tag{7.11}$$

The temperature of a mushy volume depends on whether the volume is pyrolyzing or not. If the volume is pyrolyzing then:

$$\xi_i^{n+1} = \frac{E_i^{n+1}}{(\rho_v - \rho_c)\Delta Q_{pyr}} \quad \Longrightarrow \quad T_i^{n+1} = T_{pyr} \tag{7.12}$$

If the volume is not pyrolyzing, then:

$$\xi_i^{n+1} > \frac{E_i^{n+1}}{(\rho_v - \rho_c)\Delta Q_{pyr}} \quad \Longrightarrow \quad T_i^{n+1} = T_{pyr} + \frac{E_i^{n+1} \ - \ \xi_i^{n+1}(\rho_v - \rho_c)\Delta Q_{pyr}}{\xi_i^{n+1}\rho_c c_c \ + \ (1 - \xi_i^{n+1})\rho_v c_v} \tag{7.13}$$

The new node temperature should be lower than the pyrolysis temperature. Once the temperature of the mushy cell exceeds the pyrolysis temperature, the pyrolysis reactions can again proceed, and the mushy control volume is set at pyrolysis temperature.

The temperature of a char volume is given by:

$$\xi_i^{n+1} = 1 \quad \Longrightarrow \quad T_i^{n+1} = T_{pyr} + \frac{E_i^{n+1} - (\rho_v - \rho_c)\Delta Q_{pyr}}{\rho_c c_c} \tag{7.14}$$

When the heat capacity is a function of the temperature, e.g. expressed by a polynomial, the state equation becomes an algebraic equation that can be solved with a Newton-Raphson method.

7.4.1 Conductive heat flux

The conductive heat flux is given by the law of Fourier:

$$\dot{\mathbf{q}}''_{cond} = \lambda \frac{\mathrm{d}T}{\mathrm{d}x}$$

When this is discretized centrally in a medium with variable thermal conductivity, this gives:

$$\dot{q}''_{cond,i-1/2} = -\frac{T_i - T_{i-1}}{R_{i-1/2}} \tag{7.15}$$

with

$$R_{i-1/2} = \frac{\frac{1}{2}\Delta x_{i-1}}{k_{i-1}} + \frac{\frac{1}{2}\Delta x_i}{k_i} \tag{7.16}$$

and where k is the effective thermal conductivity.

The calculation of Equation 7.15 is straightforward when the heat flux is calculated at the interface between two similar cells, i.e. two char or two virgin cells. The effective conductivity is equal to the thermal conductivity of the pure material.

When the heat flux between a mushy cell and a char or virgin cell must be calculated, it is no longer clear which conductivity to use for the mushy cell. The effective conductivity of a mushy control volume depends on the structure of the pyrolysis front. Alexiades & Solomon [1] proposed : the sharp front, the columnar front, an amorphous mixture of virgin and char material, and a "Kirchoff" transformation. The solution is sensitive to the "front model" chosen. As the sharp front and the "Kirchoff" transformation give two extreme values, these are further described.

7.4.1.1 Sharp front

In this front representation the mushy cell contains a layer of virgin material, a pyrolysis front, and a char layer in a serial arrangement. The effective thermal conductivity is then given by:

$$\frac{1}{k_i} = \frac{\xi_i}{\lambda_c(T_i)} + \frac{(1-\xi_i)}{\lambda_v(T_i)} \tag{7.17}$$

7.4.1.2 "Kirchoff" transformation

In the "Kirchoff" transformation [1] the temperature T is replaced by the "Kirchoff" temperature u which incorporates the thermal conductivity:

$$u = \begin{cases} \int_{T_{pyr}}^{T} \lambda_v(T)\mathrm{d}T & \text{if virgin} \\ \int_{T_{pyr}}^{T} \lambda_c(T)\mathrm{d}T & \text{if char} \end{cases} \tag{7.18}$$

The transformation is only possible when the conductivity is a function of temperature only. For constant conductivity the "Kirchoff" temperature is given by:

$$u = \begin{cases} \lambda_v(T - T_{pyr}) & \text{if virgin} \\ 0 & \text{if mushy } (T = T_{pyr}) \\ \lambda_c(T - T_{pyr}) & \text{if char} \end{cases} \tag{7.19}$$

or in general on a discretized grid:

$$u_i = \lambda_i(T_i - T_{pyr}) \tag{7.20}$$

The conductive heat flux can now be written as:

$$\dot{q}''_{cond} = -\lambda \frac{\mathrm{d}T}{\mathrm{d}x} = -\frac{\mathrm{d}u}{\mathrm{d}x} \tag{7.21}$$

The discrete heat flux becomes:

$$\dot{q}''_{cond,i-1/2} = \frac{u_{i-1} - u_i}{\frac{1}{2}\Delta x_i + \frac{1}{2}\Delta x_{i-1}} \tag{7.22}$$

$$= \frac{T_{i-1} - T_{pyr}}{(\frac{1}{2}\Delta x_i + \frac{1}{2}\Delta x_{i-1})/\lambda_{i-1}} + \frac{T_{pyr} - T_i}{(\frac{1}{2}\Delta x_i + \frac{1}{2}\Delta x_{i-1})/\lambda_i} \tag{7.23}$$

For two similar cells this gives the same result as Equation 7.15, while for the heat flux at the boundary $i - 1/2$ of a mushy cell i, the second term disappears and gives:

$$\dot{q}''_{cond,i-1/2} = \frac{T_{i-1} - T_{pyr}}{(\frac{1}{2}\Delta x_i + \frac{1}{2}\Delta x_{i-1})/\lambda_{i-1}} \tag{7.24}$$

It is assumed that the mushy cell does not contribute to the heat flux or acts still as a virgin cell. Thus the conductivity of the mushy control volume is not needed.

7.4.2 Convective heat flux

The convective flux consists of the sensible energy of the pyrolysis gases that are flowing through the char layer:

$$\dot{q}''_{pyr} = \dot{m}''_{pyr} \cdot h_{pyr}(T) = \dot{m}''_{pyr} \cdot c_{pyr}(T) \cdot T \tag{7.25}$$

Discretized for the one-dimensional case with an upward differencing scheme, this becomes:

$$\dot{q}''_{pyr,i-1/2} = \dot{m}''_{pyr,i} \cdot h_{pyr}(T_i) = \dot{m}''_{pyr,i} \cdot c_{pyr}(T_i) \cdot T_i \tag{7.26}$$

7.4.3 Conservation of mass

The mass flux of volatiles or pyrolysis gases is determined by the change of the total mass of the solid. The total mass is given by:

$$m_{tot} = \sum_i \Big(\rho_c \cdot \xi_i \cdot V_i + \rho_v \cdot (1 - \xi_i) \cdot V_i \Big) \tag{7.27}$$

The change of the total mass with time is then given by:

$$\frac{\mathrm{d}m_{tot}}{\mathrm{d}t} = \sum_i \left(\rho_c \cdot \frac{\mathrm{d}\xi_i}{\mathrm{d}t} \cdot V_i - \rho_v \cdot \frac{\mathrm{d}\xi_i}{\mathrm{d}t} \cdot V_i \right) = \sum_i \left(\rho_c - \rho_v \right) \cdot \frac{\mathrm{d}\xi_i}{\mathrm{d}t} \cdot V_i \tag{7.28}$$

or

$$\dot{m}''_{pyr} = -\frac{\mathrm{d}m''_{tot}}{\mathrm{d}t} = \sum_i \left(\rho_v - \rho_c \right) \cdot \frac{\mathrm{d}\xi_i}{\mathrm{d}t} \cdot \Delta x_i \tag{7.29}$$

The summation reduces to the mushy cells only.

7.5 Solution of discretized equations

There is no need to make a distinction in different phases, as was required for the “Moving meshes model” and the “Integral model”. This is a serious advantage of the “Enthalpy” model.

The Cranck-Nicholson method is used for the time discretization of Equation 7.1. The pseudo-time stepping technique requires an iterative method. The iterations are stopped when differences between the change in the energy density in between iterations, is smaller than a percentage of the value, see the solution scheme of Figure 7.3.

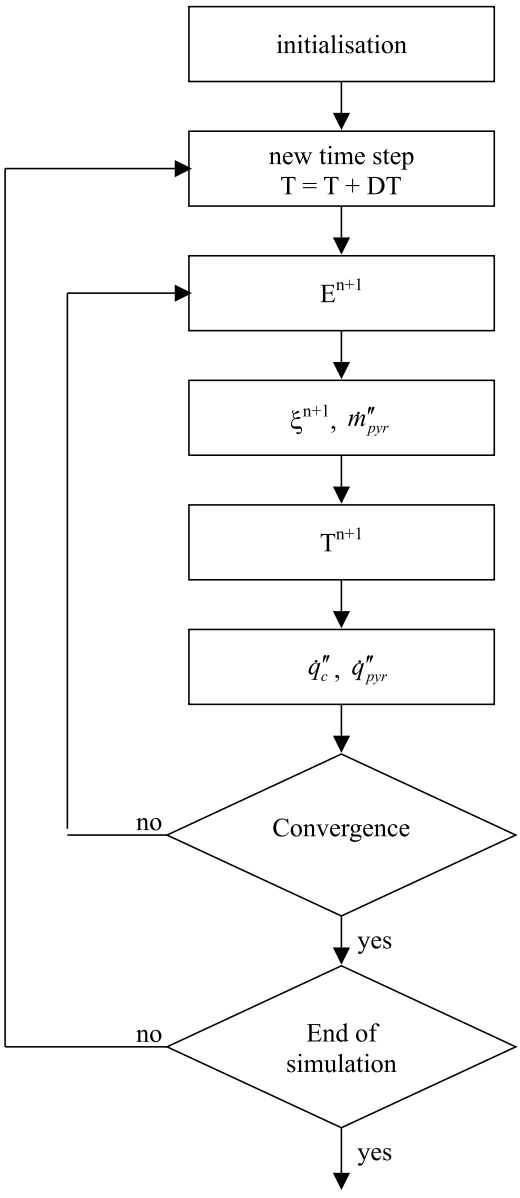

Figure 7.3: Solution scheme

The pyrolysis front can advance maximum one control volume per time step. To fulfil this demand, the time step has to be limited by:

$$\Delta t < \frac{\Delta x}{W} = \frac{\Delta x}{\left(\frac{\mathrm{d}\delta}{\mathrm{d}t}\right)_{max}} = \frac{(\rho_v - \rho_c) \cdot \Delta x}{\dot{m}''_{pyr,max}} \tag{7.30}$$

For the cases examined ($\rho_v = 650$, $\rho_c = 350\mathrm{kg/m^3}$ and $\dot{m}''_{pyr,max} = 0.015$ $\mathrm{kg/m^2.s}$)

$$\Delta t < \frac{\Delta x}{5\,10^{-5}}$$

The maximum pyrolysis rate was determined with the "Moving mesh" method. When using the "Enthalpy method", the maximum pyrolysis rate can be remarkably higher (see results). When the time step is too large, instabilities occur, and a solution can not be found. The time step size must be much smaller than the maximum time step given by Equation 7.30. So in practical calculations this equation is not enough restrictive.

7.6 Determination of time step and cell size

The physical properties and boundary conditions that were used for the simulations are the same as in the previous chapters and are given in Section 4.4 of Chapter 4. The correct solution of the simulations can be determined with the "Moving grid" model of Chapter 6.

7.6.1 Number of cells

Different cell sizes or number of cells are simulated for a small time step and a very strict convergence criterion. The release of pyrolysis gases is given in Figure 7.4. It is clear that a true grid independent solution does not exist for the number of cells examined. The mass release always drop to zero when the pyrolysis front is standing in between cells. The time and duration of these drops are determined by the grid. Only for an infinite number of cells the solution of the "Enthalpy method" will resemble the solution of the "Moving mesh" method.

The volatiles are released stepwise. When a cell is "mushy", the pyrolysis front is passing through the cell and volatiles are released. Once the pyrolysis reaction are finished, the cell becomes a char cell. Immediately after this conversion, the next cell will still be 100 percent virgin. The temperature of the cell can not yet be higher than the pyrolysis temperature, as the mushy

cell was constantly on pyrolysis temperature. Therefore, the front is located in between cells (see Figure 7.5), and no mushy cell is present. Consequently the mass release rate of pyrolysis gases drops to zero.

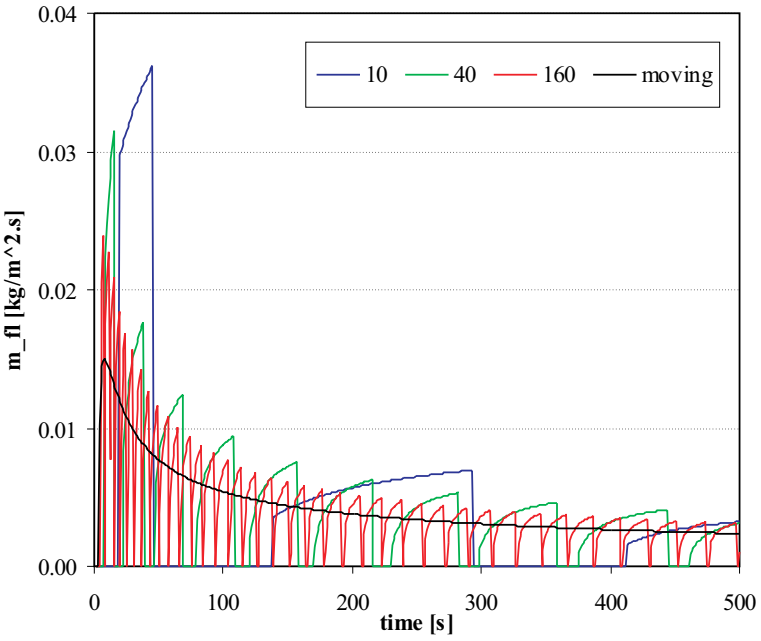

Figure 7.4: Mass flux of pyrolysis gases for different numbers of cells

Note in Figure 7.4, that the mass flux of pyrolysis gases increases during the pyrolysis of a cell. When compared with the "Moving grid", it can be concluded that this is not realistic. This increase in the mass flux is caused by the heat flux calculations and thus the definition of the effective resistance. When a mushy, pyrolyzing cell is considered, the west heat flux quickly reaches a steady state value. Thus, there is a constant input of energy to the cell. The east heat flux (heat flowing to the virgin material) is decreasing with the advancement of the pyrolysis in the cell, and thus the pyrolysis reactions will increase as well.

When the number of cells is increased, the peaks become smaller and tend to each other; the time intervals in between peaks is smaller. But even for 1280 cells (this is not shown in Figure 7.4) the mass flux of pyrolysis gases drops to zero when the front is in between cells.

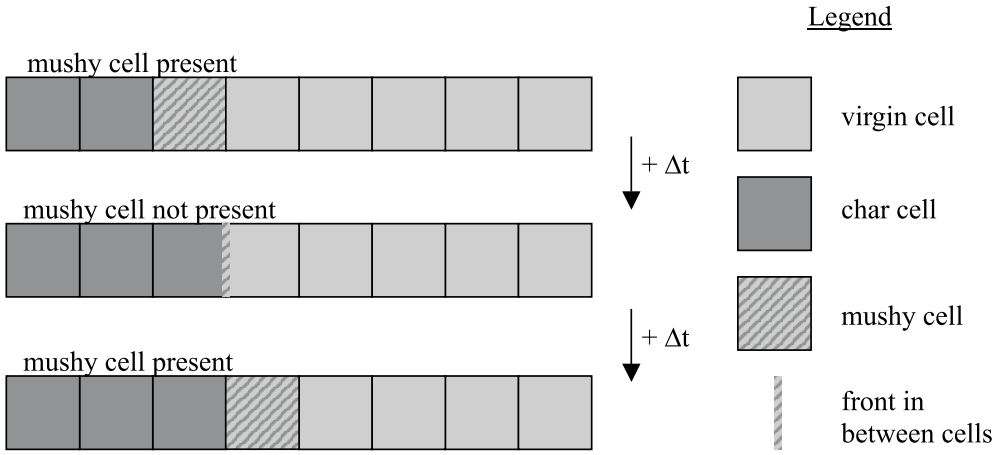

Figure 7.5: Possible configurations during pyrolysis

7.6.2 Surface temperature

In the simulations the surface temperature suddenly decreases after about 10 s, see Figure 7.6, for a constant imposed external heat flux. This unrealistic prediction is due to the extrapolation of the surface temperature. Once the first cell is pyrolyzing, its temperature remains constant (equal to pyrolysis temperature). The temperature in the second cell will continuously rise, and the extrapolation scheme

$$T_{surface} \;=\; T_1 \;+\; 0.5 \cdot \Big(T_1 - T_2 \Big) \tag{7.31}$$

will give lower surface temperatures.

When the cells are larger, it takes longer for a cell to pyrolyse. Thus the first cell will be longer on pyrolysis temperature and subsequent the surface temperature will decrease longer.

Temperatures reach quite fast a steady state, see Figure 7.6. Each time when a cell is pyrolyzing, the temperature west of it remains constant. Normally the heat flux at the mushy cell should change with time, and thus the temperature left and right of the mushy cell should change as well, but the thermal conductivity for virgin and char material is for these cases the same. Therefore, the conductive heat flux does not change, and the cells in between the front surface and the pyrolyzing cell will reach a steady state. The cells deeper in the solid (right of the pyrolysis cell in Figure 7.5) do not reach a steady state because the heat flux from the pyrolysis cell to the virgin cell is dependent on the char fraction in the pyrolysis cell and thus on the advancement of the pyrolysis front.

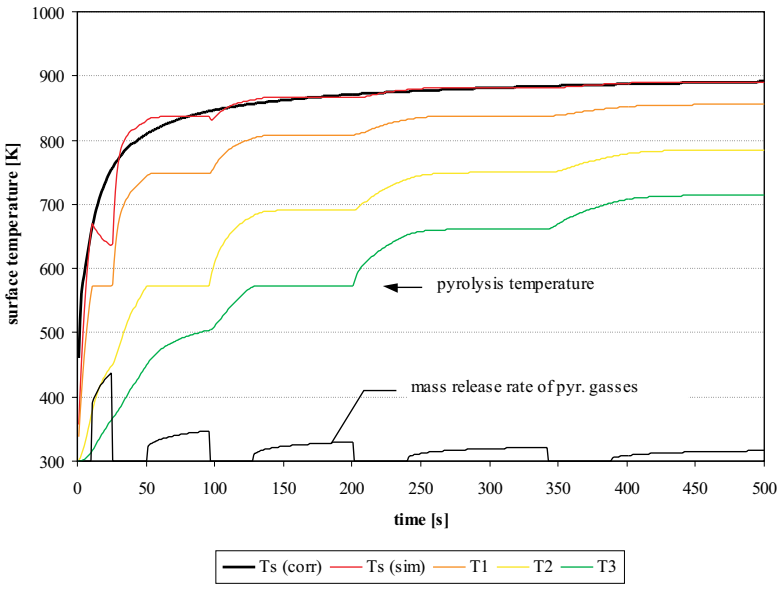

Figure 7.6: Node temperatures T_1, T_2, T_3

7.6.3 Time step size

To obtain a time step converged solution, very small time steps must be taken. For 20 cells, time steps of 0.05 s or smaller were required (see Figure 7.7). For a coarse grid, there is actually no need to minimise the time step until the solution at every time step does not change anymore, because the error of the space discretization is much larger. A time step of 0.5 s is already acceptable for 20 cells. Of course when more cells are used, the acceptable time step size will change. For the case with 200 cells time steps must be smaller than 0.05 s due to stability considerations. Because of these small time step sizes a time step converged solution was already obtained. It seems that the stability considerations are most important for determining the size of the time step. Only for large cells the time step should be smaller than the critical time step size needed for stability.

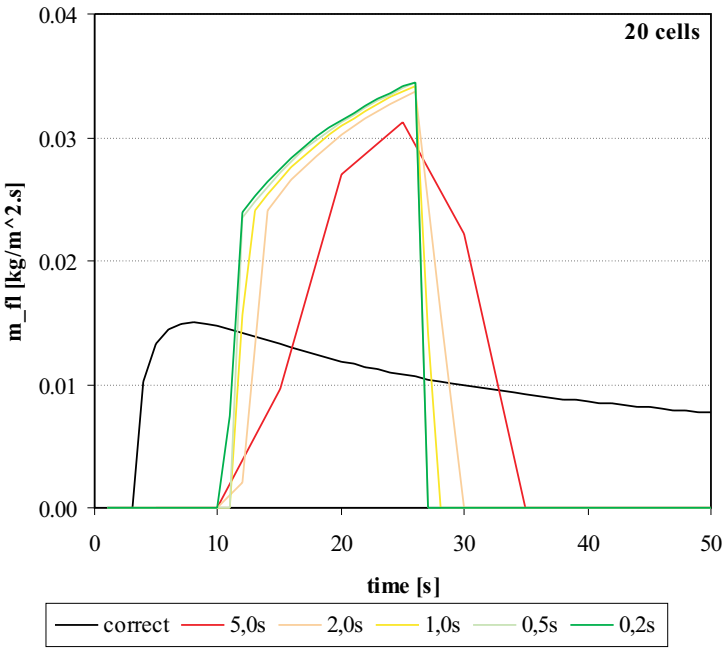

Figure 7.7: Mass flux of pyrolysis gases for different time steps

7.7 Model improvement

The results of the relative simple "Enthalpy method" are not satisfying. The oscillations in the mass flux of pyrolysis gases are unrealistic and unacceptable. In the opinion of the author, the "Enthalpy model" should be capable to perform much better. Therefore several ideas were tried to improve the "Enthalpy model".

7.7.1 Time averaged results

The results of several *small* time steps in the "Enthalpy model" can be averaged. The *final* results are then, of course, given for time steps larger than the actual used time step in the "Enthalpy model". When the grid is fine the pyrolysis front will have moved through several cells during one large *final* time step. Because of the averaging, the zero mass release periods will disappear, with a smooth mass release as result. For the application we have in mind (fire spread simulation), the *large* time step will be the time step taken by the CFD code.

Results can be found in Figure 7.8 where the averaging was done for 1 s:

$$\overline{\dot{m}''_{fl}} = \int_{\Delta t=1\,\mathrm{s}} \dot{m}''_{fl}(t)\mathrm{d}t \tag{7.32}$$

The number of nodes is relatively high because in 1 s there have to be several peaks to obtain a nicely averaged value. If the period between these drops is larger than 1 s the averaging has little or no effect (see the case of 160 nodes). The mean error [1] for 500 s, if compared with the "Moving grid" method, is for 160 cells 29.4%, for 320 cells 19.3%, 640 cells 10.8%, and for 1280 cells 5.0%. The disadvantage of this method is that a large number of cells is required.

7.7.2 Staggered grid

As the results are dependent on the grid, it was thought that the results could be made more or less grid independent by introducing a second grid. The first grid is as in Section 7.2, while the second grid was staggered to the first one, see Figure 7.9. The results of both calculations are afterwards averaged.

[1] the mean error is defined as the mean of the difference between the simulation results and the correct solution at every second. error $= \frac{1}{\text{total steps}} \sum_{i=1}^{\text{endtime}} \Big(\dot{m}''_{pyr,sim}(t + i \cdot 1\,\mathrm{s}) - \dot{m}''_{pyr,correct}(t + i \cdot 1\,\mathrm{s}) \Big) / \dot{m}''_{pyr,correct}(t + i \cdot 1\,\mathrm{s}) \cdot 100$

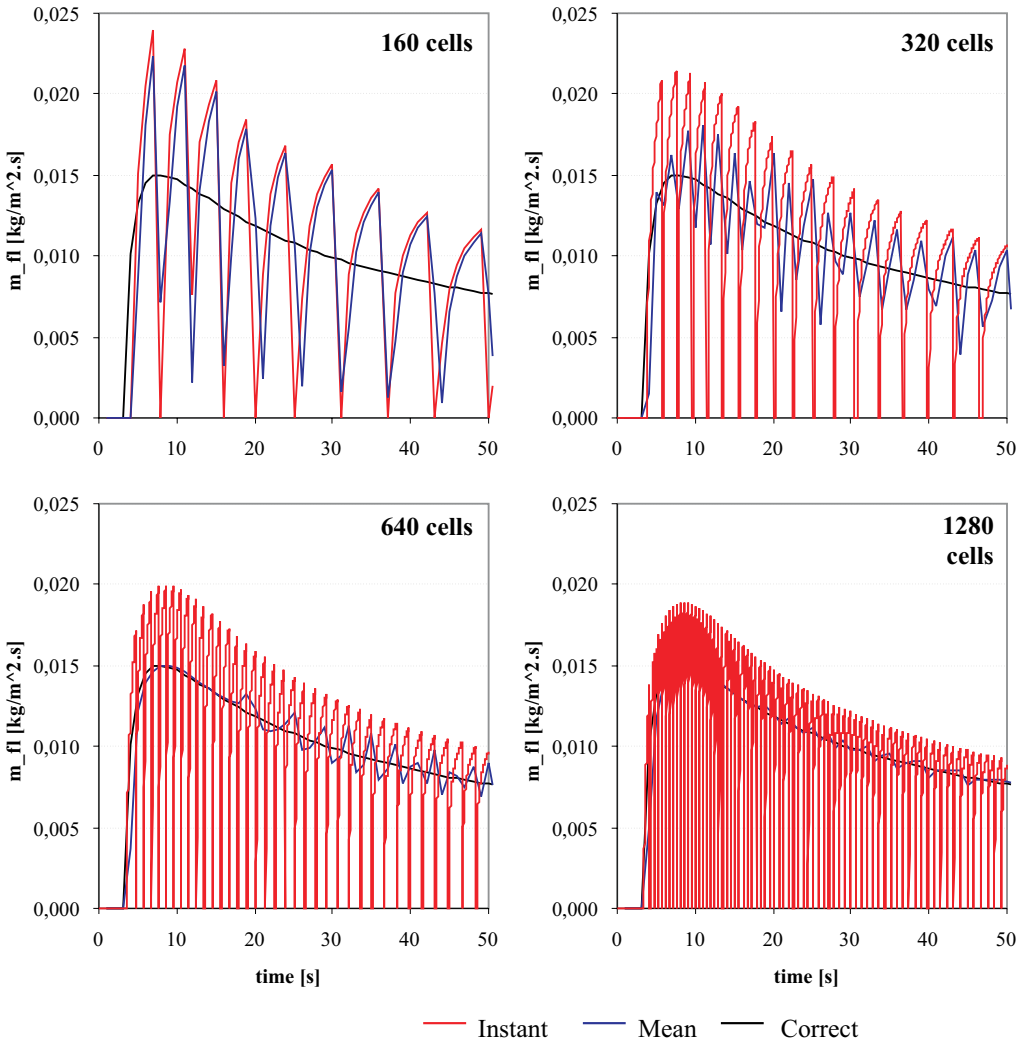

Figure 7.8: Instant and mean mass flux for 160, 320, 640, and 1280 cells

In the staggered grid, a node was placed on the boundary of the solid. This means that the first node gives the surface temperature.

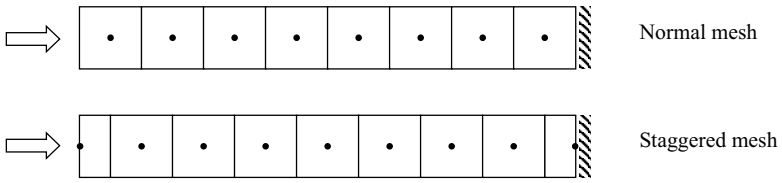

Figure 7.9: Normal and staggered grid

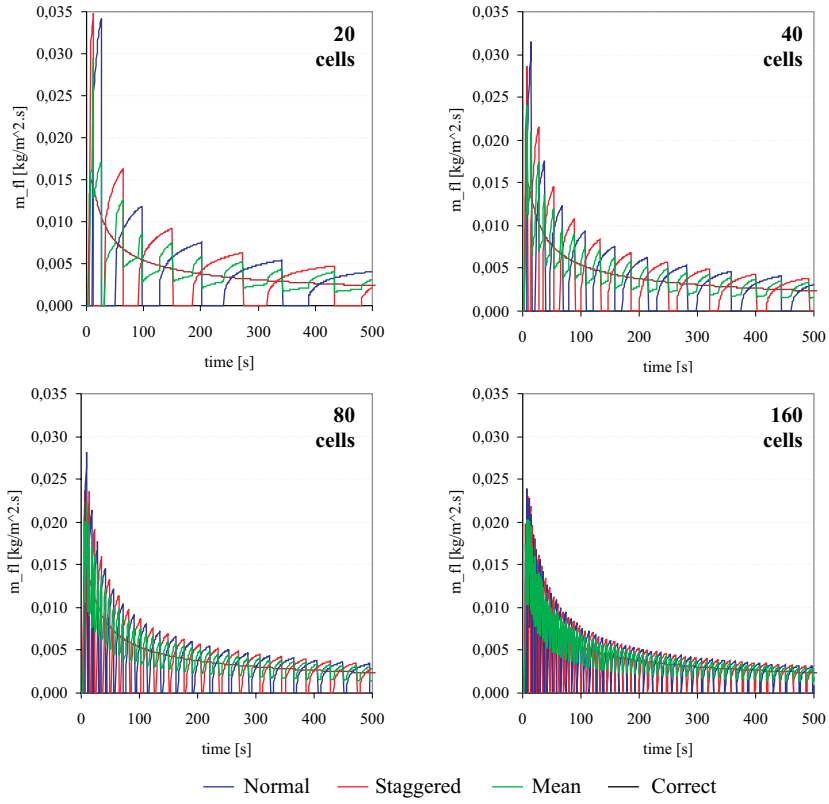

Figure 7.10: Mass flux for the averaged results of the normal and the staggered grid

The time intervals were the mass flux drops to zero, i.e. where the pyrolysis front is in between cells, occur at different times. It was hoped that in the averaged results, the grid dependence was minimised.

In Figure 7.10 the release of volatiles is shown for a different number of cells. By taking the average mass flux of the two grids, the periods of zero mass flux disappear. Still oscillations in the mass release are present. Increasing the number of cells does not improve the simulation. The oscillations round the "Moving mesh" solution remain present. With more cells the frequency of the oscillations is higher, but the amplitude does not seem to decrease.

7.7.3 Variable first cell

Further improvement can be made by using 4 or more different grids instead of only two or one. The disadvantage is that the calculation time increases linearly with the amount of grids. In this method the first node is placed in the middle of the first volume, see Figure 7.11. This is different from the first staggered method where the first node was placed on the surface of the solid. The first volume has a variable size, determined by the coefficient a.

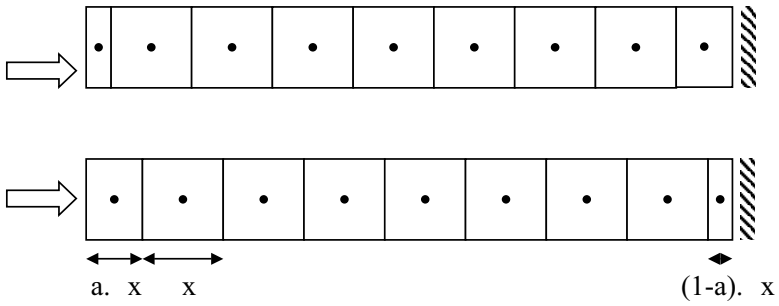

Figure 7.11: Variable first cell

The length of the first cell is given by:

$$\Delta x_1 = a \cdot \Delta x \tag{7.33}$$

while for the last cell:

$$\Delta x_N = (1 - a) \cdot \Delta x \tag{7.34}$$

The averaged results for 2 (normal and staggered, with node on surface), 4 (a = 0.25, 0.50, 0.75 and 1.0) and 10 (a = 0.1, 0.2, 0.3, 0.4, 0.5, 0.6, 0.7, 0.8, 0.9 and 1.0) grids are given in Figure 7.12. In each grid 21 cells were used. As the number of grids increases, the results are getting better: the average error compared with the "Moving mesh" method is 31.3% for the 2

grids, 20.5% for the 4 grids and only 8.2% for the 10 grids for the first 500 s. The error is largest at the start of pyrolysis. At the end of the simulation the results of the 10 grids almost resemble the results of the "Moving mesh" method.

The error in the surface temperature is a lot smaller: 0.5% for the 2 grids, 0.3% for the 4 grids and 0.2% for the 10 grids for 500 s.

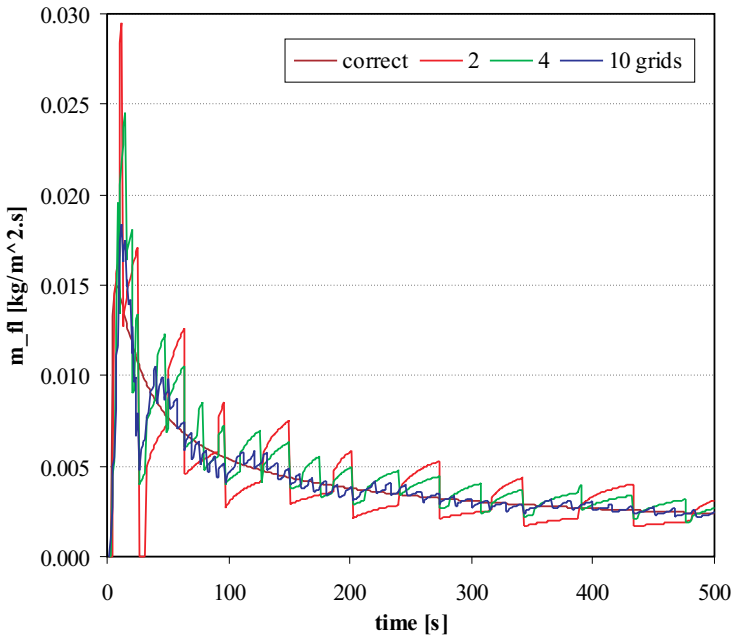

Figure 7.12: Mass flux for the averaged of 2, 4 and 10 meshes and "Moving mesh" method

7.7.4 An alternative conductive heat flux calculation

There are several options for the conductive heat flux calculation. The sharp front and the Kirchoff transformation were given in Section 7.4.1. The results of those two methods had a step wise release of volatiles, where in the first part of the step the release was too low. To improve this, an alternative conductive heat calculation scheme was examined. In this scheme the conductive heat flux near the mushy cell is determined by the neighbouring node and the crisp pyrolysis front. A pyrolyzing cell is assumed to exist of char and virgin, like in the "Moving mesh" method (Figure 7.13).

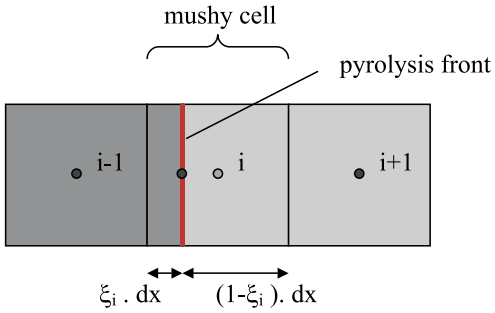

Figure 7.13: Representation of pyrolysis front

The location of the "front node" in the pyrolyzing volume is not fixed, but moves along with the (crisp) pyrolysis front. The heat flux is now determined by this variable node and its neighbour. The distance between the nodes is variable, only for the pyrolyzing cell. The other cells are treated as fixed. The heat flux for all possible cases:
Between 2 char cells:

$$\xi_{i-1} = 1 \text{ and } \xi_i = 1 \qquad \Rightarrow \qquad \dot{q}''_{cond} = \lambda_c \cdot \frac{T_{i-1} - T_i}{\Delta x} \tag{7.35}$$

Between 2 virgin cells:

$$\xi_{i-1} = 0 \text{ and } \xi_i = 0 \qquad \Rightarrow \qquad \dot{q}''_{cond} = \lambda_v \cdot \frac{T_{i-1} - T_i}{\Delta x} \tag{7.36}$$

Pyrolysis front in between a char and virgin cell:

$$\xi_{i-1} = 1 \text{ and } \xi_i = 0 \qquad \Rightarrow \qquad \dot{q}''_{cond} = \frac{T_{i-1} - T_i}{\Delta x/2\lambda_v + \Delta x/2\lambda_c} \tag{7.37}$$

Between pyrolyzing cell and virgin cell:

$$0 < \xi_{i-1} < 1 \text{ and } \xi_i = 0 \qquad \Rightarrow \qquad \dot{q}''_{cond} = \lambda_v \cdot \frac{T_{i-1} - T_i}{(3/2 - \xi_{i-1})\Delta x} \tag{7.38}$$

Between pyrolyzing cell and char cell:

$$\xi_{i-1} = 1 \text{ and } 0 < \xi_i < 1 \qquad \Rightarrow \qquad \dot{q}''_{cond} = \lambda_c \cdot \frac{T_{i-1} - T_i}{(1/2 + \xi_{i-1})\Delta x} \tag{7.39}$$

The results in Figure 7.14 show only a little improvement compared to the standard method. But the mass release at the start of pyrolyzing step is now too high. The time where there is no mass release, thus when the pyrolysis front is standing in between cells, is smaller, which certainly is an improvement. The mean error for the new method is about 48%, while the standard method gives 66%. Already from the second step in the mass release, it can be seen that the alternative method gives results closer to the "Moving mesh" method. Only at the start of the pyrolysis of a volume there is a strong overestimation. At the end of the simulation, from about 2500 s, the alternative method is remarkably better than the standard method, see Figure 7.15. The mass flux is much more constant, and the peaks at the start of a mass release step have disappeared.

For evaluation of the method, the first minutes are most important in the flame spread problem. The time intervals where the mass release is zero, are still present in the beginning of the simulation, so the alternative determination of the conductive heat flux is not considered successful.

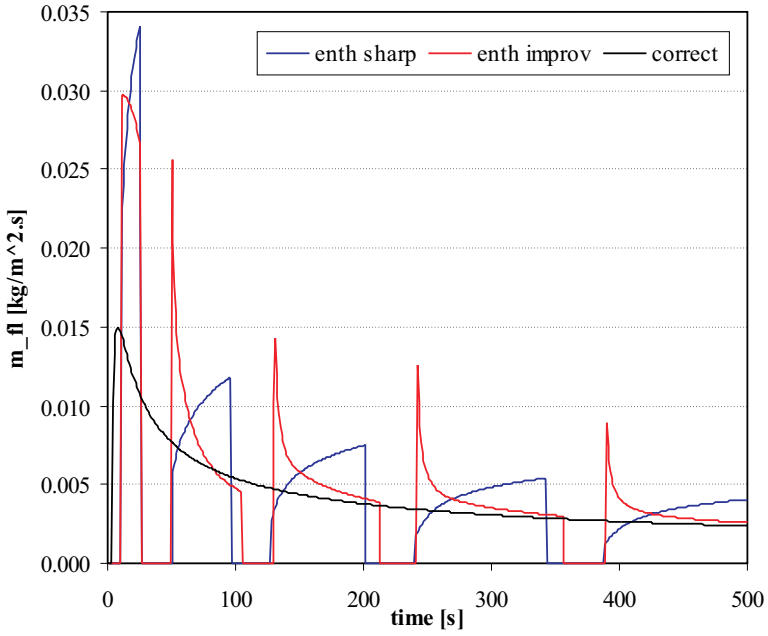

Figure 7.14: Mass flux for standard and alternative conductive heat flux calculation (0–500 s)

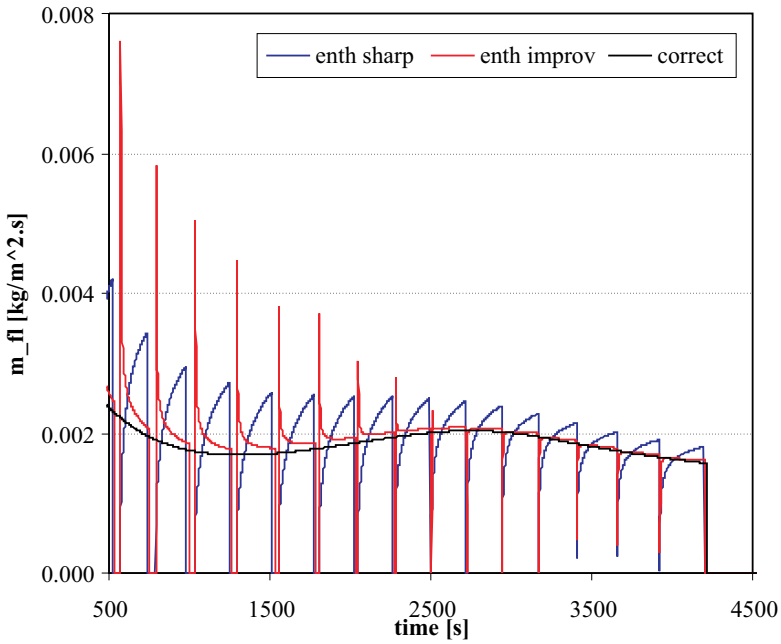

Figure 7.15: Mass flux for standard and alternative conductive heat flux calculation (500–4500 s)

7.7.5 Adaptive mesh

To improve the calculation, local grid refinement can be used. The mushy cell and its neighbours are subdivided, as shown in Figure 7.17. There are several options to subdivide the cells. Here a rather simple method is developed. The neighbouring cells of the coarse mushy cell and the coarse mushy cell itself, are fully subdivided. When the front stands in between two coarse cells, it is assumed that it still belongs to the left coarse cell. Thus the fine grid advances together with the pyrolysis front through the solid. To determine the energies and temperatures of the new introduced fine cells, there are again several options. It is possible to use a linear interpolation scheme. In combination with the conservation of heat and the heat flux at the boundaries of the coarse cell, the new temperature can be determined. Here the refinement is made very simple. A coarse cell with temperature T_i is subdivided into fine cells with each the same temperature T_i. So the heat fluxes at the boundaries of the coarse cell are not conserved when the grid is refined. It is assumed that in this zone the temperature difference and thus heat fluxes are low. The unbalance that is created by the refinement will be cleared after a few time steps, and it is assumed that it has little effect on the results.

To determine the energy of a coarse cell, where the fine grid has just passed, the conservation of energy will determine the new coarse temperature. When the heat capacities are not constant, care must be taken that energy conservation is fulfilled.

When N_c is the number of coarse cells and N_f the number of fine cells in one coarse cell, the total amount of cells is given by:

$$N_{tot,refine} = N_c - 3 + 3 \cdot N_f \tag{7.40}$$

To obtain the same size of small cells in a calculation with refinement as in a calculation without refinement (with $N_{tot,uniform\ cells}$), the two parameters N_c and N_f have to be chosen with:

$$\Delta x = \frac{L}{N_{tot,uniform}} = \frac{L}{N_c \cdot N_f} = \Delta x_{fine} \tag{7.41}$$

When the total number of cells in the refined calculation is minimized for a

Table 7.1: Number of cells in uniform and refined calculation

$N_{tot,uni}$	$N_{tot,ref}$	N_c	N_f
176	43	22	8
341	61	31	11
660	86	44	15
1302	122	62	21

certain, fixed Δx_{fine}:

$$\frac{\mathrm{d}N_{tot,refine}}{\mathrm{d}N_c} = 0 \tag{7.42}$$

$$\Rightarrow \frac{\mathrm{d}}{\mathrm{d}N_c}\left(N_c - 3 + 3 \cdot \frac{N_{tot,uniform}}{N_c}\right) = 0 \tag{7.43}$$

$$\Rightarrow 1 - 3 \cdot \frac{N_{tot,uniform}}{\left(N_c\right)^2} = 0 \tag{7.44}$$

$$\Rightarrow N_c = \lceil \sqrt{3 \cdot N_{tot,uniform}} \rceil \tag{7.45}$$

The calculations with the refinement method will be compared with a uniform grid. The number of cells, for both methods are given in Table 7.1. The size of the small cells in the refined calculation is the same as the cell size in the uniform calculation. For the refined calculation much less cells are needed for the same small cell size. Note that the length of the total refined zone ($= 3 \cdot L/N_c$) is different for the four cases.

At the end of the converged time step when the pyrolysis front has entered a new coarse cell, the grid is adjusted. For the coarse cell $i_{pyr} - 1$ that merges out of the fine cells:

$$\hat{E}_{i_{pyr}-1} = \frac{1}{N_f} \sum_{j=1}^{N_f} E_{i_{pyr}-1,j} \tag{7.46}$$

For the fine cells that are introduced in the coarse cell right of the coarse cell that contains the pyrolysis front $i_{pyr} + 1$, the energy density remains the same:

$$\hat{E}_{i_{pyr}+1,j} = E_{i_{pyr}+1} \tag{7.47}$$

Where " ˆ " has been used for the values after the adaptation of the mesh. The calculation of the temperature and the char fraction is similar. The heat fluxes are recalculated with the new temperatures and cell sizes.

Table 7.2: Calculation time for uniform and refined calculation

	Sim1	Sim2	Sim3	Sim4
$N_{tot,uniform}$	176	341	660	1320
Total calculation time (s)	2.5	21.5	167.4	1616.4
Calculation time per node and per time step (s)	$1.4\,10^{-5}$	$1.3\,10^{-5}$	$1.3\,10^{-5}$	$1.2\,10^{-5}$
$N_{tot,refine}$	43	61	86	122
Total calculation time (s)	0.9	5.2	28.0	198.1
Calculation time per node and per time step (s)	$2.1\,10^{-5}$	$1.7\,10^{-5}$	$1.6\,10^{-5}$	$1.6\,10^{-5}$
Δt (s)	$5.0\,10^{-2}$	$1.0\,10^{-2}$	$2.5\,10^{-3}$	$5.0\,10^{-3}$

The calculation times for the uniform and refined method are given in Table 7.2. The time step size was determined with the stability condition, where rounded values were taken so that a solution was provided for each second. The cell size of the uniform calculation was the same as the size of the fine cells in the refined method.

The calculation time increases with the amount of nodes and with the number of time steps taken. The calculation time per node and per time step is almost constant. When the uniform and refined method are compared, it is clear that the gain in calculation time is larger for a larger amount of cells. For the case with 1302 cells for the uniform method, and 122 cells in the refinement method the calculation time is about 10 times smaller. The results and the mean errors are similar for both methods.

The results of the adaptive mesh combined with time averaging for 1 s, are given in Figure 7.16; the black line represent the correct solution. To obtain smooth results without drops in the mass release, the grid refinement of the mushy zone is combined with the time averaged results. The results of this method resemble the results of a uniform fine grid (also combined with time averaging). The number of cells and thus the calculation time is reduced.

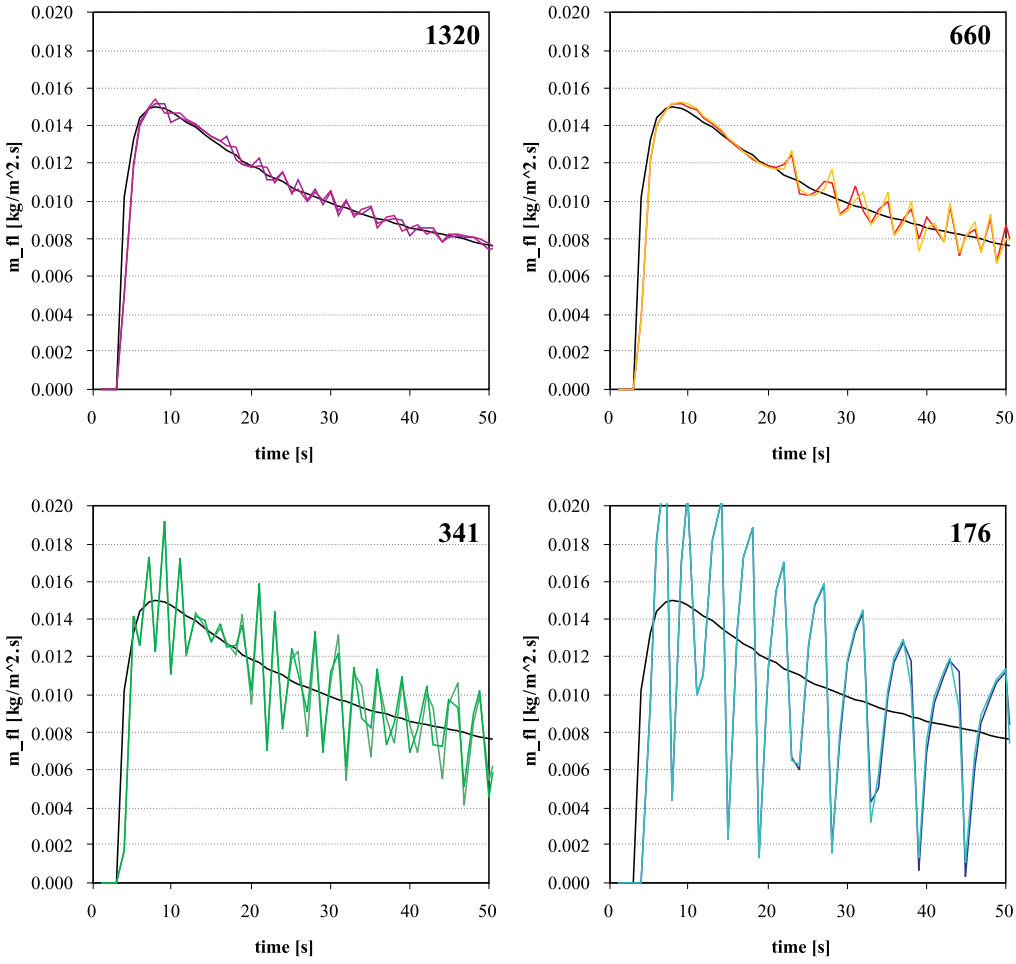

Figure 7.16: Mass flux for uniform grid (dark colours), adaptive grid (light colours) for combinations in Table 7.1

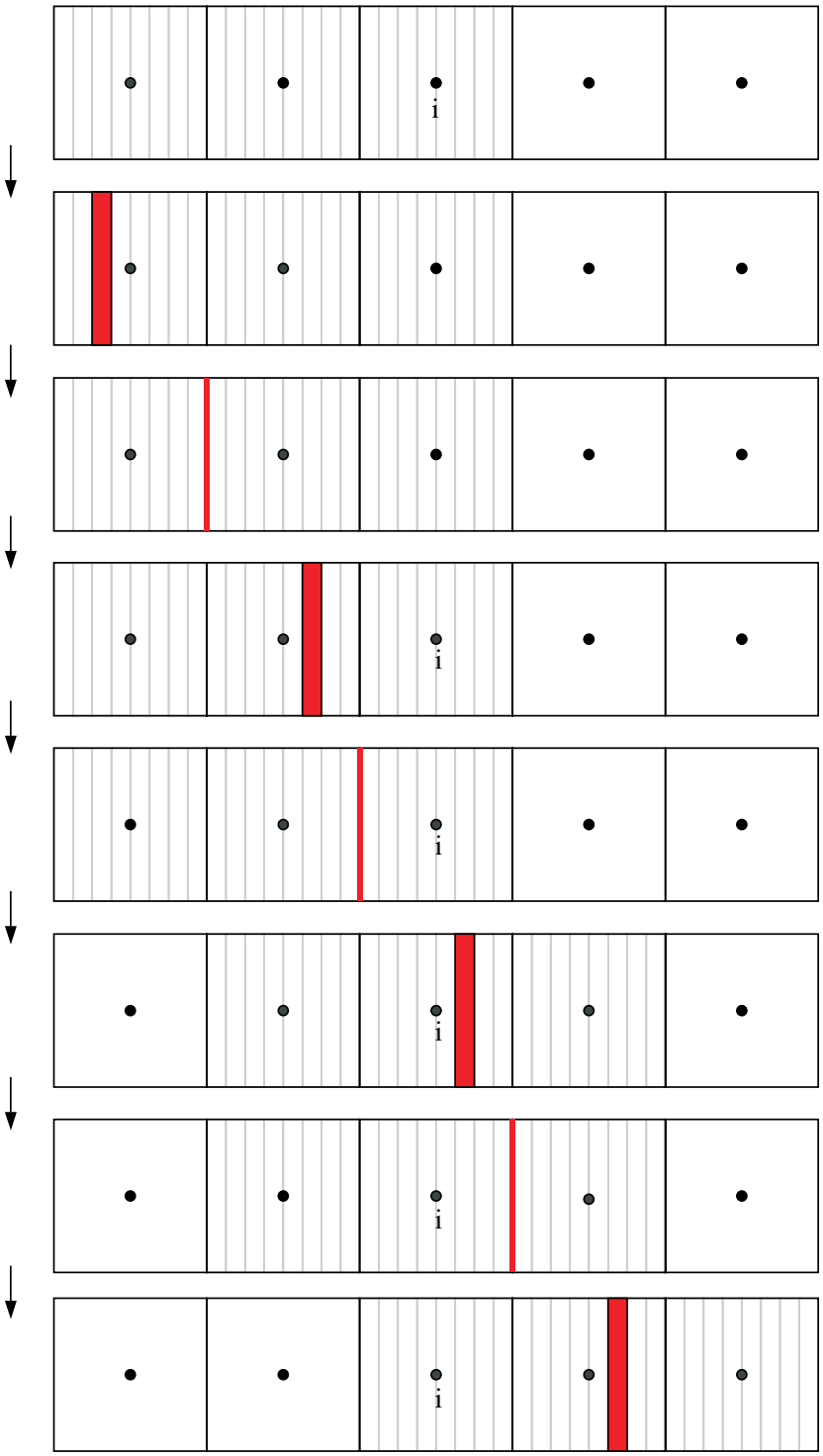

Figure 7.17: Grid refinement with movement of mushy cell

7.8 Conclusion

The "Enthalpy method" is a relative simple model to predict the mass flux of pyrolysis gases. The method is easy to implement and when coarse cells are taken, the calculation is very fast. In its standard form the mass flux inhibits strong oscillations. The pyrolysis front comes at a standstill in between cells, where the mass flux drops to zero .

This problem can be overcome by using an adaptive mesh. The coarse cells in the neighbourhood of the mushy cell are subdivided. When the adaptive mesh is combined with a time averaging technique the results were satisfying.

Alternative formulations for the heat flux calculation for the mushy cell did not improve the results satisfactory. The calculation of several different grids, where the different results were averaged afterwards, gave rather good results. Oscillations in the mass flux of the pyrolysis gases are still present, though.

The "Enthalpy method" has the advantage that it can be very easily expanded to two and three dimensions.

Chapter 8

Dual Mesh

In this section the "Dual mesh" method is given. The concept was first presented in the work of Yan and Holmstedt [126], de Ris and Yan [19] and Yan [125]. The "Dual mesh" model exhibits features of the "Arrhenius law" model of Chapter 4, of the "Moving grid" models of Chapter 6 and of the "Enthalpy" model of Chapter 7. Therefore the model is treated in a separate chapter.

8.1 Dual mesh concept

In the standard Arrhenius model a very fine grid is required to obtain reasonable results for the mass loss rate. If the grid is too coarse, oscillations appear in the mass loss rate. If the grid is very fine, (too) much computer time is needed. In fact, only in the pyrolyzing zone the fine grid is necessary because in the char and virgin zone the char volume fraction and thus the local density, is almost constant. Therefore, Yan [126] introduced a dual mesh. A coarse grid is used for the temperature solution, while a locally refined grid is used for the density calculation, see Figure 8.1.

8.1.1 Infinite rate

In the work of Yan [125] and Yan and Holmstedt [127] it is assumed that there is only one pyrolyzing cell in the refined grid. The rate equation for the pyrolysis reactions (Arrhenius law) is not used. Instead the pyrolysis reactions are assumed to proceed at a rate that keeps the solid locally at pyrolysis temperature. The reaction rate is thus infinite.

The density of an arbitrary refined grid (n,m) is given by [125]:

$$\rho_{n,m} = \min\Big(\rho_v, \max\big(\rho_c, \rho_{mix,m}\big)\Big) \tag{8.1}$$

where the density of the pyrolyzing cell is determined for the fine grid cell where the counter $m = m_{pyr}$:

$$\rho_{mix} \quad = \quad M \cdot \rho' \; - \; (m-1) \cdot \rho_c \; - \; (M-m) \cdot \rho_v \tag{8.2}$$

Here is ρ' the density in the coarse grid, m the counter of cells in the refined grid, and M the number of subcells in a coarse cell.

The energy equation is calculated on the coarse grid with Equation 4.23 where the convection of pyrolysis gases is neglected, thus:

$$\frac{\partial}{\partial t}\left(\rho c T\right) = \nabla \cdot \left(\lambda \nabla T\right) - Q_{pyr} \dot{m}'''_{pyr} \tag{8.3}$$

The volume production of pyrolysis gases in a coarse cell n is derived from the summation of density change in the fine grid:

$$\dot{m}'''_n = \frac{1}{\Delta x} \cdot \sum_m \min\left(\frac{H_{n,m}}{Q_{pyr}}, \frac{\Delta x / M}{\Delta t} \cdot \left(\rho_{n,m} - \rho_c\right)\right) \tag{8.4}$$

where $H_{n,m}$ is the available energy for the pyrolysis reactions in the subgrid cell (n, m), which is calculated with the energy equation. The endothermic pyrolysis reactions are induced as soon as the local temperature $T_{n,m}$ exceeds the pyrolysis temperature. The amount of the pyrolysis reactions will adjust itself so, that the local temperature is limited to the pyrolysis temperature. An iterative method is required. For further details see Yan [125]. The model has been applied to fire development in cable installations by Van Hees et *al.*

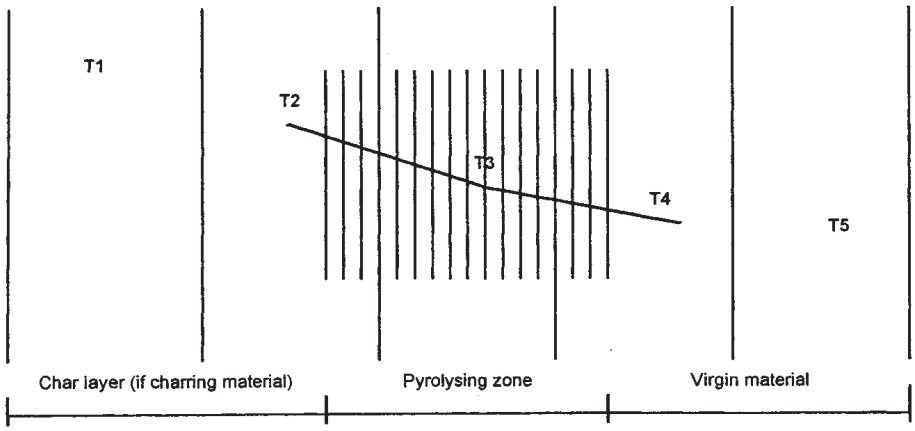

Figure 8.1: Coarse and fine grid from Yan ([126]

[118]. Notice that this formulation resembles the "Moving grid" method of Chapter 4 with the difference that the pyrolysis front is here determined by a fine grid cell instead of an infinitely thin surface. There is also resemblances to the "Enthalpy" method of Chapter 7, only there the energy equation is calculated on the same grid as for the char volume fraction.

8.1.2 Finite rate

In the model of de Ris and Yan [19] the same dual mesh concept is used. The difference with the model by Yan and Holmstedt [126] and Yan [125] is the pyrolysis rate. In the model of de Ris and Yan the pyrolysis rate is no longer assumed infinite, it is given by a linearized Arrhenius equation. The first order decomposition reaction of virgin material into char and volatiles is given by:

$$\frac{\partial \rho_s}{\partial t} = -(\rho_s - \rho_c) \cdot A \cdot \exp\left(-\frac{E}{RT}\right) \tag{8.5}$$

By assuming that the pyrolysis reactions occur in a narrow temperature range, the exponential expression can be approximated by a linear function of temperature:

$$\frac{\partial \rho_s}{\partial t} = \begin{cases} -(\rho_s - \rho_c) \cdot A_p \cdot (T - T_v) & \text{for } T \geq T_v \\ 0 & \text{for } T < T_v \end{cases} \tag{8.6}$$

Here is:

$$A_p = \frac{AE}{RT_{pyr}^2} \cdot \exp\left(-\frac{E}{RT_{pyr}}\right)$$

$$T_v = T_{pyr} \cdot \left(1 - \frac{E}{RT_{pyr}}\right)$$

This gives a match to Equation 8.5 for a characteristic pyrolysis temperature T_{pyr}.

The density change is again calculated on a fine grid, which is necessary due to the small pyrolysis zone. The temperatures in this refined grid are interpolated from the temperatures from the coarse grid. The density calculation is stopped when the local density is smaller than the char density plus a very small number.

8.2 Pseudo-implicit method

Equation 8.3 can be discretized with the implicit method (full or hybrid). The RHS and thus the production of pyrolysis gases term, is needed at the new

time step $n+1$. When the source term $Q_{pyr}\dot{m}'''_{pyr}$ is a non-linear function of temperature, an iterative method is required. With a simple explicit method - forward time differencing - there is of course no need for iterations because the RHS is set at the previous time step and thus known. But this method is not unconditionally stable.

In the pseudo-implicit method only the endothermic source term in the energy Equation 8.3 is set at the previous time step and thus independent of the new unknown temperatures. Hence an iteration cycle is avoided. The subsequent system can be solved directly by the TDMA-matrix algorithm. The solution of the temperature and density equation in a time step is decoupled, which speeds up the solution remarkably.

The new temperature is determined with:

$$\frac{(\rho cT)_i^{n+1} - (\rho cT)_i^n}{\Delta t} \cdot \Delta x = \lambda_{i-1/2} \cdot \frac{T_{i-1}^{n+\theta} - T_i^{n+\theta}}{\Delta x} + \lambda_{i+1/2} \cdot \frac{T_{i+1}^{n+\theta} - T_i^{n+\theta}}{\Delta x} - Q_{pyr} \left(\frac{\partial \rho_s}{\partial t} \right)^{n+\theta} \tag{8.7}$$

while the density change is calculated from Equation 8.5 with a fully implicit method, but lagging behind one time step.

$$\left(\frac{\partial \rho_s}{\partial t} \right)^{n+\theta} = -(\rho_{s,i}^n - \rho_c) \cdot A \cdot \exp\left(-\frac{E}{RT_i^n} \right) \tag{8.8}$$

When the reaction rate is linearized (see Equation 8.6), the density equation could be given by:

$$\left(\frac{\partial \rho_s}{\partial t} \right)^{n+\theta} \approx \frac{\rho_{s,i}^{n+1} - \rho_{s,i}^n}{\Delta t} \approx -(\rho_{s,i}^n - \rho_c) \cdot A_p \cdot (T_i^{n+\theta} - T_v) \tag{8.9}$$

and substituted in the energy equation:

$$\frac{(\rho cT)_i^{n+1} - (\rho cT)_i^n}{\Delta t} \cdot \Delta x = \lambda_{i-1/2} \cdot \frac{T_{i-1}^{n+\theta} - T_i^{n+\theta}}{\Delta x} + \lambda_{i+1/2} \cdot \frac{T_{i+1}^{n+\theta} - T_i^{n+\theta}}{\Delta x} - Q_{pyr}(\rho_{s,i}^n - \rho_c) \cdot A_p \cdot (T_i^{n+\theta} - T_v) \tag{8.10}$$

Now, only the density is lagging behind, the temperature is set at $n+\theta$. Remarkably, this was not done by Yan and de Ris. The advantage or the reason for the linearization is not clear then. The only difference seems to be the shorter calculation time of:

$$A_p \cdot (T - T_v) \tag{8.11}$$

compared to:

$$A \cdot \exp\left(-\frac{E}{RT}\right) \tag{8.12}$$

For a calculation with material properties by Karpov [53] and total simulation time of 1500 s the linearized method is 4 percent faster compared with the non linearized method (exponential). Where the last is only calculated when the local temperature is higher than the pyrolysis temperature. Thus the pyrolysis rate is set zero when the local temperature is too low. The gain in calculation time is insignificant.

8.3 Description of the implemented model

8.3.1 Governing equations

The model that is implemented was based on the model of de Ris and Yan [19]. Instead of using the local density, the model was formulated with the char density as in the previous chapters. So instead of Equation 8.6 the following equation was solved:

$$\frac{\partial \xi}{\partial t} = (1 - \xi) \cdot f(T) \tag{8.13}$$

with for the exponential reaction rate:

$$f(T) = A \cdot \exp\left(-\frac{E}{RT}\right) \tag{8.14}$$

and for the linearized reaction rate:

$$f(T) = A_p \cdot (T - T_v) \tag{8.15}$$

where A_p and T_v are determined with Equation 8.7.

The energy Equation 8.3 is discretized with the hybrid method (Cranck-Nicholson) where $Q_{pyr}\dot{m}'''_{pyr}$ is lagging behind one time step. The TDMA-algorithm can be used to solve the temperature equation in a direct way.

8.3.2 Grid

The energy equation is calculated on a coarse grid, while the char fraction Equation 8.13 is calculated on the locally refined grid, see Figure 8.2. Linear

interpolation between coarse node temperatures is used to determine the cell temperatures in the fine grid.

Half cells of the coarse grid are subdivided for the char fraction calculation. A left half coarse cell is subdivided when:

$$\xi_{left,i} \neq 1 \quad \text{and} \quad T_i > T_v \text{ or } T_{i-1} > T_v \tag{8.16}$$

and for a right half coarse cell:

$$\xi_{right,i} \neq 1 \quad \text{and} \quad T_i > T_v \text{ or } T_{i+1} > T_v \tag{8.17}$$

The calculation on the fine grid is stopped when the coarse char fraction equals almost unity:

$$\xi_{coarse} > 1 - \epsilon$$

where ϵ is a small number, in these simulations 10^{-4}. The char fraction is than fixed to 1.

This technique does not differ much from the fine mesh technique in Chapter 4. The main difference is the separate calculation of the char volume fraction on the fine mesh. In Chapter 4 the volume production of volatiles was calculated with interpolated temperatures and char fractions. In this section, the char fraction on the refined grid is determined with the Arrhenius equation and the subsequent profile is of course different from a linear interpolation.

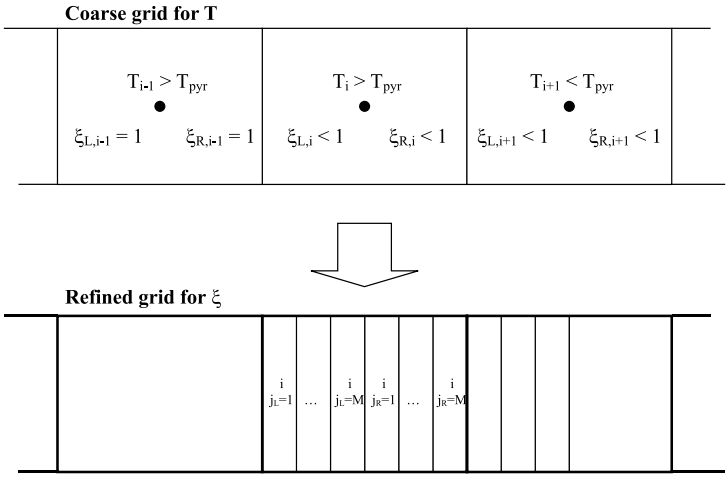

Figure 8.2: Subdivison of grid in dual mesh

8.4 Determination of time step and cells size - linearized reaction rate

First the number of coarse cells is examined. The number of fine cells is taken very high (80 cells) and the time step size very small (0.005 s) so that these will not have any influence. The results of the mass flux are given in Figure 8.3.

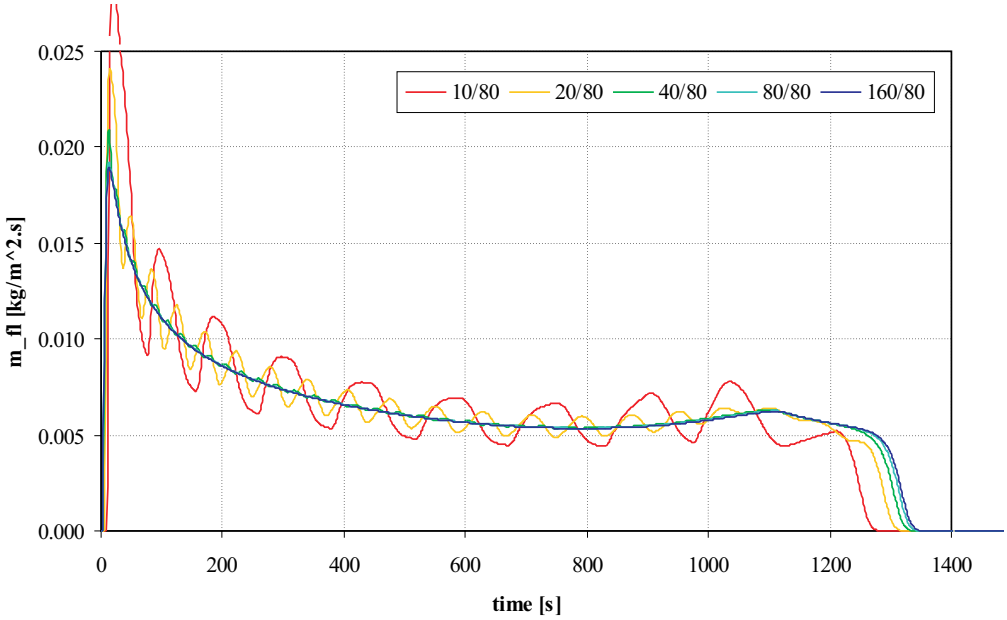

Figure 8.3: Mass flux for N_{coarse} = 10, 20 ,40, 80 and 160 and N_{fine} = 80

Then the number of coarse grid cells was set constant and the number of fine cells was decreased. When this was done for 80 coarse cells, the $N_{fine} = 2$ already gave satisfying results. For 10 coarse cells the increase of the number of fine cells is shown in Figure 8.4. Here the results are already converged with a subgrid with 10 subdivisions ($N_{fine} = 10$). The oscillation due to the coarse grid for the energy equation are still present though.

Several time steps have been tested, and time steps of 1, 2 and 4 s gave an error at the maximum mass flux of 0.36, 0.71 and 1.7 percent respectively. A time step of 1 s is proposed. For a time step of 8 s strong oscillations are noticed at the end of pyrolysis (after 1100 s in Figure 8.5). These oscillations are thought to originate from the time lagging of the source term $Q_{pyr}\dot{m}'''_{pyr}$ in the energy equation. If the time step is "too large" the adjustment of

the temperature by the endothermic pyrolysis reactions is disturbed. When the front reaches the rear, insulated surface, the remaining solid is almost at pyrolysis temperature. The equilibrium between temperature and pyrolysis reactions in this phase is more critical than in the rest of the simulation and thus this phase of the simulation is thus more prone for oscillations. When the method would be implicit (full or hybrid) instead of pseudo-implicit, these oscillations would probably not be present.

No comparison could been made with the results from Yan [126] because a number of input parameters was not given in his work, e.g. the thermal properties of the char material.

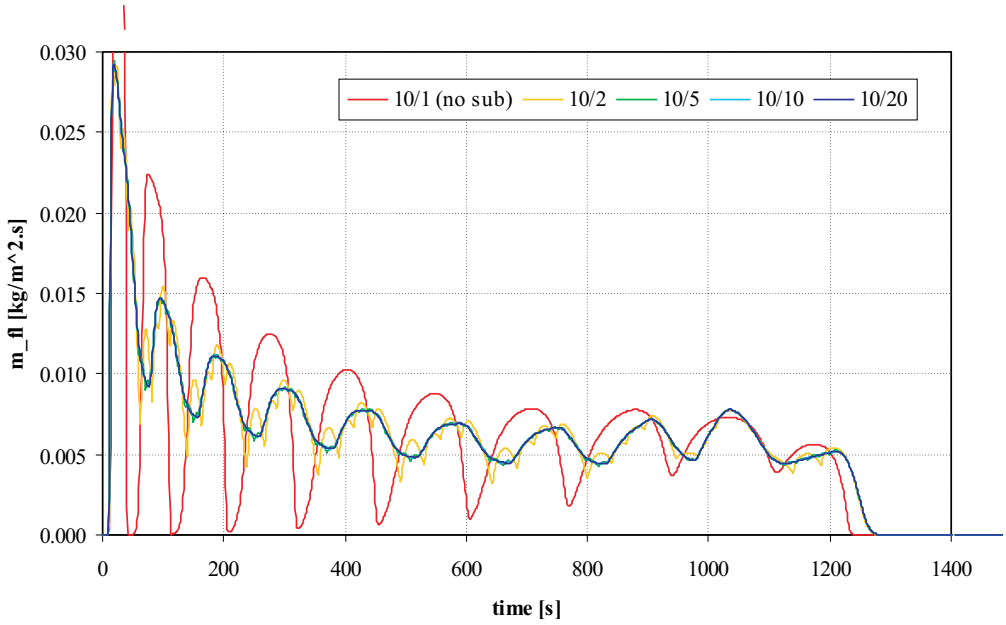

Figure 8.4: Mass flux for $N_{coarse} = 10$ and $N_{fine} = 1$, 2, 5, 10 and 20

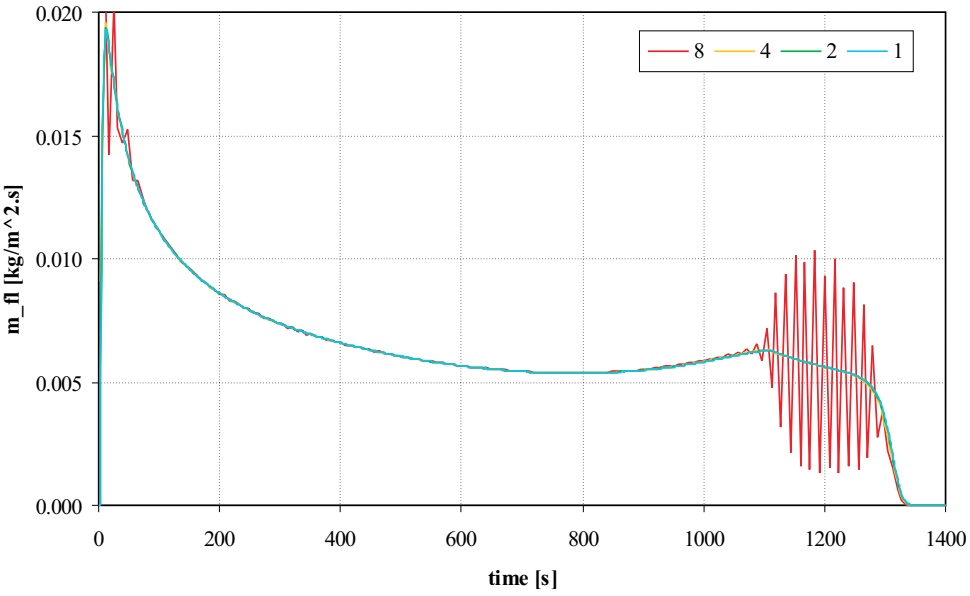

Figure 8.5: Mass flux for $N_{coarse} = 80$, $N_{fine} = 2$ and $\Delta T = 1$, 2, 4 and 8 s

8.5 Determination of time step and cell size - exponential reaction rate

In the exponential reaction rate model, the pyrolysis reactions are induced only if the coarse and fine grid temperature is greater than the pyrolysis temperature. When the *coarse* grid temperature is lower, there is no pyrolysis. This condition is set because otherwise all zones would start pyrolyzing at whatever temperature and hence the whole grid should be subdivided for the char fraction calculation. There are still two options left. In the first, there is no local pyrolysis allowed if the *local* temperature (in the fine grid) is lower than the pyrolysis temperature. In the other option the char volume calculation in the fine grid is done anyway. Simulations showed that if pyrolysis is not prevented in the fine grid, stronger oscillations in the mass flux will be present.

When the number of coarse grid cells is increased, the same trend in the mass flux rate is noticed as in the linear reaction rate. Although, slight oscillations seem still to be present. For $N_{coarse} = 80$ and $N_{fine} = 80$, the amplitude of these oscillations is small about $5\,10^{-5}$ kg/m^2.s or 0.5 to 1 percent

of the instant value (dependent on time).

The number of fine grid cells has to be higher than in the linearized reaction rate. More than 10 fine grid cells were needed to have the same magnitude of error as with the linearized reaction rate.

A detail of the mass flux course is given Figure 8.6. For 5 subcells the oscillations in the mass flux have an amplitude that is about the double of the solution with very high N_{fine} (=160).

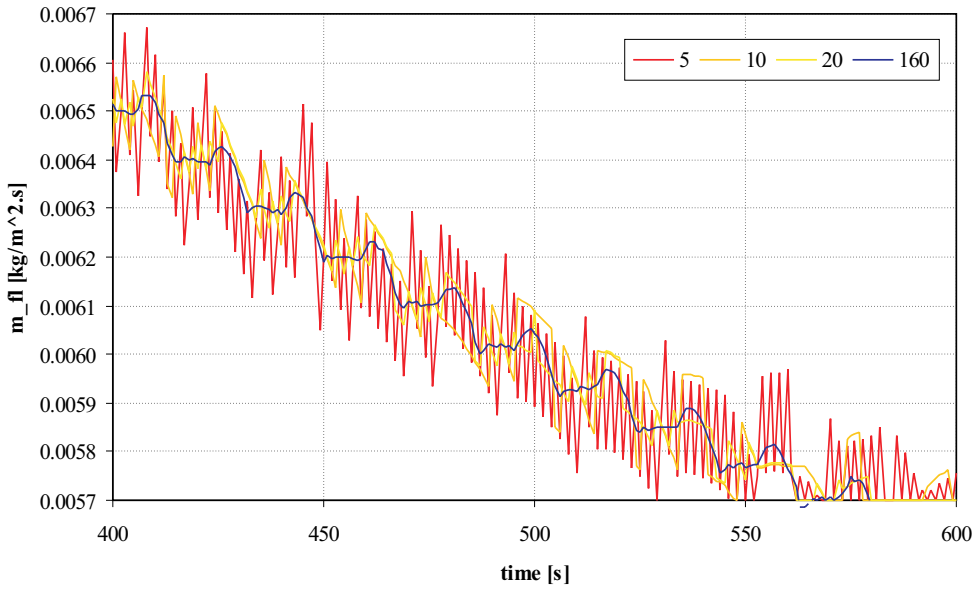

Figure 8.6: Detail of mass flux course for $N_{coarse} = 80$ and $N_{fine} = 5$, 10, 20 and 160 between 400 to 600 s

Time steps have to be taken smaller than in the linearized method. If too high, the mass flux shows oscillations at the end of the simulation, see right graph in Figure 8.7. Time steps of 0.01 s are required. Such small time

steps are required because the source term $Q_{pyr}\dot{m}'''_{pyr}$ is lagging behind, similar to the *linearized* reaction rate. The difference in time step between the linearized and non-linearized reaction rate is large (1 s compared to 0.01 s). This is thought to be caused by the stronger temperature relation in the reaction rate. If the local temperature differs much from the pyrolysis temperature, the difference in reaction rate between linearized and exponential becomes stronger. The linearized reaction rate underestimates the reactions and has a sort of damping effect.

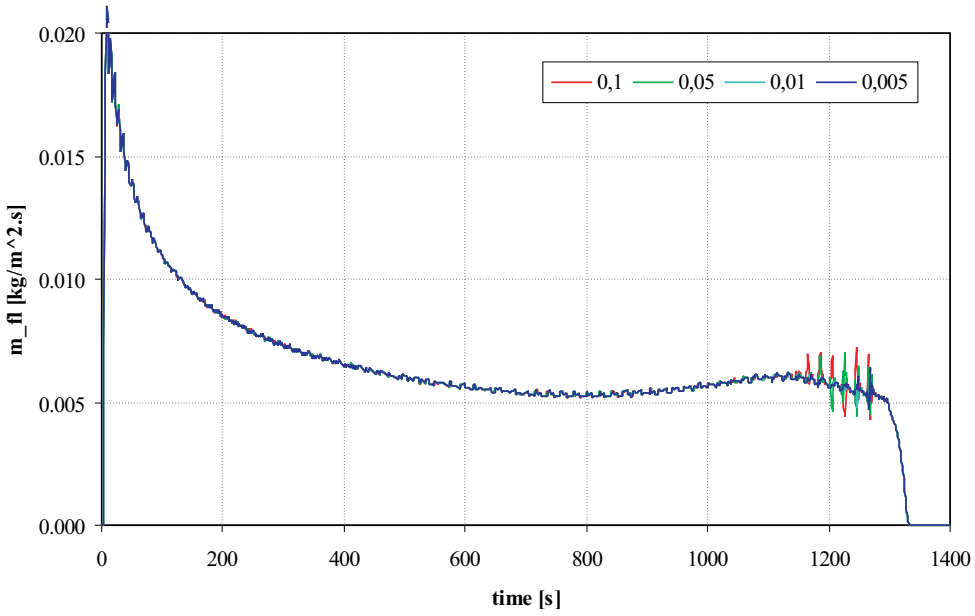

Figure 8.7: Mass flux for $N_{coarse} = 80$, $N_{fine} = 10$ and $\Delta T = 0.1$, 0.05, 0.01, 0.005 s

8.6 Comparison of exponential and linearized reaction rate

The "Dual mesh" with the exponential and linearized reaction rate are compared in Figure 8.8 and Table 8.1. The exponential reaction rate has a fine coarse and a fine subgrid. The time step is as well much smaller. The results, though, are not any better than with the linearized reaction rate. In the last, there are no oscillations in the mass release rate, while for the exponential

reaction rate still small oscillations are present, certainly near the end of the simulation.

The calculation is for the linearized reaction rate about 80 times faster (when no output to results file is permitted during the simulation this is even 300 times faster) than the exponential reaction rate. But the "Dual mesh" with exponential reaction rate is still 2 times faster than the "Arrhenius law" model of Chapter 4.

When the results are compared with the "fine" solution of the "Arrhenius law" model, we notice that the linear model predicts the first peak in the mass release rate a bit later (4 s or 44% error) and that this peak is smaller (5.6 %). For the exponential reaction rate the prediction of the first peak resembles better the correct one of the Arrhenius law model. The first peak time is almost the same, only the peak itself is a bit lower (4.1 %).

The second peak in the mass release rate, due to the "back effect", is both for the exponential and linearized reaction rate, predicted too late, 110s for the linearized and 127s for the exponential reaction rate. The height of the second peak is almost the same. Extinguishment time is some 20 s later (less than 2 %).

From this comparison we can conclude that the linearized reaction rate should be preferred above the exponential one. The model is much faster, and exhibits no oscillations in the mass release rate. Because of the linearization (and time lagging of the source term in the energy equation) small errors in the peaks of the mass release rate are introduced.

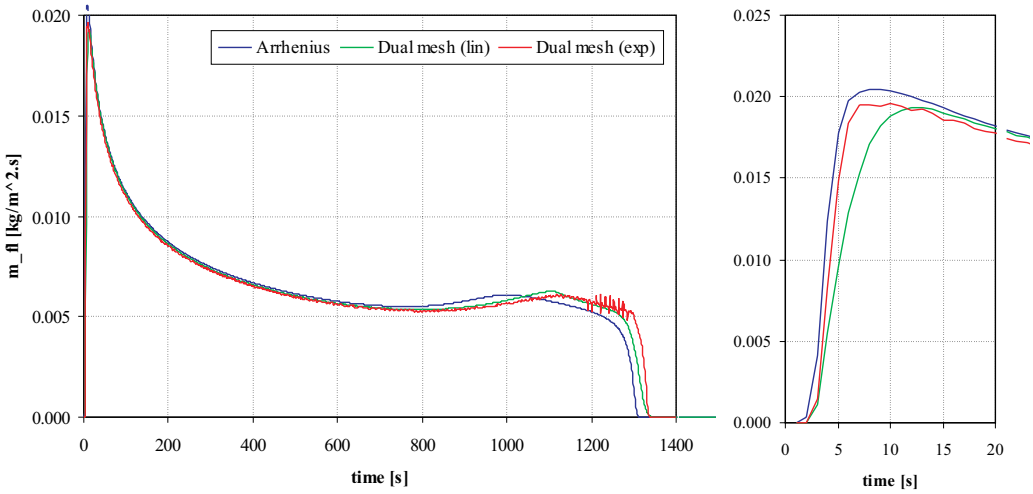

Figure 8.8: Comparison of linearized and exponential reaction rate

Table 8.1: Comparison of "Dual mesh" with exponential and linearized reaction rate and the "Arrhenius law" model

	Arrhenius	**Dual exp**	**Dual lin**	**Units**
coarse nodes	1024	160	80	-
fine nodes	-	10	2	-
time step	0.005	0.1	1.0	s
$\dot{m}''_{fl,max1}$	0.0205	0.0196	0.0193	kg/m^2.s
error-%	0.0	4.1	5.6	%
t_{max1}	9	10	13	s
error-%	0.0	11.1	44.4	%
$\dot{m}''_{fl,max2}$	0.0061	0.0061	0.0063	kg/m^2.s
error-%	0.0	0.6	3.4	%
t_{max2}	1001	1128	1111	s
error-%	0.0	12.7	11.0	%
calc. time (no I/O)	158.2 [a]	84.7	0.3	s
relative	546	292	1	-

[a] For the calculation time the Arrhenius law model was run with 256 nodes and a time step of 0.5 s. This gives similar deviations of the fully converged solution as for the linear and exponential reaction rate. The calculation time for 1024 nodes and a time step of 0.005 s is even much larger.

8.7 Conclusion

If the dual mesh concept is used, the linearized reaction rate model should be implemented. This model has the advantage of being much faster and possesses no spurious oscillations in the mass flux rate. Small errors will be produced in the maximum mass flux rate - in the examined case about 6 %. The second peak in the mass flux rate is predicted later - in the examined case about 100 s or 10 %.

Chapter 9

Validation and comparison of solid combustion models

9.1 Introduction

In this chapter the solid reaction models that were developed in Chapter 4 to 7, are compared with each other, and with experimental results. The solid models are:

- the Arrhenius law solid reaction model;
- the Integral model;
- the Variable meshes model;
- the Enthalpy model.

The "Dual mesh" model of Chapter 8 is not discussed here, because results were almost identical to the "Arrhenius law" model.

The "Integral model" is used with the non-equidistant meshes in the virgin layer. For the "Enthalpy model" several alternatives exist: the standard method, the staggered grid, the adaptive grid, and time averaging. For the adaptive grid, small cell and time step sizes are required to obtain a grid independent solution. Preliminary simulations with the adaptive grid resulted in (too) long calculation times. Therefore the "staggered grid" method with time averaging was chosen. A disadvantage of this choice is the dependency of the results on the grid. In the calculations in this chapter always 40 cells were taken for the "Enthalpy" model. This was a compromise between calculation time and accuracy.

An overview of the input parameters of the models is given in Table 9.1.

Table 9.1: Input parameters

Arrhenius law	**Integral Variable meshes Enthalpy**
density virgin/char	density virgin/char
heat capacity virgin/char	heat capacity virgin/char
conductivity virgin/char	conductivity virgin/char
pyrolysis heat	pyrolysis heat
-	pyrolysis temperature
activation energy	-
pre-exponential factor	-

9.2 Sensitivity study

9.2.1 The "back effect"

During the pyrolysis of a charring material, many experimental results show two peaks in the mass release rate of pyrolysis gases. The second peak is caused by the "back effect" [19, 109]. When the pyrolysis front reaches the rear surface, constantly less energy will flow from the front to the virgin material. The energy that flows to the virgin material can not leave the solid because of an insulated rear surface. Subsequent more heat is available at the pyrolysis front for the heat absorbing pyrolysis reactions and hence the mass loss rate will increase. When, for example, there is a strong convective boundary condition at the rear surface, the back effect will not occur.

The mass flux of pyrolysis gases is proportional with the difference in the char and virgin heat flux. This means that the mass loss rises when:

$$\left(\dot{q}_c'' - \dot{q}_v''\right) \uparrow \tag{9.1}$$

Where $\dot{q}_c''$ is the conductive heat flux from the char layer to the pyrolysis front, and $\dot{q}_v''$ the conductive heat flux from the pyrolysis front char layer to the virgin layer. These heat fluxes imply a crisp front representation, but a similar discussion can be done for a finite pyrolysis front. For the second peak, it is clear that due to the growing char layer, the heat flux to the front, $\dot{q}_c''$, is decreasing when a constant external heat flux is applied. To obtain a second peak in the mass loss rate this means that when:

$$\dot{q}_c'' \downarrow \implies \dot{q}_v'' \downarrow\downarrow \tag{9.2}$$

When the virgin material eventually reaches the pyrolysis temperature, no heat will flow anymore from the front to the virgin material. All the heat

that is provided by the char layer to the front can be used for the endothermic pyrolysis reactions. It is not because the entire virgin layer is at the pyrolysis temperature, that the whole layer will pyrolyse at once. Therefore there is insufficient energy present to compensate the absorbing pyrolysis reactions.

In order to examine the "back effect", the thickness of the solid and the rear boundary condition are varied.

9.2.2 Influence of the thickness

When the thickness of the solid is changed, the material will act differently. For a small thickness, the solid will act as thermally thin: the solid will have an almost uniform temperature. For example, in the case with a thickness of 1 mm, the temperature difference over the solid was less than 50 °C. While for a thick solid there are much larger temperature differences in the solid, because there is always solid at initial temperature.

Some flame spread models are valid for either thermally thick or either thin materials. The solid reactions models should be capable to predict both states. In the following simulations a constant external heat flux was applied.

9.2.2.1 Thermally thick

From the start of pyrolysis on, both the char and virgin heat flux are decreasing. At the first peak in the mass flux, the virgin heat flux will decrease faster than the char heat flux. At about 500 s, see thermally thick case in Figure 9.1, the virgin heat flux will decrease slower. This is due to the already heated virgin layer: when the temperature of the virgin layer is higher, less heat flows from the pyrolysis front to the virgin layer. As a result, the mass flux will increase. At about 1350 s the virgin heat flux drops to zero and the entire virgin layer is now at pyrolysis temperature. As the char heat flux is still decreasing and the virgin heat flux is not changing, the mass flux will decrease again.

9.2.2.2 Thermally thin

Materials with a small thickness are probable to act like thermally thin materials. The two peaks in the mass loss rate merge together in one peak (see thermally thin case in Figure 9.1). The virgin heat flux is already zero, before the char heat flux can decrease faster than the virgin heat flux.

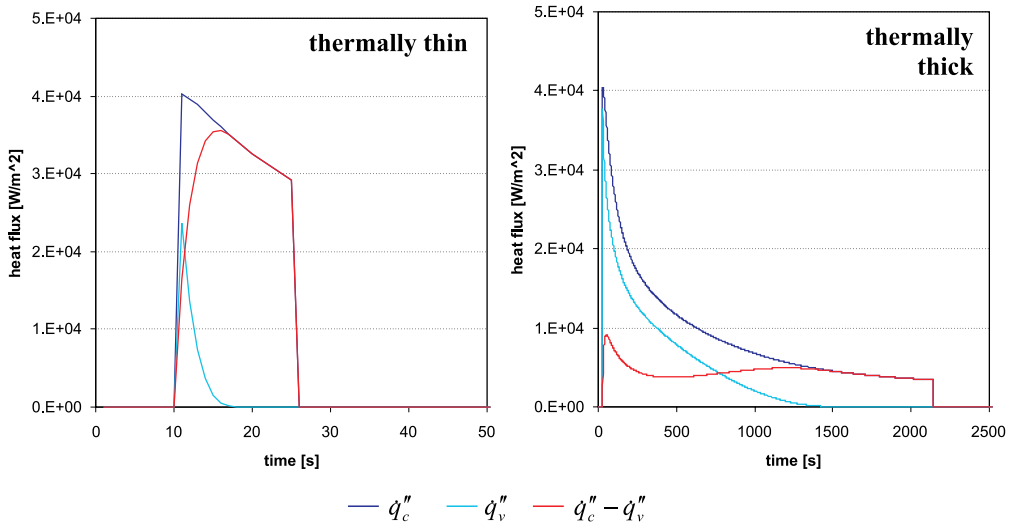

Figure 9.1: Heat fluxes at pyrolysis front for variable meshes model; (Left) $L = 1\,\text{mm}$; (Right) $L = 20$ mm

9.2.2.3 Thickness variation

A solid thickness of 1, 2, 5, 10, 20 and 50 mm was simulated with a perfect insulated rear boundary. The material properties are given in Table 9.2 [19]. The solid surface was subjected to a constant external heat flux of $50\,\text{kW/m}^2$, while heat was lost by reradiation ($\epsilon = 1$). Results are given in Figure 9.2.

The peak in the mass loss rate is for thin material much higher than for thick materials. The thin materials release their volatiles in a very short time and at a very high rate, which will result in very fast flame spread. For the thick materials the mass loss rate is significant lower but it is sustained longer. It takes more time before pyrolysis reactions disappear, for the 50 mm thick material it takes more than three hours. For thin materials a constant mass loss rate can sometimes be allowable, while for the thick material this is out of the question.

For thin materials there is only one peak in the mass loss rate while for the thick materials a second less pronounced peak appears. This second peak is caused by the "back effect". As the thickness of the solid increases, the second peak in the mass loss rate will decrease. For some thickness, the second peak in the mass loss rate is higher than the first peak (see thickness of 10 mm in Figure 9.2).

At the beginning of pyrolysis the thick materials (10 mm to 50 mm) have

Table 9.2: Input and material properties [19]

Property	**Value**	**Units**
Thickness	variable	m
Virgin density	600	kg/m^3
Char density	60	kg/m^3
Virgin heat capacity	2500	J/kg.K
Char heat capacity	2500	J/kg.K
Virgin thermal conductivity	0.36	W/m.K
Char thermal conductivity	0.23	W/m.K
Heat of vaporization (T_0)	870	kJ/kg
Pyrolysis temperature	375	°C
Activation energy	135	kJ/mol
Pre-exponential factor	10^{10}	1/s

the same mass loss rate. The mass release rate curves coincide in Figure 9.2 and they react as if the solid is semi-finite. Only when the heat front reaches the rear surface the mass loss rate starts to differ. For the thin materials this takes of course less time, and often there is no common mass release rate part.

For all thicknesses a true steady state during pyrolysis is never reached because the heat supply to the pyrolysis front is constantly decreasing due to the increasing char layer. Also the heat flux from the front to the virgin material will be constantly changing, except for the state where the virgin material has reached the pyrolysis temperature and the heat flux is zero. Though, such a steady state period with almost constant mass release rate is sometimes noticed in experiments [108].

For the "Integral model" a thicker material sometimes ignites earlier than a thin material (e.g. for 5 mm and 10 mm in Figure 9.2). The error is due to the transition from semi-infinite to finite heating. Thin materials are first calculated with the semi-infinite model but, before pyrolysis starts, the finite model is already applied. After the transition to the finite model, it seems that the surface temperature is underestimated in regard with the semi-infinite model. It is clear that a thinner material with insulated rear surface, should ignite faster than a thick model where the extra virgin material acts as a heat sink.

After the first peak in the mass release rate of pyrolysis gases, the mass loss rate in the "Integral model" gives lower values for thin materials than for thick materials (compare 10 and 50 mm). This does not correspond with the

results of the other models. Again this is near the transition from the semi-infinite to the finite model during the pyrolysis phase. For all the thermally thick materials simulated with the "Integral model", this transition point can be noticed as a kink in the mass release rate curve: for 10 mm at 51 s, for 20 mm at 182 s and for 50 mm at 1030 s.

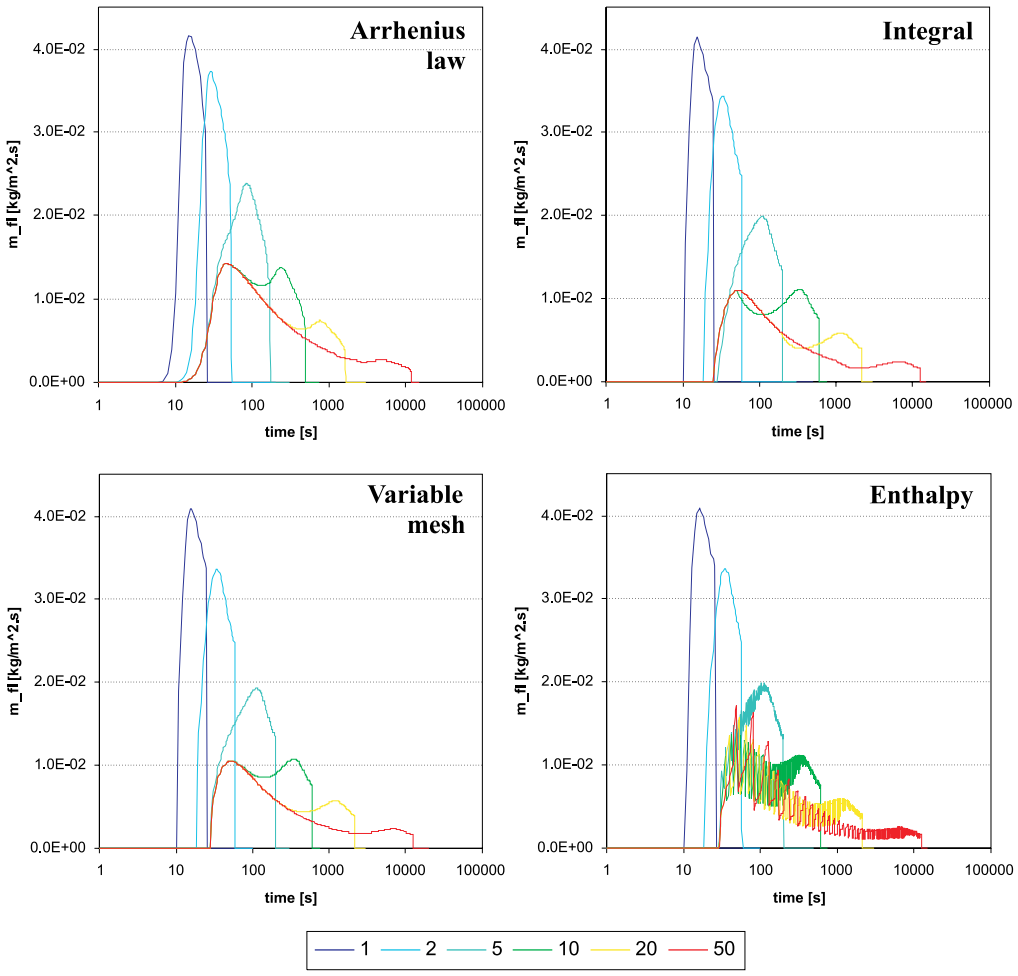

Figure 9.2: Mass flux of pyrolysis gases for different thickness (in mm)

The "Enthalpy model" shows good correspondence with the other models for small thicknesses. In a time interval of 1 s there is at least one entire peak in the mass flux, and hence the averaged value varies smoothly. For a larger thickness the cells become rather large (in all simulations 40 cells were used in the "Enthalpy model"). It takes more than 1 s to pyrolyse such a large cell and therefore the averaging on a 1 s interval basis, is no longer efficient:

oscillations in the mass flux occur. See thickness 5, 10, 20 and 50 mm in Figure 9.2. The overall trend is still predicted well.

For the "Arrhenius" model, the peak in the mass release rate is for the thin materials (1 and 2 mm) almost equal to those of the "Integral" and the "Variable meshes" model (difference less than 2 %), while for the thicker materials the difference can go up to 36 % (with variable meshes model as reference).

9.2.2.4 Conclusion

The "Integral model" is not adequate for the comparison of different thickness. At the transition from semi-infinite to finite, errors are introduced.

The "Enthalpy model" shows oscillations in the mass flux of pyrolysis gases when the ratio solid thickness to number of cells increases.

The results of the "Enthalpy method" are always grid dependent. When the adaptive grid with the time averaging technique is used, very small time steps are required and the calculation takes too much time. The results resemble then the "Variable meshes method" results but much more calculation time is needed.

9.2.3 Influence of the rear boundary

For a thickness of 20 mm the convection coefficient at the rear boundary was changed from 0 (insulated case), 5, 10 to 20 $W/m^2.K$. With a convective boundary condition at the rear surface, the second peak in the mass flux of pyrolysis gases can still occur. But, when the convection coefficient is high, which means high heat losses, the second peak will disappear, see Figure 9.3. All models predict this phenomenon.

The effect of heat supply or a heat source at the rear surface, is not examined. This boundary condition can be needed when modelling for example the Cone Calorimeter. Heat can be transferred by the top of the mounting device to the bottom. When the heat flux is high enough, it is possible that two pyrolysis fronts are created, one at the top and one at the bottom of the specimen, that advance to each other. For the "Integral" and the "Variable meshes" model it could be difficult to incorporate this. In both models a second pyrolysis front must be introduced and the equations will be altered (more complex). On the other hand, in the "Arrhenius law" and the "Enthalpy model", each volume can undergo pyrolysis reactions and different "fronts" can be formed independent of each other.

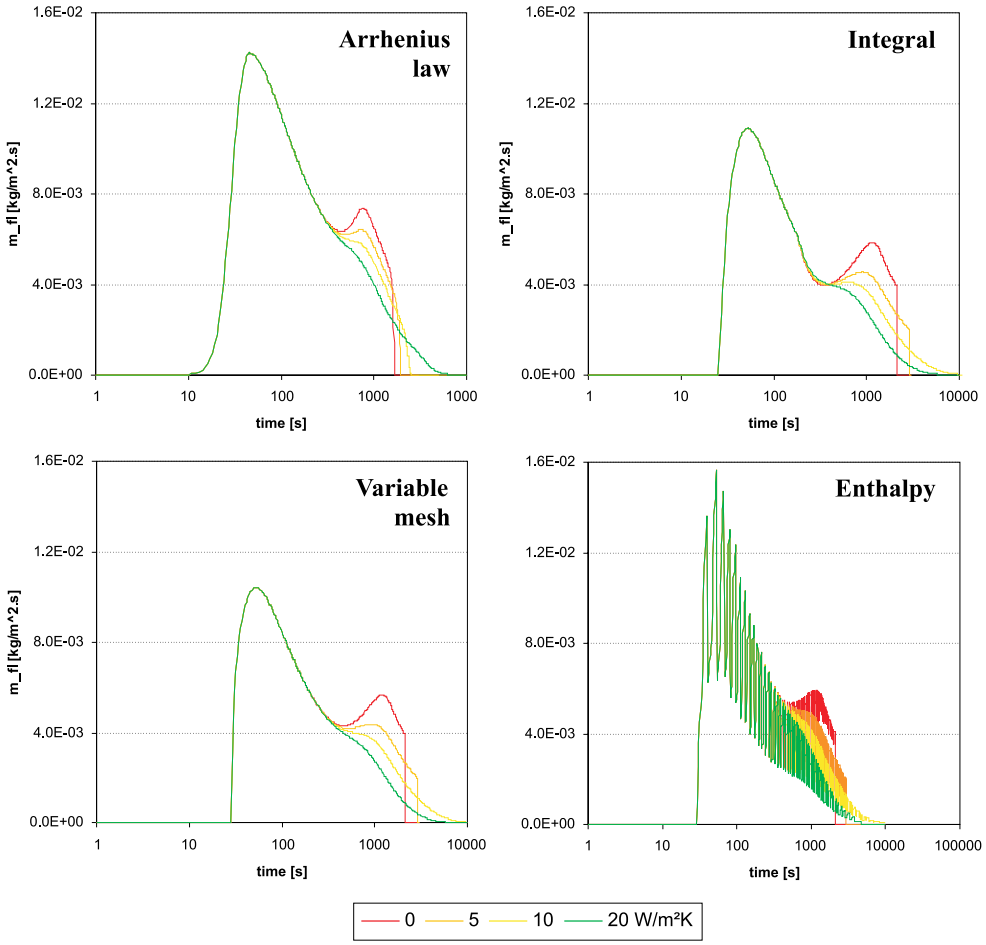

Figure 9.3: Mass flux of pyrolysis gases for different rear boundary condition (convection)

9.2.4 Influence of variation of input parameters

The input parameters for solid pyrolysis models are not fully known. For example, the thermal characteristics of char material found in the literature vary substantially. Even the properties of the virgin material can differ 25 percent or more with standard values from literature. For example the properties of Redwood change from 312 to 430 kg/m^3 [108] dependent on the author quoted. Therefore, a sensitivity study is performed to determine the most important input parameters.

To test the sensitivity of the results of the simulation, the input parameters have been changed plus or minus 25 % from a standard case (Table 9.3). Only one parameter has been changed at a time. Making all combinations for 9 parameters would give 3^9 or 19683 simulations. The front surface is submitted to an external heat flux of 50 kW/m^2.

Table 9.3: Standard properties for sensitivity study [19]

Property	**Min**	**Standard**	**Max**	**Units**
Thickness	-	0.02	-	m
Virgin density	450	600	750	kg/m^3
Char density	45	60	75	kg/m^3
Virgin heat capacity	1875	2500	3125	J/kg.K
Char heat capacity	1875	2500	3125	J/kg.K
Virgin thermal conductivity	0.27	0.36	0.45	W/m.K
Char thermal conductivity	0.1725	0.23	0.2875	W/m.K
Heat of vaporization (T_0)	652.5	870	1087.5	kJ/kg
Pyrolysis temperature	281.25	375	468.75	°C
Activation energy	101.25	135	168.75	kJ/mol
Pre-exponential factor	$7.5\,10^9$	$10\,10^9$	$12.5\,10^9$	1/s

In Figure 9.4 the parts of the curves that gave extreme values are pasted together. The simulation with standard input parameters is in black, while the extreme values are in red.

9.2.4.1 Integral and variable mesh model

The results of both models are similar. The peak in the mass release rate is primarily determined by the pyrolysis temperature. A low pyrolysis temperature will give higher mass release rates and vice versa. For only a change of 25 percent in the pyrolysis temperature, changes of 60 percent appear in the prediction of the peak of mass release rate. Changes of the other input

parameters have smaller influences on the peak of mass release rate (less than 15 percent). The time of extinction is 40 percent larger for the high pyrolysis temperature and 26 percent smaller for the low virgin density. The differences in the surface temperature are rather small (lower than 20 °C).

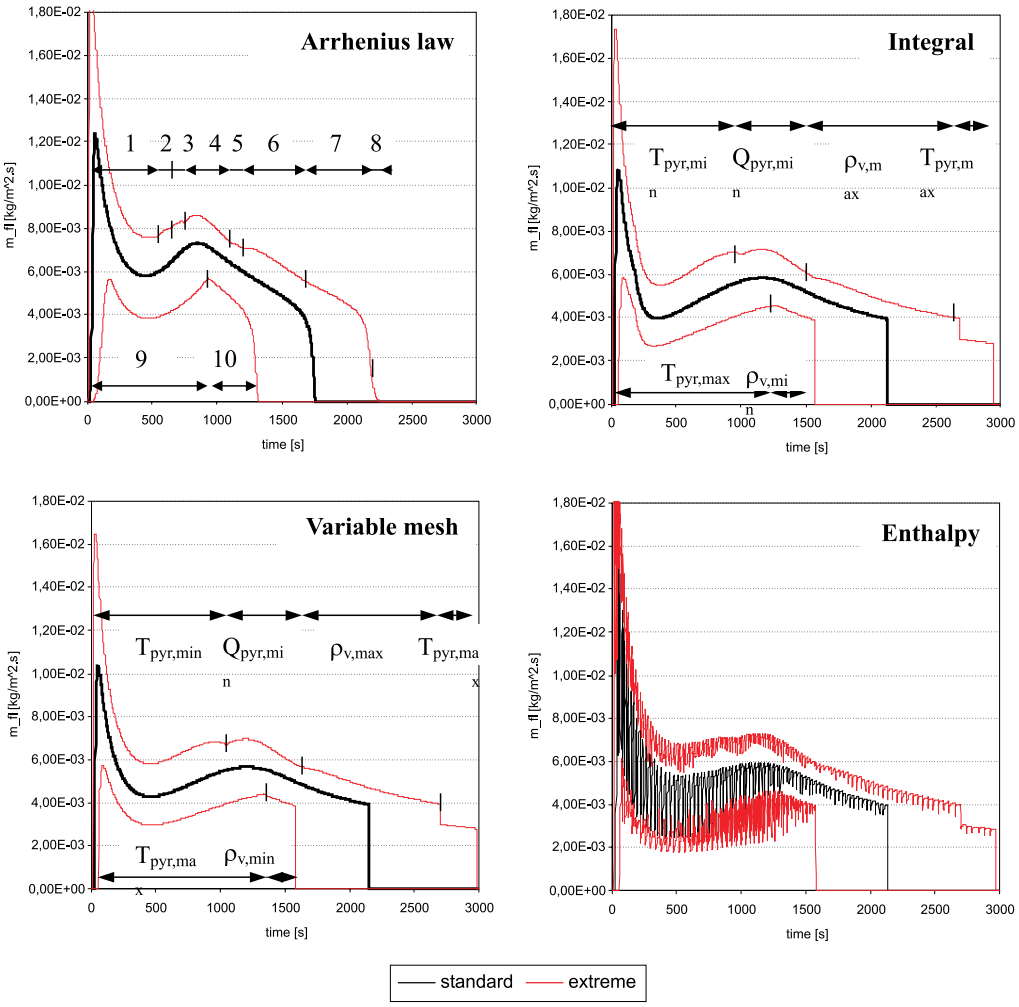

Figure 9.4: Mass flux of pyrolysis gases for a 25% change of input parameters

9.2.4.2 Enthalpy model

Due to the strong oscillation in the mass flux of pyrolysis gases, the extreme values (minimum and maximum mass flux) are determined by several input parameters. If these oscillations were filtered out, or if the adaptive mesh

Table 9.4: Zones in mass flux for Arrhenius law model

Zone	Parameter
1	$E_{a,max}$
2	$c_{v,min}$
3	$\lambda_{v,max}$
4	$Q_{pyr,min}$
5	$\rho_{v,max}$
6	$E_{a,max}$
7	$\rho_{v,max}$
8	$E_{a,max}$
9	$E_{a,min}$
10	$\rho_{v,min}$

technique was applied, then the results will probably match the "Integral" and "Variable meshes" model, because all three have the same physical model.

9.2.4.3 Arrhenius law model

The peak in the mass release rate is primarily determined by the activation energy. This corresponds with the pyrolysis temperature of the "Integral" and "Variable meshes" model. A low activation energy will give higher mass release rates and vice versa. For only a change of 25 percent in the activation energy, changes of 55 percent appear in the prediction of the peak of mass release rate. The changes of the other input parameters did have smaller influences on the peak of mass release rate; less than 15 percent. Similar conclusions were made in Novozhilov et *al.* [86]. The time of extinction is 32 percent larger for the high activation energy and 25 percent smaller for the low virgin density. The differences in the surface temperature are small and are lower than 20 °C. The minimal or maximal parameter that corresponds with the numbered zones in Figure 9.4 are given in Table 9.4.

9.2.4.4 Conclusion

The four models give the same dependence on their input parameters. The initial peak is strongly determined by the pyrolysis temperature or activation energy. It is not easy to measure or determine these properties as they imply simplification of reality. The thermal degradation reaction will not start at an infinitely rate at a fixed temperature, nor will the reaction rate follow

exactly a first order Arrhenius equation.

The surface temperature does not change a lot when input parameters are changed. The surface temperature is in principal determined by the external heat flux and the surface emissivity. The char emissivity is very close to unity, only a few percent change is possible, that is why this parameter was not changed 25 percent in the sensitivity study; values of 0.75 are not realistic. A simulation with an emissivity of 0.95 was done which gave a 5 percent change in the surface temperature. It was concluded that the influence was minor (results not shown).

9.2.5 Influence of the heating of pyrolysis gases

When the pyrolysis gases flow through the char layer, they can still absorb sensible heat from the layer. This absorbed heat will be transported out of the solid, and hence the pyrolysis process will take longer if this heat absorption is included.

It is possible to solve the flow of the pyrolysis gases in detail, with e.g. flow through porous materials. In this work the gases that are produced in the solid, flow immediately out of the solid, and hence no gases accumulate in the solid. It is assumed that the gases are on the same temperature as the solid they are flowing through. This means that the pyrolysis gases leave the solid at the same temperature as the solid surface.

To include the heating of the pyrolysis gases in the "Integral model", some modification must be made. In the conservation of energy of the char layer an extra (sink) term is included, which represents the heat absorption of the pyrolysis gases:

$$\rho_c c_c \frac{\mathrm{d}}{\mathrm{d}t} \int_0^{\delta_c} (T - T_{pyr}) \mathrm{d}x + \dot{m}''_{pyr} c_{pyr} (T_{s1} - T_{pyr}) = \dot{q}''_{net} - \dot{q}''_c \tag{9.3}$$

The heating of the pyrolysis gases, the second term in LHS, is easily incorporated in the net incident heat flux:

$$\dot{q}''_{net} = \dot{q}''_{ext} + \dot{q}''_{fl} - h(T_{s1} - T_\infty) - \epsilon\sigma(T_{s1}^4 - T_\infty^4) - \dot{m}''_{pyr} c_{pyr} (T_{s1} - T_{pyr}) \tag{9.4}$$

For the other models the heating of the pyrolysis gases was already included.

When the models are compared, it is clear that the definition of the pyrolysis temperature in the "Variable meshes", "Integral" and "Enthalpy" model and the activation energy E_a in the "Arrhenius law" model, will have a major influence on the results. When the pyrolysis temperature or activation energy is low, the pyrolysis reaction will occur at a lower temperature. When heated to the same temperature, these pyrolysis gases, will absorb

more energy. In the "Arrhenius law" model the pyrolysis gases are produced in a large temperature interval (see Section 4.5.3). The amount of heat absorbed by the pyrolysis gases will be dependent on the temperature they were produced on.

Simulations are done with the same material properties and boundary conditions as in Section 9.2. For the specific heat capacity of the pyrolysis gases a value of 1900 J/kg.K is used [97, 129]. Result are given in Figure 9.5.

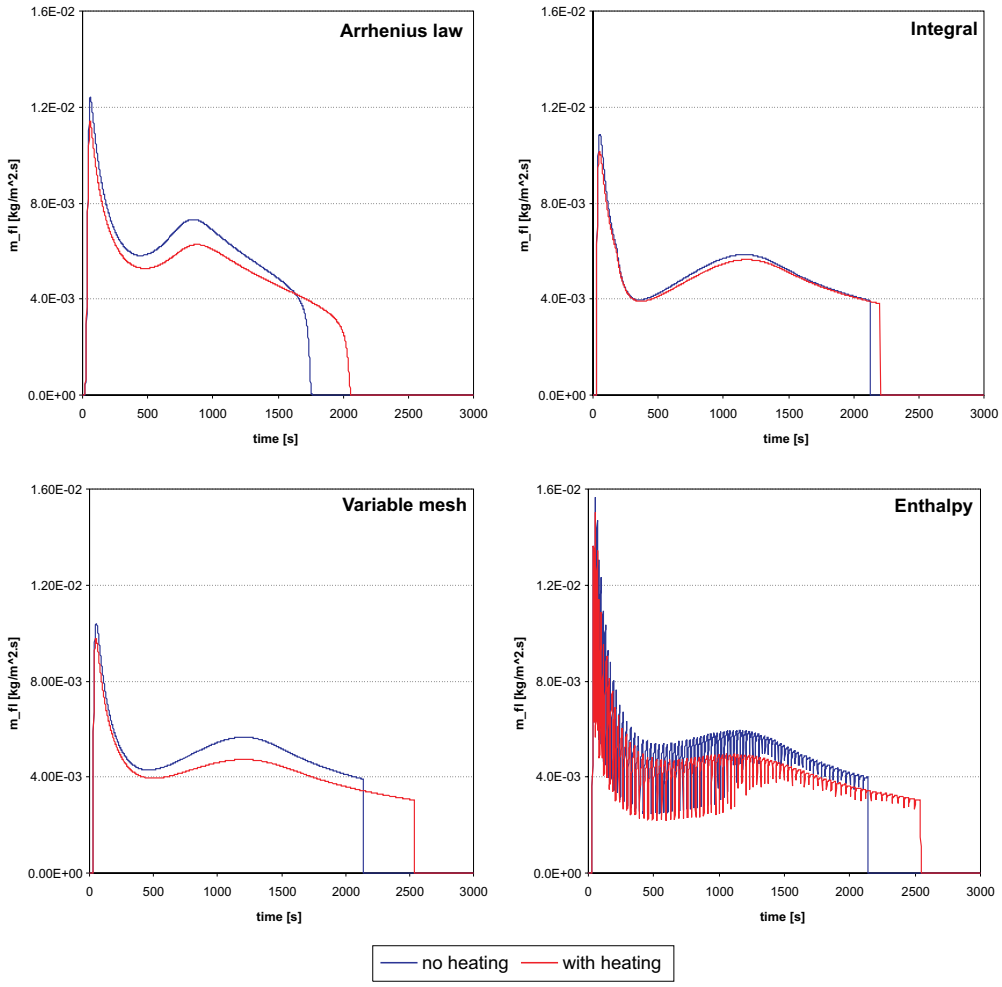

Figure 9.5: Mass flux with and without heating of pyrolysis gases in char layer

The peak mass release rate and the extinction time is given in Table 9.5. The extinction time in the "Arrhenius model" was determined as the time

Table 9.5: Summary of results (peak in heat flux/ extinguishment)

	Arrhenius	**Integral**	**Moving grid**	**Enthalpy**	
$m_{fl,max}$ (no heating)	$1.24\,10^{-2}$	$1.09\,10^{-2}$	$1.04\,10^{-2}$	$1.57\,10^{-2}$	$\frac{\text{kg}}{\text{m}^2.\text{s}}$
$m_{fl,max}$ (heating)	$1.14\,10^{-2}$	$1.01\,10^{-2}$	$0.97\,10^{-2}$	$1.50\,10^{-2}$	$\frac{\text{kg}}{\text{m}^2.\text{s}}$
Difference	8.0	6.9	6.2	4.1	%
$t_{extinguish}$ (no heating)	1769	2127	2143	2139	s
$t_{extinguish}$ (heating)	2066	2204	2542	2544	s
Difference	16.8	3.6	18.6	18.9	%

where mass flux was lower than $1/10^4$ of the value of the peak mass flux.

The trend of the surface temperature is for the four models almost the same. The difference between simulations with and without heating of the pyrolysis gases are about 20 °C.

The "Integral model" behaves differently from the other models. The time of extinction is for heating and no heating almost equal (3.6 % difference) as well is the mass flux rate. The "Integral model" predicts lower surface temperatures than the "Variable meshes" and the "Enthalpy" model. Because of this lower surface temperature the reradiation (radiative heat loss) is lower and hence more heat is available for the pyrolysis reactions.

For the heating and no heating case, the extinguishment times for the "Variable meshes" and "Enthalpy" model are almost equal, less than 0.2 %. The "Integral model" gives a slightly lower extinguishment time for the no heating case, but for the heating case the difference between the other models is significant (about 13 %). The difference with the "Arrhenius law" model can probably be minimized by adjusting the activation energy, as will be done in the following sections.

The qualitative results of the incorporation of the heating of the pyrolysis gases is similar for all models, but the least pronounced by the "Integral model".

The difference in the peak of mass release rate of pyrolysis gases between

heating and no heating cases is rather small: maximum 8 % for the "Arrhenius law" model. When the results are compared in between models, the "Enthalpy" model strongly overestimates the peak in the mass flux. Of course this is due to the oscillations typical for the model. The peak for the "Arrhenius law" model is quite higher than for the "Variable meshes" and the "Integral" model (19.2 % for no heating and 17.5 % for heating case) and again is explained by the probably too low activation energy.

9.3 Comparison with "inert" Cone Calorimeter test: Plywood

In this section the solid pyrolysis models are compared with experimental results from the Cone Calorimeter[1]. Flame spread is not yet involved, the experiments are considered to be one-dimensional.

In the paper of de Ris & Yan [19] the authors compare their pyrolysis model with experiments done by Delichatsios. A 2.54 cm thick plywood sample was exposed to an external heat flux of 50 kW/m^2 in a nitrogen atmosphere. The inert atmosphere prevents the pyrolysis gases to ignite in the gas phase. This inert test has the advantage that the incident heat flux at the top boundary condition is well known. During the entire test it is equal to the external radiation from the radiating cone, i.e. 50 kW/m^2. If, in the gas phase, combustion reactions and a flame are present, the flame heat flux has to be modelled or measured, which introduces an extra unknown. In the experiment the first peak in the mass loss rate occurred at 100 s, see Figure 9.6, the char layer thickness was about one millimetre. When the mass loss rate has decreased, it remains constant for about 500 s until it rises into a second strong peak at about 1200 s.

A problem in this test, and other Cone Calorimeter tests, is that the cause of the second peak in mass loss rate is not totally clear. It can be caused by extra heat that flows via the mounting device to the side and the rear surface of the specimen, speeding up the mass loss. While in the "steady state" phase, there is maybe a heat loss through the mounting device, causing lower mass loss rates [19]. Of course the heating up of the virgin material also contributes to the second peak ("back-effect"). The increase of the thermal conductivity of the char layer with char depth (by radiation through cracks for example) can also contribute to the second peak in the mass loss rate. A combination of the two latter, is thought to be most probable. More heat can flow to the pyrolysis front and can be used for the endothermic pyrolysis

[1]Information about the Cone Calorimeter can be found in Appendix A

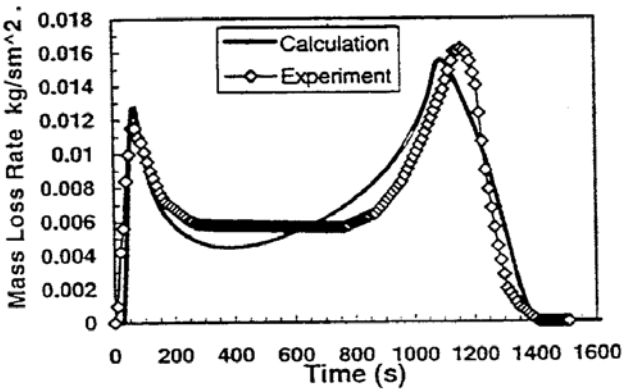

Figure 4. Calculated and Experimental Mass Loss Rates

Figure 9.6: Calculated and experimental mass loss rates (from de Ris & Yan [19])

reactions. Yet another cause of the second peak could be the change of thermophysical properties, due to the long exposure at elevated temperature of the virgin material. Several possibilities exist to explain the second peak in the mass flux and in reality probably a combination of all these factors occurs. In the simulations only the back effect is considered. The effect of the sample holder is not included as there is no information whether the rear surface received or lost heat through the sample holder, nor what the value of this heat flow could be.

In the paper of de Ris & Yan [19] there were no material properties given for plywood, the "equivalent or optimised properties" were obtained by fitting the simulated results with the experiments. de Ris & Yan wrote:

> "The simulated results show good agreement with experiment. They establish the efficacy of the mathematical technique for determining "effective properties". Unfortunately our ignorance about rear boundary condition employed by the experiment created significant uncertainty as to the actual "equivalent properties". For example if one were to assume a small amount of heat penetrates the sides of the sample holder and enters the sample from the rear over the full duration of the experiment, one obtains equally good agreement with a very different set of equivalent properties."

The values of the material properties that are optimised for only one experi-

ment, will not necessarily perform well in an other experiment. But reliable values for the material properties are scarce, and often the optimisation technique is the only alternative. Here the material properties are optimised to obtain results for the entire experiment. The optimisation is done for the "Arrhenius law", the "Integral" and the "Variable meshes" model. The "Enthalpy" model is not considered because similar results are expected as for the "Variable meshes" model, except for the oscillations. The "Integral model" is still included because in previous calculations it showed sometimes peculiar behaviour.

When using wood experiments for validation of the pyrolysis models, an extra complication is created by the moisture content. At ambient conditions most materials contain moisture from the environment. The moisture can be removed by placing the materials in a dry-oven, but in most experiments this is not done. Also in real fires the solid materials contain some moisture. When the solid material contains moisture and is heated, besides the pyrolysis front also a water vaporization front will be introduced. The pyrolysis models developed in Chapter 4 to 7 only contain a pyrolysis front but can still be used for such materials. In these models the pyrolysis and water vaporization front are seen as one front. The extra endothermic energy for the water vaporization is thus included in the pyrolysis heat. As most materials properties are determined from optimisation (see further) of experimental results, this simplification is granted. The effect of the water vapor that heats up the *deeper* virgin material can partly be included by taking a higher virgin conductivity. Including a separate water vaporization front and the flow of the water vapors in the calculation will give more accurate results, but on the other hand it will seriously complicate the calculation. Therefore, in almost all the solid combustion models found in literature the calculation is limited to the pyrolysis front [125, 19, 110, 77, 86]. The effect of the moisture content is thus included via the optimisation of the material properties. Subsequent, the determined material properties are dependent on the moisture content, but in most cases the moisture content of wood is assumed to be a pseudo-property of the material as well [110].

9.3.1 Equivalent material properties

The inert Cone Calorimeter test is used here to determine equivalent material properties. As in literature many material properties remain unknown, e.g. the char density, the char conductivity, the pyrolysis heat, ..., the inert Cone Calorimeter is seen as an apparatus to determine these unknown material properties. In the pyrolysis models the material properties have, therefore, been varied until the simulations were in good correspondence

with the experimental results. At the same time it is tested if the relative simple pyrolysis models are capable of giving useful and accurate results for the complex pyrolysis process.

To obtain the optimised or equivalent material properties, the following considerations are used. The total mass release is determined by the difference between the char and virgin density. By adjusting the emissivity, the virgin density, the virgin heat capacity, and the pyrolysis temperature (or activation energy) the first release of pyrolysis gases is optimised. By adjusting the heat of pyrolysis, the pyrolysis temperature, the virgin density, and the virgin heat capacity the first peak in the mass flux is optimised. The steady phase and the second peak are optimised by adjusting the virgin and char thermal conductivity. The optimisation was an iterative process of trial and error. About 50 simulations were done. The material properties were independent on the temperature in order to simplify the optimisation and because temperature dependent properties are not allowed in the "Integral model".

9.3.2 Arrhenius law model

The optimised material properties for the "Arrhenius model" are given in Table 9.6. The change of the surface emissivity is determined by the char fraction in the first cell. If the fraction exceeds a critical value the emissivity will change from its virgin to its char value. For the optimised case the virgin and char emissivity were both 1. Further optimisation is possible but is cumbersome and has little value.

The first peak in the mass loss rate is slightly overestimated. The difference between experiment and simulation for the start of release of volatiles and for the first peak time is about 30 s. The first peak can be better predicted, but then the second peak was worse. The steady phase in between the two peaks is not predicted. The mass loss rate rises too fast into the second peak and the second peak is underestimated. The mass loss ends abruptly, while in the experiment this is gently. This could be explained by char oxidation in the experiment.

9.3.3 Variable mesh

The optimised properties for the "Variable meshes model" are given in Table 9.7.

The "Variable meshes model" can predict both peaks in the mass loss rate. The steady phase in between the two peaks is also not present. When switching from heating to pyrolysis phase or vice versa, the mass loss rate

Table 9.6: Optimised plywood properties for Arrhenius model

Prop.	Value	Units
ρ_v	462	kg/m^3
ρ_c	60	kg/m^3
c_v	4500	J/kg.K
c_c	2000	J/kg.K
λ_v	0.60	W/m.K
λ_c	0.30	W/m.K
$Q_{pyr}(T_0)$	200	kJ/kg
T_{pyr}	350	°C
E_a	137.5	kJ/mol
A	10^{10}	1/s

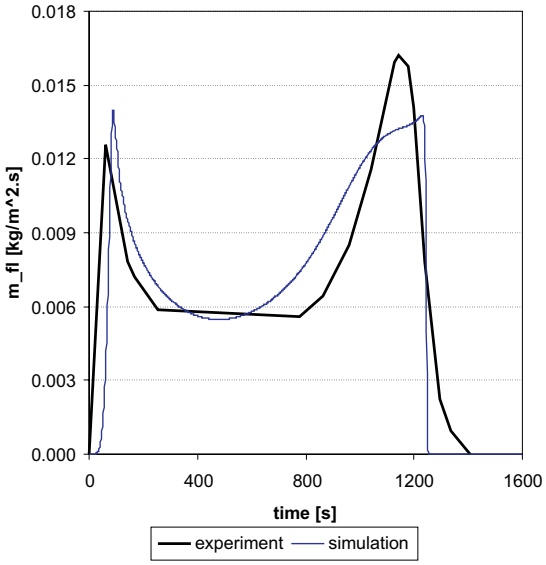

Figure 9.7: Mass loss rate for plywood in nitrogen atmosphere - Arrhenius law

Table 9.7: Optimised plywood properties for "Moving grid model"

Prop.	Value	Units
ρ_v	462	kg/m^3
ρ_c	60	kg/m^3
c_v	4000	J/kg.K
c_c	2000	J/kg.K
λ_v	0.60	W/m.K
λ_c	0.45	W/m.K
$Q_{pyr}(T_0)$	400	kJ/kg
T_{pyr}	350	°C

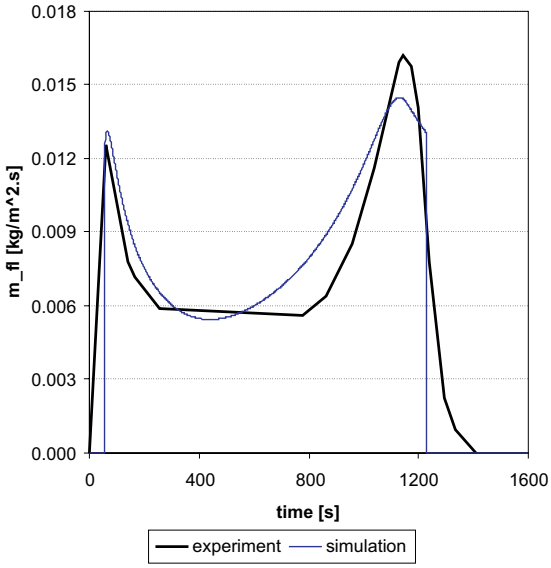

Figure 9.8: Mass loss rate for plywood in nitrogen atmosphere - Moving mesh

changes abruptly, there is no smooth increase of decrease. The mass flux rate is good predicted.

9.3.4 Integral model

Two combinations of input parameters are given in Table 9.8. The first combination is the same as for the optimised simulation for the "Variable meshes" model. The second simulation tries to optimise the entire experiment i.e. first peak, steady phase and second peak.

Table 9.8: Optimised plywood properties for "Integral model"

Prop.	Sim1	Sim2	Units
ρ_v	462	462	kg/m^3
ρ_c	60	60	kg/m^3
c_v	4000	3250	J/kg.K
c_c	2000	2000	J/kg.K
λ_v	0.60	0.80	W/m.K
λ_c	0.45	0.55	W/m.K
Q_{pyr}	400	380	kJ/kg
T_{pyr}	350	400	°C

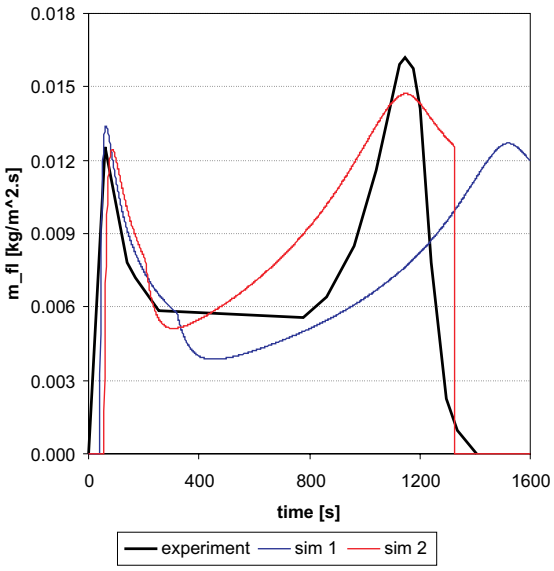

Figure 9.9: Mass loss rate for plywood in nitrogen atmosphere - Integral

In the experiment mass is lost from the start of the test. In the "Integral" and "Variable meshes" model mass loss is only possible when the surface has reached the pyrolysis temperature. Before this moment, no volatiles can be released. The transition from virgin to char is in reality not abrupt, but rather smooth as in the "Arrhenius law model".

The first peak in the mass release rate is rather good predicted by both simulations. The initial peak in the mass loss rate is for flame spread most important. The second peak appears after about 20 minutes, which is much longer than the time for the fire to spread over e.g. a vertical wall.

In *simulation 1* the second peak in the mass flux appears about 300 s later than in the "Variable meshes" model, although the same material properties are used for the two simulations! The mass flux in the "steady" zone in

between the peak is about 30 % lower than for the variable mesh. Again, the "Integral" model reacts differently than the "Variable meshes" model.

The "steady" mass flux rate between the two peaks is also not predicted by the "Integral model".

9.4 Comparison with "inert" pyrolysis test: Particle board

In this section the thermophysical material properties for partical board found in literature, are evaluated. With the experimental results optimised material properties will be determined for particle board. This material will be used in the flame spread experiments [57] and simulations. A comparison of the different models is no longer required here. In this section only the "Variable meshes" model will be used. The "Arrhenius law" model needs much more computation time which will slow down the flame spread calculations remarkably. The "Integral" and "Enthalpy" model are both faster than the "Variable meshes" model, but they do not always give correct results.

9.4.1 Description of experiment

Thermal degradation of particle board was studied by Vovell et *al.* [120]. Samples of 0.1×0.1 m were mounted vertically in a chamber of 0.3×0.45 m with a height of 0.5 m. The atmosphere was made inert by nitrogen entering at the bottom and leaving at the top of the chamber. The flow was $3\,\mathrm{m}^3/\mathrm{h}$ which gives very small gas velocities. The samples were subjected to an uniform radiant heat flux of $31\,\mathrm{kW/m^2}$ and during the experiment no flames occurred. The thickness of the sample was not given. Novozhilov et *al.* [86] used this experiment as well for his model validation and he estimated the thickness to be about 8 mm. The rear surface was insulated. The experimental conditions led to a uniform heat flux on the sample, so that thermal degradation was one-dimensional. During the experiment the surface temperature and mass loss was measured. The experimental results can be found in Figure 9.10 and Figure 9.11. The surface temperature saturates at about 500 °C. The mass loss rate has two peaks: the first at 170 s, the second at 460 s. After the second peak the mass loss slowly goes to zero. In the experiment there is already from the start of the experiment a non-zero mass loss rate, though it takes about 60 s for the surface temperature to reach 300 °C, which is a minimum pyrolysis temperature. The first mass release can be due to the release of very volatile gases (water vapor), or due to a large scan time interval.

Table 9.9: Material properties for Particle board

Property	**Value de Ris & Yan**	**Value Novozhilov**	**Units**
Virgin density	600	663	kg/m^3
Char density	60	133	kg/m^3
Virgin heat capacity	2500	2520	J/kg.K
Char heat capacity	2500	2520	J/kg.K
Volatiles heat capacity	0	-	J/kg.K
Virgin thermal conductivity	0.360	0.126	W/m.K
Char thermal conductivity	0.230	0.126	W/m.K
Surface emissivity	1.0	0.9	-
Heat of vaporization (T_0)	870	0 (!)	kJ/kg
Pyrolysis temperature	375	-	°C
Activation energy	-	125.6	kJ/mol
Pre-exponential factor	-	$5.25\ 10^7$	1/s

9.4.2 Material properties from literature

Most of the experiments in literature are not specifically designed to validate flame spread or pyrolysis models. A shortcoming of these experiments are a number of unknown material properties. Even the basic properties as the density, thermal conductivity, heat capacity of the virgin material are not always given. The uncertainty is even greater for the density, thermal conductivity, heat capacity of the char material and the pyrolysis temperature and pyrolysis heat. Two sets of material properties found in literature are examined: de Ris & Yan [19] and Novozhilov et *al.* [86], see Table 9.9. The material properties are constant and thus independent on temperature.

Some of the material properties given by Novozhilov et *al.* [86] were based on typical wood values. The heat of pyrolysis was assumed zero, probably because they optimised some parameters with the experimental results. In the formulation of the "Variable meshes" model a zero heat of vaporization is not allowed. Simulations are done with a low heat of vaporization, about 1/4 of the heat of vaporization of de Ris & Yan (200 kJ/kg). A zero heat of vaporization is certainly not realistic.

The pyrolysis temperature is determined from comparison with the Arrhenius model. In Section 4.5.3. simulations were done with $E_a = 1.257\,10^5$ J/mol and $A = 10^{10}$ 1/s, and most pyrolysis gases were released at 240 °C. The temperature at which the same reaction rate is predicted as for 240 °C in Section

4.5.3, but with E_a and A from Table 9.9, is taken as pyrolysis temperature. This was 410 °C.

The virgin density and the virgin and char specific heat capacity are almost the same. The char density, and the char and virgin thermal heat capacity, and the pyrolysis heat are quiet different between de Ris & Yan [19] and Novozhilov et *al.* [86].

For the rear surface boundary condition a heat transfer of 5 W/m^2.K is taken [19]; while for the front surface reradiation and convection, 15 W/m^2.K, was considered.

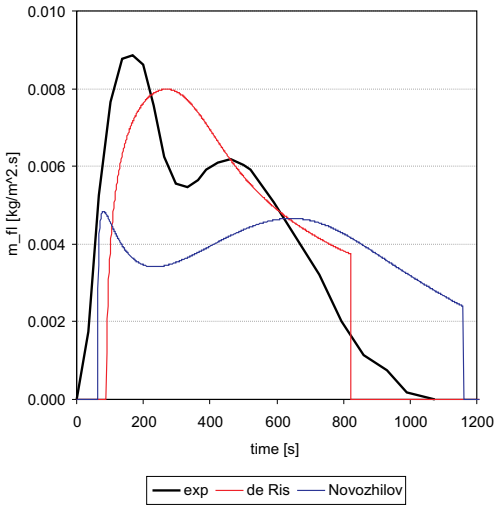

Figure 9.10: Mass flux for particle board with $q_{ext} = 31\,\mathrm{kW/m^2}$ (material properties form literature)

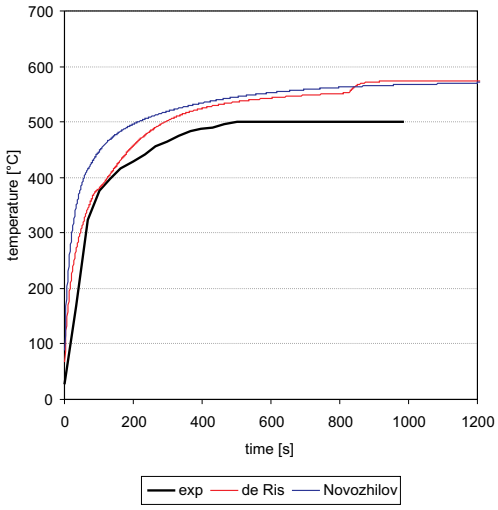

Figure 9.11: Surface temperature for particle board with $q_{ext} = 31\,\mathrm{kW/m^2}$ (material properties form literature)

Discussion of results

In the de Ris simulation the heat capacity is a bit too high. The mass loss rate curve is shifted to the right. There is only one peak in the mass loss rate, but its maximum value differs only 10 % with the maximum experimental value. The time of the peak is overestimated with 10 %. The dip in between the two peaks (at 320 s), is not predicted.

The results of the simulation with the material properties of Novozhilov give mass loss rates that are at the first half of the simulation too low (from 0 to 635 s) and for the second half too high. The height of the peak in the mass loss rate is underestimated with 46 %, while the time of the peak is underestimated with 72 %.

Both simulations give surface temperatures that are too high and rise too soon.

9.4.3 Optimised material properties

Besides these two combinations of material properties, an optimised combination is given as well in Table 9.10. In this combination a more realistic value for the virgin heat capacity and conductivity is used. In the heat transfer literature the density, the thermal conductivity, and the specific heat capacity of particle board can be found [37, 12]. Density goes from 500 to 1000 kg/m^3 regarding the type of board, i.e. low or high density. The heat capacity is for all types about 1300 J/kg.K. The thermal conductivity varies again with the density and goes from 0.078 to 0.17 W/m.K. The heat capacity and the thermal conductivity differ a lot with the values from Table 9.9. The material properties found in heat transfer literature are measured and are surely not derived from optimisation of simulation results. Therefore these values were not altered in the optimisation. For the specific heat capacity of the pyrolysis gases a value of 1900 J/kg.K is used [97, 129]. In the optimisation the char heat capacity was varied from 1300 to 2500 J/kg.K but this has little effect because of the low density of the char.

Two clearly separated peaks in the mass loss rate are only possible for a small pyrolysis heat (450 kJ/kg or lower, which is about half of what is found in literature). For all simulations the first peak occurred too soon. The second peak in the mass loss rate is not probable to be caused by the rear surface condition. A change in the rear surface condition from perfectly insulated to a heat transfer coefficient of 5 W/m^2.K, was for all combinations tested and was already felt after about 80 s. This is much earlier than the start of the second peak.

The surface temperature is for the optimal virgin thermal properties better predicted. This is due to the different virgin and char emissivity.

It is difficult to determine the optimised values for the material properties. Several combinations give qualitative similar results, though, quantitative there are serious differences.

Discussion of results

In *sim1* the char density is low (60 kg/m^3) while in *sim2* the density is high (133 kg/m^3). Because of the lower char density, *sim1* will release more mass than *sim2*. In both simulation there is only one peak in the mass loss rate. The surface temperature is for *sim2* still overestimated, but is much better than for the combination of de Ris and Novozhilov et al.

Table 9.10: Optimized material properties for Particle board

Property	**Sim1**	**Sim2**	**Sim3**	**Units**
Virgin density	660	660	660	kg/m^3
Char density	60	133	60	kg/m^3
Virgin heat capacity	1300	1300	2000	J/kg.K
Char heat capacity	1300	1300	2500	J/kg.K
Volatiles heat capacity	1900	1900	1900	J/kg.K
Virgin thermal conductivity	0.20	0.20	0.20	W/m.K
Char thermal conductivity	0.20	0.20	0.20	W/m.K
Surface emissivity virgin	0.7	0.9	0.7	-
Surface emissivity char	0.9	0.9	0.9	-
Heat of vaporization (T_0)	600	600	450	kJ/kg
Pyrolysis temperature	360	350	360	°C
Thickness	9	8	9	mm

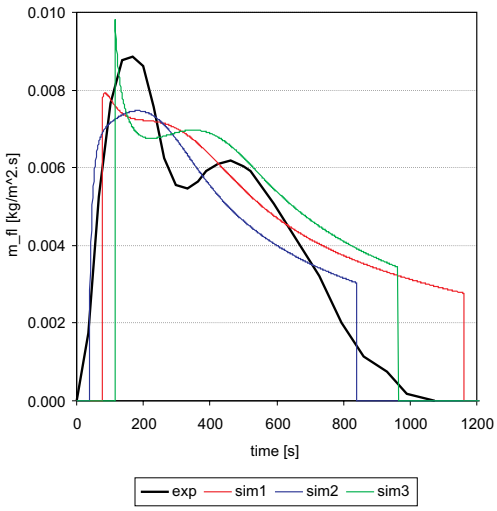

Figure 9.12: Mass flux for particle board with $q_{ext} = 31\,\mathrm{kW/m^2}$ (optimised material properties)

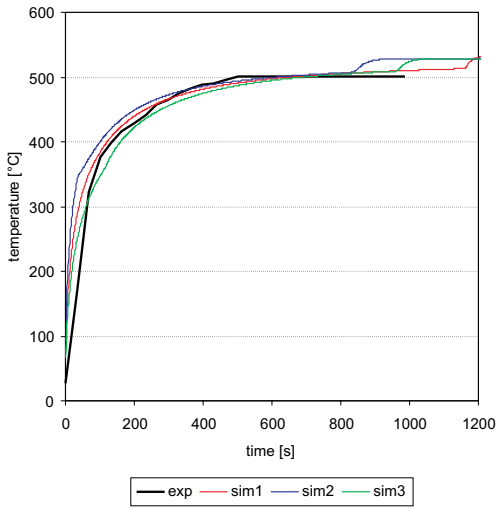

Figure 9.13: Surface temperature for particle board with $q_{ext} = 31\,\mathrm{kW/m^2}$ (optimised material properties)

In *sim3* the virgin heat capacity is taken 2000 J/kg.K instead of 1300 in literature. It is tempting to increase the virgin heat capacity because the whole mass loss curve is moved to the right and better resemblance is obtained (2 peaks in mass loss rate). In the following this high value for the heat capacity is not used because the literature data were considered to be correct and the difference between simulation and experiment is caused by other parameters.

The rear surface boundary condition is in reality not constant. When the rear surface attains a higher temperature the heat transfer coefficient (convection) will rise and the heat loss will be higher than for a constant heat transfer coefficient. Subsequent the mass loss rate will be lower at the end of the simulation which would improve the results.

9.4.4 Variable material properties

It is known that the material properties change with temperature, thickness, incident heat flux, etc. These variable properties are not incorporated in the simulations because they introduce extra unknown parameters. Most probably they will improve the simulation results. Some examples of variable material properties are given below.

The char fraction $\phi = \rho_v/\rho_c$, is known to be dependent of the incident heat flux. A formula for wood is given by [109]:

$$\phi = 0.74 \left(\frac{\dot{q}''_{cone}}{\sigma(T_s^4 - T_0^4) + h_c(T_s - T_0)} \right)^{-0.64} \tag{9.5}$$

Furthermore, the heat capacity and the conductivity can be assumed dependent on temperature by the following simple relation [41]:

$$c(T) = \frac{T}{T_{ref}} \cdot c(T_{ref}) \tag{9.6}$$

and

$$\lambda(T) = \frac{T}{T_{ref}} \cdot \lambda(T_{ref}) \tag{9.7}$$

The thermal conductivity of the char increases with specimen thickness due to the increased effect of cracks and fissures. The average thermal conductivity over a sample with thickness $L > 6\,\text{mm}$ is given by Hadvig [41]:

$$\begin{cases} L_c < L_{cr}: & \lambda_c = \frac{T}{T_{ref}} \cdot \lambda_{c,1} \\ L_c > L_{cr}: & \lambda_c = \frac{T}{T_{ref}} \cdot \frac{L}{\frac{6}{\lambda_{c,1}} + \frac{L-6}{\lambda_{c,2}}} \end{cases} \tag{9.8}$$

where L is in mm, $\lambda_{c,1}$ ($= 0.1\,\mathrm{W/m.K}$) the thermal conductivity of char for a thickness lower than 6 mm and $\lambda_{c,2}$ ($= 0.38\,\mathrm{W/m.K}$) the thermal conductivity of char for a thickness greater than 6 mm. This thickness dependency could improve the initial release of mass: the rise of the mass loss rate would grow gradually instead of rise suddenly.

9.5 Comparison with "standard" Cone Calorimeter test: Particle board

In this section simulations with the "Variable meshes" model are compared with a standard Cone Calorimeter experiment. With "standard", a normal oxidative atmosphere of 21 % oxygen is understood. The material that is tested in the Cone Calorimeter is the same material that is used in the flame spread experiment of Chapter 12. The purpose of these simulations is to check if the material properties determined in Section 9.4 are also valid for the particle board that will be used in the flame spread experiment. Or in other words, are the material properties fundamental? This section can also be seen as the modelling of the Cone Calorimeter experiment.

The results of the standard Cone Calorimeter results are not used for optimisation of all of the material properties because the boundary condition, more particular the flame heat flux, is not known. The flame heat flux introduces an extra unknown, which complicates the validation/optimisation. Also, the surface temperature is not measured during a standard Cone Calorimeter test which leaves only the mass loss rate for validation/optimisation.

The particle board that is used in the flame spread experiments has a density of 670 $\mathrm{kg/m^3}$ and a thickness of 11 mm. The density of the particle board is about the same as in the inert Cone Calorimeter test. As the density is the main factor that determines the type of particle board, it is assumed that the same kind of particle board is used in the inert and standard Cone Calorimeter test. It is assumed that material properties do not differ much. The experimental results will be compared with the combinations of material properties determined in the Section 9.4.

9.5.1 Boundary condition

9.5.1.1 Flame heat flux

The flame heat flux is sometimes approximated with the mean beam length method [100]. The average heat flux from a uniform, isothermal gas volume,

which represents the flame, to its boundaries is given by:

$$\dot{q}''_{flame} = \sigma \cdot T^4_{flame} \cdot \Big(1 - \exp(-\kappa \cdot L_m)\Big) \tag{9.9}$$

When using this formula the average flame temperature, the absorption coefficient and the mean beam length have to be determined. The flame temperature is estimated about 1200 K [41], while the absorption coefficient varies from 0.7 to $1.4\,\mathrm{m}^{-1}$ for Cone Calorimeter flames and even $1/13\,\mathrm{m}^{-1}$ for propane fires. The subsequent flame heat flux may then vary for 1.3 to $30\,\mathrm{kW/m^2}$. When the flame temperature and the mean beam length is assumed constant, the flame heat flux will be constant as well. Therefore the flame heat flux will be given a constant value of $10\,\mathrm{kW/m^2}$ [97]. The exact flame flux will influence the mass loss rate but not the ignition time because the flame flux is only introduced at the first release of pyrolysis gases or some time later.

9.5.1.2 Critical mass loss rate

A critical mass loss rate is defined as criterion for the introduction of the flame heat flux. When the mass loss rate of the solid is below this value, it is assumed that no flame can exist in the gas phase because there is not enough fuel to sustain the flame. This corresponds to the minimal amount of pyrolysis gases that are required to maintain a persistent flame. The critical mass loss rate is [97]:

$$m_{cr} = 0.003\ \mathrm{kg/m^2}$$

When the mass loss rate is lower than the critical mass loss rate, the solid boundary condition is given by:

$$-\lambda \left(\frac{\mathrm{d}T}{\mathrm{d}x}\right)_{x=0} = \dot{q}''_{net} = \epsilon \cdot \dot{q}''_{ext} - h_{s1} \cdot (T_{s1} - T_\infty) - \epsilon \cdot \sigma \cdot (T^4_{s1} - T^4_\infty) \tag{9.10}$$

When mass loss rate is higher than the critical mass loss rate, the solid boundary condition is changed into:

$$-\lambda \left(\frac{\mathrm{d}T}{\mathrm{d}x}\right)_{x=0} = \dot{q}''_{net} = \epsilon \cdot \dot{q}''_{ext} + \epsilon \cdot \dot{q}''_{flame} - \epsilon \cdot \sigma \cdot (T^4_{s1} - T^4_\infty) \tag{9.11}$$

The convective heat loss is thus replaced by the flame heat flux.

9.5.1.3 Rear surface

The particle board was mounted on a calcium silicate board. This is an insulation material with low conductivity [37]. The calcium silicate board is not included in the simulations, instead a constant low heat transfer coefficient was applied.

9.5.2 Results

The results of the simulations are compared with standard Cone Calorimeter tests at 25 and 50 kW/m^2 [57]. In the tests the particle board was backed with calcium silicate board. The experimental results are shown in Figure 9.14. Of course, the simulations should be compared with several Cone Calorimeter tests to include the variation of the experiment but this information was not available.

The calculation results are also given in Figure 9.14. The combinations of material properties determined in the previous section, do all underestimate the ignition time for a Cone heat flux of 50 kW/m^2. Only when the virgin thermal conductivity and the heat capacity is high ($\lambda_v = 0.3$ W/m.K, $c_v = 2500$ kJ/kg), this is the case for the combinations *sim3* and *de Ris*, the predicted ignition time is acceptable. For a Cone heat flux of 25 kW/m^2 the ignition time is largely overestimated by *sim3* and *de Ris*. The peak in the mass loss rate in all the simulations is too sharp, while in the experiment the mass loss rate stays for more than 60 s constant at about 0.015 kg/m^2.s. This discrepancy can be due to the flame heat flux which is assumed constant and is probably too low in the simulations. It can also be due to the pyrolysis gases that in the simulation flow immediately out of the solid, but in reality have a finite velocity. This effect will flatten the peak in the mass loss rate. Another explanation for the discrepancy is the scan interval during the measurements. When the peak occurs in between to scans, the true peak in the mass loss rate will not be captured.

The combination of *Novozhilov* gives mass loss rates that are significant lower than the other material property combinations strange enough, but the second peak (the slight rise at 731 s) for 50 kW/m^2 is predicted rather good. The combinations *sim1* and *sim2* do not predict any second peak. This second peak can be caused by the back effect or by char oxidation [109].

The simulations for a Cone heat flux of 25 kW/m^2 tend to overestimate the ignition time, see Table 9.11. The differences between experiment and simulation are large. Only combination *sim2* underestimates slightly the ignition time. The mass loss rate at 25 kW/m^2, is for all combinations rather good, the peak left out of consideration.

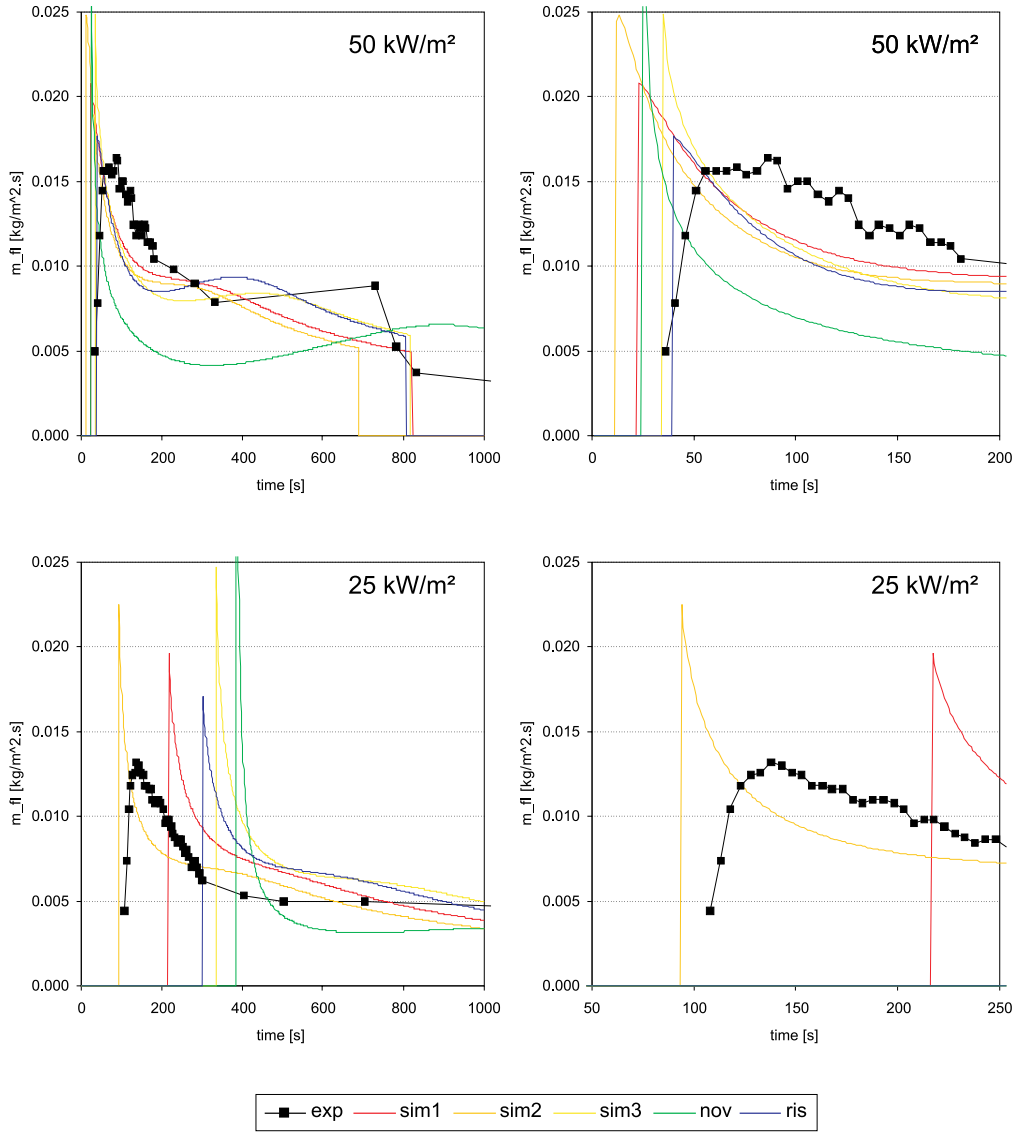

Figure 9.14: Mass flux for particle board with $q_{ext} = 50\,\mathrm{kW/m^2}$ (top) and 25 $\mathrm{kW/m^2}$ (bottom)

Table 9.11: Ignition times for different material property combinations

	25 kW/m^2		50 kW/m^2	
	(s)	(%)	(s)	(%)
Experiment	103	-	31	-
Sim1	217	111	23	26
Sim2	94	9	12	61
Sim3	334	224	35	13
Novozhilov	301	192	40	29
de Ris	384	273	25	19

It seems that the "Variable meshes" model with a single set of material properties, can not predict accurately the first mass release for the different Cone heat fluxes. For the Cone heat flux of 50 kW/m^2, the ignition time is generally underestimated while for 25 kW/m^2 the ignition time is overestimated. If material parameters are optimised for one Cone heat flux, the simulations perform worse for the other Cone heat flux.

Further tests with the Cone Calorimeter can clarify if the discrepancy is due to the variation in experimental results, or due to an incomplete physical description of the pyrolysis process. For example the difference could be explained by the heat absorbing vaporization of the water in the solid which occur at 100 °C thus before pyrolysis. Or maybe the assumption of an infinite velocity for the pyrolysis reactions is not always valid. Or maybe the assumption that the solid starts to pyrolyse at one critical temperature is only applicable in a small interval of incident heat fluxes. So the ignition or pyrolysis temperature T_{ig} is not a constant physical material property but depends on conditions prevailing at ignition [101].

When it is assumed that the incident heat fluxes in the flame spread calculation are about constant the material properties must be optimised for this heat flux. If there is a large variation in the incident heat flux, a serious error could be introduced when working with single material properties in the solid combustion model.

9.6 Conclusion

In this chapter it was demonstrated that the solid combustion models of Chapter 4 to 7 are capable to predict thermally thick and thin materials, though comparison with experiments was not done. When the solid thickness is changed, the "Integral model" sometimes gave erroneous results. These

errors are caused by the transition from semi-infinite to the finite pyrolysis phase.

The rear boundary condition is important for predicting the second peak in the mass loss rate (back effect). For the first peak it has no influence if the material is thick enough.

Material properties are often not known, especially the properties for the char layer and the pyrolysis temperature and the heat of pyrolysis. Blind calculations can give significant different results for the mass flux of pyrolysis gases than optimised calculations. The pyrolysis temperature T_{pyr} or the activation energy E_a are the most important parameters to predict the first peak in the mass flux, which is very important in the flame spread mechanism.

Determination of "optimised" material properties is ambiguous and cumbersome. Different values for the material properties can give qualitatively similar results. It is difficult to conclude what causes the difference between the simulation and the experiments. It can be due to:

- the physical model (e.g. over simplification of the pyrolysis process);
- incorrect values of the material properties;
- constant taken material properties (instead of temperature of thickness dependent).

The influence of the water content of solid material could be eliminated in experiments with for example dry polyurethane, which does not contain any water. Such inert test were not found in literature.

Standard Cone Calorimeter tests are not suitable for optimisation of material properties because the uncertainty of the flame heat flux is too large.

Flame spread calculations will reveal if the physical model with its optimised material properties is suitable.

Part III

Flame spread models

Chapter 10

Flame spread with simple gas phase model

The purpose of this chapter is to check whether conduction parallel to the solid/fluid interface (vertical) must be considered. The proportion of the conduction in the direction of the flame spread to the total heat transfer in the solid, is dependent on the rate of change of the solid boundary conditions. For example, vertical flame spread is very fast, and hence heat will be transferred to the virgin solid mainly via the solid boundaries (direct heat feedback of the flames). When the flame spread is slow on the other hand, an important portion of the energy transfer to the virgin solid is by vertical conduction through the solid.

To examine the heat transfer, realistic boundary conditions, as occurring during flame spread, must be applied to the solid. Therefore, the solid model is coupled to the simple gas phase model of the type "Direct heat feedback" of Section 3.3.1.

For the calculation of the net incident heat flux, two procedures have been followed. In the first one, the pyrolysis and the flame tip height are determined from experiments. The incident heat flux is derived from correlations dependent on pyrolysis and flame tip height. The reaction of the solid is not fed back to the gas phase and the incident heat flux. In the second procedure, the pyrolysis and flame tip height are calculated with the mass loss rate of pyrolysis gases of the solid.

The solid is solved with the "Arrhenius law" model because it includes two and three-dimensional conductive heat transfer. The height of the cells (vertical) is examined. The "Integral" and "Moving mesh" model do not allow conduction parallel to the solid/fluid interface.

10.1 Flame spread experiments

The boundary conditions for the solid are derived from upward flame spread experiments done by Brehob & Kulkarni [9]. In their experiments upward flame spread over cotton, poplar, PMMA, particle board and plywood was examined. The samples in their experiments were 30 cm wide and 120 cm high. Two side panels retained the flow two-dimensional. A line burner was used to ignite the lower edge of the sample. The igniter burner had an energy output of 18.5 kW/m. Two electric powered infrared heating panels were angled towards the sample material to supply an external heat flux.

The flame spread experiments were videotaped. By reviewing the tape the flame and pyrolysis height were determined visually. The flame height was defined as the highest location of the continuous luminous flame or the highest location of a luminous flame ball larger than 5 cm. The pyrolysis height was defined as the location of darkening of the sample surface. The results for particle board are given in Figure 10.1 for different external heat fluxes. The total heat feedback to the sample surface was measured during burning, using water-cooled Gardon circular heat flux gages. The gages were installed at heights of 10, 28, 50, 78, and 110 cm on the centreline of the sample material. The results for an external heat flux of 2.2 kW/m^2 are given in Figure 10.2. The simulations will be compared with the particle board experiments.

10.2 Simulation without feedback

10.2.1 Net incident heat flux

In the thermal flame spread model of Kulkarni and Brehob [60] the net incident heat flux was determined from correlations with experiments and given by:

$$\dot{q}''_w(x,t) \;=\; \dot{q}''_{wo} \cdot \exp\left[C_0 \left(\frac{x - x_p}{x_f - x_p}\right)\right] + \dot{q}''_{ext} - \dot{q}''_{rerad} \tag{10.1}$$

The pyrolysis height x_p and the flame tip height x_f are given in Figure 10.3. The decay factor C_o is -1.37, the maximum forward heat flux $\dot{q}''_{wo}$ is given in Table 10.1. The absorption of the external heat flux by the flame is not considered. Experiments in the Cone Calorimeter by Rhodes and Quintiere [96] showed that the flame is almost transparent ($> 90\,\%$) [109]. Equation 10.1 is used only for the forward heat flux, i.e. $x > x_p$. For the pyrolyzing

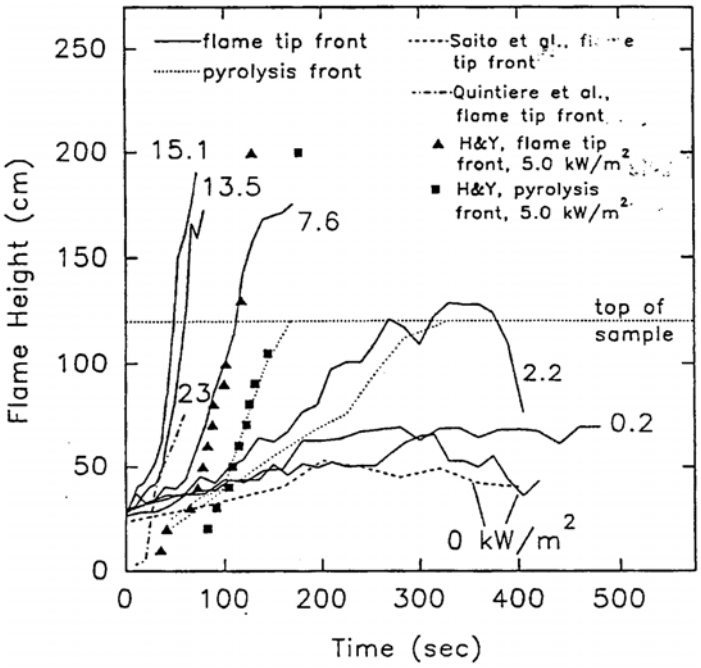

Figure 10.1: Flame spread for particle board at various levels of external radiation [9]

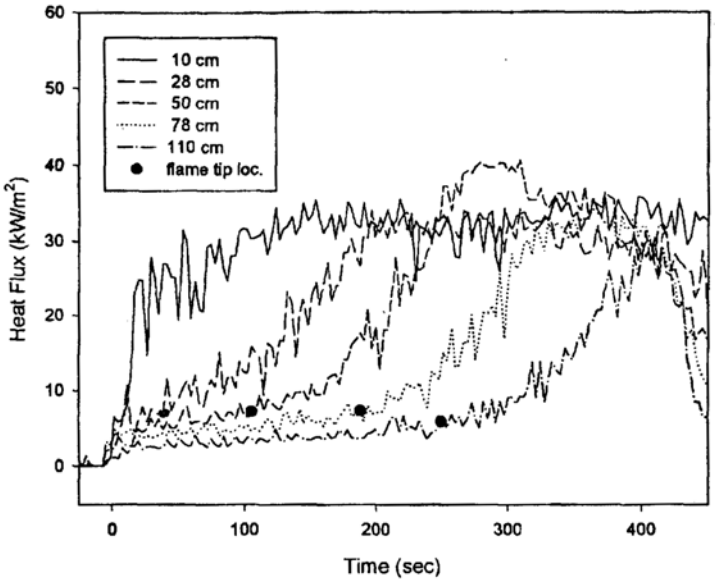

Figure 10.2: Heat flux gauge data for particle board with $\dot{q}''_{ext} = 2.2\text{kW/m}^2$ [9]

zone, i.e. $x < x_p$, no incident heat flux is needed in their flame spread model. The subsequent boundary conditions used by Kulkarni & Brehob are given in Figure 10.3.

Table 10.1: Maximum forward heat flux from Kulkarni [60]

Material	**Maximum forward heat flux $\dot{q}''_{wo}$ (kW/m^2)**
Black PMMA	31.9
Clear PMMA	34.6
Cardboard	34.5
Douglas-Fir Particle Board	24.3
Rigid Polyurethane Foam	18.8
Carpet	25.6

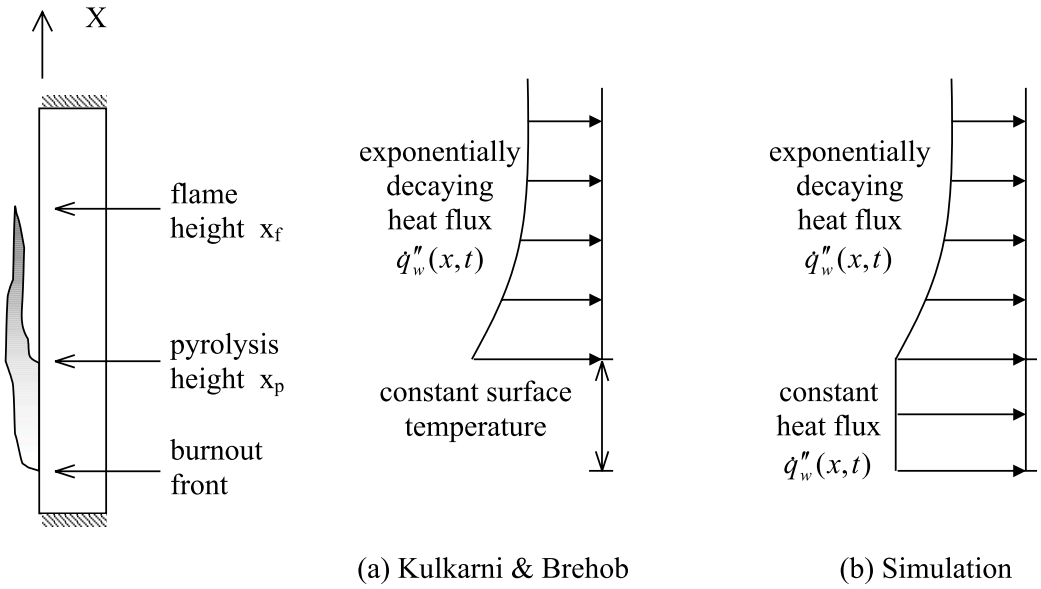

Figure 10.3: Boundary conditions for the solid material

The boundary conditions that are used for this simulation are for the heating zone (i.e. $x > x_p$) the same as in Kulkarni & Brehob [60]. For the pyrolyzing zone, no heat flux is needed in the thermal model of Kulkarni & Brehob [60]. They assumed that the surface remained on the pyrolysis temperature until burnout occurs. This is a valid assumption for non-charring

materials, but not applicable for charring materials. Here the heat flux in the pyrolyzing zone is needed as boundary condition. It is suggested, that a constant value can be taken [74]. So for the pyrolysis zone $x < x_p$:

$$\dot{q}''_w(x,t) \;=\; \dot{q}''_{wo} \;+\; \dot{q}''_{ext} \;-\; \dot{q}''_{rerad} \tag{10.2}$$

The heat flux boundary condition is shown in Figure 10.3.

The velocity of the flame tip and the pyrolysis front is assumed constant. The flame tip height x_f is determined by fitting a straight line to the results of Figure 10.1:

$$x_f \;=\; v_f \cdot t \;+\; 0.2 \tag{10.3}$$

while the pyrolysis front x_p is given by:

$$x_p \;=\; v_p \cdot t \tag{10.4}$$

The flame tip and pyrolysis front velocities are assumed equal, for $\dot{q}''_{ext} = 2.2\,\mathrm{kW/m^2}$:

$$v_f \;=\; v_p \;=\; 3.67\;10^{-3}\;\mathrm{m/s} \tag{10.5}$$

The incident heat flux to the heated zone ($x > x_{pyr}$) is given by:

$$\begin{aligned} \dot{q}''_{inc}(x,t) \;&=\; \dot{q}''_{wo} \cdot \exp\left[C_0 \left(\frac{x - x_p}{x_f - x_p}\right)\right] + \dot{q}''_{ext} \\ &=\; \dot{q}''_{wo} \cdot \exp\left[C_0 \left(\frac{x - v_p \cdot t}{0.2}\right)\right] + \dot{q}''_{ext} \end{aligned} \tag{10.6}$$

While for the pyrolysis zone ($x < x_{pyr}$) the incident heat flux is given by:

$$\dot{q}''_{inc}(x,t) \;=\; \dot{q}''_{wo} \;+\; \dot{q}''_{ext} \tag{10.7}$$

Subsequent heat fluxes at 10, 28, 50, 78, and 110 cm can be calculated and compared with the experimental results of Figure 10.2. To improve the calculations the heat flux of the igniter burner is incorporated. The flame length of these flames is determined as the flame tip height at the start of the experiment, and is about 25 cm, see Figure 10.1. For solid that is covered by these flames, an extra constant heat flux term is added which is determined from the heat flux measurement at 10 cm at the start of the experiment, see Figure 10.2.

$$\begin{aligned} \dot{q}''_{inc}(x,t) \;&=\; \dot{q}''_{wo} \cdot \exp\left[C_0 \left(\frac{x - x_p}{x_f - x_p}\right)\right] + \dot{q}''_{ext} + \dot{q}''_{ig} \\ &=\; \dot{q}''_{wo} \cdot \exp\left[C_0 \left(\frac{x - v_p \cdot t}{0.2}\right)\right] + \dot{q}''_{ext} + 20\,\mathrm{kW/m^2} \end{aligned} \tag{10.8}$$

where the last term $\dot{q}''_{ig}$ is only present for $x < 25\,\mathrm{cm}$. The incident heat flux is further improved by assuming a time lagging of the incident heat flux. In Figure 10.2 the time where the flame tip reaches the gage at 50, 78 and 110 cm is given by a black dot. Only some time after the flames have reached the gage, the incident heat flux will rise. Probably the heat flux from the tip of the flame is much lower than for the lower part of the flame. The incident heat flux is improved by assuming that the heat flux already starts decaying 35 cm beneath the pyrolysis height. The incident heat flux for $x > x_{pyr}$ is then given by:

$$\dot{q}''_{inc}(x,t) \;=\; \dot{q}''_{wo} \cdot \exp\left[C_0\left(\frac{x - v_p \cdot t + 0.35}{0.2}\right)\right] + \dot{q}''_{ext} + 20\,\mathrm{kW/m^2} \quad (10.9)$$

The calculated incident heat flux of Equation 10.9, is given in Figure 10.4. The correspondence with the measured heat flux from Figure 10.2 is very good. For the maximum forward heat flux $\dot{q}''_{wo} = 30\,\mathrm{kW/m^2}$ was used instead of $24.3\,\mathrm{kW/m^2}$.

The reradiation is described by:

$$\dot{q}''_{rerad} = \epsilon \cdot \sigma \cdot \left(T_s^4 - T_\infty^4\right) \quad (10.10)$$

where the surface emissivity is assumed 1 in the simulations.

10.2.2 Material properties

The data that are available in Kulkarni [60] were used for the material properties of particle board. Some variables and parameters were not specified in the report; these values are obtained from literature [12] when possible, or guessed, e.g. the initial temperature. The material properties are given in Table 10.2.

Table 10.2: Material properties

ρ_v	800	kg/m^3	E_a	$1.257\ 10^5$	kJ/kmol
c_v	1300	J/kg.K	A	10^{10}	1/s
λ_v	0.140	W/m.K	Q_{pyr}	$7.54\ 10^5$	kJ/kg
ρ_c	184	kg/m^3	h	1.2	m
c_c	1741	J/kg.K	l	0.0159	m
λ_c	0.121	W/m.K	T_{ini}	293	K
c_{pyr}	1006	J/kg.K	T_∞	293	K

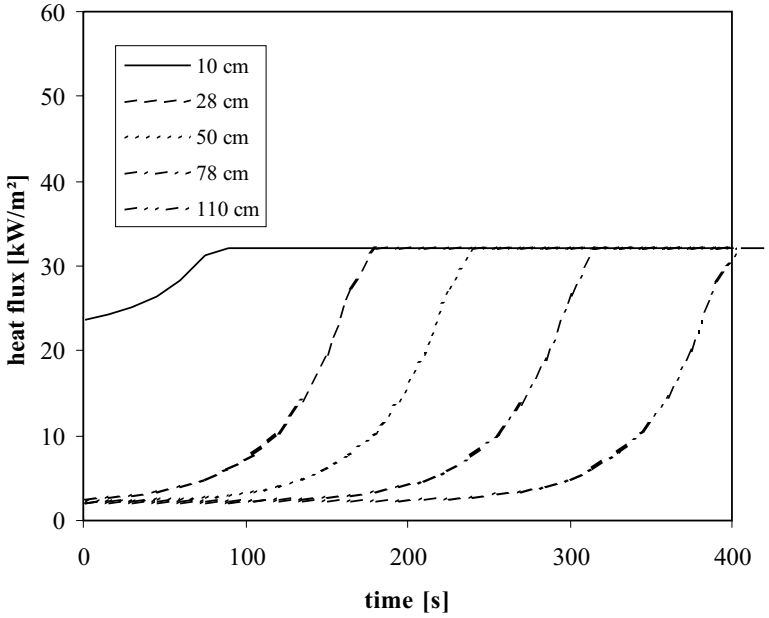

Figure 10.4: Calculated incident heat fluxes at 10, 28, 50, 78, and 110 cm

10.2.3 Results

The boundary conditions determined in Section 10.2.2 are applied to a two-dimensional solid of particle board. The solid has a length of 1.20 m and a thickness of 15.9 mm. For several mesh sizes the reaction of the solid is calculated.

Simulations were done with and without vertical heat flux (i.e. parallel to the gas/solid interface). With both horizontal and vertical heat flux, the simulations were called two-dimensional, see Section 10.2.3.1. When the vertical heat flux was neglected and only the horizontal heat flux was allowed, the simulations were called one-dimensional, see Section 10.2.3.2

10.2.3.1 Two-dimensional

Simulations are done with 200 cells in the direction perpendicular to the surface (horizontal). The cell size is fine enough according to Chapter 4 and the simulations. The number of cells in the direction of the fire spread (vertical) has been changed from 10, 25, 50, 100, 200 to 400. The surface temperature and the mass release rate of pyrolysis gases in function of the vertical height is given for the different grids in Figure 10.5. The results for the coarse grids are still good. Only at the end of the burner $x = 25$ cm, there are some significant differences. This is due to the discontinuity of the burner heat flux. The mass flux of pyrolysis gases at 200 and 300 s shows two little peaks for $x = 25$ cm. These are caused by separated pyrolysis zones. For the solid that is heated by the burner flame, the pyrolysis front is already deeper in the solid than the pyrolysis front of the solid above. In the burner zone ($x < 25$ cm), the top of the pyrolysis front, interacts in the vertical direction with cooler virgin solid of above. Heat is lost by vertical conduction and hence the production of pyrolysis gases is lower. For the solid immediately above the burner it is the other way around. The bottom of the pyrolysis front interacts in the vertical direction with the char layer from the burner zone beneath. This char layer is at elevated temperature and will provide extra heat to the pyrolysis zone. Hence the small increase in the mass release rate. Only for very small cell size in the vertical direction the two separated fronts will merge to one continuous front where part of the front will move in vertical direction. To capture the vertical movement of the front, very fine cells in vertical direction are required.

For 100 cells in vertical direction, i.e. $\Delta y = 1.2$ cm the solution already seems grid independent, except for the little peaks at $x = 25$ cm. When the burner heat flux would decrease gradually with height, the pyrolysis front would move only horizontally inwards the solid, no front separation would

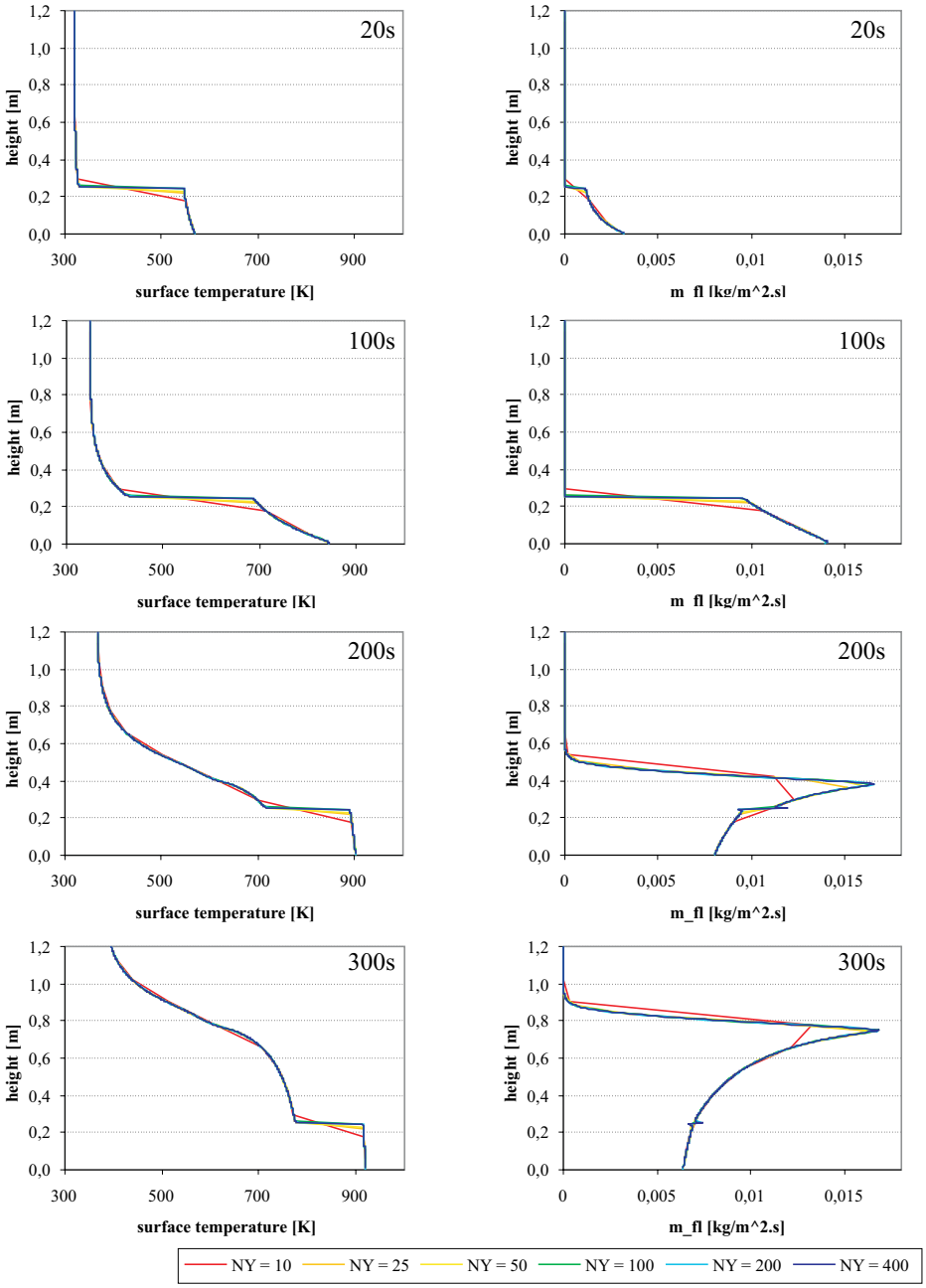

Figure 10.5: Different number of vertical cells: Surface temperature (left) Mass release rate of pyrolysis gases (right)

be present and no peaks in the mass flux of pyrolysis gases would appear.

10.2.3.2 One-dimensional

The solid reaction models that are discussed in Chapter 4 to 8, are originally all one-dimensional. Only for the "Arrhenius law" model a two-dimensional formulation is given. When the other models are coupled with a CFD code for the gas phase, only one-dimensional calculations are possible.

The "Moving grid" method can be expanded to more dimensions but this is not straightforward. A three-dimensional pyrolysis front will divide the char and virgin layer and an unstructured mesh in both layers is required. The "Enthalpy method" in its standard formulation can easily be expanded to two or three dimensions, but the techniques that were developed in Chapter 7 to obtain a grid independent solution can not easily be applied in two or three dimensions. The "Integral method" of Chapter 5 is by no means applicable for more dimensional problems. The "Dual mesh" model of Chapter 8 on the other hand, can easily be expanded to two or three dimensions.

As was seen in the previous section, the front moves mainly in the horizontal direction inwards the solid. Therefore, the vertical heat conduction parallel to the solid surface is thought to be minimal and the two-dimensional effects can probably be neglected. Therefore, the solution of the two-dimensional solid reaction problem with one-dimensional models is examined. In the one-dimensional simulations, a node is no longer dependent on its upper and lower node, see Figure 10.6. Only the left and right node will determine the temperature and hence the rate of the pyrolysis reactions. Thus the simulation exists of a series of one-dimensional problems with all different boundary conditions.

In vertical flame spread problems the main heat flux to the pyrolysis front is originating from the convective and radiative heat transfer from the flame. The vertical conductive part in the solid is rather small, certainly for fast flame spread. The simplification to one-dimensional problems is therefore justified, as will be shown with results. For opposed, lateral or downwards flame spread, the conductive part in the heat transfer is not always negligible and fully two or three-dimensional methods may be necessary.

For the one-dimensional calculation the results are independent on the vertical mesh from 100 nodes in vertical direction. The surface temperature and the mass flux of the pyrolysis gases in function of the height is given for 100 nodes in the vertical direction, in Figure 10.7. Results are compared with the two-dimensional simulation. It is clear that the two and one-dimensional simulations give almost identical results. The mean difference for a moment in time is for the surface temperature smaller than 0.05 percent while for the

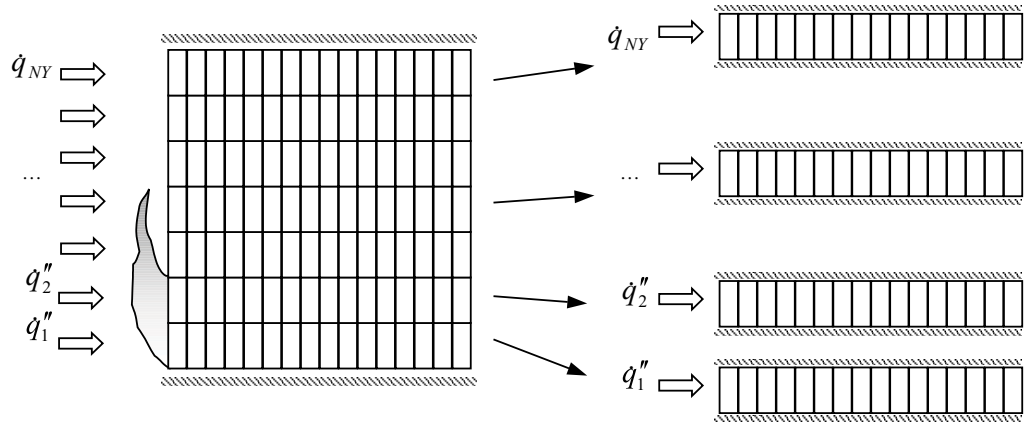

Figure 10.6: Two-dimensional problem as series of one dimensional problems

mass flux of pyrolysis gases smaller than 0.7 percent. Most of the time the difference between the two simulations is much smaller, only at the end of the burner ($x < 25\,\mathrm{cm}$) there are significant differences. The one-dimensional simulation has not the peaks in the mass flux of pyrolysis gases. Obvious, as these peaks where caused by two-dimensional conduction.

10.3 Simulation with feedback

During flame spread the heat feedback to the solid is dependent on the mass release of pyrolysis gases by the solid. A higher mass release, will give larger and hotter flames, more heat feedback, and thus more pyrolysis gases will be produced - the other way around for lower mass releases. Errors in the prediction of the mass release of pyrolysis gases can thus be amplified. The reaction of the solid material to the incident heat flux, though, is not too quick: the solid works more or less as a damper for possible oscillations in the incident heat flux. To analyse the strength of the coupling between the gas and the solid phase, a simple gas phase model is applied to the "Arrhenius model". Again, the gas phase model is based on the work of Brehob & Kulkarni [60], but it allows feedback of the mass release rate.

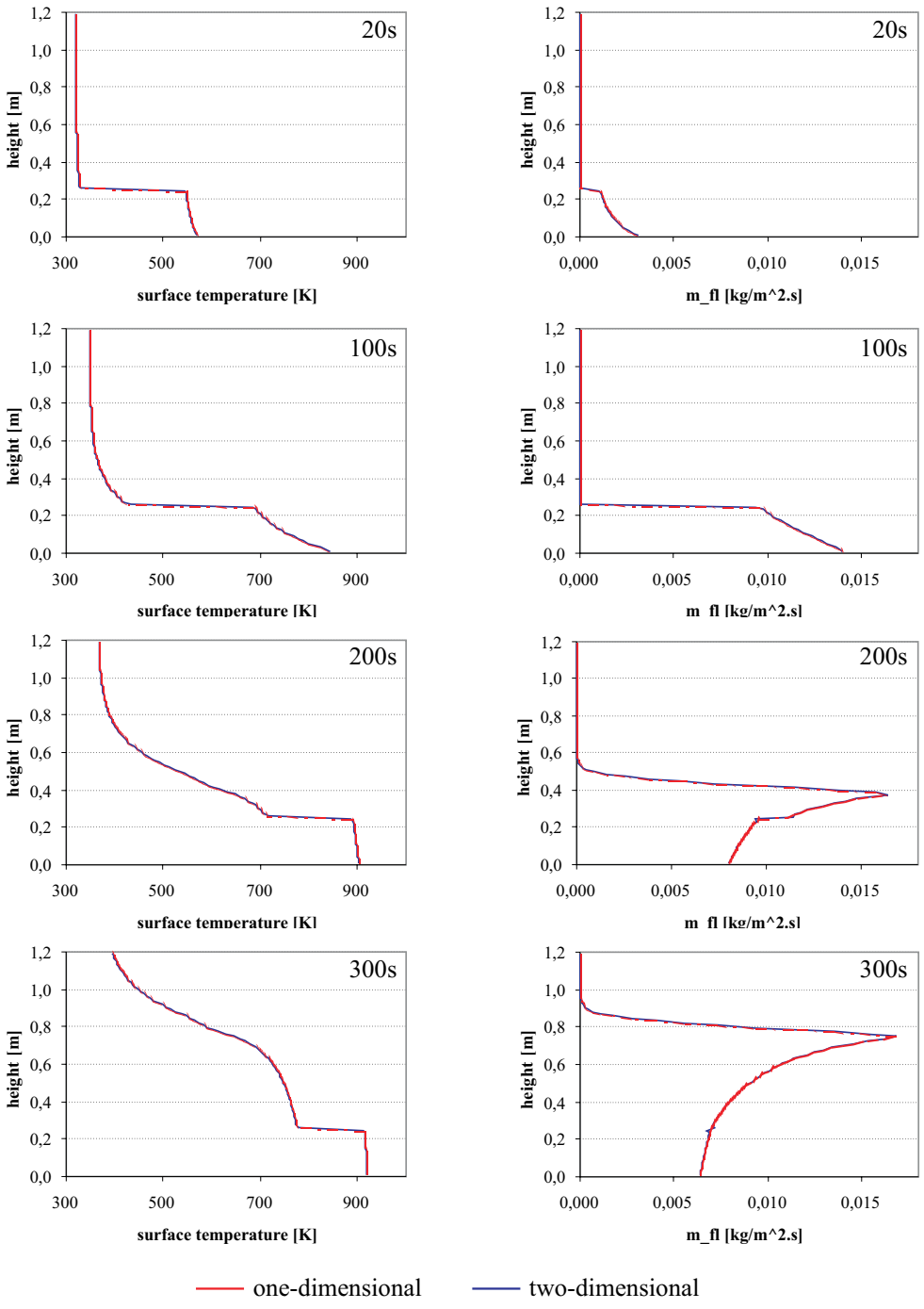

Figure 10.7: Comparison of one and two-dimensional calculations

10.3.1 Net incident heat flux

The correlation for the net incident heat flux for the heating zone, above the pyrolysis front is based on measured data and for $x > x_p$ it is given by:

$$\dot{q}''_w(x,t) \;=\; \dot{q}''_{wo} \cdot \exp\left[C_0\left(\frac{x - x_p}{x_f - x_p}\right)\right] + \dot{q}''_{ext} - \dot{q}''_{rerad} \tag{10.11}$$

And for the pyrolysis zone $x < x_p$:

$$\dot{q}''_w(x,t) \;=\; \dot{q}''_{wo} \;+\; \dot{q}''_{ext} \;-\; \dot{q}''_{rerad} \tag{10.12}$$

10.3.2 Pyrolysis front

In the flame spread model of Brehob the solid is said to be pyrolyzing when the surface temperature has reached the pyrolysis temperature. To define a vertical pyrolysis front x_p in the "Arrhenius law" model, the surface temperature will be used as well. The definition of the vertical pyrolysis front could be determined as well by a critical mass release rate of pyrolysis gases, but the temperature criterion is preferred because it is closest to the definition of the pyrolysis height x_p that is used in the correlation of Equation 10.11. The use of the formula at the start of the simulation is questionable because the forward heat flux is in reality solely determined by the burner and no contribution is yet made by the solid. The formula for the forward heat flux, Equation 10.11 in that stage of the fire spread, dependents in the simulation on $\dot{q}''_{wo}$ and is thus material dependent. In reality, the heat flux from the flame of the burner is in all cases the same.

10.3.3 Flame height

The flame height is determined by the heat release of the burning wall and of the igniter (burner) [99]:

$$x_f(t) - x_b(t) = K\left[\dot{Q}'(t) + H_c \cdot \int_{x_b(t)}^{x_p(t)} \dot{m}''_{pyr}\mathrm{d}x\right]^n \tag{10.13}$$

Herein is $\dot{m}''_{pyr}$ the local mass loss or burning rate and is predicted by the solid model. Experimental correlations gave values for $K = 0.0433$ and $n = 2/3$ [60].

In the experiments performed by Kulkarni & Brehob [60] there was no burnout front because the materials were thick and the exposure was rather

short (about 5 minutes). The formula must be altered when a burnout front occurs.

The igniter source/burner will have a decreasing contribution to the flame height when the pyrolysis zone, including the burnout front, is moving upwards. Once the burnout front has passed the flame length of the igniter source, the contribution of the igniter to the flame length is questionable.

Equation 10.13 for calculating the flame height is limited in application. When the burning surface is growing, say linearly, and burn-out effects are not considered, the flame height should be growing at least linearly. In fact, the flame height is expected to grow faster than linear, because of the higher heat output and thus larger flames. In Figure 10.8 the flame height correlation is given for a linear growing pyrolysis height, without burn-out front. After some time the correlation gives a flame length that is smaller than the pyrolysis length due to the power that is smaller than one in Equation 10.3.3. This is of course impossible and the correlation should not be used for these heights. [99]

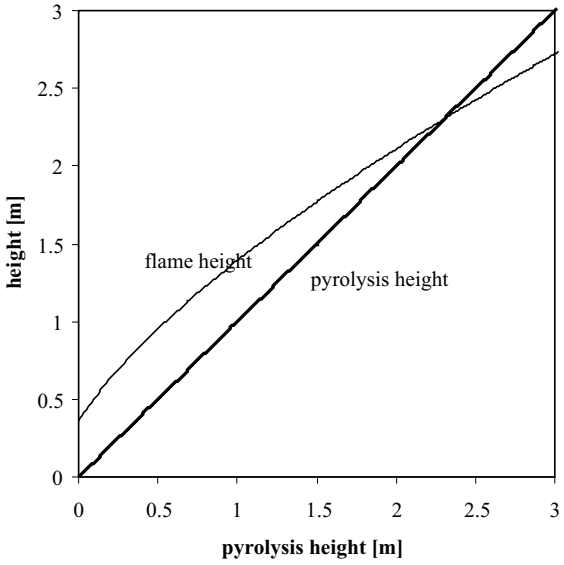

Figure 10.8: Flame height as function of pyrolysis height ($\dot{m}''_{pyr}$ assumed constant)

The procedure of the simulation is as follows. The flame length is calculated with Equation 10.13, where the mass release rate of pyrolysis gases is determined by the solid model. The location of the pyrolysis height is deter-

mined by the surface temperature. The flame and pyrolysis height determine the incident heat flux by Equation 10.11 and 10.12.

10.3.4 Results

The size of the cells in the vertical direction (the direction of the flame spread) is altered until grid independent results were obtained; 100 nodes were used. In the horizontal direction (perpendicular to the solid/gas interface) again 200 nodes were used. Calculations were done with two and one-dimensional heat transfer, both gave similar results.

When the model was run for the first time, it was noticed that overflow occurred. This overflow was due to a pyrolysis height greater than the flame tip height, see Figure 10.8. For these values the formula for the forward heat flux gives very large, unrealistic high forward heat fluxes, which cause numeric overflow. This problem is tackled by setting the flame height equal to the pyrolysis height plus a small number, only when the calculated flame height with Equation 10.13 is smaller than the pyrolysis height.

10.3.4.1 Comparison of simulations and experiments

The flame height is given in Figure 10.9 for an external heat flux of 0, 2.2 and $7\,\mathrm{kW/m^2}$. In the simulations without feedback, the flame and pyrolysis height were needed as input of the calculation, in the simulation with feedback they are results of the calculation.

The prediction of the flame tip is strongly dependent on the correlation used, i.e. Equation 10.13. For large flame heights this correlation is not good. For the case of $7\,\mathrm{kW/m^2}$ the flame height has a maximum value of about 1.3 m and decreases afterwards, where in the experiment the flame height is much larger and goes up to 1.8 m. This due to the power that is less than 1 in the flame height calculation (Equation 10.13), see Section 10.3.3. For the case of $2.2\,\mathrm{kW/m^2}$ the flame height is predicted rather good for times under 200 s. Afterwards the flame height is again underestimated. The flames do not reach the top of the sample as in the experiment. When no external heat flux is applied, the simulations are rather good. It seems that the correlation of the flame length is the main cause of the deviations in the results. Errors in the prediction of the mass release rate in the pyrolysis combustion model are not strongly amplified.

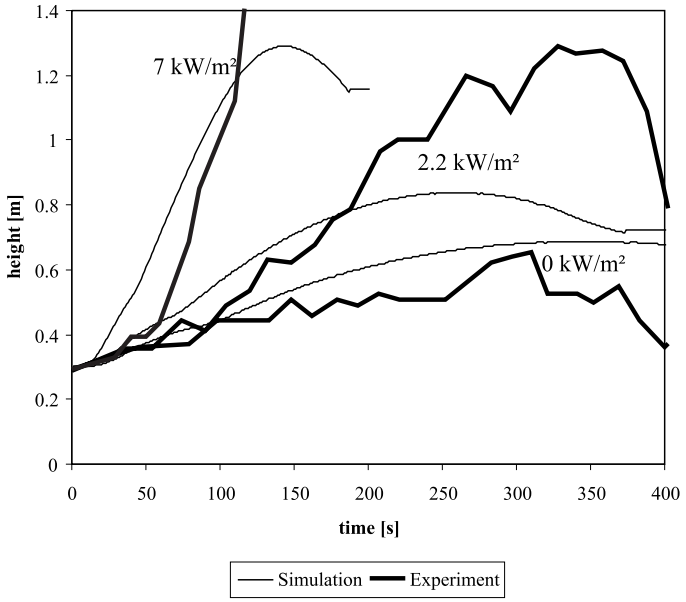

Figure 10.9: Experimental and simulated flame height, $\dot{q}''_{ext} = 0$, 2.2 and 7 kW/m^2

10.3.4.2 Further discussion of simulations

For the case with an external heat flux of 7 kW/m^2 the results are shown in more detail. In Figure 10.10 the char fraction ξ, the volume production of pyrolysis gases $\dot{m}'''_{pyr}$ and the temperature for the two-dimensional simulations are given. Notice that the scale for the X-axis (depth) is much larger than for the Y-axis (height). The front is visible in all the graphs as the zone were the char volume fraction goes form 0 to 1, or as the zone were the volume production is different from zero, or as the zone were the temperature is about 550 K. The progress of the front is shown for 20, 100, 200 and 300 s. The front moves from left to right, and is just slightly angled to the solid surface. As the temperatures in the vertical direction are almost uniform, the vertical heat flux will be small.

The conductive heat flux vectors are given in Figure 10.11. As was expected the vectors are all horizontal. In the direction perpendicular to the surface, i.e. horizontal, the conductive heat fluxes are large (order 10 kW/m^2). The convective heat transport in that direction, defined as the sensible energy contained in the pyrolysis gases, is about half of the conductive heat flux. In the direction parallel to the surface, i.e. vertical, the

conductive heat fluxes are small (order $0.01\,\mathrm{kW/m^2}$). There is no convective heat or mass transport in this direction in the solid because only horizontal flow of pyrolysis gases was allowed.

It is clear that the vertical heat conduction in the solid is negligible in regard to the two horizontal energy flows. So for vertical, fast flame spread, a one-dimensional calculation will give good results.

10.4 Conclusion

In this chapter boundary conditions as in vertical flame spread, are applied to the "Arrhenius law" solid reaction model. This is done by a prescribed incident heat flux (= without feedback) that is derived from experiments and by a simple gas phase model (= with feedback). Simulations were done with one and two-dimensional heat transfer.

There are two important conclusions from this chapter. The first one is that the size of the cells in the direction of the flame spread (vertical direction) can be taken much larger than in the direction perpendicular to the solid/fluid interface. Simulations showed that cells with a height of 1.2 cm, performed well. Even larger cells can be used, the error in the mass flux of pyrolysis gases is still small. The second conclusion is that the heat transfer in the solid is almost one-dimensional. The vertical conductive heat flux is very low and negligible. Only when there are large variations in the boundary heat flux with height, the vertical heat flux can have an influence on the mass release rate of pyrolysis gases. For example, the effect of burner in the simulation with feedback, see Section 10.2.3.1. In reality these discontinuities in the surface heat flux are not present. Therefore vertical flame spread can be calculated with a series of one-dimensional problems.

Conclusions are based on the calculations with particle board as solid material, but they are thought to hold for other building materials as well.

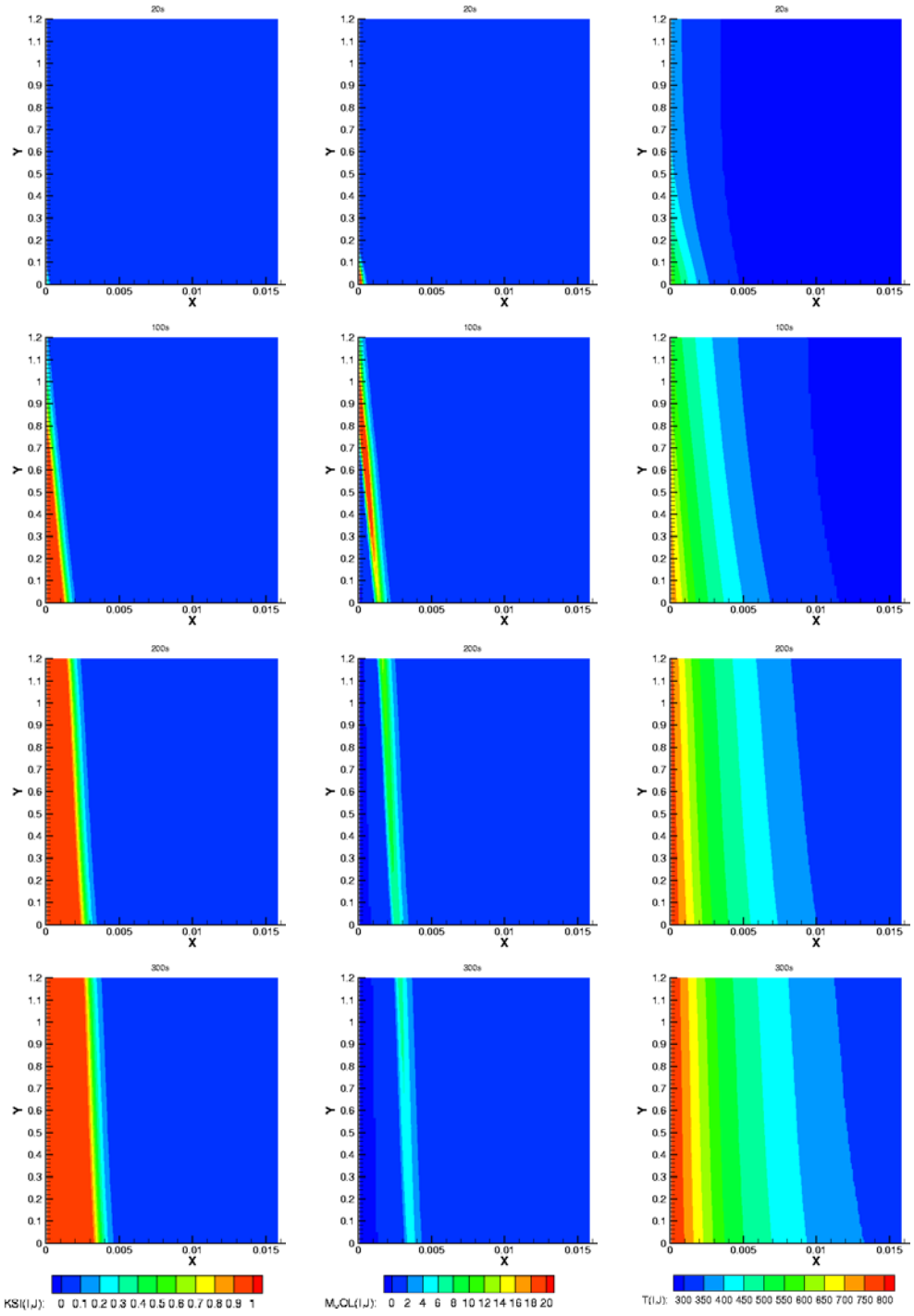

Figure 10.10: Char volmue fraction [-] (left) - Production of pyrolysis gases [kg/m^3.s] (middle) - Temperature [K] (right) for 20, 100, 200, 300 s with Y the height (m) and X the depth (m)

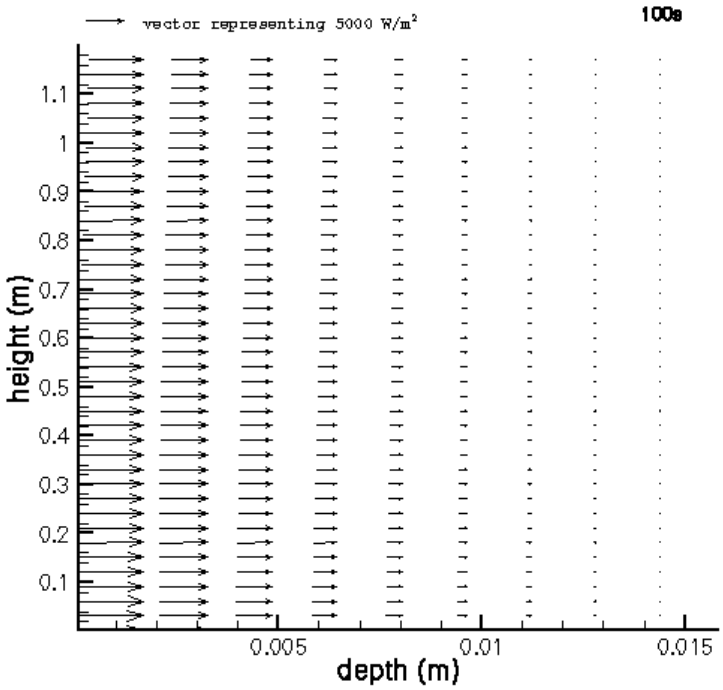

Figure 10.11: Conductive heat flux vectors

Chapter 11

Gas phase modelling

In this chapter the solution of the gas phase is discussed. A commercial computational fluid dynamics (CFD) package, CFX, is used. The calculation is rather complex: it includes turbulence, combustion, radiation and soot modelling. For each "submodel" the most important techniques, relevant for fire modelling, are given.

The solution of the gas phase, is independent on the chosen solid combustion model. All the solid combustion models described in Chapter 4 to Chapter 8, can be coupled with the gas phase model.

11.1 Governing equations

11.1.1 The conservation equations

The conservation equations for the gas phase can be derived by an infinitesimal particle, infinitesimal volume or a finite control volume analysis. The equation of continuity for the mixture is given by [63]:

$$\frac{\partial \rho}{\partial t} + (\nabla \cdot \rho \mathbf{v}) = 0 \tag{11.1}$$

The equation of continuity for a component i is given by:

$$\frac{\partial \rho_i}{\partial t} + (\nabla \cdot \dot{m}_i'') = \omega_i \quad \text{with } i = 1, 2, \ldots, N \tag{11.2}$$

or

$$\frac{\partial Y_i}{\partial t} + \mathbf{v} \cdot \nabla Y_i + \frac{1}{\rho} \nabla \cdot \rho Y_i \mathbf{V}_i = \frac{\omega_i}{\rho} \quad \text{with } i = 1, 2, \ldots, N \tag{11.3}$$

Here is Y_i the mass fraction, ω_i the chemical reaction rate of component i, $\mathbf{V}_i$ the mass diffusion velocity and $\mathbf{v}$ the mass average velocity.

The equation of conservation of momentum for a Newtonian fluid, is given by:

$$\begin{aligned}\rho\left(\frac{\partial u_i}{\partial t} + u_j\frac{\partial u_i}{\partial x_j}\right) &= \frac{\partial \sigma_{ji}}{\partial x_j} + B_i \\ &= \frac{\partial \sigma_{ji}}{\partial x_j} + \rho\sum_{k=1}^{N}(Y_k f_k)_i \\ &= \frac{\partial}{\partial x_j}\left[-p\delta_{ij} + \mu\left(\frac{\partial u_i}{\partial x_j} + \frac{\partial u_j}{\partial x_i}\right) - \frac{2}{3}\mu\left(\delta_{ij}\frac{\partial u_k}{\partial x_k}\right)\right] + \sum_{k=1}^{N}(Y_k f_k)_i\end{aligned} \tag{11.4}$$

where f_k is the (body) force per unit mass on the k-th species, B_i the body force and σ_i the stress tensor.

The equation of conservation of energy is given by:

$$\rho\frac{\mathrm{D}h}{\mathrm{D}t} - \frac{\mathrm{D}p}{\mathrm{D}t} \;=\; \dot{Q} - \nabla\cdot\mathbf{q} + \sum_{k=1}^{N}(Y_k f_k)_i\cdot(\mathbf{V}_k) + \Phi \tag{11.5}$$

with $\mathrm{D}/\mathrm{D}t$ the substantial derivative, $\dot{Q}$ the source term or the heat input, $\mathbf{q}$ the conductive heat flux, Φ dissipation by viscous stress, and the summation stands for the work done by the body forces. The viscous energy dissipation is normally assumed to be negligible in low Mach combustion processes [119].

When there are no body forces and when the viscous energy dissipation is neglected, the conservation of energy can be written as:

$$\frac{\partial \rho H}{\partial t} \;+\; \nabla\cdot(\rho\overline{U}H) \;-\; \nabla\cdot(\lambda\nabla t) \;=\; \frac{\partial p}{\partial t} \;+\; \dot{Q}_{radiation} \tag{11.6}$$

with the total enthalpy H defined by:

$$H \;=\; h + \frac{1}{2}(u^2 + v^2 + w^2) \tag{11.7}$$

The enthalpy h exists of sensible and chemical energy:

$$H(T) \;=\; \int_0^T c_p(T)\,\mathrm{d}T \;-\; \int_0^{T_{ref}} c_{po}(T)\,\mathrm{d}T \;+\; \sum H_f m_f \tag{11.8}$$

The first term is the sensible enthalpy, the second is a term to determine the reference enthalpy (zero for pure oxidant mixture at reference temperature) and the last term stands for the chemical enthalpy of the fuel.

11.1.2 Weakly or fully compressible

In the Boussinesq approximation (weakly compressible) the fluid is assumed to be incompressible.

$$\rho = \frac{p_{ref}}{RT} = \text{constant} \tag{11.9}$$

Only in the vertical-momentum equation a buoyancy term is included to model the influence of temperature upon the density:

$$(\rho - \rho_0)g \;=\; -\beta g(T - T_0) \tag{11.10}$$

where β is the thermal expansion coefficient. This approximation is only valid for small temperature differences. However, Simcox S. et *al.* [102] found that for their simulations the Boussinesq approach gave good results.

When the fluid is treated as fully compressible, a state equation is needed to determine the density:

$$\rho = \frac{p}{RT} \tag{11.11}$$

11.2 Turbulence

At low Reynolds number the flow is smooth and orderly. When the Reynolds number of a fluid flow is sufficiently high, turbulence is generated. The significant feature of a turbulent flow is its irregular nature of the small scale motion of the fluid. Within the turbulent flow, the larger eddies generate smaller eddies, and these in turn generate smaller and smaller ones. The smallest eddies have an isotropic nature. The process in which the kinetic energy is transferred into internal energy is described by the energy cascade. The kinetic energy is taken from the mean flow by the largest eddies and is transferred to smaller eddies. This energy transferring process continues until in the smallest eddies the kinetic energy is finally dissipated into internal thermal energy by the direct action of viscous stress. [46, 84]

11.2.1 Time averaging

In laminar flows, velocity and scalars have well-defined values. In contrast, turbulent flows are characterized by continuous fluctuations of velocity, which lead to fluctuations in scalars such as density, temperature and mixture fraction. In numerical simulations all these instantaneous fluctuations are not calculated because this would take too much computer time and capacity.

Besides, most of the time, these small fluctuations are not really of interest. Instead values averaged over time are calculated.

There are two sorts of averaging: conventional time or Reynolds averaging and mass-weighted or Favre-averaging. The Reynolds averaged velocity $\overline{u}$ is given by:

$$\overline{u} = \frac{1}{\Delta t} \int_{t_0}^{t_0+\Delta t} u(t)\,\mathrm{d}t \tag{11.12}$$

where Δt is a time scale, large compared to the time scale of turbulent fluctuations and small, compared to the time scale to which resolved. The instant velocity is split in its mean and fluctuating part:

$$u = \overline{u} + u' \tag{11.13}$$

The mass-weighted mean velocity $\widetilde{u}$ is defined as:

$$\widetilde{u} \;=\; \frac{\overline{\rho u}}{\overline{\rho}} \;=\; \overline{u} \;+\; \frac{\overline{\rho' u'}}{\overline{\rho}} \tag{11.14}$$

and the instant velocity is now given by:

$$u = \widetilde{u} + u'' \tag{11.15}$$

where u'' is the superimposed velocity fluctuation.

After Favre averaging the mean continuity equation becomes:

$$\frac{\partial \overline{\rho}}{\partial t} \;+\; (\nabla \cdot \overline{\rho}\widetilde{v}) \;=\; 0 \tag{11.16}$$

the mean momentum equation:

$$\frac{\partial}{\partial t}(\overline{\rho}\widetilde{u_i}) + \frac{\partial}{\partial x_j}(\overline{\rho}\widetilde{u_i}\widetilde{u_j}) = -\frac{\partial \overline{p}}{\partial x_i} + \frac{\partial}{\partial x_j}(\overline{\tau}_{ij} - \overline{\rho u_i'' u_j''}) + \overline{\rho} g_i \tag{11.17}$$

and the energy equation:

$$\frac{\partial}{\partial t}(\overline{\rho}\widetilde{h}) + \frac{\partial}{\partial x_j}(\overline{\rho}\widetilde{h}\widetilde{u_j}) = \frac{\partial \overline{p}}{\partial t} + \frac{\partial}{\partial x_j}(\overline{q}_j - \overline{\rho h'' u_j''}) + \dot{Q}_{radiation} \tag{11.18}$$

The averaging has introduced unknown terms in the momentum and energy equation, respectively $\overline{\rho u_i'' u_j''}$ and $\overline{\rho h'' u_j''}$[121]. These terms will be predicted by a turbulence model.

11.2.2 Turbulence models

A short survey of the most common turbulence models is given.

1. First order moment closure
   Boussinesq proposed a linear relationship between the Reynolds stress and the rate of strain [122]:

$$\overline{\rho u_i'' u_j''} = \frac{2}{3}\delta_{ij}\left(\overline{\rho}k + \mu_t \frac{\partial \widetilde{u_k}}{\partial x_k}\right) - \mu_t\left(\frac{\partial \widetilde{u_i}}{\partial x_j} + \frac{\partial \widetilde{u_j}}{\partial x_i}\right) \tag{11.19}$$

   The Reynolds stresses are expressed in terms of mean quantaties. The gradient-diffusion or gradient-transport model, in analogy to molecular transport processes, is adopted for turbulent flux of scalar quantities:

$$\overline{\rho u_j'' \phi_\alpha''} = -\frac{\mu_t}{\sigma_t}\frac{\partial \widetilde{\phi}_\alpha}{\partial x_j} \tag{11.20}$$

   with μ_t the turbulent viscosity and σ_t is the turbulent Prandtl / Schmidt number for variable ϕ.

   (a) Algebraic models - mixing length [119]
   This is the most simple model. The turbulent or eddy viscosity can be described by a product of a mixing length and a mixing velocity. The user has to determine the mixing length dependent of his problem (= incomplete model).

   (b) One-equation models
   The turbulent viscosity is calculated with the turbulent kinetic energy (from transport equation) and a length scale.

   (c) Linear two-equation models [63]
   Jones and Launder introduced the popular k-ε two-equation model. They also use the Boussinesq approximation but here the turbulent eddy viscosity is given by:

$$\mu_t = C_\mu \cdot \overline{\rho} \cdot \frac{k^2}{\varepsilon} \tag{11.21}$$

   The turbulent kinetic energy k and the turbulence dissipation rate ε are determined from two extra transport equations.

   (d) Non-linear two-equation models
   The Reynolds stresses are calculated from a series of functionals based on the turbulent kinetic energy k, the turbulent dissipation

rate ε, the mean strain rate and the rotation tensors. The constitutive law of Equation 11.19 is replaced by a non-linear relationship. Two extra transport equation are solved for the turbulent kinetic energy and the turbulent dissipation rate.

2. Second moment closure
   In Second moment closure models the Boussinesq relationship is no longer used to determine the Reynolds stresses. Different equations are used for each stress.

   (a) Implicit algebraic stress models
   The Reynolds stresses are calculated from a set of six algebraic equations.

   (b) Reynolds stress models
   In these models a transport equation is solved for each Reynolds stress. The unclosed terms in the transport equations for the stresses are modelled.

3. Large Eddy Simulation (LES)
   In a Large Eddy Simulation the large eddies are computed without averaging while the smaller eddies are modelled. The underlying premise is that the largest eddies are directly influenced by the boundary conditions but that the smaller-scale turbulence is nearly isotropic. Several papers have shown the applicability of the LES in fire modelling [95, 7, 6].

4. Direct numerical simulation (DNS)
   In a Direct Numerical Simulation the complete time dependent continuity, Navier Stokes and energy equations are calculated. No averaging is used and hence a very small grid and very small time steps are needed. This technique does not yet have practical use for fire modelling.

11.2.3 The k-ε turbulence model

The simulations will be done with the popular (standard) k-ε model. Therefore some more detail is given.

The turbulent kinetic energy k is obtained from its modelled transport equation:

$$\frac{\partial \rho k}{\partial t} + \nabla \cdot (\rho \mathbf{U} k) - \nabla \cdot \left(\left(\mu + \frac{\mu_t}{\sigma_k} \right) \nabla k \right) = P + G - \rho\varepsilon \qquad (11.22)$$

where the shear production term P is given by:

$$P = \tau_{ij}\frac{\partial u_i}{\partial x_j} \tag{11.23}$$

and the production of kinetic energy due to body forces G by:

$$G = -\frac{\mu + \mu_t}{\rho\sigma_\rho}\mathbf{g}\cdot\nabla\rho = \frac{\mu + \mu_t}{\sigma_T}\beta\mathbf{g}\cdot\nabla T \tag{11.24}$$

and the turbulent kinetic k energy is defined by:

$$k = \frac{1}{2}\frac{\overline{\rho u_i' u_j'}}{\overline{\rho}} \tag{11.25}$$

The turbulence dissipation rate ε is obtained from its modelled transport equation:

$$\frac{\partial\rho\varepsilon}{\partial t} + \nabla\cdot(\rho\mathbf{U}\varepsilon) - \nabla\cdot\left(\left(\mu + \frac{\mu_t}{\sigma_\varepsilon}\right)\nabla k\right) = C_{\varepsilon 1}\frac{\varepsilon}{k}\big(P + C_{\varepsilon 3}\max(G,0)\big) - C_{\varepsilon 2}\rho\frac{\varepsilon^2}{k} \tag{11.26}$$

where the turbulence dissipation rate is defined as:

$$\varepsilon = \nu\overline{\frac{\partial u_i'}{\partial x_j}\frac{\partial u_i'}{\partial x_j}} \tag{11.27}$$

The foundation of the ε equation is relatively poor. There are few direct measurements and the formulation relies to a significant extent on dimensional reasoning and the general acceptance of a closure hierarchy in which uncertainty is relegated to higher order correlations [81]. The model constants can be optimised for certain distinct cases, but general values are:

C_μ	$C_{\varepsilon 1}$	$C_{\varepsilon 2}$	$C_{\varepsilon 3}$	σ_k	σ_ε	σ_T
0.09	1.44	1.92	1.0	1.0	1.3	0.7

The constants used by the k-ε model follow from experiments. They are a compromise to get good results for all different cases, but for certain cases the constants can be improved. [106, 85]

11.2.4 Wall functions

In the region near the wall, the variables of the flow vary rapidly. One way of coping with this problem, is using a low Reynolds model where a fine grid is used to solve the boundary layer. Some damping functions are used for the turbulent viscosity in the neighbourhood of the wall. The fine grid near the wall can be avoided by using wall functions. This method uses the *law of the wall* (for fully developed flow) as the constitutive relation between velocity and surface shear stress. The shear stress is approximately constant across the log layer and the viscous sublayer. The first node has to lay inside the linear sublayer or the log layer, thus:

$$u^+ = \begin{cases} y^+ & \text{for } y^+ < y_0^+ \\ \frac{1}{\kappa} \ln (E y^+) & \text{for } y^+ > y_0^+ \end{cases} \tag{11.28}$$

with the constants $\kappa = 0.41$ and $E = 9.8$. The dimensionless velocity u^+ and distance y^+ are defined as:

$$u^+ = \frac{u}{u_\tau} = \frac{(\rho \tau_k)^{1/2}}{\tau} \cdot u \tag{11.29}$$

$$y^+ = \frac{y}{\nu / u_\tau} = \frac{(\rho \tau_k)^{1/2}}{\mu} \cdot y \tag{11.30}$$

with τ is the wall shear stress and τ_k defined as:

$$\tau_k = \rho C_\mu^{1/2} k \tag{11.31}$$

where C_μ a dimensionless constant ($= 0.09$). In Equation 11.28 y_0^+ is the cross-over point between the viscous sub-layer and the logarithmic region.

Local equilibrium is assumed in the log layer so that turbulence kinetic energy production is balanced by the dissipation in the near-wall control volume. The transport equation gives the turbulent kinetic energy with

$$\frac{\partial k}{\partial n} = 0 \tag{11.32}$$

The dissipation equation is not solved in the near-wall control volume, it is calculated from:

$$\varepsilon = \frac{u_\tau^3}{\kappa y} \quad \text{with} \quad k = \frac{u_\tau^2}{\sqrt{C_\mu}}$$

only for the grid-point near to the wall.

For the scalars the treatment is similar [13]:

$$\phi^+ = \begin{cases} \mathrm{Pr}_\phi y^+ & \text{for } y^+ < y_0^+ \\ \frac{\sigma_\phi}{\kappa} \ln(E y^+) & \text{for } y^+ > y_0^+ \end{cases} \tag{11.33}$$

where Pr is the Prandtl number μ/σ_ϕ

$$\phi^+ = \frac{(\rho\tau_k)^{1/2}}{J_\phi}(\phi_w - \phi) \tag{11.34}$$

where $J_\phi = \left(\frac{\partial\phi}{\partial n}\right)_w$is the flux of ϕ at the wall. For E_ϕ CFX uses the formula of Jayatilleke [25]:

$$E_\phi = \exp\left\{9.0\,\kappa\left[\left(\frac{\mathrm{Pr}}{\sigma_\phi}\right)^{0.75} - 1\right]\left[1 + 0.28\,\exp\left(-0.007\frac{\mathrm{Pr}}{\sigma_\phi}\right)\right]\right\} \tag{11.35}$$

11.2.5 Applicability

The k-ε model is the most widely used and validated turbulence model. It has achieved notable success in calculating a wide variety of thin shear layer and recirculating flows. The model performs particularly well in confided flows where the Reynolds stresses are most important. For unconfined flows the k-ε does not perform well. The model has also problems in swirling flows [119], and it is inaccurate with adverse pressure gradients [122]. A weakness of the k-ε model in its application to fire problems is the assumption of isotropic turbulence [14]. For example, in stratified flows the vertical component of the turbulence, and hence the vertical turbulent viscosity, is reduced compared to that in the other two directions. This reduction is not reflected in the k-ε model that is uniform and has the same turbulent viscosity in all directions [123].

11.3 Combustion

11.3.1 Theory of combustion

In a combustion process fuel and oxidizer are mixed and burned. When the fuel and oxygen are mixed at molecular level before burning, the flame is premixed. When combustion and mixing occurs simultaneously the flame is non-premixed. Often the term diffusion flame is used because at the interface or mixing layer the fuel and oxidant diffuse into each other, hence the name “diffusion flames”. This might be confusing because as well in non, as

Table 11.1: Type of combustion [121]

Mixing	**Fluid flow**	**Examples**
Non-premixed	Laminar	candle flame
	Turbulent	fire
Premixed	Laminar	Bunsen flame
	Turbulent	spark-ignited gasoline engine

in premixed flames diffusion takes place. A further categorization is made whether the fluid flow is laminar or turbulent, see Table 11.1 [121].

In enclosure fires the flames are almost always of the turbulent diffusion type. Only in very small fires laminar flames occur. In the flames, the combustion chemistry is typically fast and turbulent mixing is slower, and therefore the rate-limiting process. This implies that:

$$Da = \frac{\tau_m}{\tau_c} \gg 1 \tag{11.36}$$

where Da is the Damköhler number and τ_m and τ_c are the mixing and chemical timescales. As the reaction rate of combustion reactions is exponentially dependent on the temperature, the reaction or combustion will be restricted to thin flame zones located at the interface between fuel and oxidizer [81].

In fires, buoyancy will control the reactant mixing and combustion, so the Froude number ($Fr = u^2/gD$) or the fuel source momentum is small. The influence of buoyancy is most apparent in the near-field region of the flame (immediately above the surface). The low fuel velocity at the surface is strongly accelerated, under almost laminar flow conditions. Instabilities accompanying the buoyantly rising column then generate unsteadiness and fluctuating heat release, in turn [81].

11.3.2 Combustion mechanism

Combustion reactions are very complicated. For example, the combustion of H_2 consists of nearly 40 elementary reactions, though, the net reaction:

$$2\,H_2 \;+\; O_2 \;\longrightarrow\; 2\,H_20$$

looks quite simple. The chemical mechanism for the combustion of methane requires even many more elementary reactions. In fire simulations it is impossible to apply the full or skeletal combustion mechanism. First of all,

the composition of the gaseous fuel after pyrolysis, is not known in advance. Secondly, as there are many species in the fuel (CH_4, C_2H_6, C_2H_2, H_2, etc. [32, 87], the number of elementary reactions would lead to a prohibitive amount of computational work. As the intermediate reactions are not of direct interest in simulating fire spread, reduced mechanism are used [68].

Four combustion mechanisms can be distinguished [130]:

- Full mechanism: all the elementary reactions and intermediate species are incorporated (e.g. 49 species, 227 reactions);
- Skeletal mechanism: the full mechanism can be reduced with sensitivity analysis and rate- of production analysis of perfectly stirred reactor calculations; still a lot of species and reactions are present (e.g. 26 species and 77 reactions)
- Reduced mechanism: the skeletal mechanism can be further reduced by employing steady-state and partial-equilibrium assumptions. (e.g. 9 species, 4 reactions);
- Global mechanism: the combustion is considered to be completed in one step (e.g. 5 species, 1 reaction);

A more step mechanism can be useful when for example CO predictions are required. Soot modelling can be improved when intermediate components are known [55]. Still most of the fire simulations that are discussed in literature, use a simple one-step reaction [104, 125]. It is generally accepted that with global kinetics, the temperature profiles will be less accurate and only crude predictions of pollutant species are possible.

11.3.3 Turbulence-chemistry interaction

The influence of the turbulence on chemical reactions (or combustion) can easily be understood when we consider a simplified chemical reaction:

$$\text{fuel} + \text{oxidant} \xrightarrow{\text{k}} \text{products} \tag{11.37}$$

where k is the rate constant for the reaction. The reaction rate is strongly temperature dependent:

$$k = A \cdot \exp\left(-\frac{E}{RT}\right) \tag{11.38}$$

The instantaneous fuel disappearance rate for this simple reaction is:

$$S_f = -\rho^2 k Y_f Y_o \tag{11.39}$$

While the time mean fuel disappearance rate is given by [14]:

$$\begin{aligned}\overline{S_f} \;=\; -\,\widetilde{\rho k}\big(\overline{\rho}\widetilde{Y_f}\widetilde{Y_o} + \overline{\rho Y_f'' Y_o''}\big) \;-\; \overline{\rho(\rho k)'' Y_f''}\widetilde{Y_o} \\ -\; \overline{\rho(\rho k)'' Y_o''}\widetilde{Y_f} - \;\overline{\rho(\rho k)'' Y_f'' Y_o''}\end{aligned} \tag{11.40}$$

Reacting turbulent flow becomes very complex due to the continuous fluctuations in density, velocities, temperature and concentrations of species. The governing equations take on a very complicated, unclosed form: the Reynolds averaging gives a number of moments that contain the turbulent fluctuations and have to be modelled. Also the turbulent reaction rate is different from the reaction rate with turbulent quantities: $k\big(\overline{T}\big) \neq \overline{k(T)}$.

11.3.4 Combustion models

To include turbulence-chemistry interaction special formulation or closure methods are needed. Two popular solutions for fire applications are [121, 124]:

- Probability density function (*pdf*) methods which use a statistical description of the turbulent field together with the governing conservation equations; often a fast chemistry or equilibrium is assumed.
- Eddy-break-up models which are empirical models for the mean reaction rate in the case of fast chemistry. The reaction rate is governed by the rate of turbulent dissipation.

In fire research often a third method is considered which is the volumetric heat source (VHS). This is the simplest model for combustion, where the fire is modelled only as a volumetric heat source and the direct contribution of combustion species is totally neglected [64, 124].

11.3.4.1 Eddy-break-up models (EBU)

For laminar flows the source term in the transport equations of the reacting species is given by an Arrhenius equation:

$$S_f = -A\rho^2 Y_f Y_o \exp\left(-\frac{E}{RT}\right) \tag{11.41}$$

where A is the pre-exponential factor, E the activation energy and R the universal gas constant and T the temperature. However Spalding [107] found that the Arrhenius form did not represent the chemical reaction rate in turbulent reactive flows correctly. The predicted flame spread rate in the gas phase and the concentration profiles were not in agreement with experimental data. He suggested that the influence of the local turbulence level on the reaction rate should be taken into account.

The eddy dissipation model was first applied to turbulent diffusion flames by Magnussen and Hjertjager [71]. It assumes that the chemical reactions occur at the smallest eddy level, i.e. where the molecular transfer process is significant. When chemistry is fast, Magnussen and Hjertager suggested that the combustion rate can be determined by the rate of intermixing on a molecular scale of fuel and oxygen eddies, or in other words, by the rate of dissipation of the eddies. In a turbulent flow there exist a kinetic energy cascade, where the turbulence kinetic energy is extracted by the large eddies from the mean flow and dissipated mostly at the smallest eddies through molecular viscous dissipation. Therefore, the turbulence kinetic energy and dissipation rate, k/ε, indicates a dissipation time scale. Unlike the probability density function approach, Magnussen and Hjertager tackled the scalar variables directly. The combustion rate is expressed by:

$$S_f = A\frac{\varepsilon}{k}\min\left(\overline{Y}_f,\ \frac{\overline{Y}_o}{s}\right) \tag{11.42}$$

where $\overline{Y}_f$ is the time-averaged fuel concentration and $\overline{Y}_o$ the time-averaged oxygen concentration and s the stoichiometric ratio of oxidant to fuel. When $\overline{Y}_f$ is used, the formula represents lean fuel and oxygen rich conditions, when $\overline{Y}_o/s$ is used it represents lean oxygen and fuel rich conditions. The combustion rate is taken proportional to the time-mean mass fraction of fuel, oxygen or product, whichever is the smaller. The influence of the chemistry is entirely neglected.

An extension of the EBU model exists in which the finite rate reaction is somehow included. When the chemical induction time τ_{ch}, based on an Arrhenius equation, is smaller than the dissipation time τ_e, the reaction rate is set to zero. In all other cases, the reaction rate is unaltered. The two time scales are defined as:

$$\tau_{ch} = A_{ch}\cdot\left(\rho Y_f\right)^a\cdot\left(\rho Y_o\right)^b\cdot\exp\left(T'_A/T\right) \tag{11.43}$$

and

$$\tau_e = k/\varepsilon \tag{11.44}$$

This addresses, however, still not the central issue of turbulence-chemistry interaction. The influence of fluctuating properties is totally neglected.

11.3.4.2 Eddy-break-up model in CFX

When in CFX the EBU model is chosen, two extra transport equations are solved: one for the mean mixture fraction and one for the fuel mass fraction The mixture fraction f for a single combustion reaction can be defined as:

$$f = \frac{\chi - \chi_o}{\chi_f - \chi_o} \tag{11.45}$$

where the Schvab-Zeldovich variable χ is defined by:

$$\chi = m_f - \frac{m_o}{s} \tag{11.46}$$

and s is the ratio of the oxidant to the fuel in a stoichiometric reaction, m_f and m_o the fuel and oxygen mass fraction respectively.

If the fuel stream contains only fuel and the oxidant stream contains only oxidant, the mixture fraction can be written as:

$$f = \frac{s \cdot m_f - m_o + m_{o,oxi\,str}}{s \cdot m_{f,fuel\,str} + m_{o,oxi\,str}} = \frac{(s \cdot m_f - m_o) + 1}{s + 1} \tag{11.47}$$

The mean F of the mixture fraction f satisfies a conservative transport equation where the RHS is zero:

$$\frac{\partial \rho F}{\partial t} + \nabla \cdot (\rho \mathbf{U} F) - \nabla \cdot \left(\left(\frac{\mu_t}{\sigma_T} + \frac{\mu}{\sigma_L} \right) \nabla F \right) = 0 \tag{11.48}$$

The stoichiometric value of the mean mixture fraction is given by

$$F_{st} = \frac{1}{1 + s} \tag{11.49}$$

Beside the mixture fraction equation also a transport equation is solved for the mass fraction of the fuel, with the sink term in the RHS described by the EBU concept:

$$\frac{\partial \rho m_f}{\partial t} + \nabla \cdot (\rho \mathbf{U} m_f) - \nabla \cdot \left(\left(\frac{\mu_t}{\sigma_T} + \frac{\mu}{\sigma_L} \right) \nabla m_f \right) = \rho \frac{\varepsilon}{k} C_R C_A M_{lim} \tag{11.50}$$

where C_R is an empirical constant and $C_A = 1$ for infinite fast chemistry. For finite chemistry C_A is given by:

$$\begin{array}{lll} C_A = 1 & \text{if} & D \geq D_{ie} \\ C_A = 0 & \text{if} & D < D_{ie} \end{array} \tag{11.51}$$

where the Damköhler number D is defined as:

$$D = \tau_e/\tau_{ch} \tag{11.52}$$

and D_{ie} a critical Damköhler number. The limiting mass fraction in Equation 11.50 is determined by:

$$M_{lim} = \min\left(m_f,\, \frac{m_o}{s}\right) \tag{11.53}$$

The oxygen fraction follows from:

$$m_o = 1 - m_f - \frac{F - m_f}{F_{st}} \tag{11.54}$$

As the three components of the mixture, fuel, oxygen and products have to sum up to the unit, the mass fraction follows from:

$$m_p = 1 - m_f - m_o \tag{11.55}$$

Notice that the quality of the EBU predictions depend on the performance of the turbulence model.

11.3.4.3 Probability density function models

The probability density function models use a probabilistic approach. The probability that the fluid at certain spatial location, has a density between ρ and $\rho + \mathrm{d}\rho$, a temperature between T and $T + \mathrm{d}T$, a velocity between u and $u + \mathrm{d}u$, etc. is defined as:

$$P(\rho, T, Y_f, Y_o, u, v, w)\,\mathrm{d}\rho\,\mathrm{d}T\,\mathrm{d}Y_f\,\mathrm{d}Y_o\,\mathrm{d}u\,\mathrm{d}v\,\mathrm{d}w \tag{11.56}$$

When the density function P is known, the mean and the variation of the variable can be calculated from integrals. The problem of the influence of turbulence is now reduced to determining appropriate density functions. For the reaction rate of fuel disappearance the probability function will be dependent on the composition variables Y_f and Y_o, the mixture density and the temperature T:

$$\overline{S}_f = \int S_f(Y_f,\, Y_o,\, \rho,\, T) P(Y_f,\, Y_o,\, \rho,\, T)\,\mathrm{d}Y_f\,\mathrm{d}Y_o\,\mathrm{d}\rho\,\mathrm{d}T \tag{11.57}$$

where $P(Y_f, Y_o, r, T)$ is called the joint probability function for the scalar variables. The determination of such a function is difficult and computational

expensive (e.g. with a PDF transport equation). Therefore, simpler predefined *pdf* methods are suggested where the *pdf* is dependent on the mixture fraction f. The mean reactant mass fraction is determined by the local mixture fraction and the instantaneous reactant mass fraction by:

$$\overline{Y}_\alpha = \int_0^1 Y_\alpha(f) P(f)\,\mathrm{d}f \tag{11.58}$$

To calculate this integral there are two relations that have to be specified:

1. the mass fraction Y_α in function of the mixture fraction f;
2. the density function $P(f)$.

The probability density function is given for different flames in Figure 11.1.

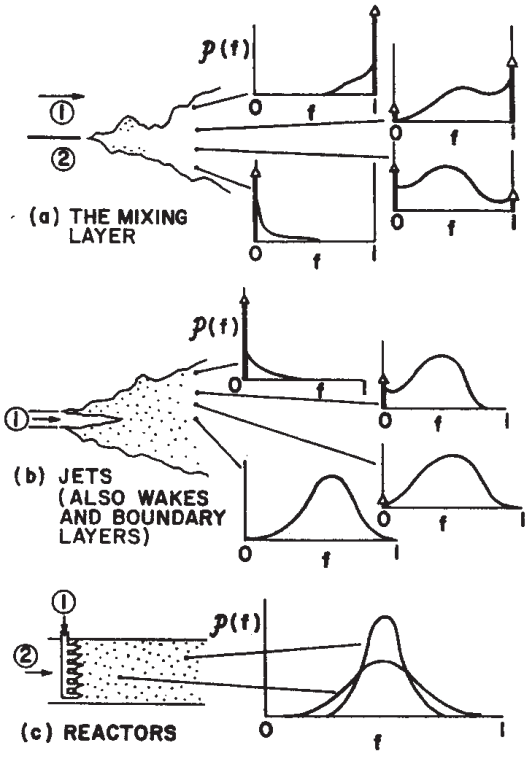

Figure 11.1: Probability density function for different flames and locations (from Kuo [63])

The relations for mass fraction $Y_\alpha(f)$ are given by:

1. Mixed-is-burnt or Burke-Schumann flame sheet:
   When the reaction time is negligibly short in comparison with the mixing time [63], it can be assumed that the chemistry is infinitely fast and that oxygen and fuel can not co-exist. This assumption implies that the instantaneous molecular-species concentrations are function only of the mixture fraction. For fuel rich mixtures ($f > f_{st}$) there will be a linear relationship between the fuel mass fraction and the mixture fraction. For stoichiometric combustion ($f = f_{st}$) the product mass fraction is maximal. The mixture exist of product, i.e. combustion gases, and the inert components of the fuel and oxygen streams. For mixtures that are fuel lean ($f < f_{st}$) (excess of oxygen) the fuel mass fraction will be zero. The mixture fraction is given by:

$$f = \frac{(s \cdot m_{fu} - m_{ox}) - (s \cdot m_{fu} - m_{ox})_{oxidant}}{(s \cdot m_{fu} - m_{ox})_{fuel} - (s \cdot m_{fu} - m_{ox})_{oxidant}} \tag{11.59}$$

   The function for the mass fraction of fuel, oxygen and product are shown in Figure 11.2 [119].

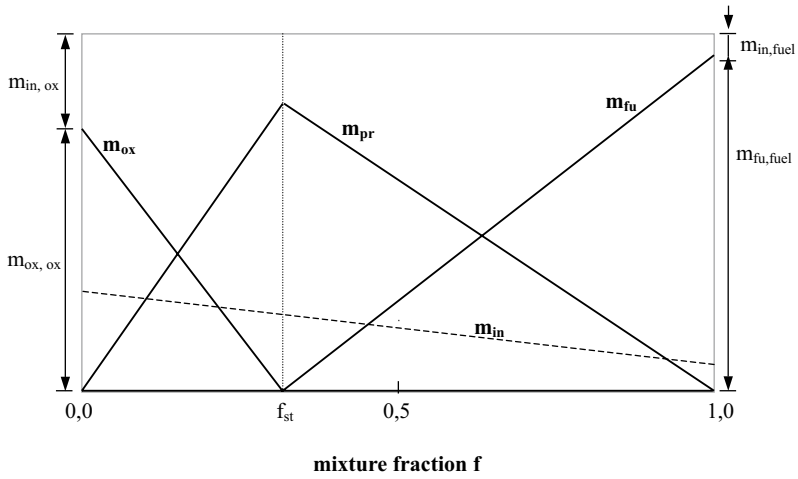

Figure 11.2: Relation between mass and mixture fraction in Burke-Schumann flame sheet

2. Chemical equilibrium:
   The relationship between the species and the mixture fraction is calculated with the assumption of chemical equilibrium. Programs as CHEMKIN, TRAN76 [34] can be used for more complex chemical reaction schemes.

3. Flamelet modelling:
   The relationship $Y_\alpha(f)$ can be obtained from laminar calculations (laminar flamelet model). The turbulent flame is then constructed of laminar flamelets. In more complex flamelet models, Y_α is dependent on f and the scalar dissipation rate χ:

$$\chi = 2D\frac{\partial f}{\partial x_k}\frac{\partial f}{\partial x_k} \tag{11.60}$$

   The function $Y_\alpha = Y_\alpha(f, \chi)$ is tabulated for different values of f and χ. [79]

4. Experiments:
   Detailed experiments can provide a library for the necessary information for the *pdf*. The state relationships of species concentrations, temperature, enthalpy, viscosity, density, and soot concentration are stored as a function of mixture fraction. Such libraries exist only for a number of simple fuels [52].

The density function $P(f)$ varies with the position in the flame, see Figure 11.1, and describes the statistical distribution of the variables. There are two options for the density function:

1. Prescribed:
   A number of functions are commonly used for the pdf:

   - Delta-function;
   - Beta-function;
   - Clipped-Gaussian.

   Those functions are dependent on the mean $\widetilde{f}$ and the variance $\widetilde{f''^2}$ of the mixture fraction. They are calculated from two extra transport equations. In empirical construction of *pdf*'s, the observation that major features of turbulent flame calculations are not sensitive to the exact shape of the *pdf* is consequently used [121].

2. Transported *pdf*:
   The shape of the *pdf* is not longer guessed since the evolution equation for the *pdf* is modelled and solved, for example, by an Eulerian, joint-scalar *pdf* transport equation. [48]

11.3.4.4 Probability density function model in CFX

CFX has the choice between a single and double delta function, and a beta function. The most popular, the beta function is defined by:

$$p(f) = Cf^{(\alpha-1)}(1-f)^{(b-1)} \tag{11.61}$$

where the coefficient C is given by the normalization of the *pdf*:

$$C = \int_0^1 f^{(\alpha-1)}(1-f)^{(b-1)}\mathrm{d}f \tag{11.62}$$

When the *pdf* is integrated over the whole mixture fraction interval, all available states are accounted, and the probability should be 1. The coefficient a and b in the beta function, are linked to the first and second moments:

$$a = \widetilde{f}\left(\frac{f(1-\widetilde{f})}{\widetilde{f''}^2} - 1\right) \tag{11.63}$$

$$b = \frac{(1-\widetilde{f})\cdot a}{\widetilde{f}} = (1-\widetilde{f})\cdot\left(\frac{f\cdot(1-\widetilde{f})}{\widetilde{f''}^2} - 1\right) \tag{11.64}$$

The Favre mean mixture fraction follows from:

$$\frac{\partial\overline{\rho}\widetilde{f}}{\partial t} + \nabla\cdot(\overline{\rho}\widetilde{f}\widetilde{\mathbf{U}}) - \nabla\cdot\left(\left(\frac{\mu_t}{\sigma_T} + \frac{\mu}{\sigma_L}\right)\nabla\widetilde{f}\right) = 0 \tag{11.65}$$

and the variance of the mixture fraction follows from a modelled transport equation:

$$\frac{\partial\overline{\rho}\widetilde{f''}^2}{\partial t} + \nabla\cdot(\overline{\rho}\widetilde{f''}^2\widetilde{\mathbf{U}}) - \nabla\cdot\left(\left(\frac{\mu_t}{\sigma_T} + \frac{\mu}{\sigma_L}\right)\nabla\widetilde{f''}^2\right) = C_{g1}\mu_T\left(\nabla\widetilde{f''}\right)^2 - C_{g2}\rho\frac{\varepsilon}{k}\widetilde{f''}^2 \tag{11.66}$$

Note that in the transport equation of the mixture fraction no source term is present which means that for this equation the turbulent closure is by-passed. This is in fact the main reason for working with a mixture fraction instead of mass fractions.

The averaged values for the fuel and oxygen mass fraction follow from *pdf* integration where the mixed-is-burnt model for $Y_a(f)$ is used:

$$\overline{m}_f = \int_0^1 \max\left(\frac{f-f_{st}}{1-f_{fs}},\,0\right)\cdot p(f)\cdot\mathrm{d}f \tag{11.67}$$

$$\overline{m}_o = \int_0^1 \max\left(1 - \frac{f}{f_{fs}}, 0\right) \cdot p(f) \cdot \mathrm{d}f \tag{11.68}$$

The product mass fraction follows from the relation $\overline{m}_f + \overline{m}_o + \overline{m}_p = 1$

11.4 Radiation

Diffusion flames are characterized by high luminosity from the incandescent carbon particles or soot that is generated at high temperature in fuel-rich conditions. A large portion of the radiation flux that is leaving the flame will, in the case of flame spread, fall on "virgin" material and raise its temperature. In upward flame spread, radiation is the most important mode of heat transfer and therefore a radiation analysis is indispensable in fire simulations.

11.4.1 Radiative transfer equation

The equation of radiative transfer which describes the radiation intensity at any position along a path S, through an absorbing, emitting and scattering media in the solid angle $\mathrm{d}\omega$ about the S direction, is given by [100]:

$$\frac{\mathrm{d}i_{\lambda'}}{\mathrm{d}S} = -a_\lambda i'_\lambda(S) + a_\lambda i'_{\lambda b}(S) - \sigma_{s\lambda} i'_\lambda(S) + \frac{\sigma_{s\lambda}}{4\pi} \int_{\omega_i}^{4\pi} i'_\lambda(S, \omega_i) \Phi(\lambda, \omega, \omega_i)\, \mathrm{d}\omega_i \tag{11.69}$$

where i is the radiation intensity (W/m^2.sr), λ the wavelength (m), a the absorption coefficient (1/m), σ_s the scattering coefficient (1/m), ω the solid angel (sr), ω_i the incident solid angle, Φ the phase function for scattering, and S the coordinate along the path of radiation. The prime $'$ denotes a directional quantity. The first term in Equation 11.69 represents the loss by absorption, the second the gain by emission of the gas, the third the loss by scattering and the last term the gain by scattering in the S direction. For isotropic scattering the phase function $\Phi = 1$.

In fires, the multi-dimensional combustion system consists of highly non-isothermal and non-homogenous medium. It is therefore necessary to introduce some simplifying assumptions and strike a compromise between accuracy and computational effort [52].

The scattering of photons by molecules and scattering by soot is negligible for heat transfer applications [75]. When no scattering is considered, the

scattering coefficient $\sigma_{s\lambda} = 0$ and the radiation equation reduces to:

$$\frac{\mathrm{d}i_{\lambda'}}{\mathrm{d}S} = -a_\lambda i'_\lambda(S) + a_\lambda i'_{\lambda b}(S) \tag{11.70}$$

The radiation energy transfer consists of, both luminous radiation from particulate soot, and non-luminous radiation, from hot product gases and unburnt fuel. The radiation problem can be divided into the solution of the integro-differential Equation 11.69, and the calculation of the radiative properties of the gas phase and the soot.

11.4.2 Solution of the radiative transfer equation

The radiative heat transfer is combined with conduction and convection and results in a highly non-linear integro-differential equation. Exact, analytical solutions are limited to simple cases with constant properties, grey medium, ...

There are several methods to solve the radiative transfer equation. They can be broadly classified into: [52, 75, 100]

- statistical methods (e.g. Monte Carlo),
- zonal methods,
- moment methods (spherical harmonics method, P-N methods),
- flux methods (e.g. six flux model and discrete ordinate method),
- hybrid methods (e.g. discrete transfer).

In CFX two algorithms for the solution of radiative heat transfer are present: the Monte Carlo and the discrete transfer algorithm. In fire problems the discrete transfer model has been the most commonly used method [17, 86, 64]. This popular model combines some of the features of the discrete ordinates, zonal and Monte Carlo methods; it is developed by Lockwood and Shah [67].

11.4.3 Solution of radiative transfer equation in CFX

The discrete transfer algorithm (DTRM) allows only isotropic scattering and diffuse or specular reflection. The radiation intensity is solved along fixed rays using the equation of radiative transfer. The paths start at solid boundaries and are generated by angular discretization. The path along a ray is

discretized by using the sections formed by breaking the path at zone boundaries. The physical quantities in each zone are assumed to be constant. The incident heat flux at the surface is calculated from integration of the different intensities (number of rays) over the solid angle.

In a fluid flow calculation the variables in one cell are influenced by the variables in the adjacent cells. In a radiation calculation the variables in one cell are influenced by all the other volume and surface cells. The radiation calculation is more complicated than the fluid flow calculation, and therfore, the radiation grid must be taken larger than the fluid flow grid to allow reasonable calculation times. In this work typically four or eight fluid cells merged in one radiation cell, see Figure 11.3.

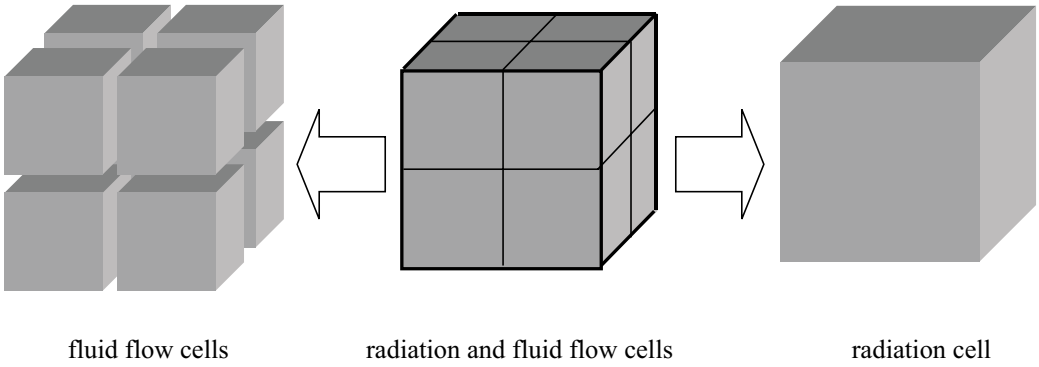

Figure 11.3: Fluid and radiation volumes

The temperature of the radiation cell is the averaged temperature of the fluid flow cells. As a consequence the emitted radiation will be lower than in the case if the same radiation grid is taken as for the fluid flow. This originates from the non-linear nature of the radiation transfer equation.

11.4.4 Determination of the radiation properties

In this work no scattering is considered because the scattering portion is small and thus not relevant in fire. Thus the only radiation property required is the absorption coefficient.

11.4.4.1 Simple correlations for the absorption coefficient

For fire applications several simple formulas for the absorption coefficient are available.

1. Constant absorption coefficient
   In their work on numerical flame spread over solid combustibles in a microgravity environment, Jiang Xi and Fan Weicheng [47] worked with a constant absorption coefficient of 0.3 m^{-1} and a constant scattering coefficient of 0.4 m^{-1} for the gas.

   Lewis et *al.* [64] used for their modelling of compartment fires a constant absorption coefficient of 0.2 m^{-1}.

   Liakos et *al.* [65] used for the modelling of stretched natural gas diffusion flames a six flux model with a constant absorption of 0.5 m^{-1} and a scattering coefficient of 0.11 m^{-1}.

2. Model of Hubband and Tien
   According to Hubband and Tien the absorption coefficient can be written as a function only dependent on temperature. This is based on linear regression analysis of experimental results:

   $$a = a_0 + b_0 \cdot T \tag{11.71}$$

   With $a_0 = 0.0517\, m^{-1}$ and $b_0 = 0.00052\, (m.K)^{-1}$ for wood. For other materials these coefficients of course will change. It is not known in advance what the validity of these numbers will be for materials other than wood. This is an approximate model as there is no dependency on concentration of species, in particular H_2O and CO_2, and the presence of soot. The model has been used by Jia et *al.* [43, 44].

3. Model of Fletcher
   For engineering applications it is said by Fletcher [30], that sufficient accurate results can be obtained with a simple relation for the absorption coefficient:

   $$a = a_g + a_s \tag{11.72}$$

   with a_g the gas absorption coefficient and a_s the soot absorption coefficient.

   The gas absorption coefficient was proposed by Gibb & Loyner [33]:

   $$a_g = 0.32 + 0.28 \exp\left(-\frac{T}{1135}\right) \tag{11.73}$$

   Luo and Beck [68] used this relation for the absorption coefficient for predicting the fire environment in a multi-room building.

The absorption coefficient for the soot was obtained from the Planck mean absorption coefficient data given in the Fire Protection Engineering Handbook [21]

$$a_s = 1264 \cdot f_v \cdot T \tag{11.74}$$

The absorption coefficient for the soot gas mixture is simply given by the sum of the absorption coefficient of the gas and of the soot. The combined Equations 11.73 and 11.74, were used by Novozhilov et *al.* [86] and Fletcher et *al.* [30]

4. Model of Magnussen and Hjertager
The model of Magnussen and Hjertager [71] relates the gas absorption coefficient to the CO_2 and H_2O concentrations

$$a_g = 0.1 \cdot (Y_{CO_2} + Y_{H_2O}) \tag{11.75}$$

This equation has been used by Zhou and Pereira [131], Jia et *al.* [45], and Kaplan et *al.* [50]. For the soot absorption coefficient they used a similar approach as in Equation 11.74.

5. Model of Modak
The absorptivity of a homogeneous and isothermal mixture of soot, CO_2, and H_2O is given in Modaks model by:

$$a = a_g + a_s - a_g a_s \tag{11.76}$$

Herein is a_g the absorptivity of the gas (CO_2 and H_2O) and approximated as in Hottel and Mangelsdorf [36]:

$$a_g = \varepsilon_g \left(\frac{T}{T_s} \right)^{0.65 - 0.2 p_w/(p_w + p_c)} \tag{11.77}$$

with T the temperature of the local gas mixture, p_w the partial pressure of H_20, p_c the partial pressure of CO_2, ε_g the emissivity of the mixture and is determined by curve fitting to detailed spectral calculations.

The soot absortivity is given by:

$$a_s = 1.0 - \frac{15}{\pi} \Psi^{(3)} \left(1 + \frac{\lambda_0 \kappa_0 T_s l}{C_2} \right) \tag{11.78}$$

where $\Psi^{(3)}$ the pentagamma function, λ_o the wavelength, T_s the black body temperature of the soot, κ_o the soot absorption coefficient ($\approx 7 f_v / \lambda_o$), l the path length, and C_2 Plancks second constant. [126, 14]

11.4.4.2 Weighted Sum of Grey Gasses

The method of Weighted Sum of Grey Gasses can be seen as a wide band model where the entire spectrum is correlated, instead of a single band. The gas is assumed to behave like a mixture of grey gases and a transparent medium. The total emissivity is given by:

$$\varepsilon = \sum_j a_j(T) \cdot \Big[1 - \exp\Big(- k_j(p_w + p_c)l - k_j\rho_s f_v\Big)\Big] \tag{11.79}$$

where p_w and p_c are the partial pressure of H_20 and CO_2, ρ_s is the soot density, and f_v the soot volume fraction, and l the pathlength. The coefficients a_j and k_j are empirically determined (e.g. in Truelove [115]).

The absorption coefficient follows from:

$$a = \frac{\ln(1-\varepsilon)}{l} \tag{11.80}$$

11.4.4.3 Wide and narrow bandmodels

The absorption and emission by gases is only significant in certain wavelength bands. In the infra-red region, for example, readily distinguished bands for H_20 are centred at 1.38, 1.87 and 2.7 mm, for CO_2 at 2.7 and 4.3 mm, for CH_4 at 2.4 and 3.3 mm and for CO at 4.7 mm. The bands originate from the vibration-rotation transitions between the different states of polyatomic gases. Each band consists of hundreds or thousands of narrow spectral lines, which partially overlap. The calculations of the absorption coefficient can be done [76]:

- Line-by-line: each line is modelled, these calculations require vast amounts of computer resources and high-resolution gas property data.
- Narrow-band: the absorption coefficient will be smoothened and averaged over a narrow spectral range. [128, 35]
- Wide-band: in principle these correlations are found by integrating narrow-band results across an entire band.

11.4.5 Radiation properties in CFX

Standard in CFX, a constant absorption and scattering coefficient is assumed. Temperature and concentration dependent absorption coefficients can be implemented via Fortran user routines. The use of band models, and weighted sum of grey gases can not be implemented via Fortran because the path

length is not available for the user. Since the beginning of 2000, CFX has included a WSGG model in its code.

11.4.6 Influence of turbulence

The inhomogeneous distributions for gaseous species, temperature and soot volume fraction along a typical radiation path are in principle instantaneous. The computed turbulent flame structure is, however, time-averaged and if only the mean properties are employed in the radiation calculation, then we imply that turbulent fluctuations play no part. Intensity predictions based on mean properties give rise, however, to substantial underestimation since the maximum mean temperature is typically much lower than the instantaneous peak flame temperature. Larger turbulence fluctuations will give larger errors [81].

The consequence of turbulence scalar fluctuations on radiation is complex. Little work has been undertaken in this area. If the temperature and radiative properties can be expressed in function of the mixture fraction f, a *pdf* method can be used for the calculation of the mean radiation intensity. It is also possible to construct a *pdf* for the scalar quantities that is dependent on the mixture fraction and the heat loss fraction [10], but a full turbulence-radiation interaction is not really present.

A more comprehensive technique is the use of the Monte Carlo method. A number of instantaneous paths is tracked where the path is divided in characteristic "eddies". The properties, temperature, emissivity and absorption of the eddies are determined by random sampling from the cumulative distribution function for mixture fraction. The difficulty in this method is the determination of the length scales for the characteristic eddies.

In literature almost all simulations do not take the turbulence-radiation interaction into account. Yan and Holmstedt [128] say that radiation based on mean scalars is in close agreement with measurements and the influence of turbulent fluctuations on the radiations, is comparable to the uncertainty in the flame structure. [42]

11.5 Soot

11.5.1 Soot production mechanism

Soot generated in fires is not uniquely defined. It consists mainly of carbon but it is quite different from graphite. Flame soot generally contains 1% by weight of hydrogen, which corresponds to an empirical formula C_8H. Gener-

ally soot particles in diffusion flames have an overall dimension of between 50 to 400 nm with a peak around 160 nm. Concerning the size of soot particles, it is difficult to generalise as many factors like fuel type, pressure, temperature or even addition of oxygen or an inert gas to the fuel play an important role in the different soot formation mechanisms.

For gaseous fuel, it is well established that smoking tendency increases with the reduction of the H/C ratio. Also fuels containing high concentrations of polycyclic aromatics produce more soot.

Although the formation and destruction of soot is not totally understood, the broad features of soot formation have been established. Six different mechanisms are involved [27]: fuel pyrolysis, nucleation, soot growth, coagulation, aggregation, and soot oxidation, see Figure 11.4.

11.5.1.1 Fuel pyrolysis

The first condensed phase material arises from the pyrolysis of the solid fuel. This includes various unsaturated hydrocarbons. When no extinction (by strain, walls and gaps) is present, the fuel decomposes to C_1 and C_2 hydrocarbons. Higher hydrocarbons which are formed after this breakdown, thus, have to be formed from these smaller hydrocarbons fragments. An important class of higher hydrocarbons are the polycyclic aromatic hydrocarbons (PAH). These compounds are usually formed under fuel-rich conditions, always present in diffusion flames. Acetylene which is formed in high amounts under rich conditions is the most important precursor of PAHs. (the competing oxidation reactions are very slow), Acetylene (C_2H_2) and PAH, obtained by cyclization even if the fuel did not contain aromatics itself, are two types of molecules that are often considered the most likely precursors of soot in flames.

11.5.1.2 Nucleation

Parent fuel pyrolysis is followed by cyclization, and produces a benzene ring structure. Further growth of the ring structure e.g. by addition of acetylene, eventually results in a small nucleus of soot being formed. These first nuclei are very small (diameter < 2 nm) and the formation of even large numbers of them involves in a negligible soot loading in the region of their formation. This region is generally confined in the more reactive regions of the flame on the fuel side of the flame front. From experiments it is known that there is a strong temperature dependence of the initiating fuel pyrolysis, confining soot formation to a narrow zone on the rich side of the stoichiometric contour and ceasing at temperatures below 1400 K.

11.5.1.3 Soot growth

During this process visible soot is created. Surface growth involves the attachment of gas species and their incorporation into the particulate phase. Surface growth reactions lead to an increase in the amount of soot but the number of particles remains unchanged by this process. It is interesting to note that the greatest contribution to the mass of soot formed is due to surface growth rather than nucleation ($> 95\,\%$).

11.5.1.4 Coagulation

This phase is purely a physical mechanism where random collisions between two or more soot particles result in one particle of larger size being formed. Therefore, the opposite of the surface growth occurs: the number of soot particles decreases but the amount of soot remains constant. Particle growth, increasing the diameter d, is the result of simultaneous surface growth reaction and coagulation. The particles have a diameter of about 30–50 nm, which corresponds to about one million carbon atoms. The particles are called the elementary soot particles.

11.5.1.5 Aggregation

After the particle growth stops, the soot particles which are roughly spherical in shape, join together in the formation of highly complex chains. This process is slow ($< 30\,\mathrm{ms}$).

It is such chains which form the fluffy soot flocculates, sometimes visible in the atmosphere. As a result, the soot volume fraction and average particle diameter increases with height in the flame, but the number density decreases [103]. There is a size distribution of the soot particles as the processes of soot growth, oxidation, coagulation and agglomeration imply a change in size and shape of the soot particles.

11.5.1.6 Soot oxidation

The soot formation process is often followed by a phase of soot oxidation in which the soot is burnt in the presence of oxidizing species to form gaseous products such as CO and CO_2. The eventual emission of soot from any combustion device will depend on the balance between these processes of formation and burnout. Soot formation and soot oxidation are competing reactions.

In seeking to model the soot formation and oxidation process, considerable simplification must be introduced. Detailed kinetic studies lead to

prohibitively large numbers of chemical species and reaction steps for practical applications.

11.5.2 Soot models

Many different soot models exist [54], only some models applied in fire simulations are shortly described.

11.5.2.1 Constant soot conversion fraction

The soot formation rate is here simply assumed to be locally proportional to the fuel supply rate. The soot volume fraction, which is central in the radiation calculation, is simply determined from the soot mass concentration by assuming a constant soot density. [127]. For some flames, little soot is produced and no soot has to be taken in consideration [94].

11.5.2.2 Coupled with mixture fraction

The soot volume fraction f_v is obtained at any location from the value of the mixture fraction. The fast chemistry assumption means that the soot fraction peaks at the stoichiometric mixture fraction and has linear variation with mixture fraction, with no soot being present at either $f = 0$ or $f = 1$. The value of f_v is obtained by integration of the instantaneous value of f_v weighted by the *pdf* over mixture fraction space. [30]

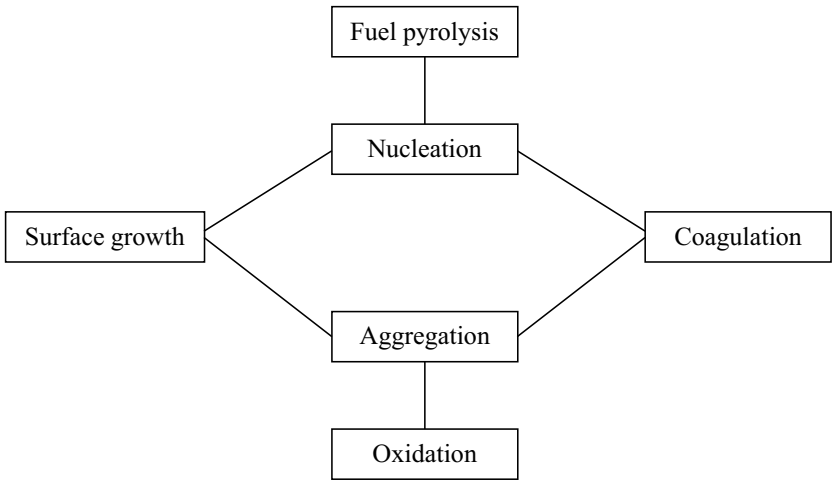

Figure 11.4: Schema of soot formation and oxidation processes

11.5.2.3 Two equation soot models

Computational soot models based on the fundamental physics of soot formation and oxidation are not yet available. Moss and Lindstedt [80, 66] have made some progress in modelling soot formation using semi-empirical models based on the mechanisms of particle inception, agglomeration, surface growth, and oxidation. Two transport equations are solved, one for the particle number density N and one for the soot mass fraction Y_s. The transport equations for both variables can be written as:

$$\frac{\partial \rho \widetilde{N}}{\partial t} + \nabla \cdot (\rho \mathbf{U} \widetilde{N}) - \nabla \cdot \left(\left(\frac{\mu_t}{\sigma_T} + \frac{\mu}{\sigma_L} \right) \nabla \widetilde{N} \right) = \widetilde{\omega_N} \tag{11.81}$$

and

$$\frac{\partial \rho \widetilde{Y_s}}{\partial t} + \nabla \cdot (\rho \mathbf{U} \widetilde{Y_s}) - \nabla \cdot \left(\left(\frac{\mu_t}{\sigma_T} + \frac{\mu}{\sigma_L} \right) \nabla \widetilde{Y_s} \right) = \widetilde{\omega_{Y_s}} \tag{11.82}$$

where ω is the production or sink term by chemical reaction [59].

The Lindstedt model solves the transport equations for soot mass fraction and soot particle number density for laminar flames with the source and sink term in the RHS given by:

$$\begin{aligned} \widetilde{\omega}_N &= \widetilde{r}_4 + \widetilde{r}_5 \overline{\rho}^2 M_s^{-1/6} \widetilde{Y}_s^{1/6} \widetilde{N}^{11/6} \\ \widetilde{\omega_{Y_s}} &= \widetilde{r}_1 M_s + \widetilde{r}_2 \overline{\rho}^{1/2} M_s^{2/3} \widetilde{Y}_s^{1/3} \widetilde{N}^{1/6} - \widetilde{r}_3 \overline{\rho}^{1/2} M_s^{1/3} \widetilde{Y}_s^{2/3} \widetilde{N}^{1/3} \end{aligned} \tag{11.83}$$

Herein are $\widetilde{r_1}$ to $\widetilde{r_5}$ reaction rates described by an Arrhenius like relation, and M_s the molecular weight of carbon. The three terms in the RHS of the soot fraction equation represent respectively nucleation, surface growth and oxidation. The two terms in the RHS of the particle number density represent nucleation and coagulation [128]. The empirical constants in the model are fuel dependent and are determined by comparison between prediction and experimental measurements in laminar flames. [80]

Two equation soot models have been applied in fire simulations by Yan and Holmstedt [128], Tuovinen and Simonson [116], and Brookes and Moss, [10].

An other two equation soot model is due to Tesner and is discussed in the next section.

11.5.3 Soot model in CFX

In CFX the Tesner model [13, 112], a two-step soot model, is available. The formation of the soot particles occurs in two steps. In the first step

radical nuclei are created, see Equation 11.84. In the second step, the rate of formation of soot particles is assumed to depend on the interaction between the active radical nuclei and the carbon radicals which, combined with the fact that the radical nuclei are destroyed on the surface of the soot particles, leads to Equation 11.85.

The concentration of radical nuclei n (mol/kg) is given by the following transport equation:

$$\frac{\partial \rho n}{\partial t} + \nabla \cdot (\rho \mathbf{U} n) - \nabla \cdot \left(\left(\frac{\mu_t}{\sigma_T} + \frac{\mu}{\sigma_L} \right) \nabla n \right) = n_0 + (f - g)n - g_0 n N \quad (11.84)$$

The soot particle concentration N (kg/kg) is given by:

$$\frac{\partial n N}{\partial t} + \nabla \cdot (\rho \mathbf{U} N) - \nabla \cdot \left(\left(\frac{\mu_t}{\sigma_T} + \frac{\mu}{\sigma_L} \right) \nabla N \right) = (a - bN)n \quad (11.85)$$

In these equations is n_o the rate at which the nuclei are spontaneously generated, given by an Arrhenius equation:

$$n_0 = A \cdot f_c \cdot C_f \cdot \exp\left(-\frac{E}{RT} \right) \quad (11.86)$$

where f_c the mass fraction of carbon in the fuel and C_f the mean concentration of fuel. The coefficients f and g in Equation 11.84 represent the processes of branching and termination in the gasphase.

$$(f - g) = 10^2 \quad (11.87)$$

and g_o is the rate of loss of nuclei due to the collisions with soot particles. In the case of acetylene flame: $A = 13.510^{36}$, $E/R = 9\,10^4\,\mathrm{K}$, $a = 10^5$ and $b = 8\,10^{-14}$.

Soot combustion or oxidation is not taken into account. This soot model must be run together with the EBU combustion model as temperatures and concentrations are derived from the Eddy Dissipation Concept.

This formulation does not give insight in the detailed kinetic mechanisms, but they give some kind of sensitivity to local conditions. The influence of turbulence interactions on the process of soot formation and oxidation are largely omitted and formation rates are evaluated at mean property levels [80].

The Tesner model was applied in enclosure fires by Luo & Beck [69]. The Tesner soot model is not always adequate for modelling flame spread. Often a constant soot conversion can give better results (Personal communication with Y. Sinai, CFX).

11.6 Implementation in CFX

The gas phase is solved with the commercial CFD code CFX (version 4.2 [13]). This code is capable of solving turbulent, combusting flow with radiation on a structured mesh. Several models for turbulence and combustion are provided, most of them were discussed already in this chapter.

11.6.1 Short description of CFX

CFX exist of a pre-processor (CFX-BUILD), a solver (CFX-SOLVER), and a post-processor (CFX-VISUALISE) [13]. In the pre-processor the geometry is drawn and a grid is created (geometry file). This geometry file is used for the generation of a radiation geometry file. The number of zones for the calculation of the radiative heat transfer is in most cases 4 to 8 times less than the number of fluid cells.

The two geometry files are combined with a command and a Fortran file. In the command file the physical and numerical description is given, such as the properties of the fluid, the chosen turbulence, combustion and radiation model, the solvers, the boundary conditions, ... The Fortran files allow the user to modify boundary conditions, transport equations, output options, ... for which the standard command file is inadequate. These Fortran user-routines are used to couple the solid pyrolysis model to the gas phase model.

The four files, see Figure 11.5 are fed to the solver which solves the problem. During the calculation the residuals for the different equations and monitoring points are given to check convergence. The generated output files can be analysed in a graphical way with the post-processor.

11.6.2 Implementation

The solid pyrolysis model is implemented via the Fortran user-routines. The solid pyrolysis program needs the net incident heat flux, determined by CFX, to calculate the surface temperature and the rate of pyrolysis gases that are released. The output of the solid model is fed to CFX via two Fortran user-routines USRBCS and USRSCR. In USRBCS the solid surface temperature is set, while in USRSRC the release of the pyrolysis gases in the gas phase is implemented, see Figure 11.6.

All transport equations in CFX are written in the following form:

$$\int_V \frac{\partial \rho\phi}{\partial t}\mathrm{d}V \; + \; \int_S \rho\mathbf{U}\cdot\mathbf{n}\phi\mathrm{d}S \; - \; \int_S \Gamma\nabla\phi\cdot\mathbf{n}\mathrm{d}S \; = \; \int_V S\mathrm{d}V \qquad (11.88)$$

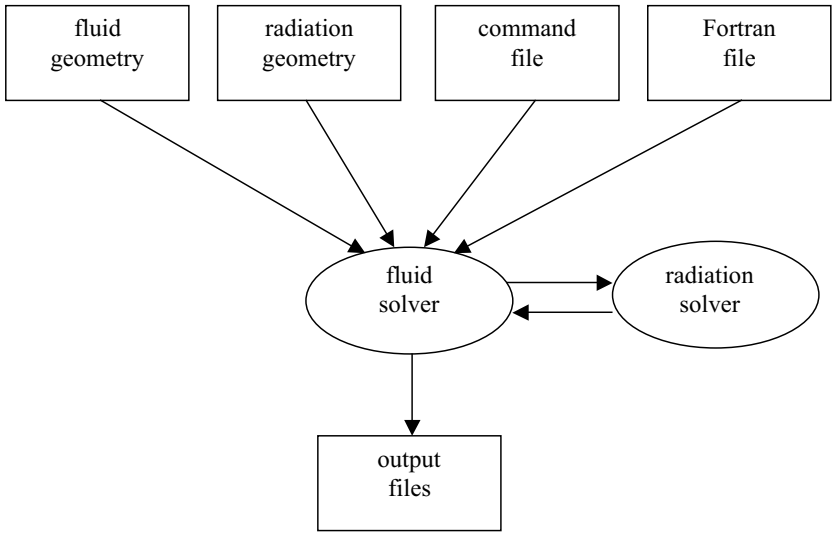

Figure 11.5: Input and output files in CFX

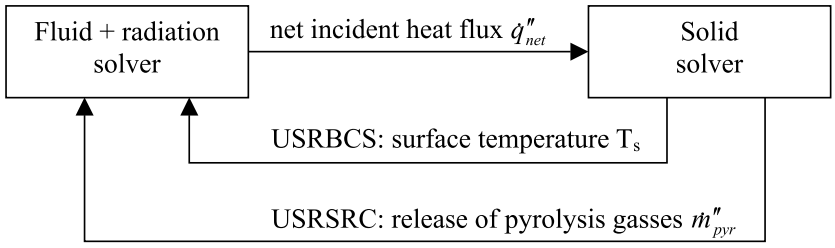

Figure 11.6: Input and output files in CFX

The RHS stands for the source or sink terms and they can be defined via the user-routines in USRSRC. The source terms are linearized and are written as:

$$\int_V S \, \mathrm{d}V = S_u + S_p \cdot \phi \tag{11.89}$$

The pyrolysis gases that enter the model (at the surface of the solid combustible) are modelled with such source terms. A source term is added for the mass, vertical velocity (momentum), energy, mixture fraction and mass fraction equation as followed:

Mass in kg/s

$$S_u = \dot{m}_{pyr} \tag{11.90}$$

Momentum perpendicular to the wall in kg.m/s^2 (u_{pyr} is set zero is most calculations):

$$S_u = \dot{m}_{pyr} \cdot u_{pyr} \tag{11.91}$$

Energy in J/s

$$S_u = \dot{m}_{pyr} \cdot m_f \cdot \left(H_{pyr} + \int_0^T c_p(T) \mathrm{d}T - \int_0^T c_{po}(T) \mathrm{d}T \right) \tag{11.92}$$

Mixture fraction in kg/s

$$S_u = \dot{m}_{pyr} \cdot F_{pyr} \tag{11.93}$$

Mass fraction fuel in kg/s

$$S_u = \dot{m}_{pyr} \cdot m_f \tag{11.94}$$

The source terms are added in the relevant equations in the cells immediately near the solid surface (see Figure 11.7).

The burner is fed with propane. Therefore the source terms in the fluid cells near the combustible wall, will be treated as sources of propane. If the heat of combustion of the pyrolysis gases is known, the mass flux can be adjusted so that the same amount of energy is produced when the pyrolysis gases are burnt.

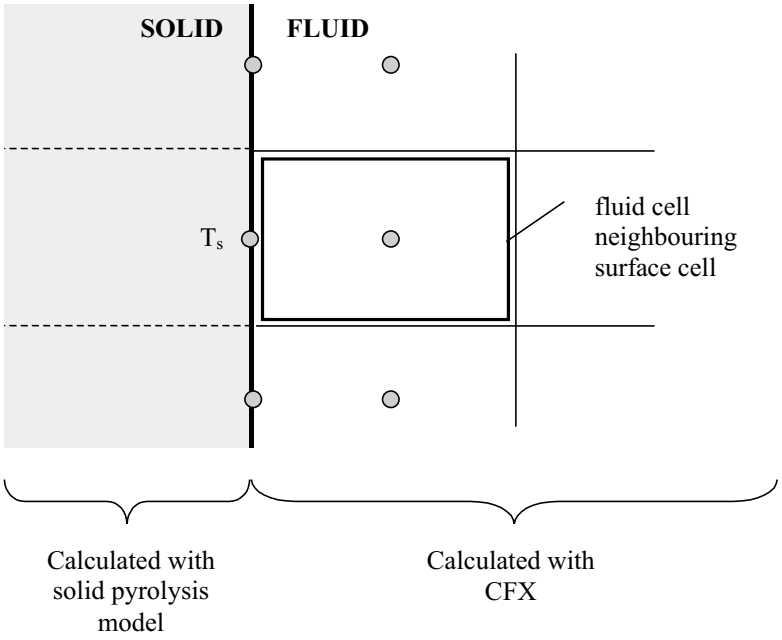

Figure 11.7: Cell modified with source term

Chapter 12

Coupled simulations

In this chapter *coupled simulations* (full gas phase plus solid model) are compared with two full scale experiments taken from literature. The first experiment (A) describes a room configuration, which represents the typical (intended) application of the developed fire model. The experiments were done at SP in Sweden by Sundström [111]. Extra measurements were done by Yan [128]. In the simulations of experiment A, only some parameters of the solid combustion model have been changed. For the gas phase *standard* models are used, like was done by Yan & Holmstedt [126] and by Jia *et al.* [44]. From this comparison a first evaluation of the coupling method can be made.

The second experiment (B) concentrated on two-dimensional vertical flame spread [58]. It was carried out by the Technical Research Centre of Finland (Valtion teknillinen tutkimuskeskus or VTT). The simulation of experiment B is seen as a different application of the fire model. Here, the purpose is to resolve the small scale phenomena near a combustible vertical wall. The grid is thus finer compared to the grid of experiment A. Such fine grid can at the time of writing hardly be used for practical fire problems because it would require too much computer time (practical fire problems are three-dimensional and transient).

One of the reasons of simulating experiment B, were the somewhat disappointing results (due to the gas phase modelling) of the simulations of experiment A. Therefore, in the simulations of experiment B, the influence of some gas phase models has been investigated. Experiment B is assumed to be more appropriate for such investigations because more detailed measurements were made. The experiment itself was also less complex because the fire spread was supposed to be two-dimensional. In experiment A, which is fully three-dimensional, interaction with different flame fronts and the hot

smoke layer in the room must be considered. This complicates comparison and validation.

Maybe it would have been more logical to have started directly with experiment B and then move on to the more complex experiment A. But during this work it was assumed that after the one-dimensional pyrolysis simulations (Chapter 9) and the two-dimensional simple flame spread simulations (Chapter 10) the coupled three-dimensional CFD calculations (as in experiment A) were the next logical step. As the two experiments are considered to be kind of different, i.e. experiment A is rather large scale while experiment B is rather small scale, the chronology of the simulations is maintained.

12.1 Experiment A

12.1.1 Description

All tests were carried out in a fire test room of length 3.6 m, width 2.4 m and height 2.4 m. At the centre of the short wall there is a doorway of 2.0 m by 0.8 m, see Figure 12.1.

The ignition source in the test configuration is a propane gas burner. The burner is square, has a side length of 17 cm, and is placed in a corner opposite to the doorway wall. Propane is supplied to the burner at a rate corresponding to 100 kW heat output for the first 10 minutes. If no flashover occurs, the heat output is increased to 300 kW.

In total 18 tests were done on different materials such as wood based boards, foamed plastics and wall papers. Only the tests with particle board will be discussed here.

12.1.2 Instrumentation

Continuous measurements were performed of rates of heat release, flame spread, heat convected out the doorway, surface and gas temperatures and productions of smoke and several gas species.

The vertical temperature distribution inside the test room, 30 cm from the walls of the corner transversely to the burner, was measured with thermocouples (0.25 mm diameter, spot welded) and suction pyrometers at heights: 0.67, 0.97, 1.27, 1.42, 1.57, 1.72 and 2.1 m. The suction pyrometers were constructed with a thermocouple inside a thin tube through which a high speed air stream was forced. Radiation errors in the measurements were thus minimized. By comparison of the suction pyrometers with the thermocouple measurements the radiation error could be estimated. The measured

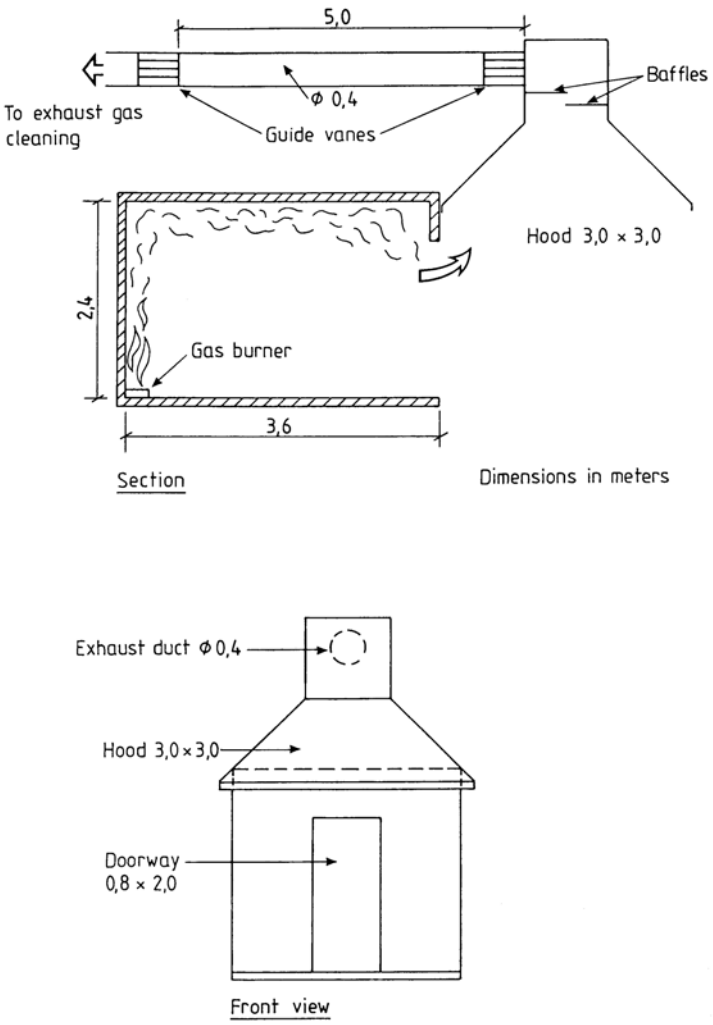

Figure 1 Fire test room.

Figure 12.1: Fire test room

gas temperatures are given in Figure 12.2. It can be noticed that there must be a crisp interface that separates the hot and cold gas layer. For almost the whole simulation the interface is between 1.57 and 1.72 m, the temperature jump goes up to 300 °C. Only after 120 s the hot gas layer will come down, which can be seen by the sudden increase in temperature for the thermocouple at 1.57 m at 120 s and for 1.42 m at about 150 s.

The surface temperature for the ceiling materials was measured with thermocouples. The results are given in Figure 12.3. Floor temperatures were measured at three locations along the centerline of the floor. The three temperatures are averaged afterwards. Because of this averaging they are not included in the comparison with the simulations.

The heat flux to the centre of the floor was measured with a Gardon type heat flux meter, the results are given in Figure 12.4.

In the experiments the time to flashover was determined as the time when flames emerge form the doorway. The reason for this definition was that when flames leave the room, there is a sudden increased risk of further fire spread, and secondly, the flashover is easy to determine accurately. In the test with particle board it took about 150 s to reach flashover.

Further measurements in the experiments were the mass flow and the convective heat flow rate through the doorway, and the heat release rate measured in the exhaust duct by oxygen depletion technique. These are all indirect measurements, thus derived or calculated from real measured variables such as the pressure, oxygen concentrations, temperatures, ... For example, the mass flow rate through the door was based on only three (vertical) velocity measurements, and Sundström says:

> The results are, however, crude due to the few measuring points.

Therefore these derived measurements were not included in the comparison between simulations and experiments.

12.2 Simulation of experiment A

12.2.1 Input

The geometry of the fire room is basically the same as in Figure 12.1. At the doorway the calculation domain is extended with a part of the environment (beneath the hood). This way, the flow through the doorway is better predicted. When the calculation domain would end at the doorway, the applied boundary condition (pressure) would not be appropriate. In reality the pressure will vary along with the height due to the fire generated pressures.

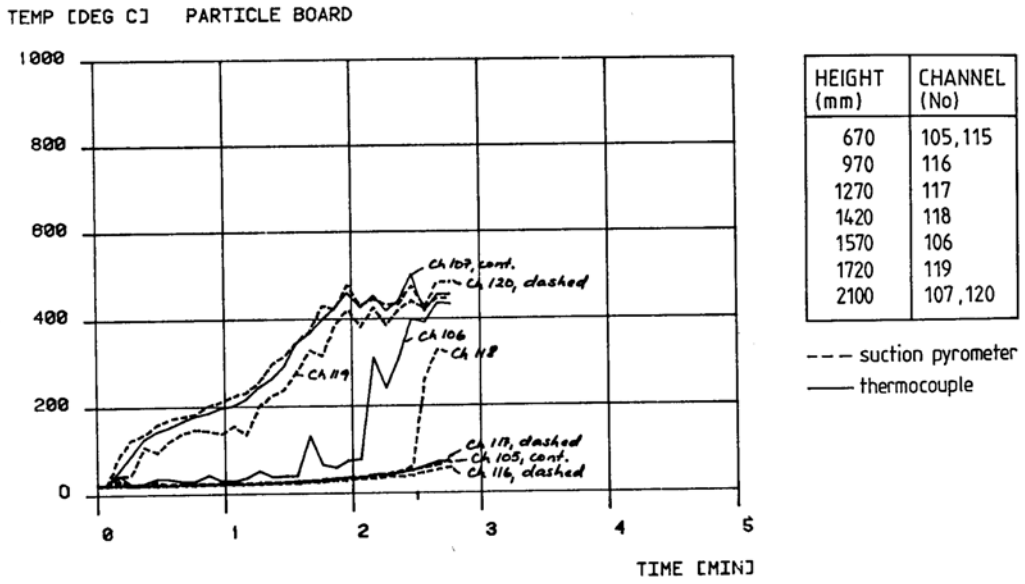

Figure 12.2: Gas temperatures in experiment [111]

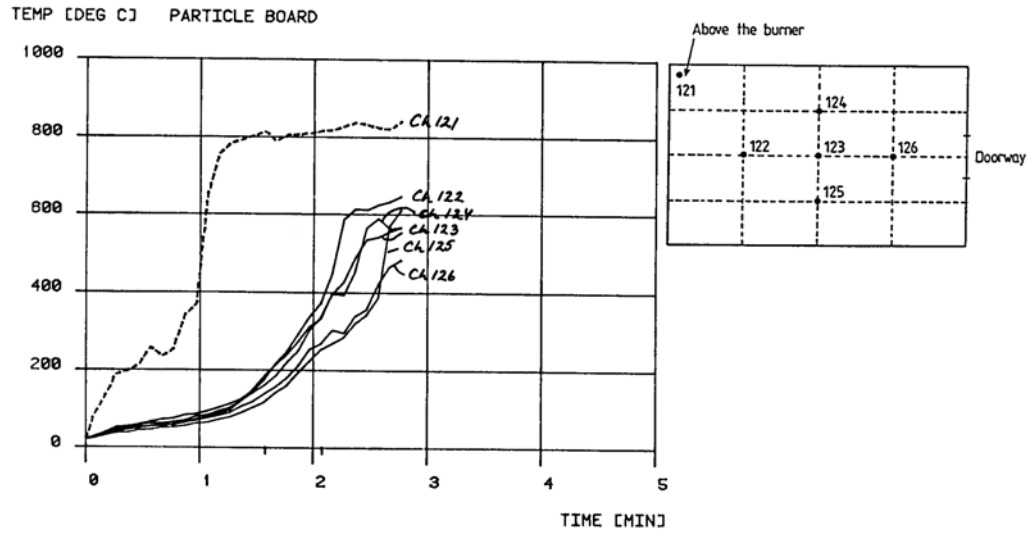

Figure 12.3: Surface temperatures in experiment [111]

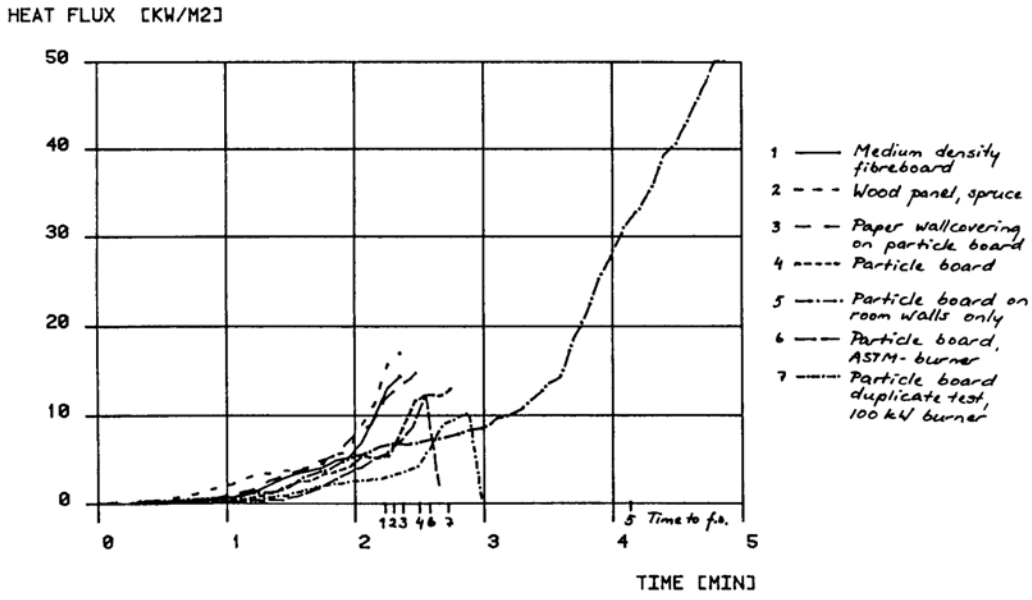

Figure D:6 Heat flux to the floor.

Figure 12.4: Floor heat flux in experiment [111]

Table 12.1: Physical models used in simulations

Compressibility	Weakly
Turbulence	$k-\varepsilon$
Combustion	EBU
Soot	Constant soot fraction
Radiation equation	Discrete transfer
Radiation properties	Model Fletcher

Therefore, the boundary conditions (pressure patch) are applied some distance of the door. At the outside of the room, extra walls were introduced to prevent the cross-flow between pressure boundaries. The hood of the gas analysis system is not modelled.

The walls that are covered with particle board, i.e. the left, rear, right and top wall, are calculated with the solid combustion model. The floor and the front inside wall are assumed conductive, but they are also calculated with the solid model but without pyrolysis (no pyrolysis reactions, only conduction). The outside temperature of the wall between the room and the (extended) environment is kept constant. The wall is not modelled as a conductive solid in CFX, because this would introduce very small fluid cells in the doorway. The assumption of a constant outside temperature of the wall is not entirely correct, but it will have negligible influence on the conditions in the room.

The propane burner is modelled as an inlet. The velocity and thus the flow rate of fuel at the inlet is constant and corresponds with 100 kW.

For the standard case, i.e. simulation A.1, the material properties of the particle board are those determined in Chapter 9 from optimisation of Cone Calorimeter tests. They are given in Table 12.2. The backing material, i.e. the light weight concrete, has a thermal capacity of 837 kJ/kgK, a thermal conductivity of 0.128 W/mK and a density of 500 kg/m^3 [39].

The geometry was divided into $25 \times 20 \times 22$ control volumes for the depth $\times$ width $\times$ height. The grid was made more dense near the burner and in the upper layer zone. As the grid is structured this refining made the grid elsewhere as well finer, see Figure 12.5.

The solid phase is simulated with the "Moving grid" model of Chapter 6. The gas phase is solved with CFX [13]. The physical models that are used in the simulations are given in Table 12.1. They were in all simulations the same. Only parameters of the solid model are changed.

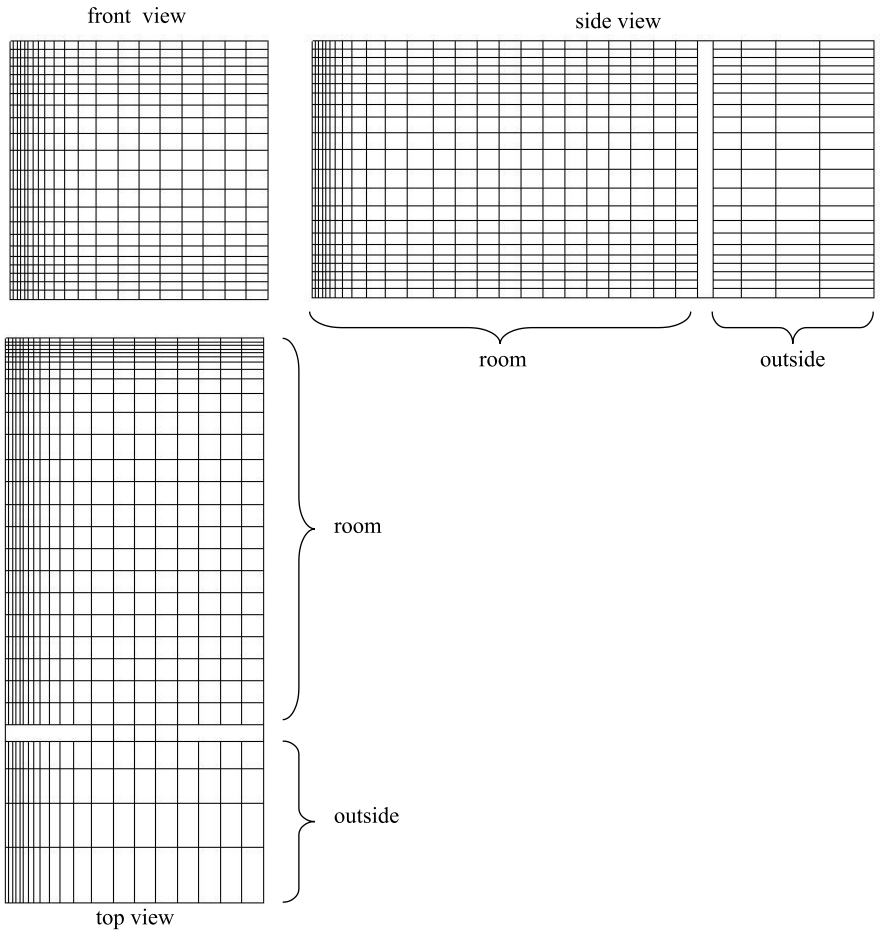

Figure 12.5: Grid

Table 12.2: Material properties of solid

Prop.	**Sim A.1**	**Units**
ρ_v	660	kg/m^3
ρ_c	133	kg/m^3
c_v	1300	J/kg.K
c_c	1300	J/kg.K
c_{pyr}	1900	J/kg.K
λ_v	0.20	W/m.K
λ_c	0.20	W/m.K
Q_{pyr}	600	kJ/kg
T_{pyr}	300	°C
Q_{comb}	15	MJ/kg
soot fraction burner	0.02	-
soot fraction wall	0.04	-

12.2.2 Results and discussion

12.2.2.1 Simulation A.1: "standard"

The results of the first "standard" simulation are given in Figures 12.6 to 12.10. At the start of the simulation time steps of 0.1 s are taken, after a few seconds the time step is increased to 1.0 .

Qualitative description
In Figure 12.10 some snapshots of the surface temperature of the particle board is given. When the temperature is higher than 300 °C, the solid is pyrolyzing (the pyrolysis temperature for this simulation was set at 300 °C). This means that the red zones in the figure correspond with pyrolyzing solid. At 15 s the plume of the burner is heating the walls - the burner is placed in the left far corner in the figure. At 30 s the particle board in the corner above the ignitor burner is burning. The smoke rises and flows under the ceiling. At 60 s a hot smoke layer of about 40 cm has been formed in the room. The temperature in that hot layer is not uniform. Near the burner the temperature is much higher than in the opposite corner. At 75 s the hot smoke layer has a thickness of about 80 cm. The temperature is still not uniform. At 90 s almost all the walls are pyrolyzing (flashover). Only near the floor there is a small region where the particle board is still in the heating phase. The sudden involvement of all the combustible material in the room points at flashover. There is no distinction between a cold and hot layer

anymore, though the temperature is not uniform. The highest temperatures are not always located near the ceiling. The heat generating combustion reactions proceed where there is sufficient oxygen available, which is close to the door. The highest temperatures are noted in that region. On the other hand, close to the door, the combustion gases mix with the cold ambient air which lowers the temperature. From the moment of flashover on, almost the entire room is filled with combustion gases.

Gas temperature
The flashover in the room can be seen in Figure 12.6 as the point were all the calculated temperatures suddenly rise, this is after about 90 s. The lowest temperature which corresponds with the thermocouple at 0.67 m, captures a temperature jump of about 600 °C! After the jump the temperatures seem to be uniform in the vertical direction. This is so for the thermocouple tree, but in other spots this is not really the case. The clear distinction between hot and cold gas layer has disappeared. Some 15 s later, the temperatures fall again and a vertical temperature gradient is again established. Near the rear wall, though, the gradient is less pronounced. The temperature in the lower, cold layer is strongly overestimated. In the experiments the two lowest temperature sensors stay at their initial value while in the simulations their reach values of 800 °C.

It is clear that the gas temperatures in the simulation, see Figure 12.6 are too high when compared with the experiments. Before flashover, the trend of the temperature is good, but their value is too high. The height of the interface between hot and cold layer is predicted too low. In the experiment this interface is before 150 s between 1.57 and 1.42 m, while afterwards it is between 1.42 and 1.27 m. In the simulation the interface is already after 20 s beneath 1.27 m.

When the experimental gas temperatures are compared with the experimental surface temperatures, it becomes clear that the thermocouple tree stand in a region with lower temperatures in the room. The surface temperatures are at the end of simulation between 500 and 850 °C. These surface temperatures must be the result of higher gas temperatures, because it are the combustion reactions in the gas phase that produce heat. Therefore, the gas temperature must certainly be higher than 850 °C. This means that the predicted temperatures are not totally unrealistic, but that the locations of theses high temperature do not correspond with the experiment.

Surface temperature
The predicted surface temperatures are generally too high. For the first 90 s the trend is good though, but the heating of the wall seems to happen too

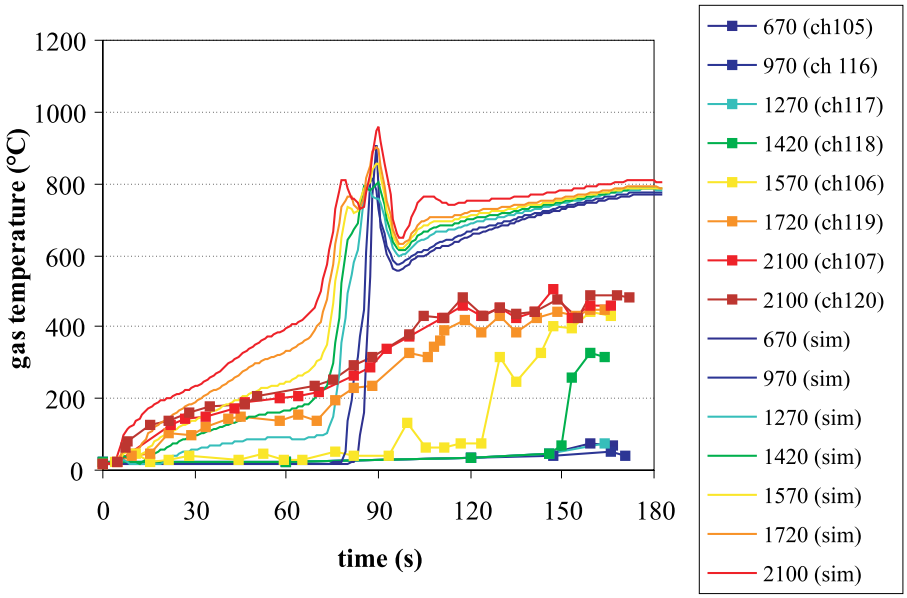

Figure 12.6: Vertical gas temperature for Sim1

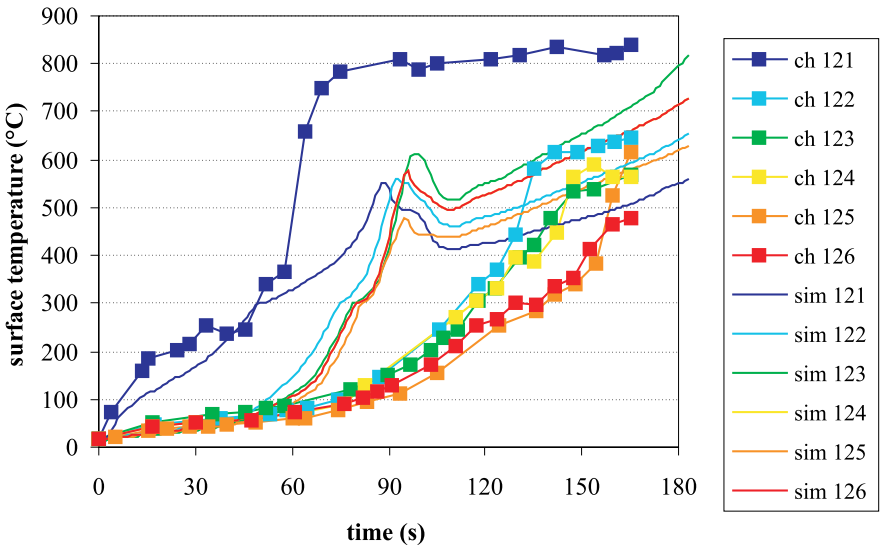

Figure 12.7: Surface temperature for Sim1

fast in this simulation. For the first 60 s there is very good correspondence with the experiments but this is quiet normal as errors in the incident heat flux are kind of damped. If the incident heat flux is too high, the solid temperature will rise which will results in more reradiation (emission) and more heat loses by conduction to deeper solid. These extra losses will again lower the surface temperature.

After 60 s the surface (ceiling) temperature above the burner is underestimated by about 300 to 400 °C. The thermocouple above the burner behaves differently than the other thermocouples.

Surface heat flux

With CFX it is not possible to trace the total incident heat flux during a simulation. Only at the end of the simulation the flux can be given. This is a consequence of the coupling of the CFD with the radiation package and illustrates the disadvantage of working with a closed commercial code. In an open code it would be rather easy to write the total incident heat flux every time step or second. For simulation A.1 the total incident heat flux is given every 30 s, which is the result of different simulations.

The measured, net and total incident heat flux are different. The measured heat flux at the gauge is given by, see Figure 12.8:

$$\dot{q}''_{measured} = 1 \cdot \dot{q}''_{inc.\,rad} - \dot{q}''_{rerad}(T_{gauge}) + \dot{q}''_{convection}(T_{gauge}) \tag{12.1}$$

The gauge is water cooled and its surface temperature is unknown, but assumed to be close to the cooling water temperature. The emissivity of the surface of the gauge is assumed unity. The reradiation and the convective part is dependent on the surface temperature of the gauge. When the reradiation and the convection term is small, the measured heat flux approximates the total incident heat flux. The net incident heat flux at the wall is given by, see Figure 12.8:

$$\dot{q}''_{net.\,inc} = \epsilon \cdot \dot{q}''_{inc.\,rad} - \dot{q}''_{rerad}(T_{wall}) + \dot{q}''_{convection}(T_{wall}) \tag{12.2}$$

In this equation the reradiation term is not negligible. The surface is not cooled by a water flow, so its temperature can rise remarkably. The net incident heat flux is always lower than the total incident heat flux because of the reradiation.

Both the total and net heat flux in Figure 12.9 rise too fast, with a very high peak at flashover. This peak in the net incident heat flux is caused by the high temperatures in the gas phase and the still low surface temperature (which means low reradiation). Before 90 s the total incident heat flux and the net incident heat flux are almost equal, but after 90 s (after flashover)

there is a big difference between the two, caused by reradiation. In the simulations it is noticed that the surface temperature rises quickly at 90 s. The higher the surface temperature, the higher the reradiation, the greater the difference between the net and total heat flux.

In the experiments the time to flashover is 150 s (flames outside the door opening), the measurement of the floor heat flux stopped some 15 s later. In a test with particle board on the room walls only, the flashover time was about 4 minutes with a floor heat flux of about 30 kW/m^2, afterwards the heat flux rose to 50 kW/m^2 at the end of the test. For other materials (polyurethane foam, textile wall covering, expanded polystyrene) the floor heat flux rose to 50 kW/m^2 or more. Therefore, it is thought that the peak in the predicted heat flux is probably too early, but its value can be correct.

From the comparison with the experiments it is clear that the calculated heat release, the gas temperature and thus the release of pyrolysis gases, is too fast.

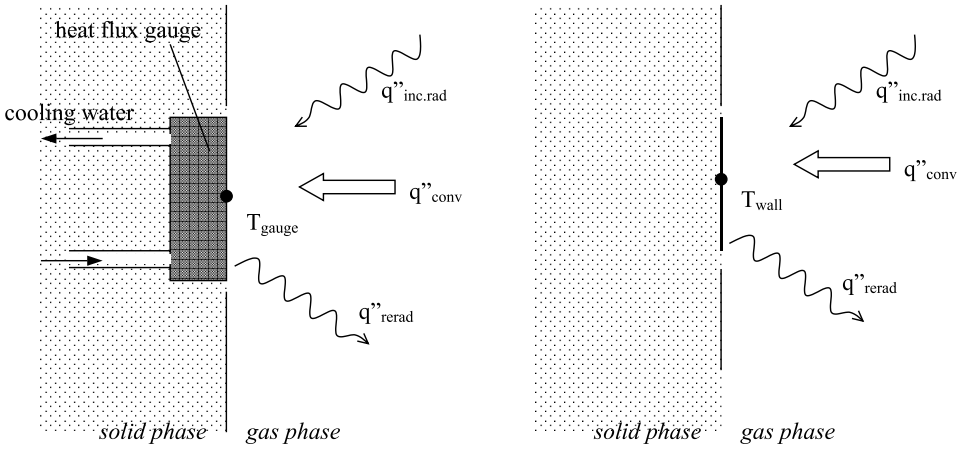

Figure 12.8: Measured and net incident wall heat flux

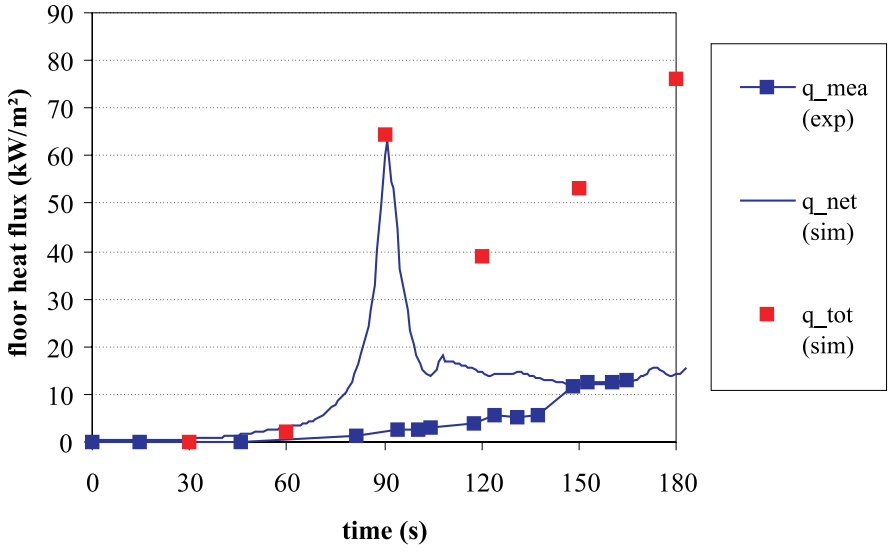

Figure 12.9: Floor heat flux for Sim1

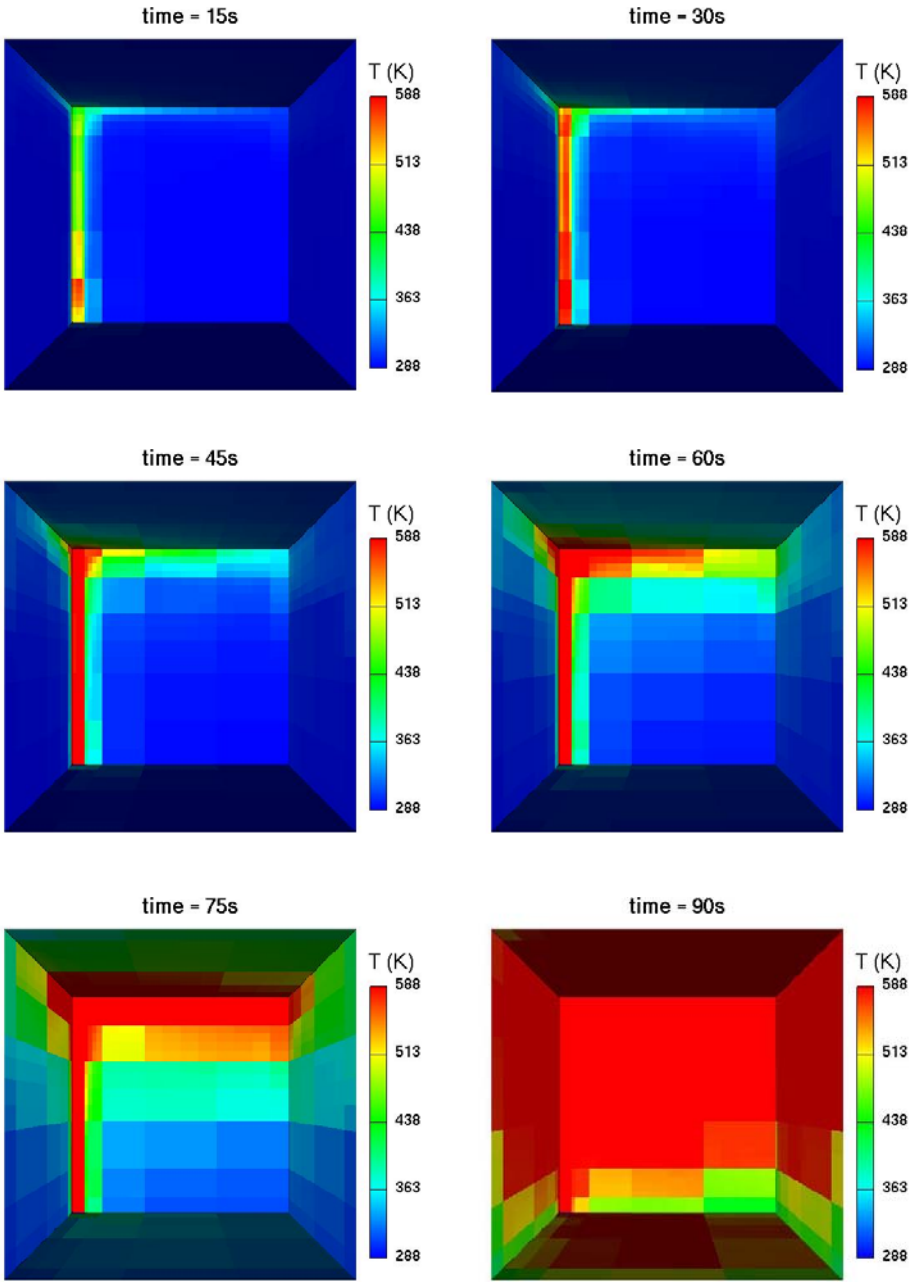

Figure 12.10: Snapshots of surface temperature

12.2.2.2 Simulation A.2: grid refinement

Simulation A.1 has been redone with a refined grid. About twice as much cells have been used in this calculation. Only some slight differences have been noticed.

12.2.2.3 Simulation A.3: time step refinement

In simulation A.3 the time steps have been refined. Time steps of 0.2 s instead of 1.0 s were taken. Before flashover the results are similar, except that for the small time step flashover is predicted about 10 s earlier. After flashover the gas and surface temperatures and the net heat flux showed an oscillating behaviour. The combustion in the room is pulsating with a time period of about 45 s.

Simulation A.1 is thus not yet totally grid and time step independent. But the error made by using a coarse grid and larger time steps is estimated to be of the same order as the variance of the measurements. Two fire test with the same conditions will always give substantial differences in their measurements, no two fires can be identical. The coarse grid and time steps are a compromise between accuracy and calculation time (transient).

12.2.2.4 Simulation A.4: influence solid heat capacity

In this section the influence of the material properties are examined. In the first simulations it became clear that the release of pyrolysis gases occurred too early (flashover already at 90 s). To postpone the release, the material properties have been changed. In Chapter 9 different combinations of material properties have been proposed to improve the Cone Calorimeter predictions. Here, it is chosen to augment the heat capacity of the virgin and char material to both 2000 J/kgK, which is closer to the proposed values by de Ris & Yan [19].

The results are shown in Figure 12.11 to 12.13. In the newly calculated results, flashover is postponed to 150 s (which corresponds with the experiment).

The gas temperatures are much better than in simulation A.1 but still there is a tendency of overestimation, see for example the gas temperature at 1.27, 1.42 and 1.57 m. After flashover the gas temperatures are again too high and do not correspond anymore with the experiments.

The surface temperatures are good up to 90 s, but afterwards they are a little underestimated. Channel 121, above the burner, is for the whole simulation strongly underestimated. This can partially be explained by the

lack of oxygen near the burner. When oxygen is missing, no vertical combustion plume can be formed in the corner. Therefore, no hot combustion gases reach the ceiling in the corner, which explains the low temperature. In the simulations of Yan & Holmstedt [126], the temperature above the burner is predicted better. Results elsewhere are similar to the calculations presented here.

The calculated heat flux is rather good if we assume that before flashover the total equals the net incident heat flux.

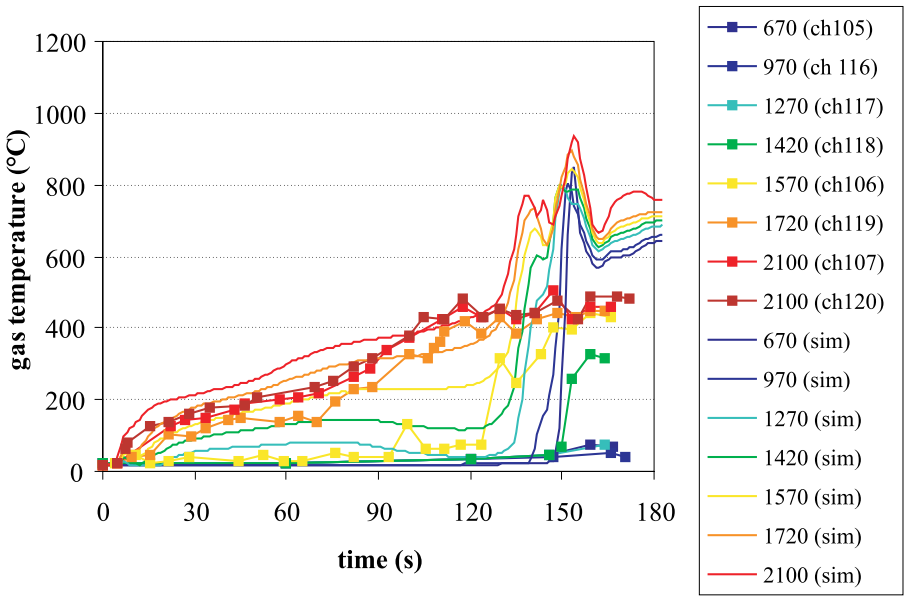

Figure 12.11: Vertical gas temperature for Sim4

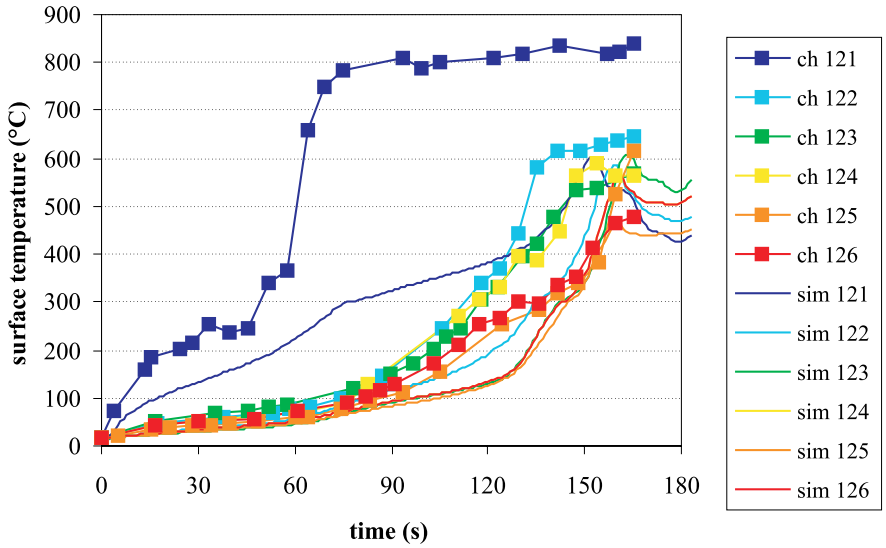

Figure 12.12: Surface temperature for Sim4

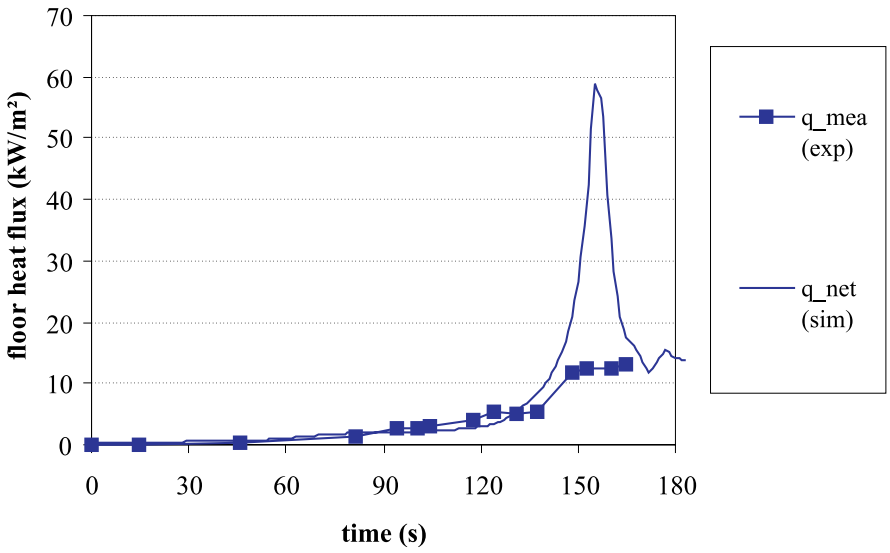

Figure 12.13: Floor heat flux for Sim4

12.2.2.5 Simulation A.5: influence soot fraction

The soot fraction is here assumed another material property. For the burner and walls the fraction has been varied, see Table 12.3.

Table 12.3: Soot fraction simulations

Simulation	Soot fraction	
	Burner	Wall
Sim A.1	0.02	0.04
Sim A.5.1	0.02	0.02
Sim A.5.2	0.00	0.04
Sim A.5.3	0.00	0.02

In the beginning (the first 60 s) there is no or less difference between the simulations where the wall soot fraction has been changed (between sim A.1 and A.5.1, and between sim A.5.2 and A.5.3). Obvious, in the early stages pyrolysis of walls has not started yet and therefore the wall soot fraction is not yet involved. Once the walls start pyrolyzing, the heat feedback to the walls is reduced when lowering the wall soot fraction. Subsequent flashover is postponed.

The burner soot fraction is thus also important in the calculation. For example, the results of simulation A.5.2 (where the burner soot fraction has been set zero) resemble to simulation A.4 (with increased heat capacity) and are again a significant improvement of the standard simulation.

On the other hand, when both the burner and the wall soot fraction are diminished (sim A.5.3) almost no material starts to pyrolyse. Surface temperatures and incident heat fluxes are strongly underestimated, while still some gas temperatures are overestimated. The last denotes that part of the error in the gas temperatures, originates already from the gas burner simulation, and not from the fire spread model. A simulation of an inert room with only a burner would already give large differences with experiments.

12.2.3 Conclusion

In this section an attempt has been made to determine the influence of some input parameters of the solid combustion model. Calculations with standard models and non-optimised parameters are examined. These represent blind calculations.

From the simulations of experiment A, it can be concluded that the material properties of the solid material have a strong influence on the results. This was proven by varying the solid heat capacity and the wall and burner soot fraction. Modifying other material properties is believed to have the same importance as was already discussed in Chapter 9.

The results of the simulations before flashover can be improved by adjusting material properties (optimisation technique). Moderate to good correspondence with experiments can be obtained, certainly when the variance of the measurements would be taken into account. The results after flashover strongly differ from the experiments.

It is known that the standard k-ε overestimates the entrainment of horizontal, stable-stratified flows. This can explain the strong mixing and the loss of the two-layer situation after flashover.

The implementation of the "Moving grid model" is cumbersome. First of all, the different phases must be implemented, and second, all types of switching between phases must be foreseen. For example, the state were the first pyrolysis time step is interrupted because of a too low incident heat flux. The method is more susceptible to errors than the "Enthalpy method", "Arrhenius model" and "Dual mesh model". This special treatment (switching) was not necessary in the simulations with a constant heat flux because there was only trivial switching between phases and the solid continuously rose in temperature.

Working with a commercial code has pros and cons. The code is immediately at use, and it possesses a lot of numerical (e.g. differencing schemes) and physical models (e.g. turbulence models). The disadvantage is that the code is closed. This limits the user and often complicates simulations. Inventivity is required for implementing own code and doing "non-standard" calculations.

12.3 Experiment B

12.3.1 Description

This experiment is fully described in VTT Research Note 1834, Large-scale upward flame spread tests on wood products, by Kokkala et *al.* [58]. Here, only a short description of the experiment will be given. As this experiment was made two-dimensional, and as there were detailed measurements in the solid and in the gas phase, this experiment was chosen to investigate the influence of some physical models of the CFD model.

In the experiment upward flame spread of wood is examined. Samples

with a height of 2.4 to 7.5 m are ignited with a propane burner at the base of the samples. The burner dimensions are 1.2 m × 0.1 m × 0.1 m, it is sand-filled. The output of the burner was in the range of 40–300 kW and it was kept constant during the test with automatic control, based on the mass flow measurement in the feed line.

The experimental system is shown in Figure 12.14. Sidewalls were attached to obtain a symmetrical flow pattern. In the project in total 13 test were carried out, where 4 different materials were tested: particle board, porous fibre board, textile wall covering, and pine wood. Simulations will be done for particle board only. Besides these flame spread test, standard Cone Calorimeter test were performed under an irradiance of 25 and 50 kW/m^2.

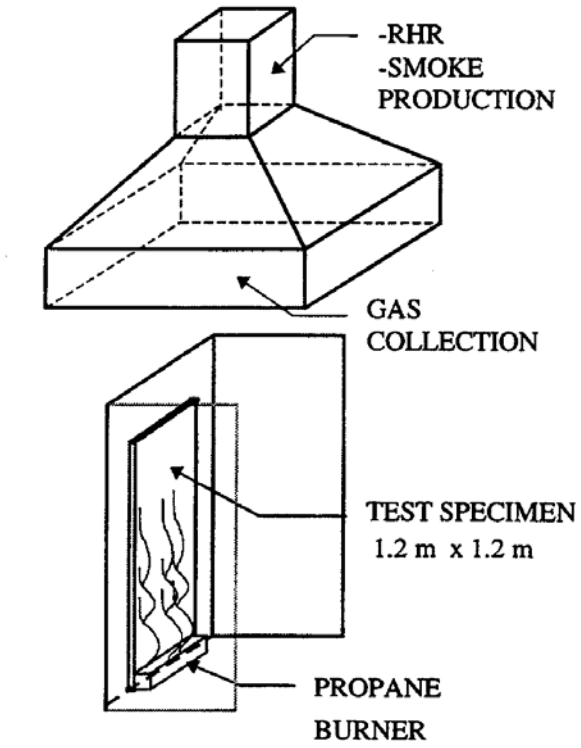

Figure 12.14: Schematic picture of the experimental system [57]

12.3.2 Instrumentation

The instrumentation of the experiment comprised:

- a video camera and two cameras for still photographs;
- gas phase thermocouples to determine the position of the flame front;
- surface thermocouples to determine the location of the pyrolysis front and to calculate the surface heat transfer;
- a total heat flux gauge facing the specimen to measure the radiation out of the flame;
- bi-directional probes to measure the flow profile of the wall plume and to calculate the convective heat flow and;
- duct instrumentation to determine the total heat release rate and CO-production as a function of time.

12.3.2.1 Temperature

The temperature was measured with K-type thermocouple made of 0.2 mm or 0.12 mm wires. The wires were bend so that 10 to 15 mm of the leads around the junction were horizontal, to prevent conduction. The leads of the surface thermocouples were taken through the wall board via holes that were 20 mm apart. A shallow groove was made between the holes and the junction was tightened against the surface by pulling from the back side of the specimen.

When measuring the temperature of a gas, a thermocouple can indicate only its own temperature. In general, this will not be equal to the gas temperature. The temperature difference between the thermocouple and gas temperature is determined by four phenomena [3]: heat transfer between thermocouple and environment by radiation; heat transfer in the wires by conduction; conversion of kinetic energy to thermal energy in the boundary layer around the thermocouple; heat transfer from the boundary layer to the junction by convection. Due to the low velocities, the third phenomenon can be neglected. The conduction in the wires is minimized by bending the wires so that 10 to 15 mm of the leads around the junction were horizontal. The radiation error is given by:

$$T_{gas} - T_{junction} = \frac{F \cdot \sigma \cdot A_r \cdot \epsilon \cdot \left(T_{junction}^4 - T_{wall}^4\right)}{h_c \cdot A_c} \tag{12.3}$$

where F is the view factor, σ the Stefan-Boltzmann constant, ϵ the emissivity of the junction, A_r the radiation heat transfer area, A_c the convection

heat transfer area, and h_c the convective heat transfer coefficient. The heat transfer coefficient h_c is for wires normal to the flow given by [3]:

$$\mathrm{Nu} = \frac{h_c \cdot d}{\lambda} = 0.44 \cdot \mathrm{Re}^{0.5} \tag{12.4}$$

where d the diameter of the thermocouple, λ the conduction coefficient of the fluid, and Re the Reynolds number. In order to calculate the correction coefficient, the velocity and the diameter of the junction must be known. The measured velocities go up to 4 m/s, but these are not measured in the same position as the temperature measurements in the gas phase. The velocity is measured at a height of 2.1 m and 50 mm from the wall, while the temperature measurements along the centerline are at height from 0.25 to 2.045 m and at 20 mm from the wall. Due to the boundary layer it is possible that the velocity at the thermocouple in the gas phase is much lower. If velocities are varied from 1 to 4 m/s and the diameter of the thermocouple from 0.2 to 1.0 mm, then the convection coefficient goes from 84 to 373 $\mathrm{W/m^2K}$. When a thermocouple measures 600 °C, this can correspond to a gas temperature of 690 to 1000 °C. The error can be significant, and is time and position dependent. When the wall temperature rises, the error will be smaller. It can be concluded that the measured temperatures are an underestimation of the real gas temperatures. It is very difficult to quantify that error. Temperature measurements with thermocouples and suction pyrometers in experiment A, showed no significant radiation error, though, the configuration (enclosure opposed to open domain) will have an important influence.

To let the simulations correspond with the experiments, a convection coefficient of about 33 $\mathrm{W/m^2K}$ is required. Such a low convection coefficient is obtained for very low velocities (0.2 m/s).

12.3.2.2 Heat fluxes

The total heat flux gauges were of the Gardon type (Medtherm) and were mounted flush with the surface. For the difference between the measured, net and total heat flux, see Section 12.2.2.1.

12.3.2.3 Sensor locations

The surface and gas temperature were measured along the centerline of the sample. The gas temperature was measured at a distance of 20 mm from the leads to the surface. The heights, measured from the burner are given in the table beneath. The coordinate system is shown in Figure 12.15.

Z (mm)	250	450	650	850	1100	1250	1450	1645	1840	2045
T_s (No.)	1	2	3	4	5	6	7	8	9	10
T_{fl} (No.)	1	2	3	4	5	6	7	8	9	10

The velocity (bi-directional probes) were located at a height of 2100 mm. The distances from the surface are given in the table beneath.

X (mm)	0	-50	50	-100	100	150
Y (mm)	50	100	150	200	250	300
V	1	2	3	4	5	6

During the flame spread test, the maximum gas temperature was most of the time located at 7 mm from the surface ($\pm$ 60 % of the measurements). The thermocouple near the wall noted only once (1 % of the measurements) the maximum temperature.

At a height of 1100 mm the gas temperature close to the surface was measured. The distance from the surface to the leads is given in the table beneath. The measurements were 410 mm out of the centerline.

Y (mm)	2	7	16	21	28	36	44	55	75	94

The total heat fluxes were measured at:

X (mm)	200	-200	200	-200	200
Z (mm)	250	645	1090	1450	1840

12.4 Simulation of experiment B

12.4.1 Input

The simulations are done in two dimensions. The geometry and the boundary conditions are given in Figure 12.16. Note that the figure is not in proportion and that the dimensions are in meters. The propane burner is located in the left bottom corner. It is 10 cm high and 10 cm wide, and it is modelled as an inlet of fuel. The velocity of the inlet corresponds with a heat output of 100 kW. The sample is placed at the left vertical wall. This boundary is calculated with the solid combustion model. Above the sample but still

vertical, a perfectly insulated wall is added in order to minimize the effect of the top boundary pressure condition on the flow pattern at the combustible wall. At the right side and at the top of the geometry a pressure boundary is used. The boundary is taken far enough from the sample wall to be sure that the flow is fully developed. The bottom wall and the vertical wall of the burner are taken as isothermal surfaces.

In CFX no true two-dimensional simulations can be done. In fact, the geometry is three-dimensional with a thickness of one cell. The symmetry boundary conditions are applied on the side faces (i.e. the front and rear wall in Figure 12.16).

For the simulations a coarse and a fine mesh are used. For the coarse mesh, the wall is divided vertically into 25 volumes; for the fine mesh in 50 volumes. The volumes are also refined in the direction perpendicular to the combustible wall, but the size of the first fluid cell has been retained because of the validity of the log law. The coarse and the fine mesh are given in Figure 12.17. A detail of the mesh close to the combustible wall, above the burner is given in Figure 12.18.

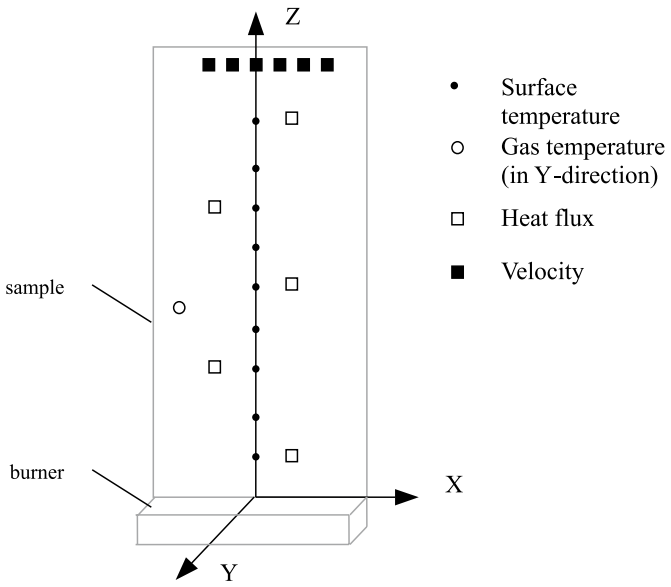

Figure 12.15: Coordinate system for location of sensors

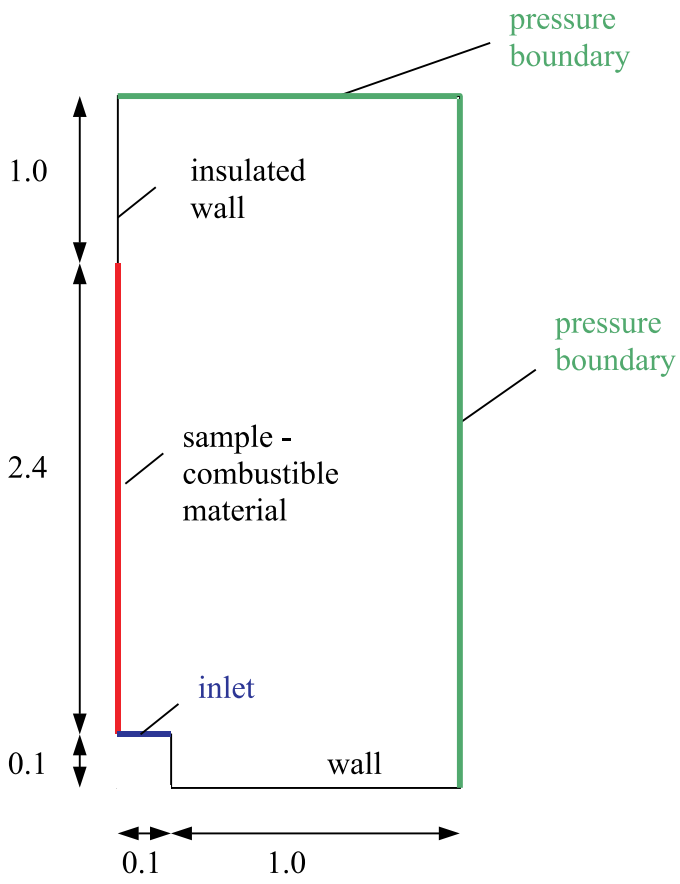

Figure 12.16: Geometry and boundary conditions

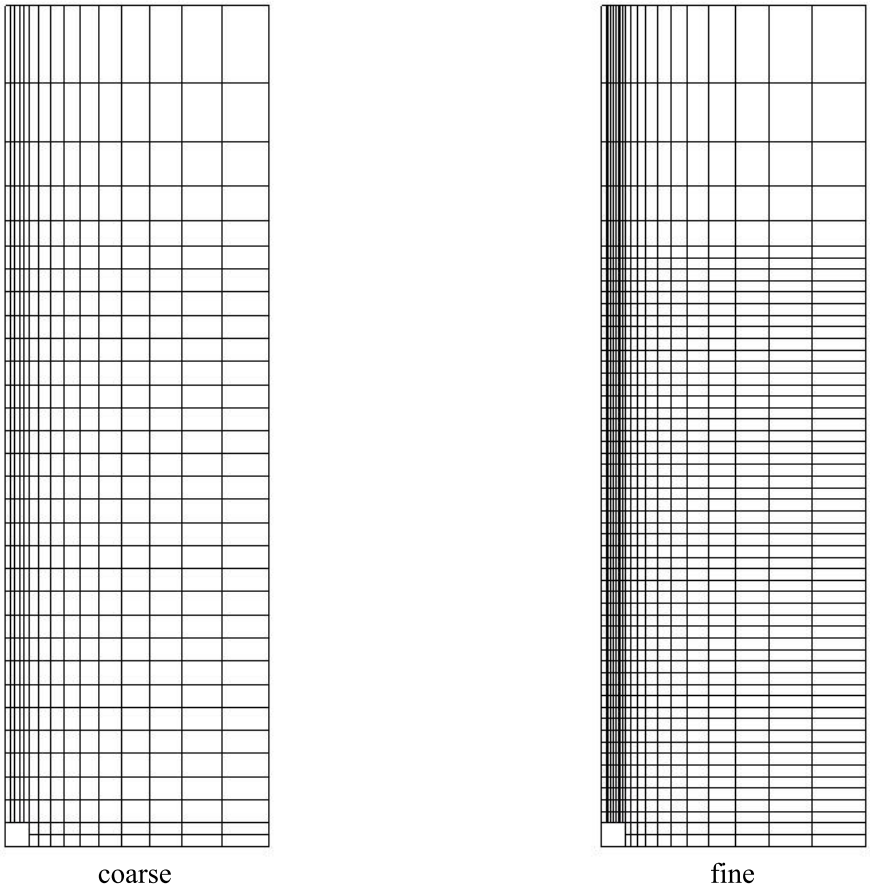

Figure 12.17: Coarse mesh (left); fine mesh (right)

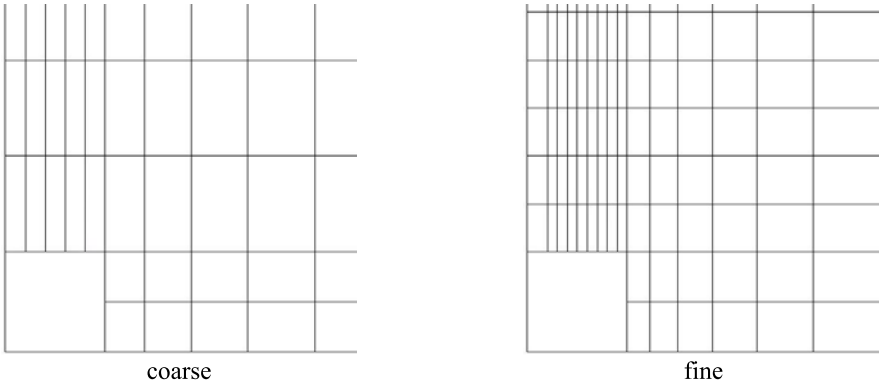

Figure 12.18: Detail of left corner: coarse mesh (left); fine mesh (right)

12.4.2 Results and discussion

Simulations are not given chronologically. First some simulations with particle board were done. But as the results were not satisfying, simulations with an inert wall were examined. The wall was then covered with calcium silicate board of 12 mm thick. No fire spread was occurring, only the flames of the propane burner were present. These tests were done to evaluate the calculated burner flame and to find out if the initial disappointing results were due to the pyrolysis model.

12.4.2.1 Simulation B.1: inert wall

In this simulation no flame spread appeared, only the flame of the burner is modelled. The wall was covered with calcium silicate board, which had a density of 950 kg/m^3, conductivity of 0.06 W/mK, and a heat capacity of 1000 J/kgK [58, 37].

The results (surface and gas temperatures, velocity) with the standard models, see Table 12.1, are given in Figures 12.19 to 12.21. The heat flux is not discussed for reasons already given in experiment A.

Experimental temperatures
The experimental gas temperatures seem a bit low. The maximum temperature is about 600 °C and is captured at 0.25 m above the burner. According to the report of Kokkala et *al.* [57] this thermocouple is located in the flame zone as the flame height for a burner output of 100 kW was about 0.5 m. From calculations with the McCaffrey plume equations [26, 52], the temperature in the continuous flame region is about 840 °C. This temperature is independent on the heat output, but for large fires it is known that this temperature can be as high as 1200 °C [52]. From above reasoning, it is concluded that in this experiment the radiation error must be significant.

Gas temperature
In the simulations the gas temperatures rise very quickly and after about 10 s they reach already a steady state. The temperatures in the experiment rise slowly, and it takes about 40 s to reach a more or less steady state. The time constant for a thermocouple with a diameter of 0.2 mm is, dependent on the convection coefficient (see above), 1 to 5 s. So the time constant alone cannot explain the difference between experiments and simulation. Most probably the influence of the wall (slow heating) is felt by the thermocouple.

The simulated gas temperatures are very high compared to the experimental ones. For a thermocouple in steady state that is heated by convection and loses energy by radiation, the difference between the fluid temperature

T_{fl} and the junction temperature $T_{junction}$ is given by [3]:

$$h \cdot A_{conv} \cdot (T_{fl} - T_{junction}) = F \cdot \sigma \cdot A_{rad} \cdot \epsilon \cdot (T^4_{junction} - T^4_{enviro}) \quad (12.5)$$

For a junction temperature of 600 °C, a view factor F and emission coefficient ϵ of 1, a convection coefficient of 84 to 363 W/m^2K, and equal radiation and convection areas, a fluid temperature of 690 to 1000 °C is found. Thus even when the radiation error in the temperature measurements is considered, the calculated temperatures are still too high. The combustion reactions are to intense and the plume loses not enough energy, which can be concluded from the gas temperatures at higher levels. The region with high temperature is limited to a single cell. The neighbouring cells have already a much lower temperature (like in the experiments). This already indicates a too coarse mesh, though the finer mesh gave similar results (too high gas temperatures). In the simulation the flame is stable and close to the wall. In the experiments the flames are not continuously and not always attached to the wall. They are intermitted, which may explain part of the low experimental gas temperature.

In the simulations the EBU model has been replaced by the mixed-is-burnt model, though less improvement was noticed. Therefore the new results are not given here. Both models do not take into account incomplete combustion, which in fires can be significant. To check if the surface temperature calculation could be the cause, simulations have been done with an isothermal wall at ambient temperature and with an adiabatic wall. Both simulations still gave high gas temperatures. To check if the heat loss by radiation could be the cause, simulations with a doubled and an even constant emission coefficient have been performed. Again no significant improvement was noticed. To examine the influence of the wall function a simulation has been done with the low Reynolds turbulence model. Of course the grid near the wall has been seriously refined, but again no serious improvement was noticed.

The standard k-ε turbulence model seriously underestimates the spreading rate of vertical buoyant jets [125]. As a consequence the plume is less wide and vertical velocities and temperatures at the center are too high. Similar effects are noticed here: a too small plume with high temperatures. It is thought that the main error is the gas temperature is caused by the turbulence and combustion model. A flamelet approach for combustion could improve the results, but as this is not present in the version of CFX at the time of writing, no such simulations have been done.

It must be noticed that calculation results of fire plumes (so without fire spread) in literature [31, 78] with more advanced gas phase models (e.g. LES), also overestimate the gas temperature when compared with the Mc-

Caffrey correlation. In our case the McCaffrey correlation already gives an overestimation of the experimental results.

Velocity
The velocities at the height of 2.1 m, are overestimated. Near the wall they the calculation results are the double of the experiments. At 0.3 m from the wall the predicted velocity corresponds good with the experiment. The velocity is low (about 0.25 m/s) which means that this location forms the outer region of the plume. The high vertical velocities near the wall are a consequence of the overestimated gas temperatures (buoyancy). If a better gas temperature is predicted, the velocities will also be better.

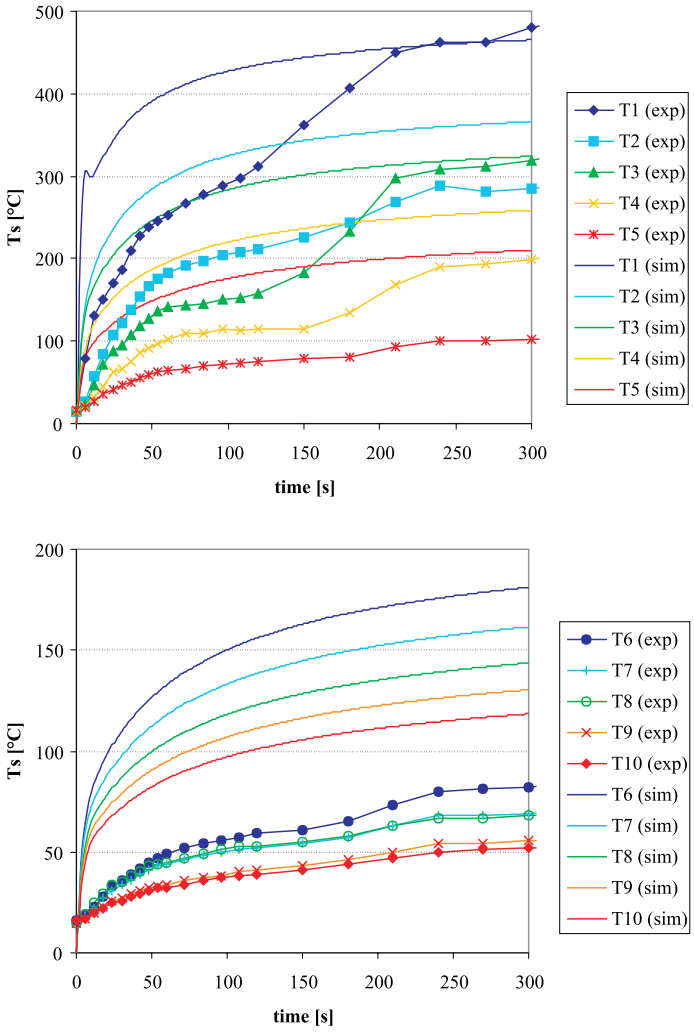

Figure 12.19: Centerline surface temperature for inert wall (standard properties)

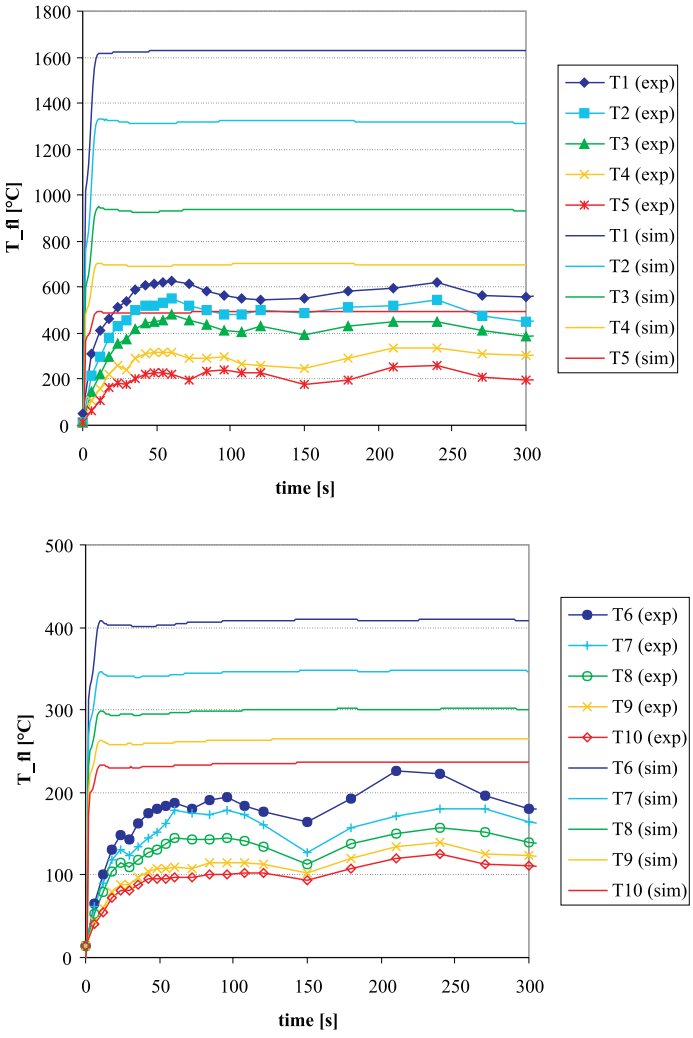

Figure 12.20: Centerline gas temperature for inert wall (standard properties)

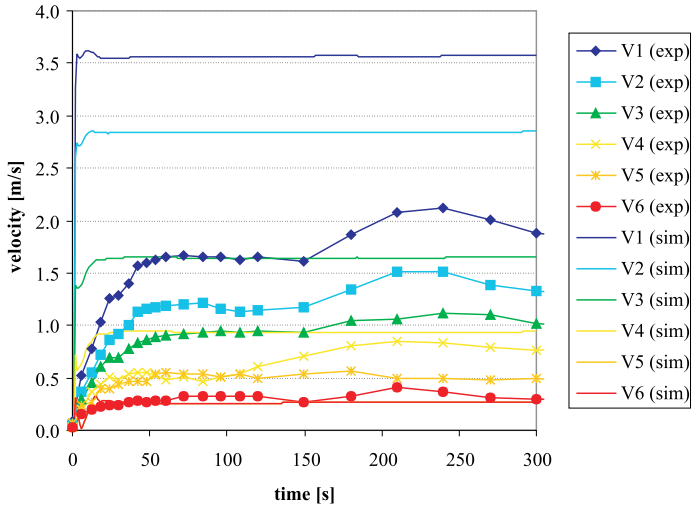

Figure 12.21: Velocity at z= 2.1 m for inert wall (standard properties)

12.4.2.2 Simulation B.2: particle board

For the simulation of flame spread over particle board the same problems appear as in the simulations with the inert wall. The gas temperatures (at a height of 1100 mm) are too high and they rise too fast.

In the experimental results the maximum gas temperature appeared most of the time, at about 7 mm from the surface. The centerline gas temperature was measured at 20 mm from the surface, and thus gave not always the maximum temperature in the boundary layer (gas phase). The variance is small though, and therefore the high gas temperatures in the simulations can not be explained by the variation of the gas temperature over the boundary layer. In the experiments no gas temperature higher than 834 °C was measured.

Simulations are done for a virgin density of 600 kg/m^3, a char density of 133 kg/m^3, the char and virgin conductivity are both 0.2 W/mK, the char and virgin heat capacity are both 1300 J/kgK, and the heat capacity of the volatiles is 1900 J/kgK. The backing material was calcium silicate board, with a density of 950 kg/m^3, conductivity of 0.06 W/mK, and a heat capacity of 1000 J/kgK. The calcium silicate plate, is included in the simulation because it has a significant effect on the flame spread. From the tests done by Kokkala et *al.* [58] it was shown that the flame spread was different for a substrate of mineral wool than for calcium silicate.

For completeness, results are given in Figure 12.22 to 12.24. Again, gas temperatures are too high and rise too fast. As long as the results of the inert wall (only burner) are not satisfying, the results with particle board will remain disappointing. The surface temperature could be improved by adjusting the thermal properties for the solid material, as was done for experiment A. This is not done here because the error in the gas temperature was still too large.

On the other hand the qualitative results of the flame spread model are good as can be seen in Figure 12.25. The pyrolysis height during the simulation is given plus some visual experimental results. There is good correspondence. The main trend of a growing fire which then decreases, is well predicted.

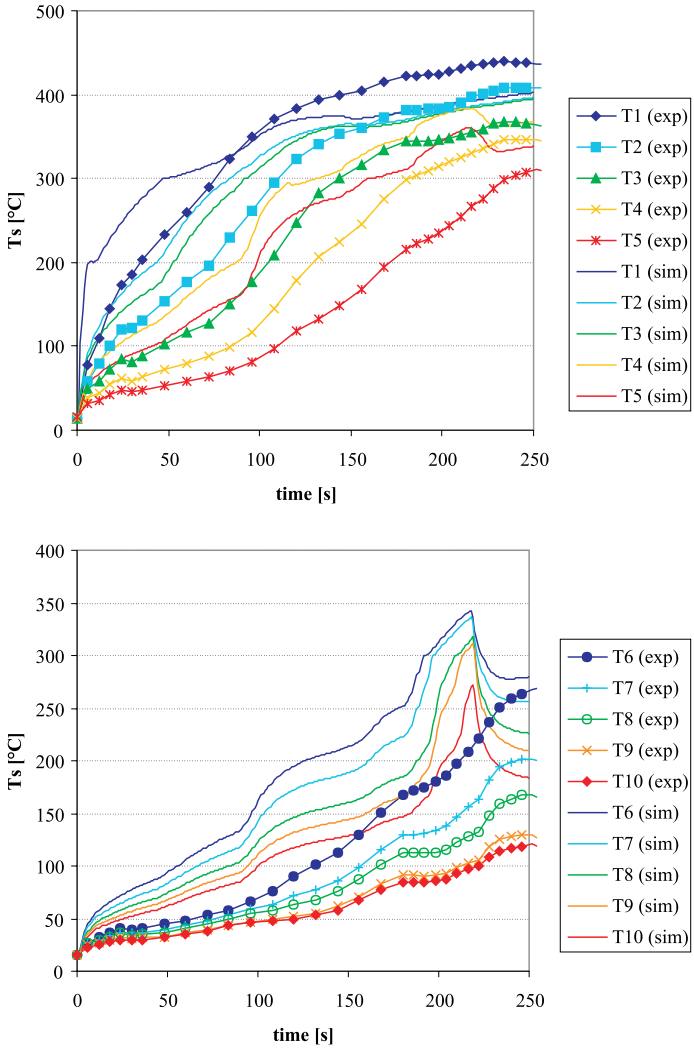

Figure 12.22: Centerline surface temperature for particle board (standard properties)

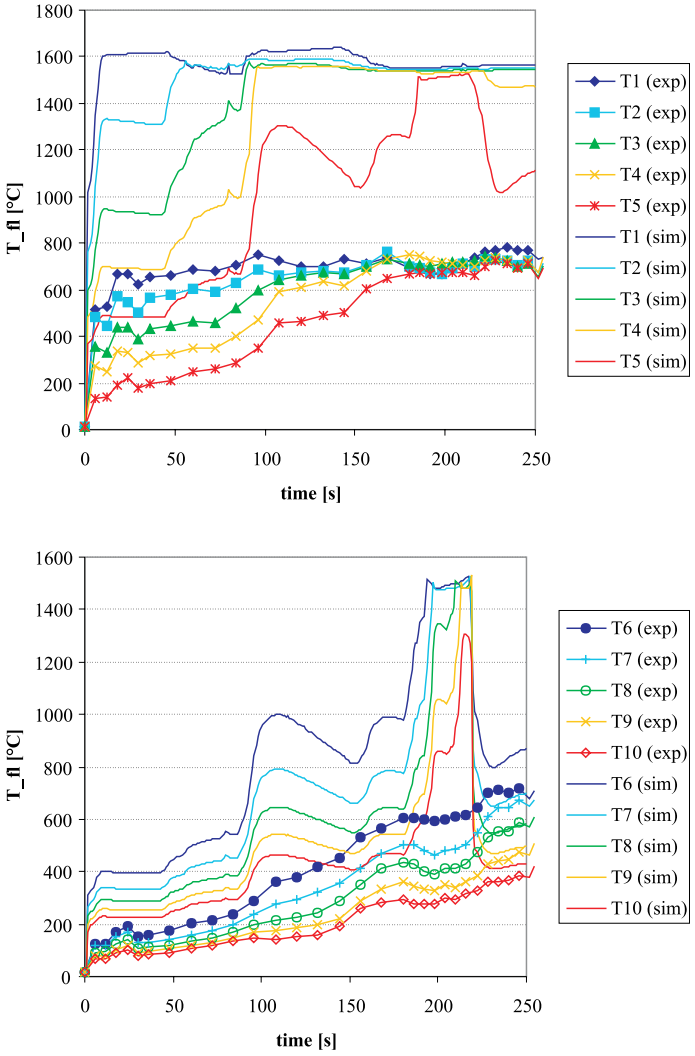

Figure 12.23: Centerline gas temperature for particle board (standard properties)

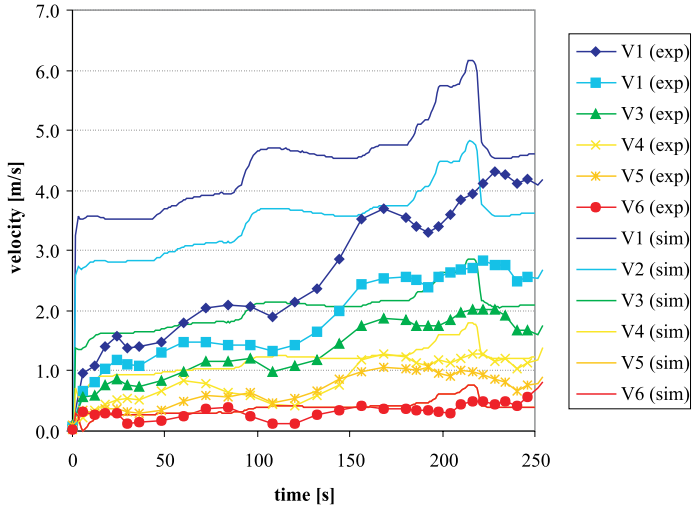

Figure 12.24: Velocity at z= 2.1 m for particle board (standard properties)

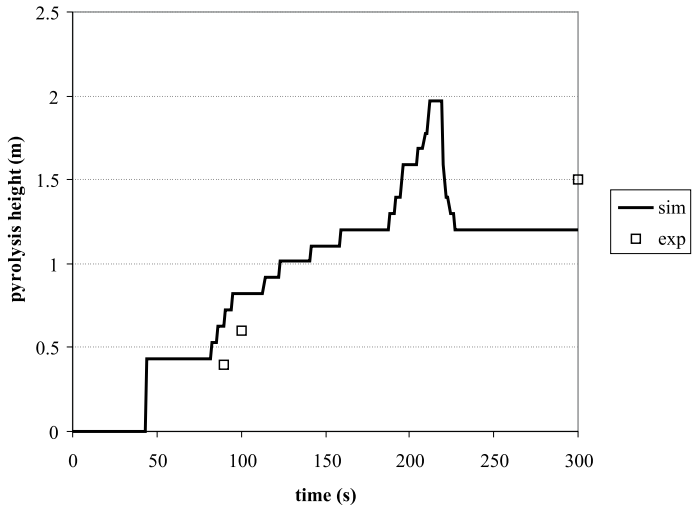

Figure 12.25: Pyrolysis height (standard properties)

12.4.3 Conclusion

In the simulations of experiment B, some physical models have been changed but it was not the intension to perform a full or thoroughly examination of all kinds of turbulence, combustion, soot and radiation models. The simulations of experiment B were not satisfying for the inert wall, and neither for the particle board. But on the other hand, some experimental results seems questionable. For further evaluation, more detailed and accurate measurements are needed.

In the future some of the models discussed in Chapter 11 should be used to improve the solution of the gas phase. The second experiment is here more to see as the first steps of further research, rather than as the validation of the gas phase. Attention should go to improving the turbulence and combustion calculation.

Flame spread calculations are quite complex. The quantative results are not yet useful. Accurate blind predictions of complex fire spread with different materials, are at the moment of writing not possible. Qualitative results seem promising.

Chapter 13

Conclusion

Fire and flame spread calculations are complex: they comprise turbulence, combustion, soot, radiation and solid degradation modelling. In this work especially the solid degradation has been given some more attention. The other aspects of fire modelling are solved in a more standard way with the models available in the commercial CFD package CFX.

13.1 Solid combustion models

In total five solid combustion or degradation models have been examined:

1. Arrhenius law model;
2. Integral model;
3. Moving mesh model;
4. Enthalpy model;
5. Dual mesh model.

All the models belong to only two basic physical models: or the one step pyrolysis reaction rate is described by an (linearized) Arrhenius equation, or the pyrolysis reaction rate is assumed infinite which introduces the *pyrolysis temperature* and *front*. The different solid combustion models solve these physical models in a different way which has sometimes small repercussions to the physical model. For example, in the "Enthalpy model" the front is represented by a cell and thus has a finite thickness. All of the models produce similar results, but of course each model has it pros and cons.

In the "Arrhenius model" the pyrolysis front has a finite thickness and pyrolysis gases are released in a temperature interval of about 100 °C. It

requires a fine grid, and subsequent large calculation times. The model can easily be expanded to two or three dimensions.

In the "Integral model" the pyrolysis front is represented by a single surface. Prescribed temperature profiles are assumed in the char and virgin zones. Care should be taken when using the "Integral model" for parameter study. At the transition from the semi-infinite to the finite phase, errors occur. This was noticed for the pure heating phase, as for the pyrolysis phase. Another disadvantage of the model is the presence of different phases (heating, pyrolysis, semi-infinite, finite). The model can only be applied for one-dimensional cases. On the other hand, a serious advantage is the short calculation time.

The "Moving grid model" is for fire applications new. It has been used for validating the "Integral model". The "Moving grid" model works also with different phases, but there are less phases than in the "Integral model". The calculation time is for a non-uniform grid in the virgin layer remarkably shorter than for a uniform grid. The model can be expanded to more dimensions, but this requires a significant effort.

In the "Enthalpy model", also new for fire applications, special precautions have to be taken to avoid oscillations in the release of pyrolysis gases. Several techniques have been examined and time-averaging combined with a variable grid was the best solution. This model can easily be expanded to more dimensions.

The "Dual mesh model" uses a coarse mesh for the temperature and a fine for the density calculation. Preference is given to the linearized reaction rate because of its shorter calculation time (larger cells, larger time steps).

For implementation in a coupled CFD calculation, the "Moving grid" and the "Dual mesh" model were most appropriate.

Material properties are often not known, especially the properties for the char layer and the pyrolysis temperature and the heat of pyrolysis. Blind calculations can give significant different results for the mass flux of pyrolysis gases than optimised calculations. But the determination of "optimised" material properties is ambiguous and cumbersome. Different values for the material properties can give qualitative similar results.

In the one-dimensional it is not yet possible to predict the mass release rate of pyrolysis gases for different external heat fluxes with only one and the same set of material properties. As long as the simple one-dimensional experiments at different external heat fluxes can not be accurately predicted with one set of material properties, the results of the coupled simulations will remain questionable. The results of the coupled simulations are strongly dependent on the material properties of the solid model.

13.2 Simple gas phase model

In vertical flame spread it is often assumed that two-dimensional heat transfer is not required. This assumption has been proven with a simple gas phase model coupled to the two-dimensional version of the "Arrhenius law" model. The simple gas model provided solid boundary conditions as encountered in vertical flame spread. The heat conductive heat flux in the direction of the flame spread (or solid/gas interface) is very low and negligible.

These simulations also granted the use of large cells in the direction of the fire spread. There is no need to use the same cell size in horizontal and vertical direction.

Simulations with a simple gas phase model have a limited application domain. Due to the correlations and assumptions, some parameters must often be optimised to obtain correspondence with experiments.

13.3 CFD gas phase model

Working with a commercial code has pros and cons. The code is immediately at use, and it possesses a lot of numerical (e.g. differencing schemes) and physical models (e.g. turbulence models). The disadvantage is that the code is closed. This limits the user and often complicates simulations. Inventiveness is required for implementing self-written code and doing "non-standard" calculations.

The "Moving grid model" has been coupled with the commercial CFD code CFX. The *coupled simulations* have been compared with two experiments from literature: a room configuration and two-dimensional vertical flame spread.

The implementation of the "Moving grid model" is cumbersome because of the presence of different phases. All kinds of transitions between phases must be foreseen. The method is more susceptible to errors than the "Enthalpy", the "Arrhenius" or the "Dual mesh model".

From the simulations of the room configuration it can be concluded that the material properties of the solid have a strong influence on the calculation results. This was proven by changing the thermal heat capacity (from 1300 to 2000 J/kgK) and the wall and burner soot fraction. Good optimised material properties are essential in fire spread simulations. With the optimised material properties the simulations agreed much better with the experiments, but for some measurements there remains a discrepancy.

The simulations of the two-dimensional flame spread experiment, were not satisfying. Therefore, first a simple inert experiment (no flame spread, only

burner) was simulated. The calculated gas temperatures and velocities were strongly overestimated. But it must be said that some experimental results remain questionable. More detailed and accurate experiments are desirable. Some physical model (combustion, radiation, wall treatment) were changed, but less improvement was made. On the other hand, the qualitative results of the fire spread simulation are promising.

13.4 Further developments

The fire spread model that is presented in this work is not considered as finished or definite. It is rather a first step in a search to better fire models. Many improvements can still be made to both the gas and solid phase. Some proposals are given, but the list is far from complete.

Improvement of the gas phase prediction can be done by using new and better physical models. One can simply wait for new releases of CFX or one can implement own written models. In most CFD codes it is possible to implement own written code through user-routines. Attention should go to improvement of the turbulence and combustion calculation. Of course improvement of the soot and radiation calculation can also be examined. This research area is rather wide.

The solid combustion models can be improved in many ways. For example, many practical building materials are non-isotropic: wood and layered composite materials. Inclusion of such materials would extend the application domain of the fire models. A further step in the improvement of the solid models could be the incorporation of several degradation reactions instead of only a single step. The evaporation of the moisture in the solid, for example, could be introduced in this way. Other effects that can be included are smouldering, char oxidation, foaming, bubbling, cracking, curling, ... The problem is that most of these phenomena are not well known, and are thus difficult to describe in a mathematical model.

Part IV

Appendices

Appendix A

The Cone Calorimeter

The Cone Calorimeter was developed at NIST (National Institute of Standards and Technology) in the early 1980s [4]. Today it is the preferred apparatus for measuring the bench-scale heat release rate of a building material. The apparatus and the test procedure are standardized [113, 38]. Besides the HRR it also measures [5]:

1. effective heat of combustion;
2. mass loss rate;
3. ignitability;
4. smoke and soot;
5. toxic gases.

The heat release is measured based on the *oxygen consumption method*. For a large number of organic solids, liquids and gases is was shown that the net amount of heat released per unit mass of oxygen consumed is more or less constant (13.1 kJ/g). So, from the consumption of oxygen the heat release rate can be determined [40]:

$$\dot{q} = E \cdot (\dot{m}_a Y^a_{O_2} - \dot{m}_e Y^e_{O_2}) \tag{A.1}$$

where

$\dot{q}$ = heat release rate (W);
$\dot{m}_a$ = the mass flow rate of combustion air (kg/s);
$\dot{m}_e$ = the mass flow rate of combustion products (kg/s);
$Y^a_{O_2}$ = the mass fraction of oxygen in the combustion air (g/g);
$Y^e_{O_2}$ = the mass fraction of oxygen in the combustion products (g/g);
E = the heat release per mass unit of oxygen consumed (13.1 kJ/g).

When O_2 and CO_2 are measured this can be written as [40]:

$$\dot{q} = E\frac{\phi}{1+\phi(\alpha-1)}\dot{m}_e\frac{M_{O_2}}{M_a}(1-X^a_{H_2O}-X^a_{CO_2})X^{A^a}_{O_2} \tag{A.2}$$

with

$$\phi = \frac{X^{A^a}_{O_2}(1-X^{A^e}_{CO_2})-X^{A^e}_{O_2}(1-X^{A^a}_{CO_2})}{(1-X^{A^e}_{O_2}-X^{A^a}_{CO_2})X^{A^a}_{O_2}} \tag{A.3}$$

where

ϕ = oxygen depletion factor;
α = volumetric expansion factor (recommended value = 1.105)
M_{O_2} = molecular weight of oxygen;
M_a = molecular weight of the combustion air;
$X^a_{H_2O}$ = actual mole fraction of water vapour in the combustion air;
$X^a_{CO_2}$ = actual mole fraction of carbon dioxide in the combustion air;
$X^{A^a}_{O_2}$ = measured mole fraction of oxygen in the combustion air;
$X^{A^e}_{O_2}$ = measured mole fraction of oxygen in the exhaust flow;
$X^{A^a}_{CO_2}$ = measured mole fraction of carbon dioxide in the air;
$X^{A^e}_{CO_2}$ = measured mole fraction of carbon dioxide in the exhaust flow.

The main components of the Cone Calorimeter are given in Figure A.1. They consist of the load cell, the sample, the igniter, the radiating cone and the gas analysis. The sample of 10 by 10 cm is mounted in the sample holder. The sample is placed on the load cell and is heated by the radiating cone, hence the name of the apparatus. The cone is electrically heated, and during the test the surface temperature of the heating element is kept constant. The maximum irradiance to the specimen exceeds $100\,\mathrm{kW/m^2}$, but dependent on the current through the heater any irradiance level between 0 and $100\,\mathrm{kW/m^2}$ can be set. The pyrolysis gases are ignited by a small pilot flame from a gas burner or by an electrical spark igniter. As soon as the sample is burning for longer than 4 s, the ignition source is removed. During the test the mass loss is measured and the gas analyzed. With formula A.2 the heat release rate is calculated.

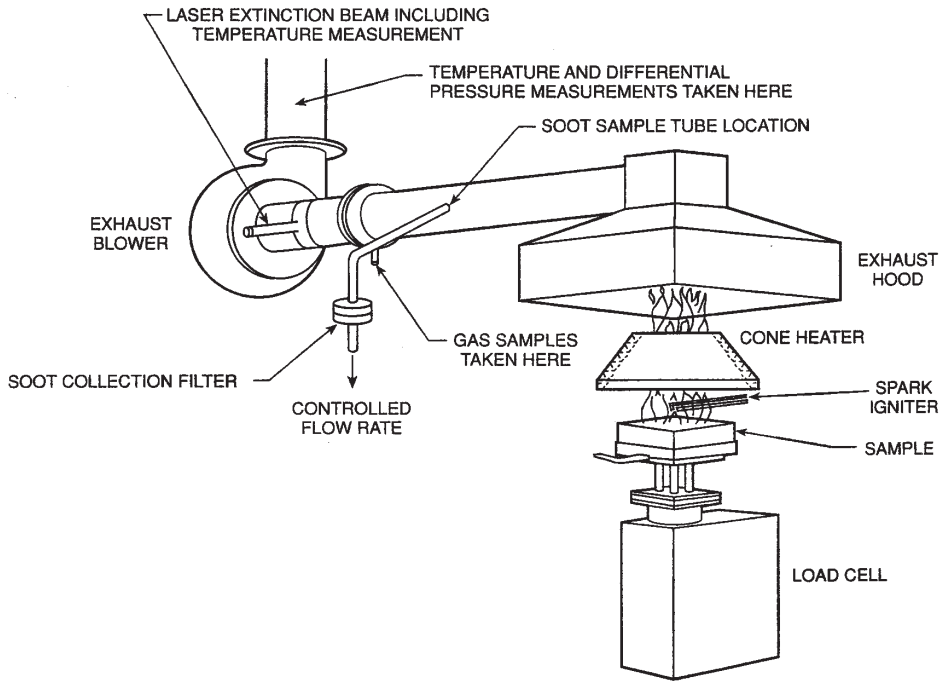

Figure A.1: Schematic view of Cone Calorimeter

Appendix B

Example of determination of global characteristics

Quintiere and Harkleroad have developed a theory for the countercurrent flame spread. The method needs global characteristics that can be determined as follows [92] [93]:

1. Determine the ignition time at different radiation levels in the LIFT apparatus as described in ASTM E-1321. Start at a high heat flux and decrease this flux with steps of 5 kW/m^{2}until no ignition occurs in less than 20 minutes. Determine the minimum flux for ignition, defined as the critical ignition heat flux $\dot{q}''_{cr}$ in step

2. in a graph draw $\dot{q}''_{cr}/\dot{q}''_{e}$ in function of $\sqrt{t_{ig}}$.

3. Draw the best fitting straight line through the results.

4. Determine the parameters b and t^*, as respectively the slope of the line and the intercepts of the line with the horizontal line through the (0,1).

5. Determine the ignition temperature with the following equation:

$$\dot{q}''_{cr} = h_c(T_{ig} - T_\infty) + \sigma(T_{ig}^4 - T_\infty^4) \approx h_r(T_{ig} - T_\infty) \tag{B.1}$$

   where:

   - $\dot{q}'_{cr}$ = the critical ignition heat flux (W/m^2)
   - T_∞ = the ambient temperature (K)
   - T_{ig} = the ignition temperature (K)
   - h_c = the convection coefficient, (= 15 W/m^2)

- h_r = the linearized equivalent convection coefficient where radiation losses are included (W/m^{2}K)
- σ = the constant of Boltzmann (5.67 10^{-8} W/m.K^4)

6. Calculate the apparent $\lambda\rho c$ with:

$$\lambda\rho c = \frac{4}{\pi}(\frac{h_{ig}}{b})^2 \tag{B.2}$$

where:

- λ = the conduction coefficient (W/m^{2}K)
- ρ = the density (kg/m^3)
- c = the specific heat capacity (J/kgK)
- h_{ig} = the convection coefficient at ignition (W/m^{2}K)
- b = the slope of the best fitting line determined in 4 (s$^{-1/2}$)

This method assumes that the material is thermally thick.

Appendix C

n^{th} order polynomial

An n-th order polynomial can be used for the semi-infinite heat-up phase in the "Integral model".
The temperature can be written as:

$$T = \sum_{i=0}^{n} a_i (\delta - x)^i \tag{C.1}$$

Hence the m^{th} derivative, where $0 < m < n$:

$$\frac{\mathrm{d}^m T}{\mathrm{d}x^m} = \sum_{i=m}^{n} (-1)^m \frac{i!}{(i-m)!} a_i (\delta - x)^{i-m} \tag{C.2}$$

The natural and smoothing conditions are:

$$\begin{cases} -\lambda \left(\frac{\mathrm{d}T}{\mathrm{d}x}\right)_{x=0} &= \dot{q}''_{net} \\ \left(T\right)_{x=\delta} &= T_0 \\ \left(\frac{\mathrm{d}^m T}{\mathrm{d}x^m}\right)_{x=\delta} &= 0 \quad \text{for} \quad m = 2, \cdots, n \end{cases} \tag{C.3}$$

From the derivatives at the thermal penetration depth:

$$a_i = 0 \quad \text{for} \quad i = 1, \cdots, n-1 \tag{C.4}$$

while the temperature gives:

$$a_0 = T_0 \tag{C.5}$$

The highest coefficient follows from the boundary condition on the left surface:

$$a_n = \frac{\dot{q}''_{net}}{n \cdot \lambda \cdot \delta^{n-1}} \tag{C.6}$$

The integrated temperature follows from the energy equation:

$$\frac{\mathrm{d}\theta}{\mathrm{d}t} = \frac{\dot{q}''_{net}}{\rho c} \tag{C.7}$$

When the integrated temperature θ is known, the thermal penetration depth follows from substitution of the temperature function:

$$\theta = \int_0^{\delta} (T - T_0)\mathrm{d}x = \int_0^{\delta} a_n(\delta - x)^n \mathrm{d}x = \frac{a_n}{n+1}\delta^{n+1} \tag{C.8}$$

Which gives:

$$\delta = \sqrt{\frac{n \cdot (n+1) \cdot \theta \cdot \lambda}{\dot{q}''_{net}}} \tag{C.9}$$

Bibliography

[1] V. Alexiades and A.D. Solomon. *Mathematical modelling of melting and freezing processes*. Hemisphere Publishing Corporation, 1993.

[2] D.A. Anderson, J.C. Tannchill, and R.H. Pletchen. *Computational Fluid Mechanics and Heat Transfer*. Hemisphere publishing corporation, 1984.

[3] T. Arts and Charbonnier J.-M. Temperature measurements. In Van den Braembussche R., editor, *Measurement techniques in fluid dynamics - An introduction*. von Karman Institute for Fluid Dynamics, 1994.

[4] V. Babrauskas. Development of the cone calorimeter – a standard bench-scale heat release rate apparatus based on oxygen consumption. *Journal of Fire and Materials*, 8:81–95, 1984.

[5] V. Babrauskas. The cone calorimeter. In P.J. DiNenno, editor, *The SFPE handbook of fire protection engineering*, pages 3.37–3.52. National Fire Protection Association, Quincy, MA, USA, 1988.

[6] H.R. Baum and K.B. McGrattan. Simulation of large industrial outdoor fires. In M. Curtat, editor, *Fire Safety Science - Proceedings of the Sixth International Symposium*, pages 611–622. IAFSS, 1999.

[7] H.R. Baum, K.B. McGrattan, and R.G. Rehm. Three dimensional simulations of fire plume dynamics. In Hasemi Y. and Tsukuba, editors, *Fire Safety Science - Proceedings of the Fifth International Symposium*, pages 511–522. IAFSS, 1997.

[8] E.G. Brehob and A.K. Kulkarni. Time-dependent mass loss rate behaviour of wall materials under external radiation. *Fire and Materials*, 17:249–254, 1993.

[9] E.G. Brehob and A.K. Kulkarni. Experimental meausrements of upward flame spread on a vertical wall with external radiation. *Fire Safety Journal*, 31:181–200, 1998.

[10] S.J. Brookes and J.B. Moss. Predictions of soot and thermal radiation properties in confined turbulent jet diffusion flames. *Combustion and Flame*, 116:486–503, 1999.

[11] H.S. Carslaw and J.C. Jaeger. *Conduction of heat in solids*. Oxford University Press, London, 1959.

[12] Y.A. Cengel. *Heat Transfer: A practical approach*. WCB-McGraw-Hill, 1998.

[13] CFX International, AEA Technology, Harwell UK. *CFX-4.2: Solver Manual*, 1997.

[14] G. Cox. Basic considerations. In G. Cox, editor, *Combustion fundamentals of fire*. Academic Press Limited, 1995.

[15] G. Cox. The modelling of fire using computational fluid dynamics. In *Principles and practice of fire modelling*. CMS Press, 1997.

[16] D.R. Croft and D.G. Lilley. *Heat transfer calculations using finite difference equations*. Applied Science Publishers LTD, Barking Essex, England, 1977.

[17] P.S. Cumber and M. Faireweather. Evaluation of participating media models for fire simulation. In M. Curtat, editor, *Fire Safety Science - Proceedings of the Sixth International Symposium*, pages 337–348. IAFSS, 1999.

[18] J.L. de Ris. Spread of laminar diffusion flame. In *Twelfth Symposium (International) on Combustion*, pages 241–252, Pittsburgh, PA, USA, 1969. The Combustion Institute.

[19] J.L. de Ris and Z. Yan. Modeling ignition and pyrolysis of charring fuels. In *Proceedings of the 5th International Conference on Fire and Materials '98*, pages 111–121, San Antonio, TX, USA, 1998.

[20] M.M. Delichatsios, M.K. Mathews, and M.A. Delichatsios. An upward fire spread and growth simulation. In G. Cox and B. Langford, editors, *Fire Safety Science - Proceedings of the Third International Symposium*, pages 207–216. IAFSS, Elsevier Applied Science, N.Y., 1991.

[21] DeNenno, editor. *The SFPE Handbook of fire protection engineering*. NFPA, Quincy, MA, USA, 1988.

[22] C. Di Blasi. Processes of flames spreading over the surface of charring solid fuels: effects of fuel thickness. *Combustion and Flame*, 97:225–239, 1994.

[23] C. Di Blasi. Mechanics of two-dimensional smoldering propagation through packed fuel beds. *Combustion Science and Technology*, 1995.

[24] C. Di Blasi. Reports of university of napels. In *Reaction to fire of combustion products Area B: Fire Modelling*, pages 11–130. Construction Research Communications Ltd., London, 1996.

[25] E. Dick. *Algemene stromingsmechanica*. Academia Press, Gent, Belgium, 1992.

[26] D. Drysdale. *An introduction to Fire Dynamics*. John Wiley and Sons, 1985.

[27] F. Dupuis. Soot production and thermal radiation in turbulent diffusion flames. Master's thesis, School of mechanical engineering, Cranfield University, 1996.

[28] A.C. Fernandez-Pello. The solid phase. In G Cox, editor, *Combustion fundamentals of Fire*, pages 31–101. Academic Press Limited, 1995.

[29] A. Fernando. A cellular automata approach to cfd flame spread modelling. In M. Curtat, editor, *Fire Safety Science - Proceedings of the Sixth International Symposium*, pages 625–636. IAFSS, 1999.

[30] D.F. Fletcher, J.H. Kent, V.B. Apte, and A.R. Green. Numerical simulations of smoke movement from a pool fire in a ventilated tunnel. *Fire Safety Journal*, 23:305–325, 1994.

[31] J.E. Floyd, H.R. Baum, and K.B. McGrattan. A mixture fraction combustion model for fire simulation using cfd. In *International Conference on Engieered Fire Protection Engineers*, pages 279–290, San Francisco, June 2001. CA. Society of Fire Protection Engineers.

[32] R. Font, A. Fullana, J.A. Caballero, J. Candela, and A. Garcia. Pyrolysis study of polyurethane. *Journal of Analytical and Applied Pyrolysis*, 58–59:63–77, 2001.

[33] J. Gibb and P.L. Loyner. Liddell boiler reheat metal temperature: gas side heat transfer analysis. Technical Report Report: R/M/N1029, Central Electricity Generating Board, 1978.

[34] S. Gordon and B.J. McBride. Computer program for calculation of complex chemical equilibrium compositions and applications, analysis. Technical Report NASA Reference Publication 1311, NASA, 1994.

[35] W.L. Grosshandeler. Radcal: A narrow-band model for radiation of calculations in a combustion environment. Technical Report NIST Technical note 1402, National Institute of Standards and Technology, Gaitherburg, MD, USA, 1993.

[36] H.C. Hottel and H.G. Mangelsdorf. Heat transmission by radiation from non-luminous gases ii. experimental study of carbon dioxide and water vapor. *Trans. Am. Inst. Chem. Engng*, 31:517–549, 1935.

[37] F.P. Incropera and D.P. DeWitt. *Fundamentals of heat and mass transfer*. John Wiley & Sons, Inc., 1996.

[38] ISO. Fire test - rate of heat release from building products, iso 5660. Technical report, International Standard Organisation, 1993.

[39] W.S. Janna. *Engineering heat transfer*. Van Nostrand Reinhold, 1986.

[40] M. Janssens. Calorimetry. In P.J. DiNenno, editor, *The SFPE handbook of fire protection engineering*, pages 3.16–3.36. National Fire Protection Association, Quincy, MA, USA, 1988.

[41] M. Janssens. *Fundamental thermophysical characteristics of wood and their role in enclosure fire growth*. PhD thesis, Faculteit van de toegepaste wetenschappen, Universiteit Gent, 1991.

[42] S.-M. Jeng, M.-C. Lai, and G.M. Faeth. Non-luminous radiation in turbulent buoyant axisymmetric flames. *Combustion Science Technology*, 40:41–53, 1984.

[43] F. Jia, E.R. Galea, and M.K. Patel. The prediction of fire propagation in enclosure fires. In *Fire Safety Science- Proceedings of the Fifth international symposium*, pages 439–450. IAFSS, 1997.

[44] F. Jia, E.R. Galea, and M.K. Patel. The numerical simulation of enclosure fires using a cfd fire field model coupled with a pyrolysis based solid fuel combustion submodel - a first approximation. *Journal of Fire Protection Engineering*, 9(4):1–17, 1999.

[45] F. Jia, E.R. Galea, and M.K. Patel. The numerical simulation of fire spread within a compartment using an integrated gas and soid

phase combustion model. *Journal of Applied Fire Science*, 8(4):327–352, 1999b.

[46] F. Jia, E.R. Galea, M.K. Patel, and N. Hoffmann. Combustion model of turbulent diffusion flames. Technical Report Paper No 95/IM/09, Centre of numerical modelling and process analysis, University of Greenwich, 1995.

[47] X. Jiang and W. Fan. Numerical flame spread over solid combustibles in a microgravity environment. *Fire Safety Journal*, 24:279–298, 1995.

[48] W.P. Jones and M. Kakhi. Pdf modeling of finite-rate chemistry effects in turbulent nonpremixed jet flames. *Combustion and Flame*, 115:210–229, 1998.

[49] S. Kaka and Y. Yener. *Heat conduction*. Taylor & Francis, 1993.

[50] C. Kaplan, C.R. Shaddix, and K.C. Smyth. Computations of enhanced soot production in time-varying ch4 / air diffusion flames. *Combustion and Flame*, 106:392–405, 1996.

[51] B. Karlsson. Models for calculating flame spread on wall lining materials and the resulting heat release rate in a room. *Fire Safety Journal*, 23:365–386, 1994.

[52] B. Karlsson and J.G Quintiere. *Enclosure Fire Dynamics*. CRC Press LLC, 1999.

[53] A.I. Karpov and V.K. Bulgakov. Prediction of the steady rate of flame spread over combustible materials. In T. Kashiwagi, editor, *Fire Safety Science - Proceedings of the Fourth International Symposium*, pages 373–384. IAFSS, 1994.

[54] I.M. Kennedy. Models of soot formation and oxidation. *Progress in Energy and Combustion*, 23:95–132, 1997.

[55] I.M. Kennedy, C. Yan, D.C. Rapp, and R.J. Santoro. Modeling and measurements of soot and species in a laminar diffusion flame. *Combustion and Flame*, 107:368–382, 1996.

[56] M. Kokkala. Thermal models of flame spread. In *Reaction to fire of combustion products Area B: Fire Modelling*, pages 364–386. Construction Research Communications Ltd., London, 1996.

[57] M. Kokkala, D. Baroudi, and W.J. Parker. Upward flame spread on wooden surface products: experiments and numerical modelling. In *Fire Safety Science- Proceedings of the Fifth international symposium*, pages 309–320. IAFSS, 1997.

[58] M. Kokkala, E. Mikkola, M. Immonen, H. Juutilainen, P. Manner, and W.J. Parker. Large-scale upward flame spread tests on wood products. Technical Report VTT Research Notes 1834, Technical research centre of Finland, Espoo, Finland, 1997.

[59] A. Kronenburg, R.W. Bilger, and J.H. Kent. Modeling soot formation in turbulent methane-air jet diffusion flames. *Combustion and Flame*, 121:24–40, 2000.

[60] A.K. Kulkarni, E. Brehob, S. Manohar, and R. Nair. Turbulent upward flame spread on a vertical wall under external radiation. Technical Report NIST-GCR-94-638, National Institute of Standards and Technology, Gaithersburg, MD, USA, 1994.

[61] H.C. Kung. A mathematical model of wood pyrolysis. *Combustion and Flame*, 18:185–195, 1972.

[62] H.C. Kung. The burning of vertical wooden slabs. In *15th International Symposium on Combustion*, pages 243–253, Pittsburgh, PA, USA, 1975. The Combustion Institute.

[63] K. Kuo. *Principles of combustion*. John Wiley & Sons, 1986.

[64] M.J. Lewis, J.B. Moss, and P.A. Rubini. Cfd modelling of combustion and heat transfer in compartment fires. In *Fire Safety Science - Proceeding of Fifth International Symposium*, pages 463–475. IAFSS, 1997.

[65] H.H. Liakos, M.A. Founti, and N.C. Markatos. Modelling of stretched natural gas diffusion flames. *Applied Mathematical Modelling*, 24:419–435, 2000.

[66] R.P. Lindstedt. A simple reaction mechanism for soot formation in non-premixed flames. In *Conference on Aerothermo-chemistry in Combustors*, Taipei, Taiwan, June 1991. IUTAM.

[67] F.C. Lockwood and N.G. Shah. A new radiation solution method for incorporation in general combustion prediction procedures. In *18th International Symposium on Combustion*, pages 1405–1414, Pittsburgh, PA, USA, 1981. The Combustion Institute.

[68] M. Luo and V. Beck. The fire environment in a multi-room building - comparison of predicted and experimental results. *Fire Safety Journal*, 23:413–438, 1994.

[69] M. Luo and V. Beck. A study of non-flashover and flash-over fires in a full-scale multi-room building. *Fire Safety Journal*, 26:191–219, 1996.

[70] R.E. Lyon. Heat release kinetics. In *US-Japan UJNR Panel on Fire Research and Safety*. UJNR, 2000.

[71] B.F. Magnussen and B.H. Hjertager. On mathematical modelling of turbulent combustion with special emphasis on soot formation and combustion. In *16th International Symposium on Combustion*, Pittsburgh, PA, USA, 1976. The Combustion Institute.

[72] G.H. Markstein and J. de Ris. Wall-fire radiant emission, part i: Slot-burner flames: comparison with jet flames. In *23d International Symposium on Combustion*, page 1685, Pittsburgh, PA, USA, 1991. The Combustion Institute.

[73] H.E. Mitler. An algorithm to describe the spread of a wall fire under a ceiling. Technical Report NISTIR 5547, National Institute of Standards and Technology, Gaitherburg, MD, USA, 1994.

[74] H.E. Mitler and K.D. Steckler. Spread - a model of flame spread on vertical surfaces. Technical Report NISTIR 5619, National Institute of Standards and Technology, Gaitherburg, MD, USA, 1993.

[75] M.F. Modest. *Radiant Heat Transfer*. McGraw-Hill, New York, 1992.

[76] M.F. Modest. Narrow-band radiative properties and heat transfer models for high-temperature combustion gases, project summary. Mechanical Engineering, Pennsylvania State University, 1998.

[77] B. Moghtaderi, V. Novozhilov, D. Fletcher, and J.H. Kent. An integral model for the transient pyrolysis of solid materials. *Fire and Materials*, 21:7–16, 1997.

[78] D. Morvan, B. Porterie, and J.C. Loraud. Numerical simulation of a buoyant methane-air diffusion flame. In M. Curtat, editor, *Fire Safety Science - Proceedings of the Sixth International Symposium*, pages 277–288. IAFSS, 1999.

[79] J.B. Moss. Turbulent diffusion flames. In G. Cox, editor, *Combustion Fundamentals of Fire*, pages 221–272. Academic Press Limited, 1995.

[80] J.B. Moss and P.A. Rubini. Coupled soot and radiation calculations in a compartment fire. In *Second International Conference of Fire Research and Engineering 10-15 august 1997*, Gaithersburg, Maryland, USA, 1997. NIST.

[81] J.B. Moss, C.D. Stewart, and K.J. Young. Modelling soot formation and burnout in a high temperature laminar diffusion flame burning under oxygen-enriched conditions. *Combustion and Flame*, 101:491–500, 1995.

[82] F.W. Mowrer and R.B. Williamson. Flame spread evaluation for thin interior finish materials. In G. Cox and B. Langford, editors, *Fire Safety Science - Proceedings of the Third International Symposium*, pages 689–698. IAFSS, Elsevier Applied Science, N.Y., 1991.

[83] NFPA. Guide for smoke management systems in malls, atria and large areas. Technical Report NFPA 92B, National Fire Protection Assosciation, 1991.

[84] F.T.M. Nieuwstadt. *Turbulentie, inleiding in de theorie en toepassingen van turbulente stromingen.* Epsilon Uitgaven, Utrecht, 1998.

[85] K.A. Notarianni and D.W. Davis. The use of computer models to predict temperature and smoke movement in high bay spaces. Technical Report NIST 5304, Building and Fire Research Laboratory, National Institute of Standards and Technology, Gaitherburg, MD, USA, 1993.

[86] V. Novozhilov, B. Moghtaderi, D.F. Fletcher, and J.H. Kent. Computational fluid dynamics modelling of wood combustion. *Fire Safety Journal*, 27:69–84, 1996.

[87] T.J. Ohlemiller, T. Kashiwagi, and K.Werner. Wood gasification at fire level heat fluxes. *Combustion and Flame*, 69:155–170, 1987.

[88] W.J. Parker. Prediction of the heat release rate of wood. In C. E. Grant and P.J. Pagni, editors, *Fire Safety Science - Proceeding of First International Symposium*, pages 207–216. IAFSS, Hemisphere Publishing, 1986.

[89] J. Quintiere. Surface flame spread. In P.J. DeNenno, editor, *The SFPE Handbook of Fire Protection Engineering*, page 2.205. National Fire Protection Association, 1995.

[90] J. Quintiere. Some aspects of fire growth. Technical Report NIST GCR 00-795, National Institute of Standard and Technology, Gaithersburg, MD, USA, 2000.

[91] J. Quintiere and T.G. Cleary. Heat flux from flames to vertical surfaces. *Fire Technology*, 30(2):209–231, 1994.

[92] J. Quintiere and M. Harkleroad. New concepts for measuring flame spread properties. Technical Report NBSIR 84-2943, National Institute of Standard and Technology, Gaithersburg, MD, USA, 1984.

[93] J. Quintiere, M. Harkleroad, and W. Walton. Measurements of material flame spread properties. Technical Report NBSIR 82-2557, National Institute of Standard and Technology, Gaithersburg, MD, USA, 1982.

[94] P.R. Ramachandra, R.A. Altenkirch, S. Bhattacharjee, L. Tang, K. Sacksteder, and M.K. Wolverton. The behaviour of flames spreading over thin solids in microgravity. *Combustion and Flame*, 100:71–84, 1995.

[95] R.G. Rehm, K.B. McGrattan, H.R. Baum, and K.W. Cassel. Transport by gravity currents in building fires. In Hasemi Y. and Tsukuba, editors, *Fire Safety Science - Proceedings of the Fifth International Symposium*, pages 391–402. IAFSS, 1997.

[96] B.T. Rhodes. Burning rate and flame heat flux for pmma in the cone calorimeter. Technical Report NIST-GCR-95-664, National Institute of Standard and Technology, Gaithersburg, MD, USA, 1994.

[97] S.J. Ritchie, K.D. Steckler, A. Hamins, T.G. Cleary, J.C. Yang, and T. Kashiwagi. The effect of sample size on the heat release of charring materials. In Hasemi Y. and Tsukuba, editors, *Fire Safety Science - Proceedings of the Fifth International Symposium*, pages 177–188. IAFSS, 1997.

[98] W.M. Rohsenow and J.P. Harnett. *Handbook of heat transfer*. McGraw-Hill, 1973.

[99] K. Saito, F.A. Williams, and J.G. Quintiere. Upward turbulent flame spread. In *Fire Safety Science - Proceedings of the First International Symposium*, pages 75–86. IAFSS, Hemispere Publishing, 1986.

[100] R. Siegel and J.P. Howel. *Thermal Radiation Heat Transfer*. Hemisphere Publishing Corporation, 1992.

[101] G.W.H. Silcock and T.J. Shields. A protocol for analysis of time-to-ignition data from bench scale test. *Fire Safety Journal*, 24:75–95, 1995.

[102] S. Simcox, N.S. Wilkes, and I.P. Jones. Computer simulation of the flows of hot gases from the fire at king's cross underground station. *Fire Safety Journal*, 16:49–73, 1992.

[103] R.F. Simmons. Fire chemistry. In G. Cox, editor, *Combustion fundamental of fire*. Academic Press Limited, 1995.

[104] Y.L. Sinai. Exploratory cfd modelling of pool fire instabilities without cross-wind. *Fire Safety Journal*, 35:51–61, 2000.

[105] E. Smith. Mathematical model of a fire in a compartment having combustible walls and ceiling. In *Series 248, 81*, pages 64–74. American Institute of Chemical Engineers, 1985.

[106] N. Soonil and G.B. Robert. Numerical simulation of thermal plumes. *Fire Safety Journal*, 21:231–256, 1993.

[107] D.B. Spalding. Mixing and chemical reaction in steady confined turbulent flames. In *Thirteenth Symposium (International) on Combustion*, pages 649–657, Pittsburgh, PA, USA, 1971. The Combustion Institute.

[108] M.J. Spearpoint. Predicting the ignition and burning rate of wood in the cone calorimeter using an integral model. Technical Report NIST GCR 99-775, National Institute of Standard and Technology, Gaithersburg, MD, USA, 1999.

[109] M.J. Spearpoint and J.G. Quintiere. Predicting the burning of wood using an integral model. *Combustion and Flame*, 123:308–324, 2000.

[110] M.J. Spearpoint and J.G. Quintiere. Predicting the piloted ignition of wood in the cone calorimeter using an integral model - effect of species, grain orientation and heat flux. *Fire Safety Journal*, 36:391–415, 2001.

[111] B. Sundstroöm. Full scale fire testing of surface materials. Technical Report SP Report 1986:45, SP Swedish National Testing and Research Institute, Fire Technology, 1986.

[112] P.A. Tesner, T.D. Snegiriova, and V.G. Knorre. Kinetics of dispersed carbon formation. *Combustion and Flame*, 17:253–260, 1971.

[113] ASTM Fire test standards. Test method for heat and visible smoke release rate for materials and products using an oxygen consumption calorimeter, astm e 1354-93. American Society for Testing and Materials, 1993.

[114] E. Theuns, J. Vierendeels, and P. Vandevelde. A moving grid model for the pyrolysis of charring materials. *International Journal of Numerical Methods for Heat & Fluid flow*, 12(5):541–559, 2002.

[115] J.S. Truelove. Mixed grey gas model for flame radiaton. Technical Report Report AERE HL 76/3448, UK Atomic Energy Authority, 1976.

[116] H. Tuovinen and M. Simonson. Incorporation of detailed chemistry into cfd modelling of compartments fires. Technical Report SP Report 1999:03, SP Swedish National Testing and Research Institute, Fire Technology, 1999.

[117] P. Van Hees. *Meestroomvlamuitbreiding bij vloerbekledingen Ontwikkeling en validatie van grootschalige en kleinschalige meettechnieken*. PhD thesis, Faculteit van de Toegepaste Wetenschappen, Universiteit Gent, 1995.

[118] P. Van Hees, J. Axelsson, A.M. Green, and S.J. Grayson. Mathematical modelling of fire development in cable installations. *Fire and Materials*, 25:169–178, 2001.

[119] H.K. Versteeg and W. Malalasekera. *An introduction to Computational Fluid Dynamics -The Finite Volume Method*. Logman Scientific and Technical, 1995.

[120] C. Vovelle and R. Akrich J.L. Delfau. Mass loss rate measurements on solid materials under radiative heating. *Combustion Science and Technology*, 36:1–18, 1984.

[121] J. Warnatz, U. Maas, and R.W. Dibble. *Combustion, Physical and chemical fundamentals, modelling and simulation, experiments, pollutant formation*. Springer-Verlag, Berlin Heidelberg, 1999.

[122] D.C. Wilcox. *Turbulence modelling for CFD*. DCW Industries, 1993.

[123] P.J. Woodburn and R.E. Britter. Cfd simulation of a tunnel fire- part 1. *Fire Safety Journal*, 26:35–62, 1996.

[124] H. Xue, J.C. Ho, and Y.M. Cheng. Comparison of different combustion models in enclosure fire simulation. *Fire Safety Journal*, 36:37–54, 2001.

[125] Z. Yan. *Numerical modeling of turbulent combustion of flame spread.* PhD thesis, Center of Combustion Science and Technology, Department of Fire Safety Engineering, Lund University, Sweden, 1999b.

[126] Z. Yan and G. Holmstedt. Cfd and experimental studies of room fire growth on wall lining materials. *Fire Safety Journal*, 27:201–238, 1996.

[127] Z. Yan and G. Holmstedt. Cfd simulation of upward flame spread over fuel surface. In *Fire Safety Science- Proceedings of the Fifth international symposium*, pages 345–356. IAFSS, 1997.

[128] Z. Yan and G. Holmstedt. Three-dimensional computation of heat transfer form flames between vertical parallel walls. *Combustion and Flame*, 117:574–588, 1999.

[129] R. Yuen, R. Casey, G. De Vahl Davis, E. Leonardi, G.H. Yeoh, V. Chandrasekaran, and S.J. Grubits. A three-dimensional mathematical model for the pyrolysis of wet wood. In Y. Hasemi, editor, *Fire Safety Science- Proceedings of the Fifth international symposium*, pages 189–200. IAFSS, 1997.

[130] X.Y. Zhou and J.C.F Pereira. Comparison of four combustion models for simulating the premixed combustion in inert porous media. *Fire and Materials*, 22:187–197, 1998.

[131] X.Y. Zhou and J.C.F. Pereira. A multidimensional model for simulating vegetation fire spread using a porous media sub-model. *Fire and Materials*, 24:37–43, 2000.